PLANAR BEAM-STEERED ACOUSTO-OPTIC LIGHT DEFLECTORS

by

Ernest Bruno Riemann

B.Eng. (Physics), McMaster University, 1969

M.A.Sc., University of British Columbia, 1972

A THESIS SUBMITTED IN PARTIAL FULFILMENT OF

THE REQUIREMENT FOR THE DEGREE OF

DOCTOR OF PHILOSOPHY

in

THE FACULTY OF GRADUATE STUDIES

(Department of Electrical Engineering)

We accept this thesis as conforming to

the required standard

THE UNIVERSITY OF BRITISH COLUMBIA

June, 1977

In presenting this thesis in partial fulfilment of the requirements for an advanced degree at the University of British Columbia, I agree that the Library shall make it freely available for reference and study. I further agree that permission for extensive copying of this thesis for scholarly purposes may be granted by the Head of my Department or by his representatives. It is understood that copying or publication of this thesis for financial gain shall not be allowed without my written permission.

Department of E. E.

The University of British Columbia
2075 Wesbrook Place
Vancouver, Canada
V6T 1W5

Date 4/22/78

ABSTRACT

A theoretical and experimental study has been made of planar acousto-optic light deflectors with particular emphasis on acoustic beam steering as a means of improving device performance. The theoretical model takes into account the electrical drive characteristics of beam-steered interdigital surface acoustic wave (SAW) transducers, anisotropic diffraction of acoustic waves and the rigorous theory of the interaction between guided optical waves and high frequency surface acoustic waves.

The experiments were carried out on nickel indiffused waveguides on Y-cut $LiNbO_3$ substrates. A four-section, three finger pair transducer array was used to launch acoustic waves with propagation direction centered at 21.8° from the Z axis. A center frequency of 200 MHz was chosen as a compromise between high acousto-optic bandwidth and ease of fabrication. The deflector had a bandwidth of more than 60 MHz and gave 44 resolvable spots with an optical wave 2.5 mm wide. The observed frequency response of the diffraction efficiency was in excellent agreement with the theory. It was concluded that beam steering is an advantageous technique for devices requiring large bandwidth and high diffraction efficiency.

TABLE OF CONTENTS

Page

LIST OF TABLES

LIST OF ILLUSTRATIONS

NOMENCLATURE

Chapter 2.

A,B	amplitude coefficients of OWG TE modes
Ai	Airy function
c	velocity of light in free space
d	OWG thickness
D	gap between OWG and prism coupler
E	electric field
k	OGW propagation vector
ℓ	length of coupling region on prism base
m	OGW mode index
n_a	refractive index of air
n_e	extraordinary index
n_m	OGW mode index
n_o	index at graded-index OWG surface; also ordinary index
n_p	prism coupler index
n_s	substrate index
P	power/unit width carried by a guided TE mode
V	phase velocity of light in substrate
W	width of incident light beam
W_p	width of light beam on prism base
y_m	WKB turning point
y_o	last zero crossing of WKB solution
Z_m	normalized WKB turning point
α	prism angle
α_c	prism coupler radiation-loss coefficient
β	z component of OGW propagation vector
η_t	prism coupler efficiency

(Chapter 2.)

θ	angle of light incidence on prism base
θ_m	internal angle of incidence of OGW on waveguide surface
λ	light wavelength in free space
μ	angle of light incidence on couping prism
μ_o	permeability of free space
ω	angular frequency of light waves

Chapter 3.

a	IDT electrode metallization factor
A	IDT finger width (Section 3.4) SAW amplitude (Section 3.5)
A_{kq}, B_{kq}	SAW partial wave amplitudes
b	constant in parabolic velocity surface approximation
B_a	IDT radiation susceptance
c_{ijkl}	elastic stiffness constants
C_T	IDT static capacitance
D_i	electric displacement
e_{ijk}	piezoelectric constants
E_i	SAW electric field
f	SAW frequency
f_o	IDT center frequency
G_a	IDT radiation conductance
G_o	IDT radiation conductance at f_o
J_1	first order Bessel function of the first kind
K	SAW wavevector
K(q),K(q)	complementary elliptic integrals of the first kind
L_s, L_p	series and parallel IDT matching inductors

(Chapter 3.)

N	number of IDT finger pairs
P_a	acoustic power
P_{ea}	electrical part of acoustic power
P_{ma}	mechanical part of acoustic power
Q_a, Q_e	acoustic and electrical IDT quality factors
r_f	Fresnel distance
R_a	IDT radiation resistance
R_e	IDT finger series resistance
R_o	radiation resistance at f_o
$\mathrm{sinc}(x)$	$\sin(x)/x$
S_{ij}	acoustic strain
t	IDT metallization thickness
T_{ij}	acoustic stress
u_i	particle displacement from equilibrium
v	SAW velocity
V, V_o, V_f	r.m.s. voltage
W	IDT radiating aperture
X_a	radiation reactance
Z	complex impedance
Δ	$\Delta v/v$, the change in SAW velocity when the substrate surface is covered with an ideal,massless conductor.
ε_{ij}	permittivity constants
Λ	SAW wavelength
Ω	SAW angular frequency
ϕ	angle between SAW propagation vector and the power flow direction
Φ	SAW electric potential field

(Chapter 3.)

ρ	density in equation 3.4 resistivity in equation 3.44
ρ_s	sheet resistivity

Chapter 4.

A	width of diffracted light beam aperture
$\hat{\hat{B}}$	inverse dielectric permittivity tensor
D	width of radiating aperture of one section of beam -steered transducer
$\vec{E}$	OGW electric field vector
$\tilde{E}_i^r$	real part of SAW electric field
$E_i^r(y)$	amplitude of SAW electric field
f	acoustic frequency
f_h, f_ℓ	high and low frequencies at which the Bragg angle is matched
Δf_m	deflector Bragg bandwidth
f_1	IDT array frequency
G	width of one section of beam-steered IDT, including electrodes
H	beam-steered IDT step height between adjacent sections
i	electric current
$\vec{k}_0$	incident OGW wavevector
$\vec{k}_1$	wavevector of first-order diffracted beam
$\vec{K}$	SAW wavevector
ℓ	diffraction order number
L	acousto-optic interaction length
m	TE mode index
M	number of sections in beam-steered IDT
n	refractive index
N	superscript denoting normalized

(Chapter 4.)

N_s	number of resolvable spots
P_a	acoustic power
P_e	electrical power dissipated in IDT
P_{100}	acoustic power for 100% diffraction efficiency
p_{ijkl}	photoelastic constants
P	integer number of $\Lambda_o/2$ steps in H
$\tilde{S}_i^r$	real part of acoustic strain
$S_i^r(y)$	amplitude of real part of acoustic strain
$U_m(y)$	normalized OGW electric field as a function of depth
r_{ijk}	electooptic constants
$\vec{x}$	radius vector
$\|Z\|$	magnitude of impedance
Γ_{nOp}	acousto-optic overlap integral
$\delta\varepsilon_{ij}$	permittivity change for acousto-optic interaction
$\Delta\theta$	difference between incident and Bragg angles
$\Delta\phi$	angular width of diffracted light beam
$\hat{\varepsilon}$	relative permittivity tensor
$\hat{\varepsilon}_s$	substrate relative permittivity
η	acousto-optic diffraction efficiency
η_b	beam-steered deflector diffraction efficiency
η_o	diffraction efficiency when $\Delta\theta=0$
θ_b	Bragg angle
θ_o	light angle of incidence to SAW planes of constant phase
θ_1	angle of propagation of first order diffracted beam
ρ_c	complex transmission line reflection coefficient
τ	transit time of sound wave across light beam
$\phi_b(f)$	Bragg angle as a function of frequency

(Chapter 4.)

$\phi_{\ell}(f)$	coupling constant for ℓ^{th} diffraction order
$\phi_{o}(f)$	angle of propagation of principal maximum of array function
ω_{o}	angular frequency of incident light
ω_{1}	angular frequency of first-order diffracted light
Ω	SAW angular frequency

ACKNOWLEDGEMENT

I thank my supervisor, Dr. L. Young, for his support and guidance during the course of this research. Mr. Arvid Lacis did the scanning electron microscopy and electron microprobe analysis. Helpful suggestions and assistance were received from Mr. Rodger Bennet and Mr. Peter Musil on the cutting and polishing of crystals, and from Mr. Jack Stuber in the machine shop. Professor R. Butters helped with the x-ray fluorescence measurements. Special thanks are due to Dr. E.V. Jull and Mr. Hans Hogenboom for numerous helpful discussions, and to Miss Sannifer Louie for typing the thesis. Financial support of the National Research Council of Canada, through a Science Scholarship and also Grant No. A3392, is gratefully acknowledged.

1. INTRODUCTION

The principal objective of this thesis was to do a combined theoretical and experimental study of acoustic beam steering as a means of improving the performance of planar acousto-optic light deflectors. In an increasingly digital age, integrated optics and surface acoustic wave (SAW) devices are among the few analog technologies likely to remain competitive. In addition to potential applications as light switches, deflectors and modulators, the devices studied here promise the realization of more complex signal processing functions such as convolution and spectral analysis on an essentially real-time basis [75].

The technology of bulk acousto-optic devices for the deflection and modulation of light is reasonably well developed [92]. The planar geometry utilizing surface optical waveguides and acoustic surface waves promises to give devices that are physically smaller, more efficient and that have higher performance than their bulk counterparts.

A review of selected topics of the theory of dielectric slab waveguides is presented in Chapter 2. Techniques for the fabrication of high quality optical waveguides (OWG) in $LiNbO_3$ by nickel indiffusion are given. Methods for coupling to optical waveguides are discussed, and the design and fabrication of rutile coupling prisms is described. The measured properties of a 6-mode OWG are given and the electric field distributions of the three guided TE modes are calculated by the WKB method.

In Chapter 3, the properties of interdigital transducers and acoustic surface waves on $LiNbO_3$ are reviewed, and an experiment testing the theory is described. The theory of the surface wave acousto-optic interaction is presented in Chapter 4. Expressions describing the far-field acoustic radiation pattern of beam-steered interdigital transducers

are developed, as are equations for predicting the performance characteristics of planar beam steered light deflectors. The diffraction efficiency is calculated from first principles, using the photoelastic and electrooptic properties of $LiNbO_3$ and the detailed description of the OGW and SAW radiation fields. Several experiments are described, and the results are compared with theoretical calculations.

In Chapter 5, techniques for making high resolution photomasks and for fabricating interdigital transducers are discussed.

2. DIELECTRIC OPTICAL WAVEGUIDES

2.1 Uniform Dielectric Slab Waveguides

Consider the asymmetrical dielectric slab illustrated in Fig. 2.1. The refractive indices in the three regions indicated are related by the inequality

$$n_m > n_s > n_a,$$

where n_m is the mode index of the mth guided optical mode. If we restrict our consideration to guided TE waves propagating in the z direction, the wave equation reduces to

$$\frac{\partial^2 E_x}{\partial z^2} + \frac{\partial^2 E_x}{\partial y^2} = \frac{n^2}{c^2}\frac{\partial^2 E_x}{\partial t^2} .$$

For time harmonic fields with propagation constant β in the z direction, the wave equation becomes

$$\frac{d^2 E_x}{dy^2} + (n^2 k^2 - \beta^2) E_x = 0 \qquad (2.1)$$

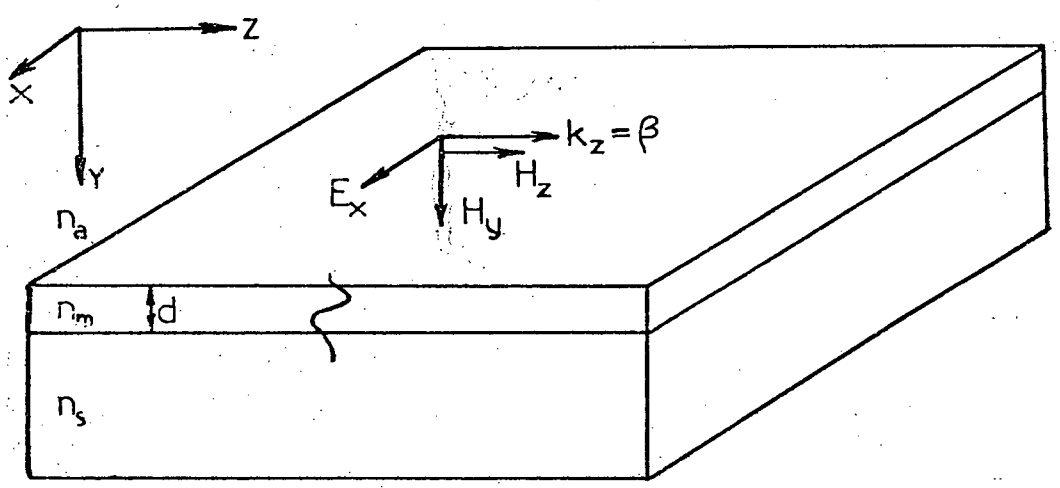

Fig. 2.1 Slab Dielectric Waveguide.

Boundary conditions require that E_x and H_z be continuous at y = 0 and y = d, and that E_x vanish at $y = \pm\infty$. Solutions satisfying these requirements have been shown [1] to take the form

$$\begin{aligned} E_x &= A\exp(\delta y), && y \le 0 \\ &= A\cos(\kappa y) + B\sin(\kappa y), && 0 \le y \le d \\ &= (A\cos(\kappa d) - B\sin(\kappa d))\exp[-\gamma(y+d)], && d \le y \le \infty \end{aligned} \tag{2.2}$$

where

$$\begin{aligned} \delta &= (\beta^2 - n_a^2 k^2)^{1/2} \\ \kappa &= (n_m^2 k^2 - \beta^2)^{1/2} \\ \gamma &= [(n_m^2 - n_s^2)k^2 - \kappa^2]^{1/2} \end{aligned} \tag{2.3}$$

and where $\vec{k}$ is the wavevector in free space. This solution is mathematically identical with that for the quantum mechanical problem of a particle incident on a square potential well.

Continuity requirements on H_z give the eigenvalue equation

$$\tan(\kappa d) = \kappa(\gamma + \delta)/(\kappa^2 - \gamma\delta),$$

thereby limiting wave propagation to a discrete spectrum of guided modes. In addition, it can be shown [1] that the waveguide also supports a continuous spectrum of radiation modes, which form a complete orthonormal set together with the discrete modes. The propagation vector of the guided wave has the magnitude

$$\beta = n_m k \sin\theta_m \tag{2.4}$$

along the direction of propagation, where θ_m is the angle between $\vec{k}$ and y.

Examination of equation (2.3) reveals that γ becomes imaginary when $\beta < n_{Si}k$; as a result, the guided mode becomes radiative and confinement is no longer possible. Thus, $\gamma = 0$ is the cutoff condition for wave guidance. The equation

$$\tan(\kappa d_c) = \delta/\kappa \tag{2.5}$$

can then be used to determine the minimum thickness d_c that will support a particular guided mode. It is interesting to note that a symmetrical waveguide ($n_a = n_s$) always has at least one guided mode [1]. As the guiding layer becomes thinner, proportionately more power is carried by the evanescent fields.

A more intuitive treatment of wave guidance is based on a ray-optic approach to light propagation in the waveguide. Consider a wave in the guiding layer incident on the air-waveguide interface at an angle θ_m.

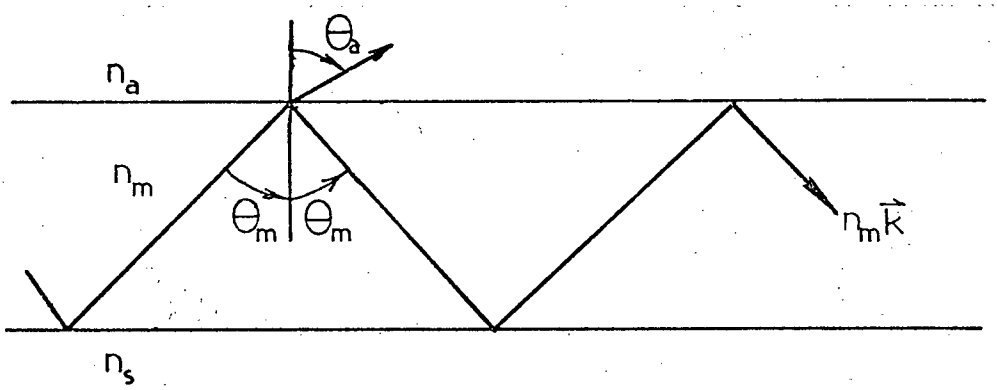

Fig. 2.2 Zig-Zag Wave Propagation.

Snell's law is

$$n_m \sin\theta_m = n_a \sin\theta_a.$$

When $n_m \sin\theta_m > n_a$, critical internal reflection occurs and the wave cannot escape from the waveguide. At the lower interface, the equivalent condition is

$$n_m \sin\theta_m > n_s.$$

Since $n_s > n_a$, satisfaction of the second inequality implies satisfaction of the first. Thus, three kinds of propagating modes are obtained:

(1) air modes, when $n_m \sin\theta_m < n_a$,

(2) substrate modes, when $n_s > n_m \sin\theta_m > n_a$,

and (3) guided modes when $n_m \sin\theta_m > n_s$.

Propagation of guided modes is possible only when the multiple reflections of plane waves from the waveguide surfaces are in phase. This imposes the eigenvalue condition

$$2kn_m d \cos\theta_m - 2\phi_{ms} - 2\phi_{ma} = 2m\pi \ , \qquad (2.6)$$

where ϕ_{ms} and ϕ_{ma} are the phase shifts on reflection at the air and substrate interfaces, respectively. The vertical component of the guided mode forms a standing wave between the waveguide boundaries, so that propagation appears to be in the horizontal direction only.

For a limited waveguide thickness d, only a limited number of integer values of m will satisfy the phase matching condition (2.6). In fact, when the appropriate expressions for ϕ_{ms} and ϕ_{ma} are substituted into (2.6), the eigenvalue equation (2.3) is obtained.

2.2 Modes in Graded Index Waveguides

Diffusion is a convenient technique for making high quality optical surface waveguides. It is particularly advantageous for acousto-optic devices, since a high degree of overlap between the acoustic surface wave and optical fields is possible. However, the description of guided modes is considerably more difficult, owing to the non-uniform refractive index profile obtained. As a result of either in- or out-diffusion, the refractive index near the surface takes the form

$$n(y) = n_s + \Delta n \, f(y) \qquad (2.7)$$

where n_s is the substrate index, $\Delta n = n_o - n_s$ is the change in index at the surface, and the exact form of f(y) depends on the details of the

diffusion process. Waveguides with Gaussian [3], erfc [3,4] and Fermi function refractive index profiles have been reported. In general, the solution for the electric field of a graded index waveguide takes the form

$$E(y,z,t) = E_x(y)\, e^{j(\beta z-\omega t)}. \tag{2.8}$$

Substitution into the one-dimensional wave equation gives

$$\frac{d^2E_x}{dy^2} + \kappa^2(y)\, E_x = 0, \tag{2.9}$$

where $\kappa^2(y) = n^2(y)k^2 - \beta_m^2$.

For most index profiles of interest, solution in terms of known functions is not possible. Exact solutions have been obtained for an exponential permittivity profile by Conwell [6] and a piecewise-linear permittivity profile by Marcuse [9]. Otherwise, it is expedient to solve instead the equation

$$\frac{d^2E_x}{dy^2} + [\kappa^2(y) - \sqrt{\kappa(y)}\,\frac{d^2}{dy^2}\,(\frac{1}{\sqrt{\kappa(y)}})]E_x = 0,$$

solutions of which closely approximate the exact solutions under appropriate conditions. This is the WKB method of Quantum Mechanics, for which the following solutions for TE guided modes [7,9] are obtained:

$$E_x = A\exp(\gamma y) \qquad y \le 0 \tag{2.10}$$

$$E_x = B\sqrt{\kappa_o/\kappa(y)}\; A\cos(\phi(y) - \pi/4) \qquad y_m > y \ge 0 \tag{2.11}$$

$$E_x = \frac{B}{2j}\sqrt{\kappa_o/\kappa(y)}\; A\exp\{\int_{y_m}^{y}|\kappa(y)|\,dy\} \qquad \infty \ge y > y_m \tag{2.12}$$

where

$$\gamma^2 = \beta_m^2 - k^2, \tag{2.13}$$

$$\kappa_o^2 = n_o^2k^2 - \beta_m^2, \tag{2.14}$$

$$\kappa^2(y) = n^2(y)k^2 - \beta_m^2 , \tag{2.15}$$

$$\phi(y) = \int_y^{y_m} \kappa(y)\,dy , \tag{2.16}$$

A and B are constants, k is the wavevector in free space, n_o is the surface index and β_m is the z-component of the propagation vector of the TE_m mode. The solution is oscillatory over the interval $(0,y_m)$ and decays to zero on either side.

The turning point of the mth mode is y_m, defined by $\kappa(y_m) = 0$; it marks the division between oscillatory and exponential behaviour.

The WKB method is only usable (Schiff [8]) if $\kappa(y)$ changes slowly with y. The condition for this may be written as

$$\left|\frac{d\kappa}{dy}\right| << \kappa/\lambda \tag{2.17}$$

At the turning point (y_m), this condition is violated, and the solutions (2.12) have validity only in an asymptotic sense within several wavelengths of y_m. This restricts the accuracy of solution, particularly for lower order modes. Conwell, however has stated that even in this case the solutions obtained are often of reasonable accuracy. For higher order modes, good accuracy is obtainable. Special techniques must be used in the vicinity of y_m the turning point, where there is a pole in E_x.

Hocker and Burns [10] have shown that the modes of diffused waveguides can be described by just two quantities, an effective diffusion depth which can conveniently be chosen to be y_m, and an effective mode index,

$$n_m = \beta_m/k . \tag{2.18}$$

Marcuse [9] has analysed the TE modes of graded index slab waveguides with the WKB method and a piecewise-linear approximation of

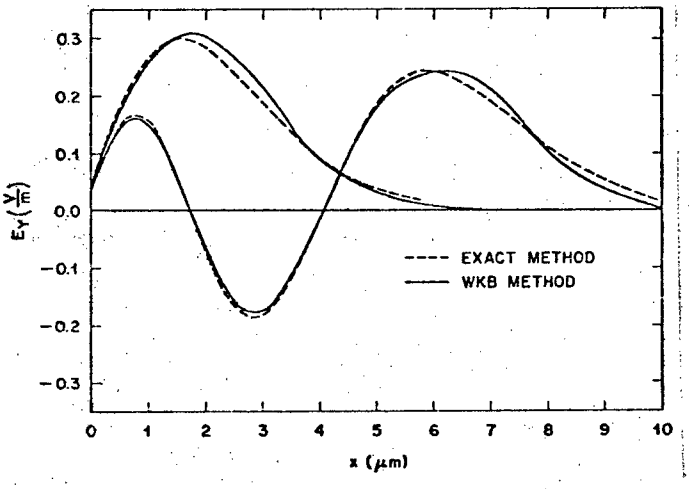

Fig. 2.3 Comparison between WKB and Exact Solutions (after Marcuse [9]).

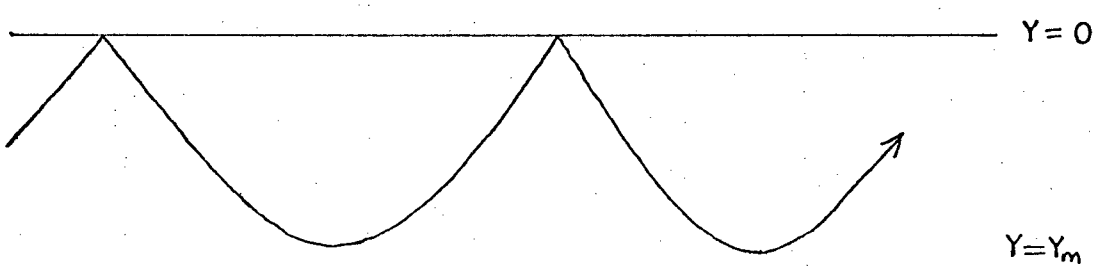

Fig. 2.4 Zig-Zag Wave Propagation in Graded Index Waveguides.

the index profile. The solutions were found to be in close agreement with exact solutions of the piecewise-linear permittivity profile, and less cumbersome mathematically (fig. 2.3).

Comparison of eqs. (2.10)-(2.16) with the TE modes of a uniform slab waveguide reveals the greater mathematical complexity of the graded-index solutions. Numerical methods of analysis are usually required. The ray-optic picture of wave guidance is also more difficult to apply, since the "reflection" from the bottom waveguide surface is gradual rather than instantaneous (Fig. 2.4). Tien et al [5] have shown that the phase shift on reflection is very nearly $\pi/4$ at y_m and $\pi/2$ at

$y = 0$. Using this, White and Heidrich developed a method of determining the turning points y_m of the WKB method, given the mode indices $n_1, n_2 \ldots n_m$. Equation (2.16) then takes the form [11]

$$\frac{\phi(0)}{2} = \int_0^{Z_m} (n^2(Z) - n_m^2)^{1/2}\, dZ = \frac{4m - 1}{8}$$

where $m = 1, 2 \ldots M$, and where $Z = y/\lambda$. Use of the piecewise-linear approximation gives the following solution for the turning points Z_m of the mth guided mode:

$$Z_1 = \frac{9}{16}\left(\frac{n_o + 3n_1}{2}\right)^{-1/2}(n_o - n_1)^{-1/2}, \quad (m = 1) \tag{2.19}$$

$$Z_m = Z_{m-1} + \left[\frac{3}{2}\left(\frac{n_{m-1} + 3n_m}{2}\right)^{-1/2}(n_{m-1} - n_m)^{-1/2}\right]\left\{\left(\frac{4m-1}{8}\right) - \frac{2}{3}\sum_{k=1}^{m-1}\right.$$

$$\left.\left(\frac{n_{k-1} + n_k}{2} + n_m\right)^{1/2}\left(\frac{Z_k - Z_{k-1}}{n_{k-1} - n_k}\right) \times \left[(n_{k-1} - n_m)^{3/2} - (n_k - n_m)^{3/2}\right]\right\},$$

$$m = 2, 3 \ldots M \tag{2.20}$$

where $Z_o = 0$ and $n_o = n(0)$. Note that $m = 1$ for the zeroth order mode. These equations require an estimate of the surface index n_o as well as the mode indices n_m, so that successive Z's may be calculated by iteration.

In order to determine whether the estimate of n_o is reasonable, the sum of squares of the second differences,

$$r^2 = \sum_{k=0}^{M-2}\left[\frac{\dfrac{n_{k+2} - n_{k+1}}{Z_{k+2} - Z_{k+1}} - \dfrac{n_{k+1} - n_k}{Z_{k+1} - Z_k}}{\dfrac{Z_{k+2} + Z_{k+1}}{2} - \dfrac{Z_{k+1} + Z_k}{2}}\right]^2, \tag{2.21}$$

is calculated. The minimum in r^2 corresponds to the smoothest index profile, and the corresponding value of n_o was somewhat arbitrarily selected by White and Heidrich to be the best one.

The index profile obtained can then be used with (2.10) to (2.16) to calculate the electric field distributions of the modes, either by assuming a piecewise-linear profile or by fitting a function (i.e., erfc) to the points obtained.

2.3 Coupling to Optical Waveguides

Coupling to guided optical modes presents some difficulty, owing principally to the small (often less than 10 μm) dimensions of optical waveguides. Initially, lenses (Fig. 2.5) were used to reduce the diameter of light beams. Low coupling efficiency and a lack of selectivity in exciting guided modes made this an unsatisfactory method.

The prism coupler, announced by Tien and also Harris and Schubert in 1969, overcame these limitations. In Fig. 2.6, light enters a prism with refractive index n_p, where $n_p > n_m$, at an angle μ such that it is critically internally reflected at the prism base. If the spacing between prism and the optical waveguide is about $\lambda/2$ or less, coupling of light energy into the waveguide is possible, through overlap of the evanescent fields of the reflected light outside the prism base and guided modes of the film. Mathematically, this mechanism of energy transfer resembles the quantum mechanical tunneling of a particle through a potential barrier; consequently, it is frequently called optical tunneling. Coupling can only occur if the horizontal electric field component of light at the prism base matches that of a guided mode. This may be expressed by the phase matching condition for the mth guided mode:

$$\beta_m = k\, n_p \sin\theta_m, \tag{2.22}$$

where β_m is the horizontal component of the guided wavevector. The mode index n_m is

$$n_m = \frac{\beta_m}{k} = n_p \sin\theta_m \cdot \qquad (2.23)$$

Thus, it is possible to selectively excite any one particular guided mode by varying the angle of incidence θ of light on the prism base, provided that the indices of adjacent modes are sufficiently different. A number of theoretical treatments of coupling efficiency have been published [2,9,16,17]. Most of these deal with the special case of a uniform or Gaussian light beam intensity profile coupling into a uniform dielectric slab waveguide, in which case the maximum attainable coupling efficiency is about 80%. By altering the beam profile and/or tapering the gap between waveguide and prism, 100% efficiency is theoretically possible, and over 90% has been achieved experimentally. Marcuse [9] gives a method of estimating the coupling efficiency to a graded-index slab waveguide. For high coupling efficiency, the mode and prism index must be very closely matched.

In practice, the prism is held in close proximity to the waveguide by the use of an adjustable clamp. Because of nonuniformities in the mechanical contact between prism and guide, coupling efficiencies of over 25% are difficult to achieve, particularly for light beams more than 1 mm in diameter.

A number of otherssuccessful optical couplers have been developed. Dakss et al [18] announced the grating coupler (Fig. 2.7) in 1970. An optical grating of periodicity 0.67 μm was formed in photoresist on the waveguide surface by exposure in a laser interferometer. A more recent fabrication technique employs sputter etching of the resist pattern, thus etching the grating into the waveguide itself. The phase matching condition for grating couplers is

$$\beta_m = k \sin\theta + 2m\pi/d, \qquad (2.24)$$

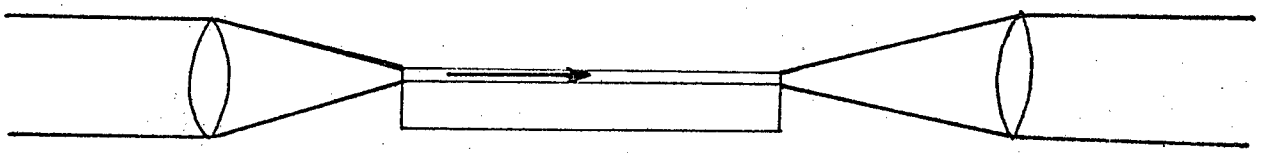

Fig. 2.5 Lens Coupler.

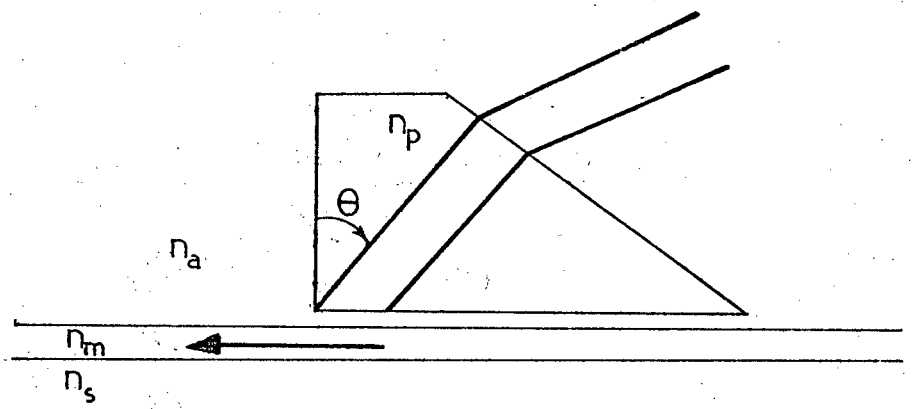

Fig. 2.6 Prism Coupler.

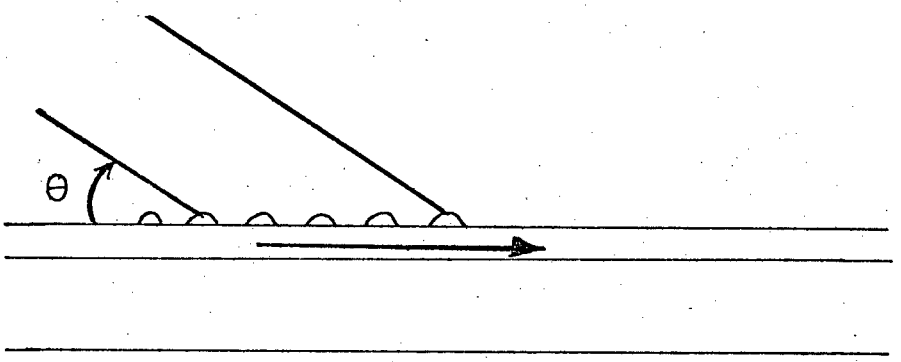

Fig. 2.7 Grating Coupler.

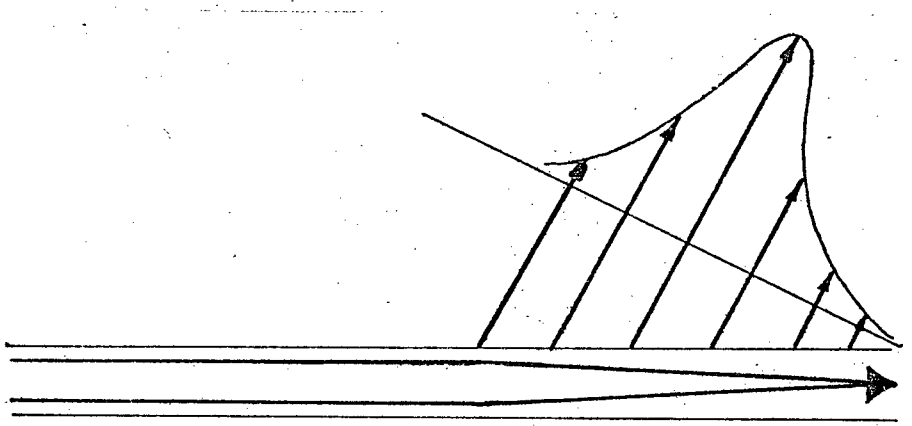

Fig. 2.8 Generalized Leaky Wave Coupler.

where d is the grating period and θ the angle of incidence. Selective mode coupling is again possible. The maximum efficiency observed by Dakss et al was 40%; with suitable techniques, 100% is theoretically possible.

The grating coupler is mechanically more stable than the prism coupler, and coupling over larger areas is easy to achieve. Prism couplers, however, have the advantage that they are not attached to the waveguide and can easily be moved to different orientations.

At the OSA meeting on Integrated Optics in 1972, Tamir and Bertoni presented a unified theory of coupling to optical waveguides. If the medium adjacent to the waveguide surface has suitable structure, an optical waveguide is capable of supporting the propagation of either a guided wave or a leaky surface wave. The leaky wave propagates with a field variation $\exp(i\beta' - \alpha)z$, where α is an attenuation constant denoting the loss of energy to regions adjacent to the guide. If α is suitable, this leakage will give rise to a beam of light propagating out of the guide at an angle θ, determined by a phase matching condition similar to (2.23) or (2.24), depending on details of the structure adjacent to the guide. Because the leaky wave decays exponentially, the emerging beam has a non-uniform intensity profile, as illustrated in Fig. 2.8. In general, the leaky wave can be supported by either multi-layered (i.e., prism) or periodic (i.e., grating) structures. By reciprocity, light can be coupled into the waveguide by reversing the propagation direction; however, for maximum coupling efficiency, the incident beam intensity profile must have the shape illustrated in Fig. 2.8. Thus, for optimal coupling from a Gaussian or uniform beam profile, it is necessary to taper α along the direction of guided mode propagation such that the required input beam profile is symmetric.

2.4 Prism Coupler Design

Prisms suitable for coupling to Ni/$LiNbO_3$ diffused waveguides were designed and made of rutile (crystalline TiO_2), one of the few materials with higher refractive indices than $LiNbO_3$. Rutile is birefringent (uniaxial positive), with the crystal optic axis coincident with the crystallographic c axis. The highest possible mode index anticipated was 2.4, based on Kaminow and Schmidt's results [3]. The indices of rutile are $n_e = 2.582$ and $n_o = 2.486$ [9,19], so coupling is possible with any relative orientation of the prism and substrate crystal axes. Rutile has a hardness of 6 to 6.5 on the Mohs scale, sufficient to resist scratching by most common materials.

Three factors must be considered in prism coupler design: the relative crystallographic orientation of prism and substrate, the magnitude of the prism angle, and the coupling efficiency. For the prism illustrated in Fig. 2.9, the phase velocity matching condition

$$n_m = \frac{\beta_m}{k} = n_p \sin\theta_\mu \tag{2.23}$$

must be satisfied before coupling to guided modes can occur. The angles θ, γ, and α in triangle ABC' are related by the equation

$$\theta = \alpha + \gamma, \tag{2.24}$$

where α is the prism angle. At the upper air-prism interface, Snell's law is

$$\sin\mu = n_p \sin\gamma$$

so that

$$\begin{aligned} n_m &= n_p \sin[\alpha + \arcsin(\frac{\sin\mu}{n_p})] \\ &= \cos\alpha \sin\mu + \sqrt{n_p^2 - \sin^2\mu}\, \sin\alpha \end{aligned} \tag{2.25}$$

It is more useful to write this with μ as the independent variable,

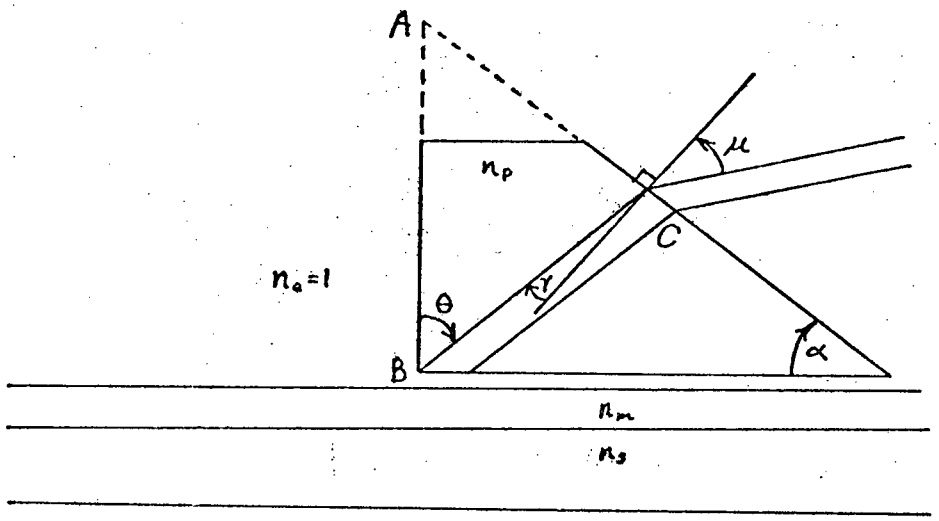

Fig. 2.9 Prism Coupler Geometry.

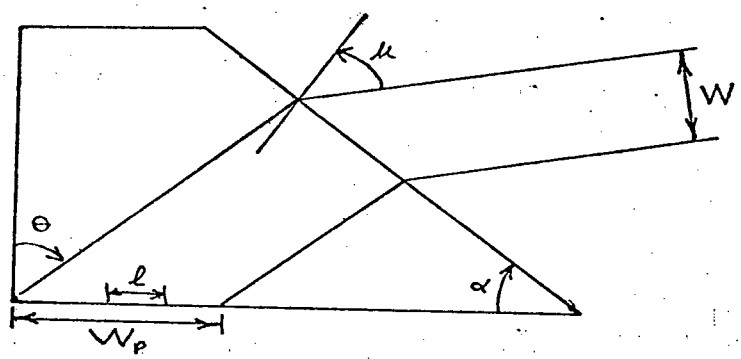

Fig. 2.10 Broadening of the Input Light Beam

$$\mu = \arcsin[n_m \cos\alpha - \sqrt{n_p^2 - n_m^2}\,\sin\alpha]. \qquad (2.26)$$

If we know the prism index and have an estimate of the guided mode index n_m, we can use this equation to calculate the range of prism angles α over which coupling is possible. This range is such that $-\frac{\pi}{2} < \mu < \frac{\pi}{2}$, although angles of incidence near the limits $\pm \pi/2$ are not usable because broadening of the input light beam reduces the coupling efficiency. From Fig. 2.10, we see that the fraction of the light incident on the active coupling region of length ℓ is

$$\eta_\ell = \frac{\ell}{W_p} = \frac{\ell\cos\theta\cos\mu}{W\cos\gamma} \qquad (2.27)$$

where W is the incident beam thickness. Usually a lens of long (> 20 cm) focal length is used to focus the laser beam to a small spot on the prism base. The degree of beam convergence is usually small over the dimensions of the prism (typically ∿ 0.5 cm), so it may be neglected in (2.27). In Fig. 2.11, η_ℓ is plotted as a function of prism angle for the case $\ell/W = 1$, $n_p = 2.582$ and 2.86, and $n_m = 2.23$. If maximum coupling efficiency is desired, it is necessary that the coupling length ℓ be greater than the projection of the light beam diameter in the prism.

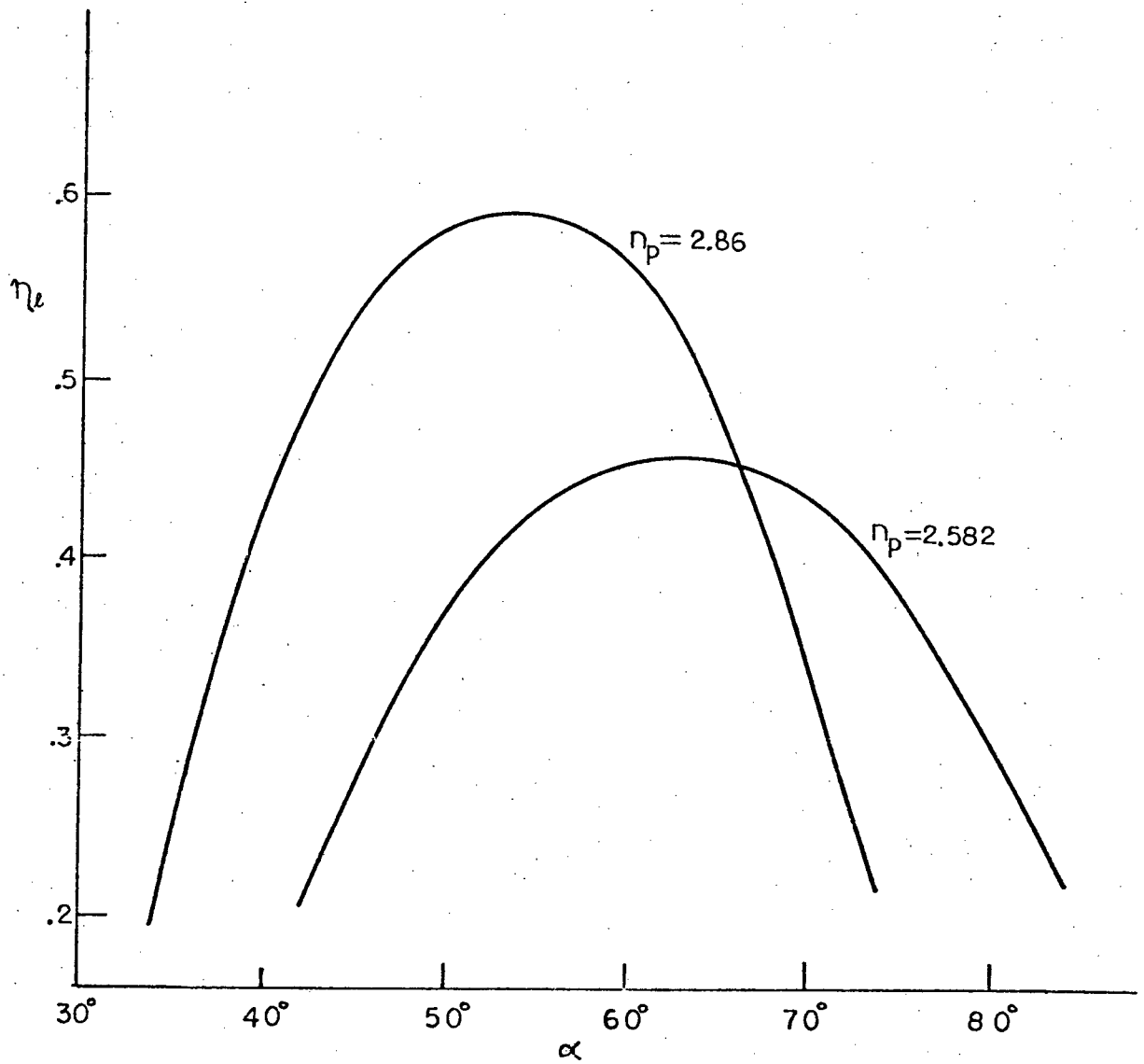

Fig. 2.11 Effect of Beam Broadening on Coupling Efficiency (assumes $\ell/W = 1$, $n_m = 2.23$).

The overall coupling efficiency is

$$\eta_t = \eta_\ell \, \eta_c = \eta_c \, \frac{\ell \cos\theta \cos\mu}{W \cos\gamma}, \quad W_p > \ell,$$

or

$$\eta_t = \eta_c \qquad W_p < \ell, \tag{2.28}$$

where η_c is a factor dependent on prism, gap and waveguide parameters. For coupling across a uniform gap of width D into TE modes of a graded-index optical waveguide (OWG), Marcuse [9] obtained the radiation-loss amplitude coefficient

$$\alpha_c = \frac{|A|^2 B^2 \, \sigma \, \gamma^2 \, \kappa_o^2}{2\omega\mu_o P\{[(\kappa_o\sigma-\gamma^2)\sinh(\gamma D)]^2 + [\gamma(\sigma+\kappa_o)\cosh(\gamma D)]^2\}}, \tag{2.29}$$

where γ and κ_o are given by (2.13) and (2.14), $\sigma^2 = k^2(n_p^2 - n_m^2)$ and $|A|^2 B^2 \, (2\omega\mu_o P)$ is determined by the mode normalization integral,

$$P = \frac{\beta_m}{2\omega\mu_o} \int_{-\infty}^{\infty} E_x^* \, E_x \, dy \tag{2.30}$$

The parameter P is the power per unit width carried by the mode. Marcuse normalizes the electric field by setting $\sqrt{P\omega\mu_o} = 1$ V/m for each guided mode. The coupling efficiency η_c is then given by

$$\eta_c = 1 - \exp(-\alpha_c \ell) \tag{2.31}$$

In the derivation of (2.29), Marcuse assumed that the electric field in the gap consisted of plane waves, and that the input beam intensity profile was rectangular. The first assumption is less accurate for lower order modes, whilst the second leads to overestimation of α_c for Gaussian beams. The effect of changing the prism index in (2.29) can be seen more clearly if we take D = 0. Then

$$\alpha_c = \frac{|A|^2 B^2 \, \sigma \, \kappa_o^2}{2\omega\mu_o P(\sigma+\kappa_o)^2}. \tag{2.32}$$

The prism index enters this expression through $\sigma = k\sqrt{n_p^2 - n_m^2}$. Differentiation with respect to σ reveals that α_c has a maximum when $n_p = n_o$, the OWG surface index of refraction. When a choice of prism index exists (as in the case of rutile), the lower index will give a higher coupling efficiency, provided, of course, that $n_p > n_o$.

In diffused waveguides, there is usually little difference between the indices of modes of adjacent order. Consequently, the coupling angles μ are close together, making the observation of individual modes and accurate determination of the mode indices more difficult. The derivative of μ_c with respect to n_m provides a measure of the separability of individual guided modes,

$$\frac{d\mu_c}{dn_m} = \frac{\cos\alpha + n_m(n_p^2 - n_m^2)^{-1/2}\sin\alpha}{[1 - (n_m\cos\alpha - \sqrt{n_p^2 - n_m^2}\sin\alpha)^2]^{1/2}} . \qquad (2.33)$$

This expression is plotted in Fig. 2.12 as a function of α for rutile, with $n_m = 2.23$. The minima of Fig. 2.12 coincide with the maxima of Fig. 2.11; that is, the mode separability is least when the coupling efficiency due to beam broadening is greatest.

In Fig. 2.13, the limiting prism angles are plotted against mode index for the prism indices 2.582 and 2.86. Equation (2.27) was solved for α by Newton's method for $\sin\mu = \pm 1$. The upper curves are for an angle of incidence $\mu_i = \pi/2$; the lower, for $\mu_i = -\pi/2$. From [3], we expect $2.15 < n_m < 2.5$; then the limits to the prism angle are given by $41° < \alpha < 86°$ for $n_p = 2.582$ and $34° < \alpha < 74°$ for $n_p = 2.86$.

In order to simplify the calculation of mode indices, it is desirable to select the crystallographic orientation in such a way that light in the prism propagates with either n_o^* or n_e, the extreme value

---

* In the rest of this section, n_o refers to the ordinary rather than the surface index of refraction.

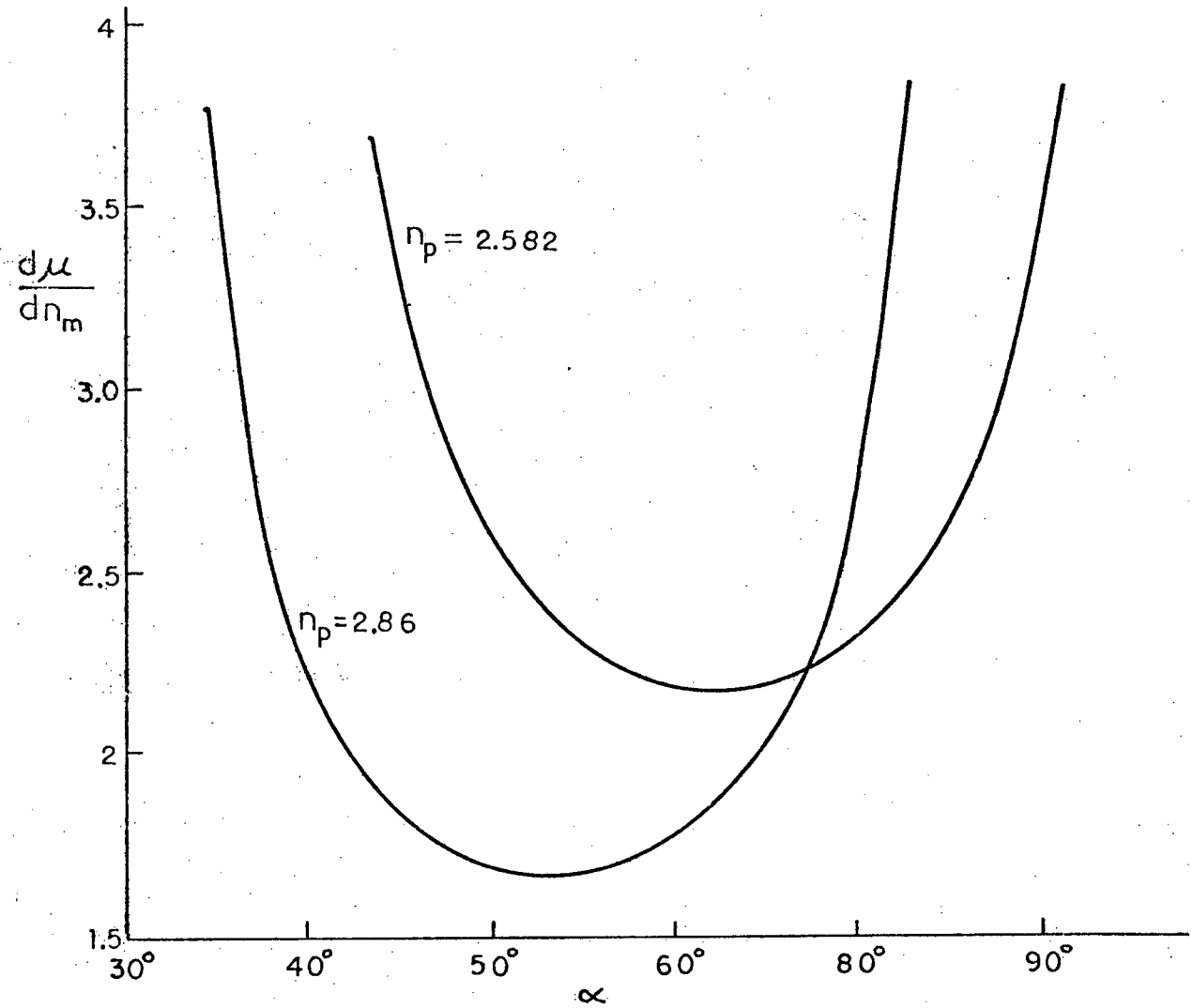

Fig. 2.12 Mode Separability vs. Prism Angle for $n_m = 2.23$.

of the extraordinary index. When the extraordinary ray axis lies along the back corner of the prism (Fig. 2.14), TE waves propagate with the index n_e and TM with n_o. This can be shown by making the substitutions

$$n_1 = n_2 = n_o = 2.582$$

$$n_3 = n_e = 2.86$$

and $V_z = 0$ in the phase velocity determinant (Appendix II) to obtain

$$V_x^2 + V_y^2 = n_e^2 V^4/c^2 \quad \text{(TE)}$$

$$V_x^2 + V_y^2 = n_o^2 V^4/c^2 \quad \text{(TM)} \qquad (2.34)$$

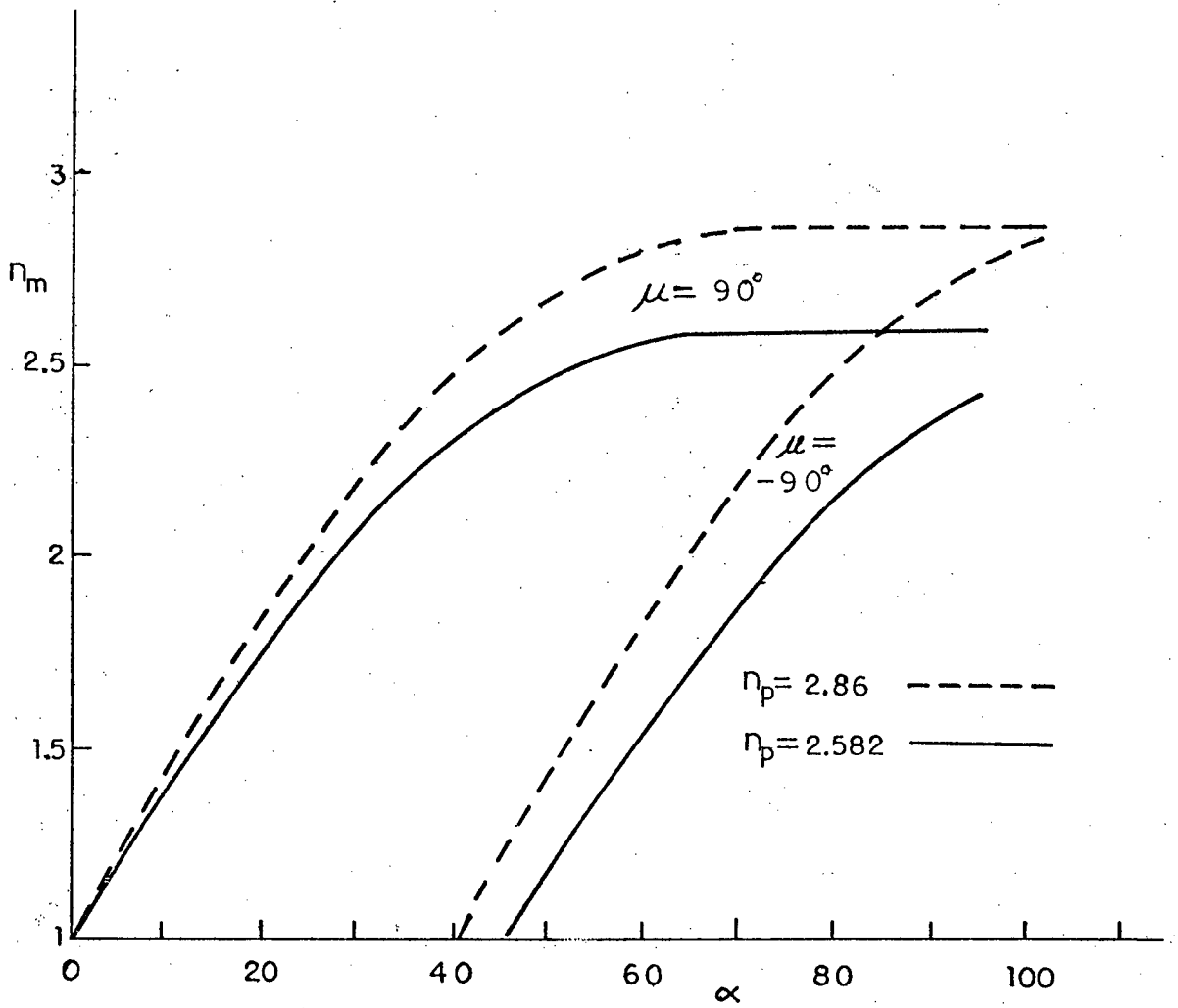

Fig. 2.13 Limiting Mode Indices vs. Prism Angle for Rutile.

The phase velocity surface is used here (rather than the ray velocity surface) because it is the phase of light incident at the prism base that determines whether coupling takes place. Since both equations (2.34) represent circles, the index of propagation does not vary with the angle of incidence. This then is the preferred orientation when both TE and TM modes are to be excited.

In Fig. 2.15, the c axis is vertical. The substitutions

$$n_1 = n_2 = n_o$$

$$n_z = n_e$$

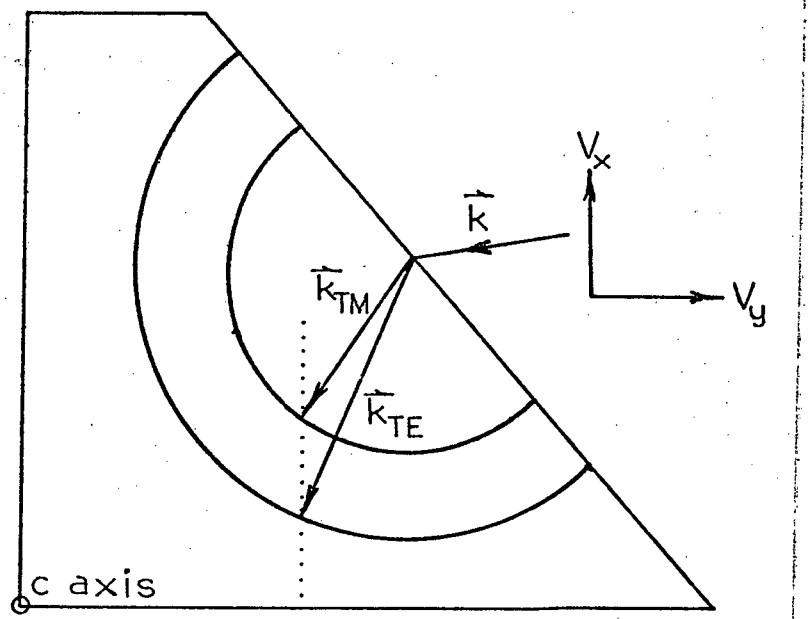

Fig. 2.14 Phase Velocity Surface for Rutile with c Axis Horizontal.

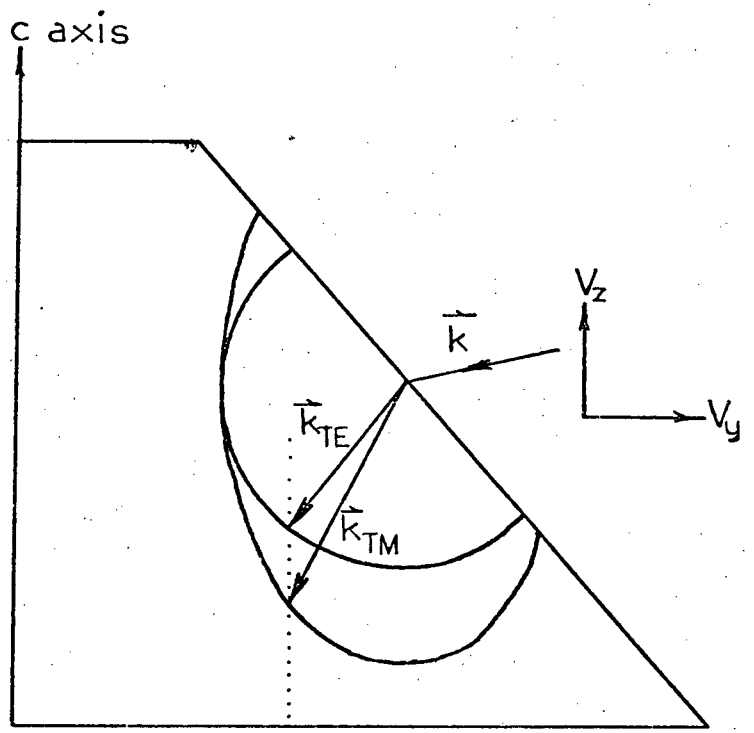

Fig. 2.15 c Axis Vertical.

and $V_x = 0$ give

$$V_y^2 + V_z^2 = n_o^2 V^4/c^2 \quad \text{(TE)}$$

$$\text{and} \qquad n_2^2 V_y^2 + n_3^2 V_z^2 = n_o^2 n_e^2 V^4/c^2 \quad \text{(TM)} \tag{2.35}$$

for the projections of the phase velocity surface on the yz plane. Thus, TE modes propagate with the ordinary index. However, the index for TM waves varies with the angle of light propagation in the prism. In the acoustooptic experiments described in Chapter 4, only TE modes were used, so this orientation was satisfactory. It provides a somewhat higher degree of mode separability and coupling efficiency.

2.5 Coupler Fabrication

Initially, an attempt was made to construct grating couplers by the method of simultaneous exposure and development, using Gaf PR-102 positive photoresist. This technique, which gives reduced exposure times and deeper grooves with sharper ridges than conventional methods, was first used by Tsang and Wang in 1974 [20] to make high quality submicron gratings with Shipley AZ-1350 positive photoresist. In Fig. 2.16, light from an argon laser is split into two beams which are individually spatially filtered, then passed through an optical flat to interfere at the photoresist-coated substrate. It can be shown that the grating period is

$$\Lambda_g = \lambda/(2 n_d \cos(\arcsin(\sin\theta_i/n_d))), \tag{2.36}$$

where n_d is the developer index of refraction and θ_i the angle of incidence on the optical flat.

Before use, the developer was diluted 1:3 with deionized water and passed through a .45 μm filter to reduce light scattering. The photoresist, diluted 1:1 with reagent grade methyl ethyl ketone, was

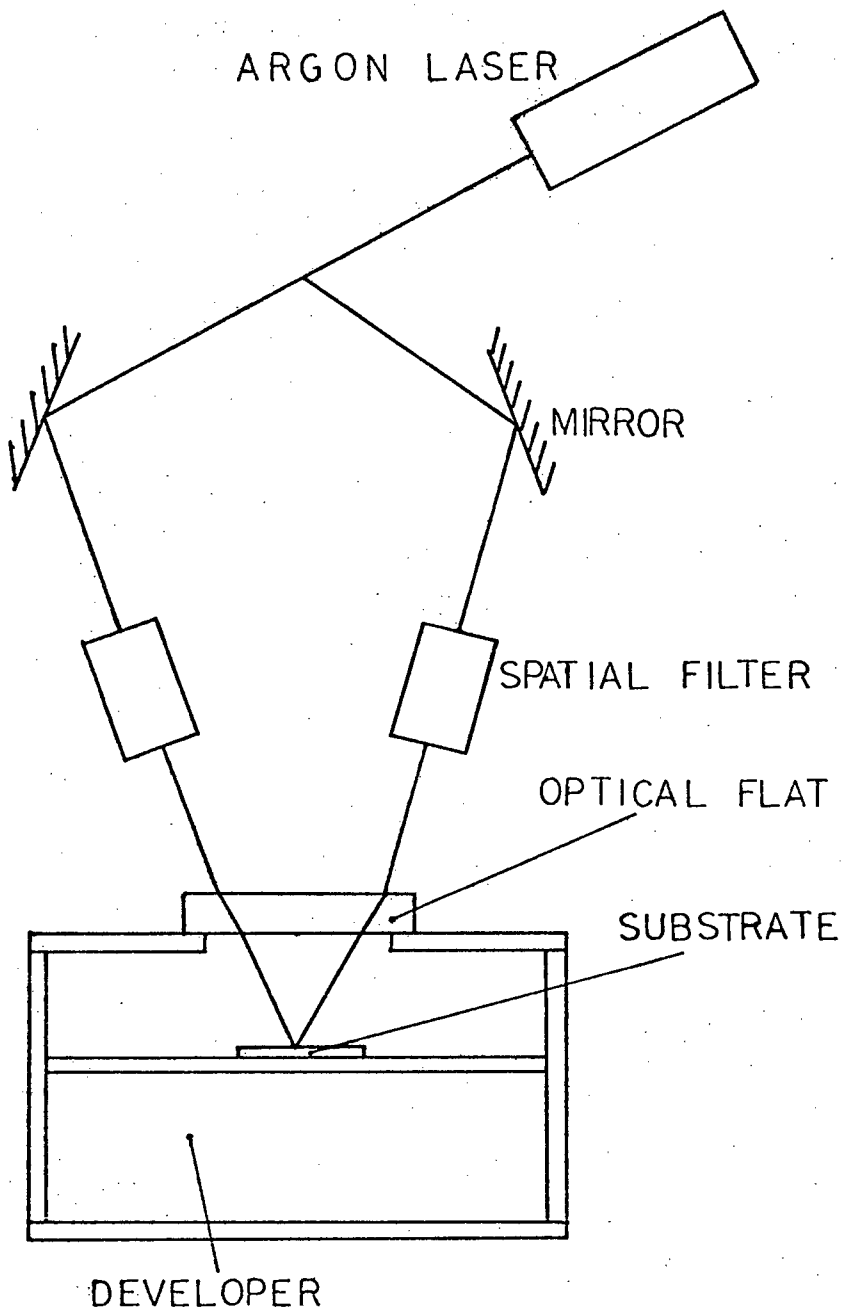

Fig. 2.16 Photoresist Exposure for Grating Coupler Fabrication.

spin coated at 4000 RPM for 10 seconds. The coatings were measured to be about 2000 A° thick with a Sloan Angstrometer. After drying in air for 15 minutes, the photoresist was baked at 65°C for half an hour.

During exposure, the light intensity was measured to be about 60 mW/cm^2. A series of test exposures were undertaken with times ranging from 10 seconds to 10 minutes. Three minutes was found to give good results. The gratings were rinsed and blown dry with nitrogen before examination in a scanning electron microscope. A grating period of 5400 A° was obtained. Fig. 2.17 shows the shallow ridges of an underexposed portion, and Fig. 2.18 shows a correctly exposed area at lower magnification.

Unfortunately, usable gratings were not obtained, primarily due to a lack of adhesion of the photoresist when development of the grooves was carried through to the substrate (Fig. 2.19). This problem could not be overcome by variation of process parameters, so a rutile crystal was ordered from NL Industries in New Jersey. The crystal was about $2\frac{1}{2}$ cm x $1\frac{1}{2}$ cm diameter and had a very pale yellow colour, although the transmittance was quite high.

A number of prisms were made with the c axis vertical. First, several 5 mm slices were cut with a fine diamond saw. The crystal was held in place with a thermoplastic cement. Caution was required during heating and cooling to avoid cracking. The slices were remounted flat on the holder and diced into 5 mm cubes. The crystal orientation was marked on the top, which was not ground until last. A succession of wetted emery paper grades was used to shape the prisms, with 600 grit being the last for surfaces requiring polishing. During this process, it was found best to hold the prisms by hand (Fig. 2.20).

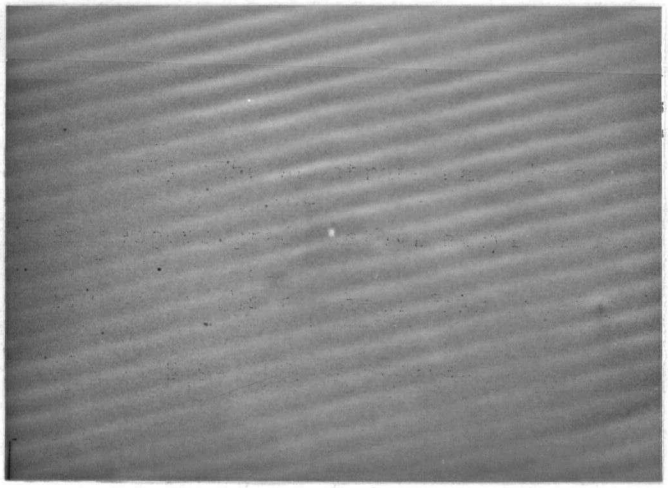

Fig. 2.17 Underexposed Grating.

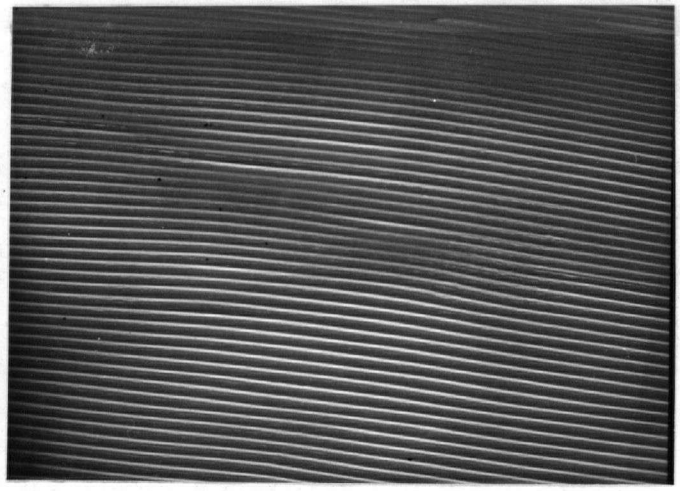

Fig. 2.18 Correctly Exposed Grating.

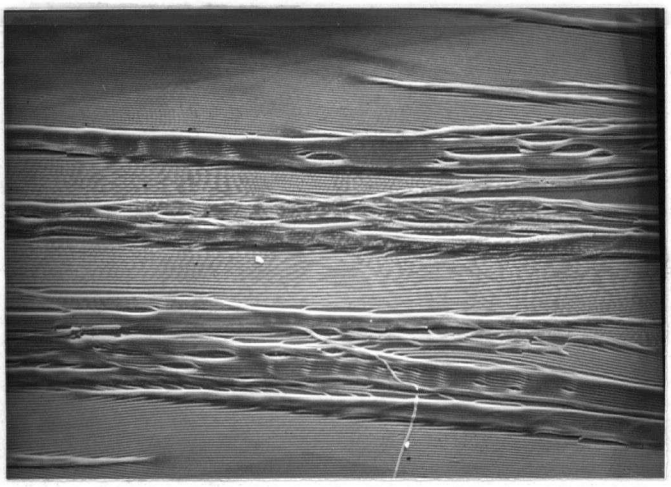

Fig. 2.19 Result of Insufficient Photoresist Adhesion.

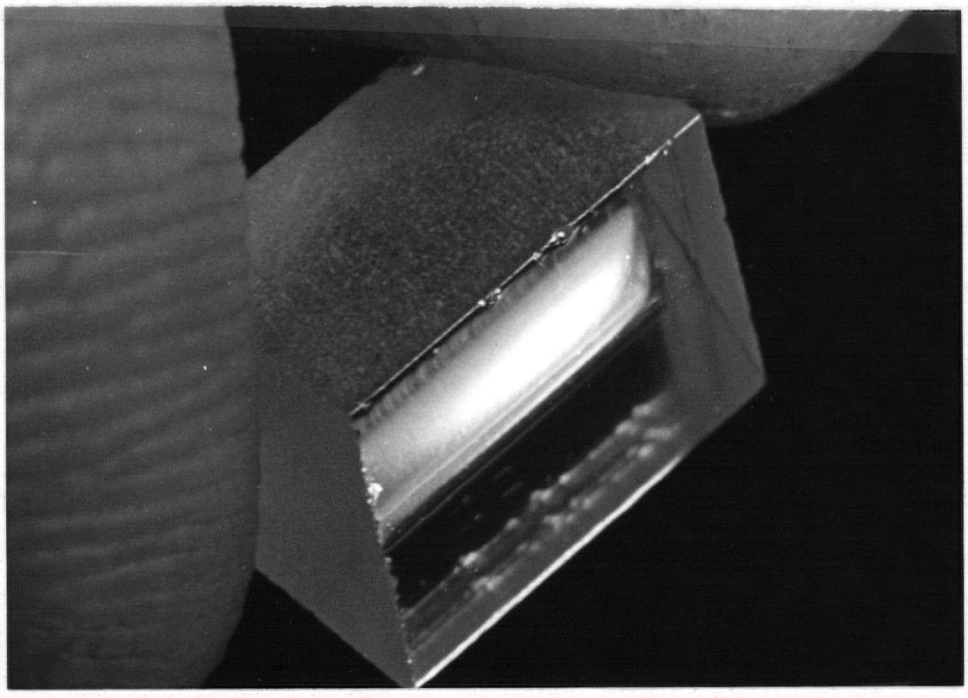

Fig. 2.20 Rutile Coupling Prism (∿8X).

Frequent examination for large scratches was necessary, as these were more easily removed with coarser grades of emery paper.

After considerable grinding with 600 grit paper, the crystals were washed and dried. A variety of polishing techniques were attempted before a successful method was found. Five micron diamond paste lubricated with a light oil on a napless polishing cloth revolving at 250 RPM gave good results. After prolonged polishing, the crystal faces became clear and polishing was completed with 1 μm diamond paste. After cleaning, the vertical back surface was painted black to prevent light from passing directly through to the optical waveguide. Prisms with angles between 55° and 82° were made; for most coupling experiments, a pair of 68° prisms were used.

2.6 Optical Waveguide Fabrication

Several techniques were tried for fabrication of optical waveguides, including thermal oxidation, reactive sputtering and diffusion. Because the ultimate objective was to study acoustooptic interactions in $LiNbO_3$, it was necessary to use a material with higher refractive index than 2.214. Again, TiO_2 was one of the few suitable materials.

Initially, the thermal oxidation of 1 μm thick Ti films was tried, at 800°C with an oxygen flow rate of 1 ℓ/min. Even prolonged treatment, however, did not give films with low optical absorption, so this approach was abandoned.

Better films were obtained by reactively sputtering Ti in an argon-oxygen mixture at pressures of .01 and .002 torr, respectively. (Sputtering in pure oxygen gave brownish films similar in appearance to thermally oxidized titanium.) A series of films of different thicknesses was deposited on a silicon slice in order to measure the oxide thickness by ellipsometry. Comparison between the experimental ψ, Δ curve (Fig. 2.21) and calculated tables gave a refractive index of 2.15 at 632.8 nm. This surprisingly low value was most likely caused by the presence of several oxides of titanium in the film. Annealing overnight in oxygen at 500°C increased the index to about 2.25, as did sputtering at slightly higher oxygen concentrations. Sputtering onto a heated substrate would likely have increased it further, but this was not feasible in the existing sputtering system. Even the best films appeared to be somewhat lossy, however, so subsequent experiments were aimed at the fabrication of waveguides by diffusion.

Coupling to guided modes of a 1 μm thick TiO_2 film on glass was observed. The film absorption appeared to be quite high, since the

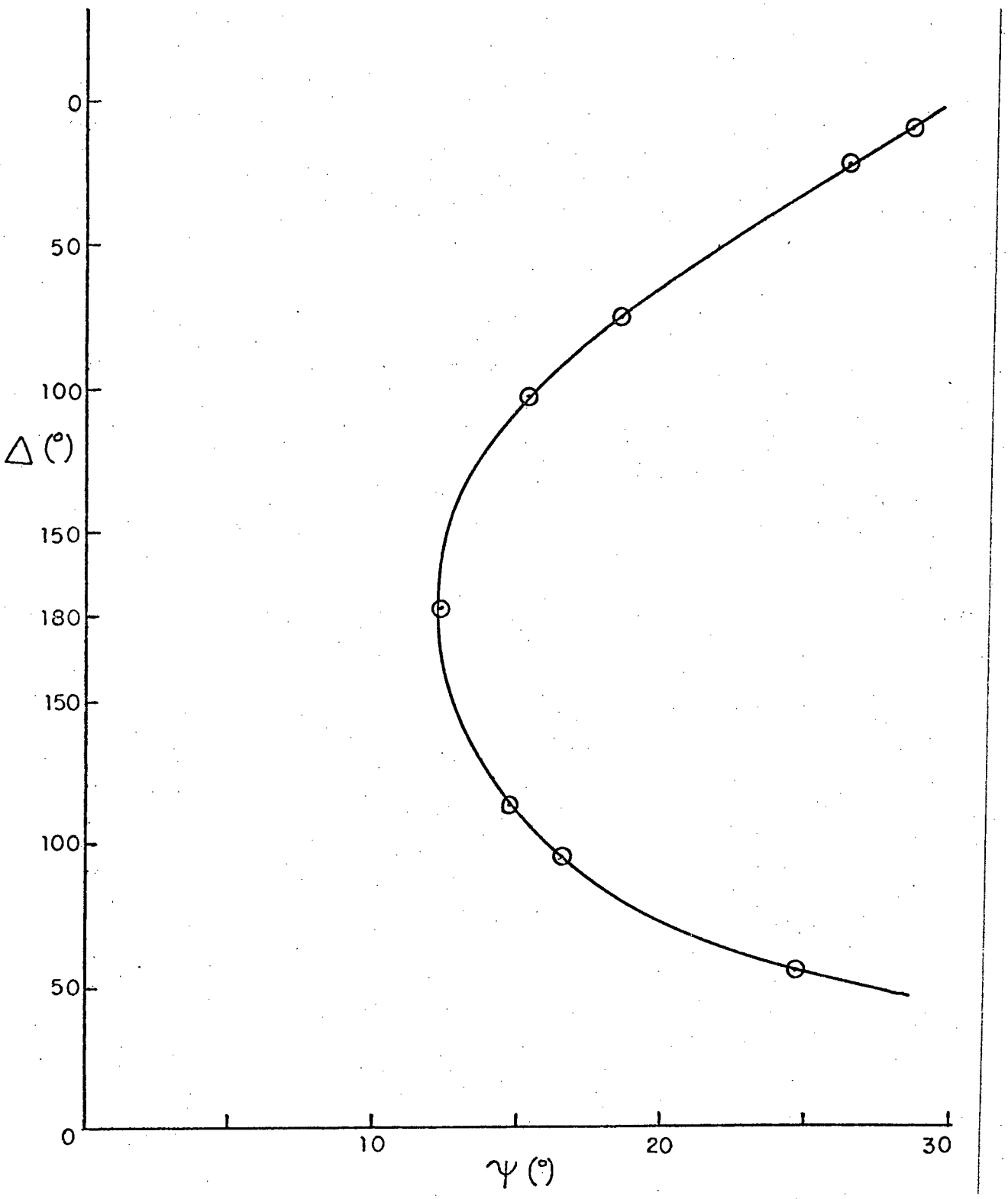

Fig. 2.21

bright streak characteristic of guided waves was strongly attenuated over a distance of less than one centimeter. The dynamic range of the human eye is about 27 dB, so the film probably had losses in excess of 30 dB/cm [1].

2.7 Diffused Optical Waveguides in $LiNbO_3$

Lithium niobate has an unusual combination of physical properties (Appendix I). It is birefringent (uniaxial negative) and ferroelectric, with a Curie temperature between 1100 and 1080°C, depending on stoichiometry. It has relatively large electrooptic, acoustooptic and non-linear optical coefficients, as well as high transmissivity in the visible spectrum. These characteristics make it a very desirable material for the fabrication of optical waveguides, since their propagation characteristics may be altered by electric fields, acoustic surface waves or non-linear effects to provide modulation, switching, deflection, and mode coupling of guided waves.

The first diffused waveguides in this material were reported by Kaminow and Carruthers in 1973 [4,21]. Lithium niobate crystals exhibit variable stoichiometry of the form $(Li_2O)_a(Nb_2O_5)_{1-a}$, where $0.48 < a < .50$. The degree of non-stoichiometry was found to affect the magnitude of the extraordinary ray index of refraction. By holding crystals at a temperature of 1100°C and a pressure of 6×10^{-6} torr for times ranging between 21 and 64 hours, the index in a surface layer was reduced sufficiently by lithium outdiffusion to produce excellent waveguides. Discoloration of the crystals resulting from this treatment was corrected by further heating in air for two hours before cooling. These waveguides had an error function diffusion profile, with guided modes that extended as much as 100 μm or more into the substrate.

In 1974, Kaminow and Schmidt reported that the indiffusion of transition metals also produced excellent waveguides in $LiNbO_3$. Diffusion times were much shorter (as little as a few hours), and greater control was possible over the shape of the diffusion profile, which could be varied from complementary error function to Gaussian, depending on whether all the metal was diffused in from the substrate surface. Their results indicated that nickel diffusion in $LiNbO_3$ was particularly rapid, so that waveguiding layers several microns deep could be made at 800° in a few hours.

Even better optical waveguides have been made [5] from solid-solution $LiNbO_3$-$LiTaO_3$ films grown on $LiTaO_3$ substrates by liquid phase epitaxy [12]. A steeper Fermi function diffusion profile was obtained. The difference between mode and substrate indices was greater than with diffused waveguides ($\Delta n \sim 0.07$ compared with $\Delta n \sim 0.01$). As a result, the individual guided modes have better angular separation when excited with prism or grating couplers. These waveguides have the disadvantage, however, that the $LiTaO_3$ must be repoled, since its Curie temperature is only 600°C.

2.8 Ti/$LiNbO_3$ Diffusion

Sputtered Ti films 500 A° thick were deposited on 2 inch diameter YZ $LiNbO_3$ slices obtained from Crystal Technology, Inc., of Mountain View, California. The crystals had been grown from a congruent melt, and were specified to have the following impurity concentration by the manufacturer.

Cr	2.8 ppm
Fe	18 ppm
Ni	3.7 ppm
Cu	2.6 ppm .

The diffusion process outlined by Kaminow and Schmidt was followed. The substrates were cleaned by a method similar to that recommended by Brandt et al [24] for the fabrication of low-loss optical waveguides. Ultrasonic cleaning for 10 minutes in a .01% Alconox solution in deionized (DI) water was followed by three DI water rinses and one hour in a DI cascade washer. Before deposition, the $LiNbO_3$ slices were blown dry with nitrogen and treated with a Zerostat anti-static gun ($LiNbO_3$, being pyroelectric, tends to develop polarization charges which attract dust). After deposition, the Zerostat was again used before insertion of the substrate into the quartz tube of a cold diffusion furnace. Argon gas (99.995%) with the following impurity contentaaa

$O_2 < 10$ ppm	$H_2O < 10$ ppm
$H_2 < 2$ ppm	$CO_2 < .5$ ppm
$N_2 < 23$ ppm	$CH_4 < .5$ ppm

was passed through the furnace tube at a rate of 2 ℓ/min. After a 6-hour diffusion at 960°C, the furnace was turned off and allowed to cool for 12 hours while oxygen was passed through at a rate of 1 ℓ/min. This step was used by Kaminow to reoxidize the $LiNbO_3$, which tends to become brownish from oxygen loss during the diffusion. On removal from the furnace, the substrate was coated with an oxide layer; this was removed by lightly polishing by hand with 1 μm diamond paste on a napless nylon cloth.

Attempts to couple to guided modes with a 68° rutile prism were unsuccessful, even though Kaminow and Schmidt had observed 6 guided modes in similarly treated samples. The diffusion profile (Fig. 2.22) was determined by examination of a 10° taper section of the substrate in an electron microprobe. The effective diameter of the x-ray source was estimated using [22]

$$S = .033(V^{1.7} - V_k^{1.7})A/(\rho Z) + D, \qquad (2.37)$$

where S is the source diameter in μm, V is the accelerating potential, V_k = 5 kV for the Ti K_α line and D is the electron beam diameter. Using V = 10 kV, ρ = 7.45 g/cc with the units indicated, D = 1 μm, and an average value for the atomic number Z and atomic weight A,

$$S \sim 1.4 \text{ μm}.$$

The taper section increased the apparent diffusion depth from 2 to 11.5 μm, so reasonable accuracy was possible. The profile is approximately fitted by

$$R = \text{erfc}(y/1.05), \qquad (2.38)$$

where R is the Ti to surface Ti count ratio, and y is in μm. The value 1.05 closely matches Kaminow and Schmidt's value of 1.1, so the diffusion attained the correct depth. It was concluded that either the coupling prism did not work as expected, or the Ti concentration was considerably less than required.

A sputtered glass waveguide, provided by Dr. G. Mitchell of the University of Washington, Electrical Engineering Department, was used to verify that the prisms worked (Fig. 2.23). Calculations showed that the prism should have been able to couple to mode indices ranging from 1.9 to 2.6, so it was concluded that the Ti concentration in the guide was low. This may have been caused by formation of an oxide or nitride of titanium early in the diffusion, which reduced the number of Ti atoms available.

The substrates were not restored to their original transparency, even after prolonged treatment in O_2 at 700°C. However, this absorption was insufficient to prevent guided modes from being observed, since substrate modes were clearly visible in the coupling attempts.

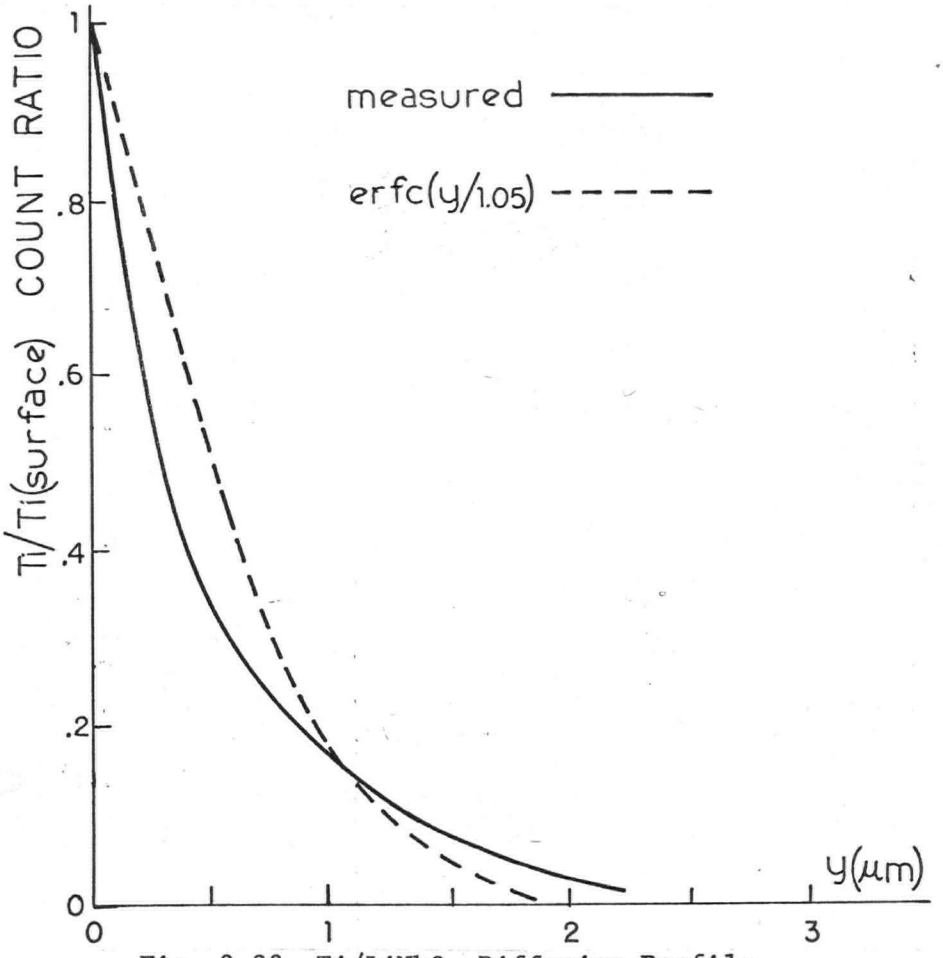

Fig. 2.22 Ti/$LiNbO_3$ Diffusion Profile.

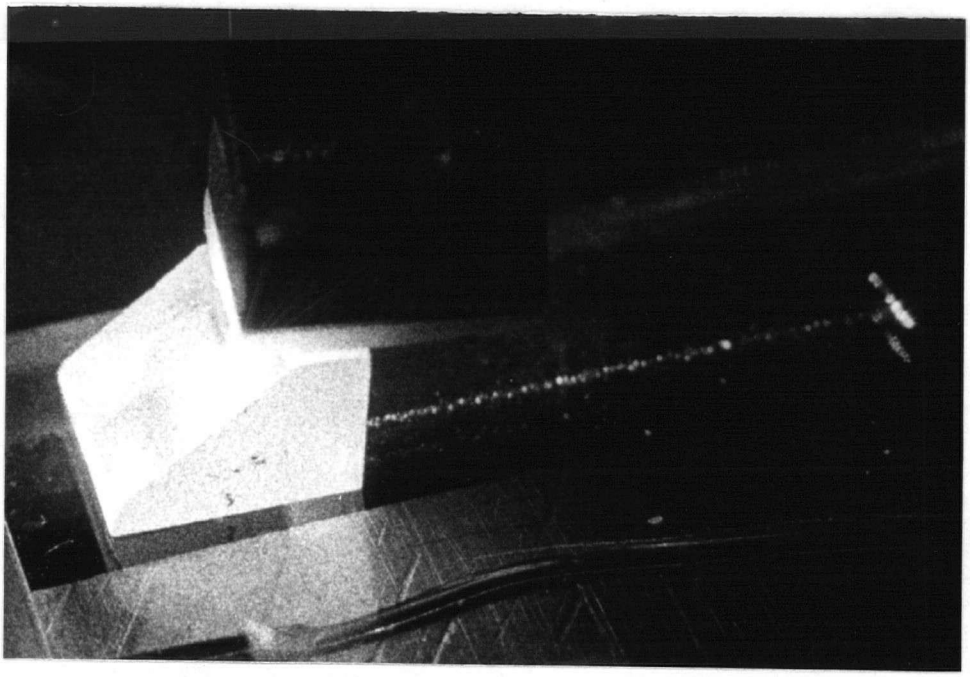

Fig. 2.23 Coupling to a Glass Sputtered OWG.

The most likely cause of difficulty was presumed to be the O_2, N_2 and H_2O impurity concentration in the argon gas. From Fig. (6.13) of [26], it can be inferred that a 500 A° layer of Ti would oxidize in seconds or less at 960° in O_2 at atmospheric pressure. At the very low partial pressure of oxygen encountered during diffusion, the rate of oxidation is difficult to estimate, but samples heated briefly to 960°C and cooled in argon were also observed to have an oxide layer. Since TiO_2 is a very stable compound with a large free energy of oxidation (-162 k cal/mole), this explanation seems quite plausible.

2.9 $Ni/LiNbO_3$ Diffusion

In subsequent experiments, nickel was used rather than titanium because of its higher diffusivity in $LiNbO_3$. An effort was made to remove O_2, N_2 and H_2O from the argon gas. Pascard and Fabre [25] have shown that a Ti-Zr mixture (50% atomic) is effective for oxygen and nitrogen removal from argon at temperatures in excess of 800°C. To implement this, a Ti-Zr sponge mixture was inserted into a 3 cm quartz tube and held in place with Ti strips cut from sheet metal. The furnace connections are shown in Fig. 2.24. Water was removed with silica gel.

The Perkin-Elmer sputtering system was calibrated so that thin (< 500 A°) layers of Ni could be made repeatably. Six depositions of different thicknesses were made on a clean glass slide with an rf forward power of 100 watts and an argon pressure of 1.2×10^{-2} torr. A thin nickel layer was then deposited over the entire slide, in order to make all the steps easily visible in a Sloan Angstrometer. The results are summarized below in Table 2.1.

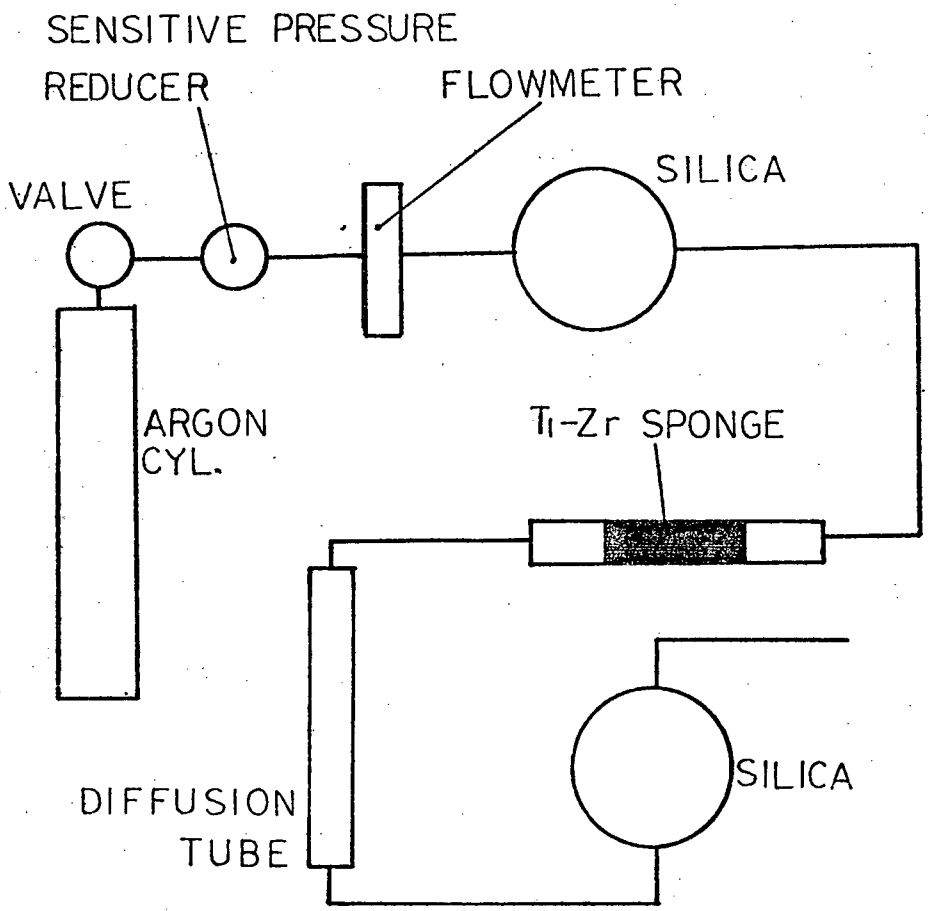

Fig. 2.24. Gas Flow Connections for Ni/$LiNbO_3$ OWG Diffusion.

Table 2.1 Ni Sputtering Calibration.

t(min)	d(A°)	r = d/t(A°/min)
2	196 ± 100	98 ± 50
4	245 ± 41	61 ± 10
4	236 ± 59	59 ± 15
6	384 ± 64	54 ± 10
8	433 ± 43	54 ± 5
10	575 ± 72	57.5 ± 7

Neglecting the 2 minute result, the average sputtering rate is

$$\bar{r} = \overline{d/t} = 59.1 \pm 3.3 \text{ A°/min},$$

where the probable error 3.3 was calculated from

$$\text{P.E.} = 0.67\sqrt{\sum_{i=1}^{n} (r_i - \bar{r})^2/n}\,.$$

A vital step in each nickel deposition was the preliminary removal of any residual target oxide layer by sputtering onto the shutter at maximum power ($\sim$ 400 W) for several minutes. Only then was the sputtering rate stable enough to give predictable results.

The Ti-Zr sponge furnace was turned on (with an argon flow rate of 2 ℓ/min) one hour before commencement of the $LiNbO_3$ diffusion in order to reach the operating temperature of 900°C. A series of tests were made to determine the effect of argon purification on the quantity of nickel diffused into the substrate by x-ray fluorescence. The magnitude of the Ni K_α to Nb K_α line count ratio was taken as an estimate of the nickel concentration in the top ($\sim$ 10 μm) [22] layer of the specimen. Table 2.2 summarizes the results. The Ni/Nb ratios tabulated are to be regarded as proportional only to the atomic Ni/Nb ratio.

Some interesting conclusions can be drawn from Table 2.2. In each case, including the 6 hour diffusion at 950°C, most of the nickel remained on the surface in the form of an oxide or possibly nitride residue. Also, the effect of argon purification on the quantity of in-diffused nickel is seen to be considerable.

All of the substrates were pale brownish-grey in color, with the sample diffused at 950°C being the most discolored. Measurement of the optical absorption of $LiNbO_3$ substrates was made in a Carey dual

Table 2.2 X-Ray Fluorescence of Ni/$LiNbO_3$

No.	Description of Sample	Ni/Nb Ratio
1	$LiNbO_3$ Substrate.	0
2	500 A° Ni deposited on $LiNbO_3$.	0.278
3	500 A° Ni diffused into $LiNbO_3$ @ 800°C for 3½ hr. in treated Ar.	0.210
4	No. 3 polished to remove oxide residue.	0.05
5	Same as no. 3 except diffused at 950°C for 6 hr.	0.230
6	No. 5 polished.	0.036
7	Same as no. 3, but Ar not treated.	0.226
8	No. 7 polished.	0.01

beam spectrophotometer, and the results plotted in Fig. 2.25. New substrates had little absorption in the visible spectrum and appeared perfectly clear to the eye. All substrates heated in argon and cooled in oxygen had an absorption peak around 450 nm. Substrates heated to 950°C were conspicuously absorbing. A letter from Crystal Technology, Inc., suggested baking the crystals at 1000°C in O_2 for 2-3 days. This was not feasible, since the nickel would have diffused too deeply and eliminated the waveguide. The absorption may be the same as that observed at 482 nm by Ballman and Gernand [27], who attributed the discoloration to Nb^{4+} ions formed when oxygen is lost from the crystal lattice. The absorption could also be due to Ni^{2+} (as suggested by Crystal Technology, Inc.), or Fe^{2+} (Staebler and Philips [33]). The small ($\sim$ 18 ppm) iron impurity level in the crystals makes the latter possibility less likely.

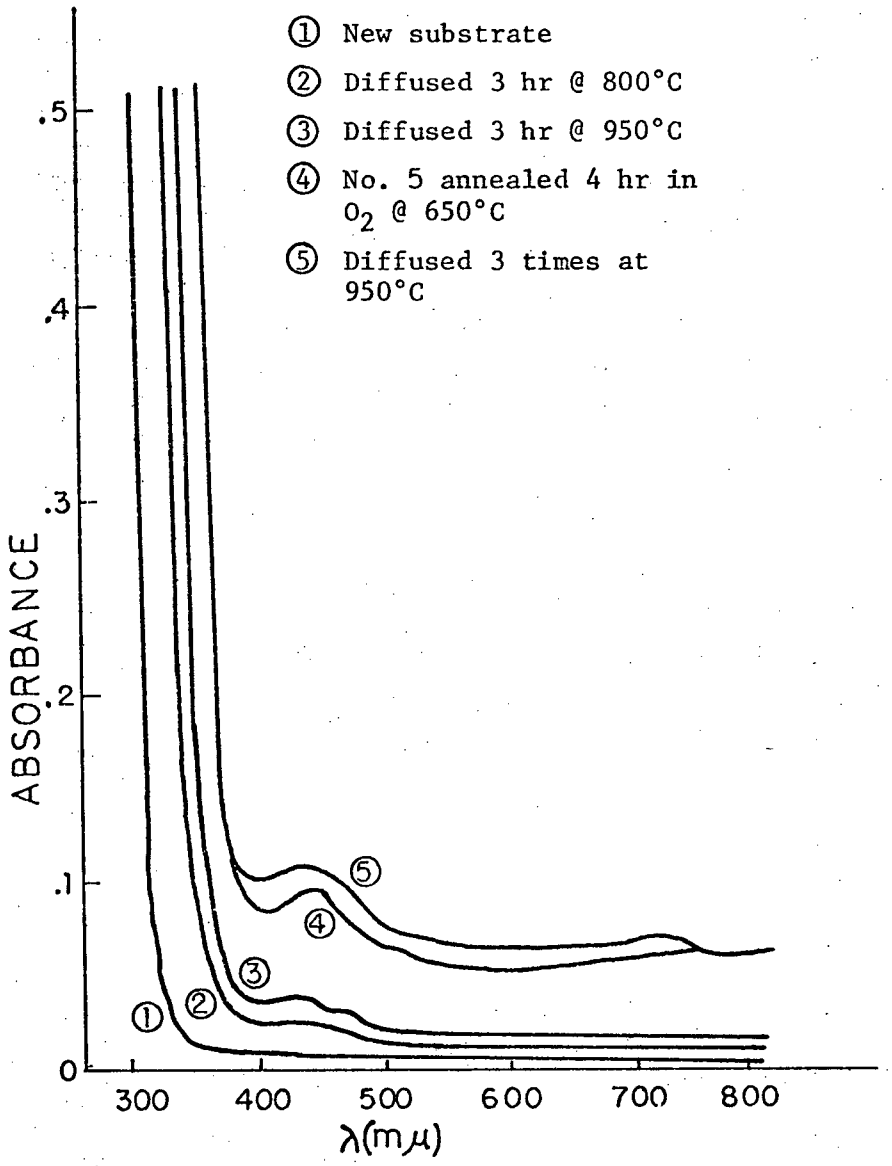

Fig. 2.25 Absorbance of $LiNbO_3$ Waveguide Substrates.

There is doubt also regarding the exact composition of the residue left after diffusion. Lithium atoms diffuse rapidly in $LiNbO_3$, so they are likely to be present. Nickel oxide (NiO) is a p-type semiconductor for which lithium is an excellent dopant [28]. The doped oxide appears black [29], although the lithium concentration may not have been great enough for this degree of discoloration, which was not observed. A number of nitrides of nickel are stable compounds, but most of these are formed only at higher temperatures. Ni_3N is formed at

500°C, but is black and a conductor [30]. When lithium is present, however, nickel and nitrogen react at 550°C with Li_3N to form $(Li,Ni)_3N$ [31]. Unfortunately, neither x-ray fluorescence nor microprobe analysis are suited to the detection of elements of low atomic number, so a direct test of the residue composition could not be made by these methods.

2.10 Properties of $Ni/LiNbO_3$ Waveguides

Several $Ni/LiNbO_3$ diffused optical waveguides were made by the following process. A 350 A° layer of nickel was sputtered onto a clean YZ $LiNbO_3$ substrate, which was then inserted into a diffusion furnace. Argon, purified with Ti-Zr sponge at 900°C was passed through at a rate of 2 ℓ/min. The furnace was turned on to 850°C, and one hour later the temperature had stabilized. After a total of 6½ hours, the temperature was reduced to 600°C and oxygen introduced with a 1 ℓ/min flow rate. This step increased the re-oxidation of the $LiNbO_3$. At 8½ hours total elapsed time, the furnace was shut off and allowed to cool slowly to room temperature. The substrate was removed from the furnace when cool, and the residue polished off. The resulting 6-mode optical waveguides were excellent, although the substrate remained a pale brownish color.

Figure 2.26 shows the diffusion profile obtained by electron microprobe analysis. The nickel to surface nickel ratio is fitted reasonably well by erfc(y/11.5), as was expected from the noticeable nickel oxide or nitride residue, which apparently acted as a constant diffusion source. An accurate quantitative microprobe analysis of $Ni/LiNbO_3$ is difficult, since lithium was not detectable in the microprobe used, and oxygen counts tended to be inaccurate.

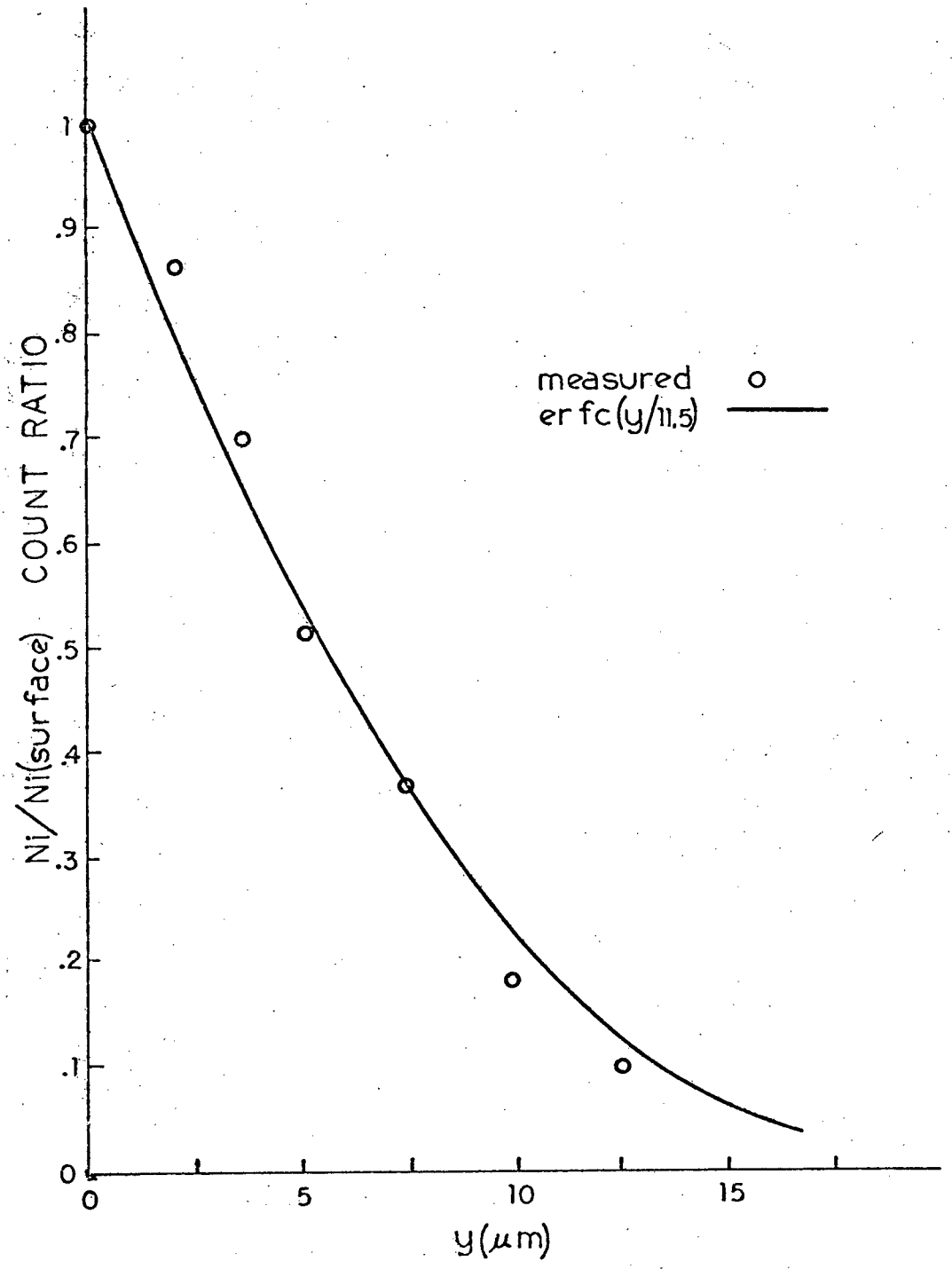

Fig. 2.26 $Ni/LiNbO_3$ Diffusion Profile.

Figure 2.27 shows the stage used in the optical coupling and acoustooptic experiments. Five degrees of freedom of movement were possible, and the substrate could easily be positioned for coupling to guided modes. On the stage were two adjustable arms for clamping prisms to the waveguide. The coupling procedure was as follows. The prism was positioned on the waveguide and the clamp adjusted until a brownish spot became visible on the bottom. This area was then close enough to the OWG surface for coupling to take place. Caution was required, as the substrates were easily cracked by excessive pressure. Light from a He-Ne Spectra-Physics 155 laser was focussed on this spot by means of a 25 cm lens. The stage was rotated about a horizontal axis until the angle of critical internal reflection at the prism bottom was found. Coupling was then attained by small rotational and translational adjustments until a bright streak was obtained. A scale attached to the substrate table was used to measure the coupling angles within 1/2 minute of arc.

Figure 2.28 shows coupling to the TE_o and TM_o modes of a two mode $Ni/LiNbO_3$ optical waveguide. The beam stops at a surface scratch, from which it radiates brightly. The periodic variations in streak brightness are caused by spatial mode beating. In Fig. 2.29, the guided wave is coupled out as well, and the bright spot to the right is the TE_o guided mode. The line passing through the spot is due to scattering of light into guided modes not collinear with the initial direction of propagation. Most of this scattering is probably due to fine surface scratches sustained while polishing off the diffusion residue. The direction of polarization was tested with a piece of ordinary plastic polaroid. Its direction was checked by examining light reflected from a smooth surface; the minimum in transmittance on rotation of the polariod

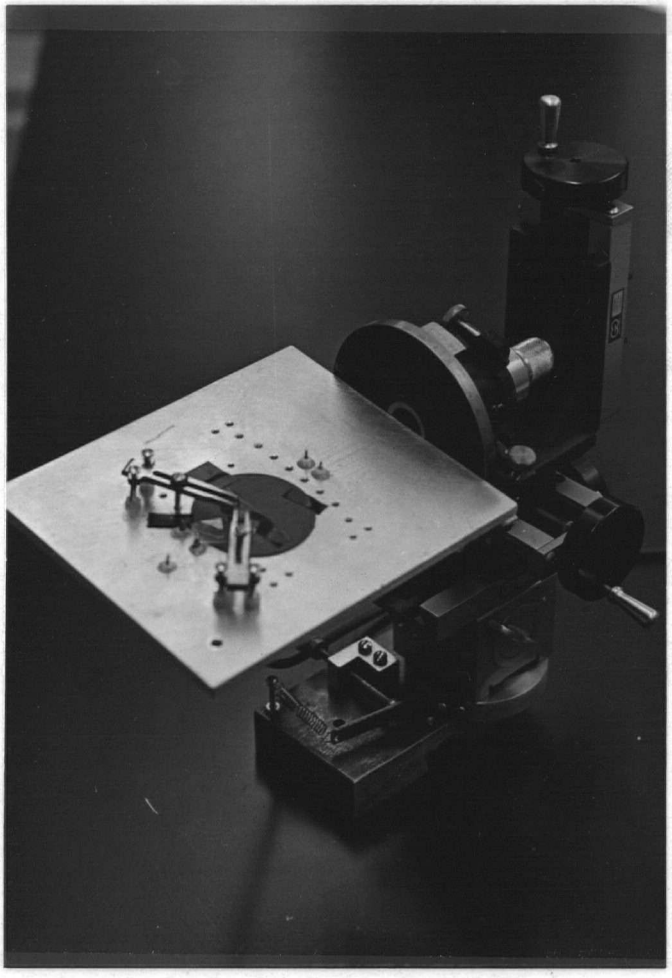

Fig. 2.27 Stage for Coupling to Optical Waveguides

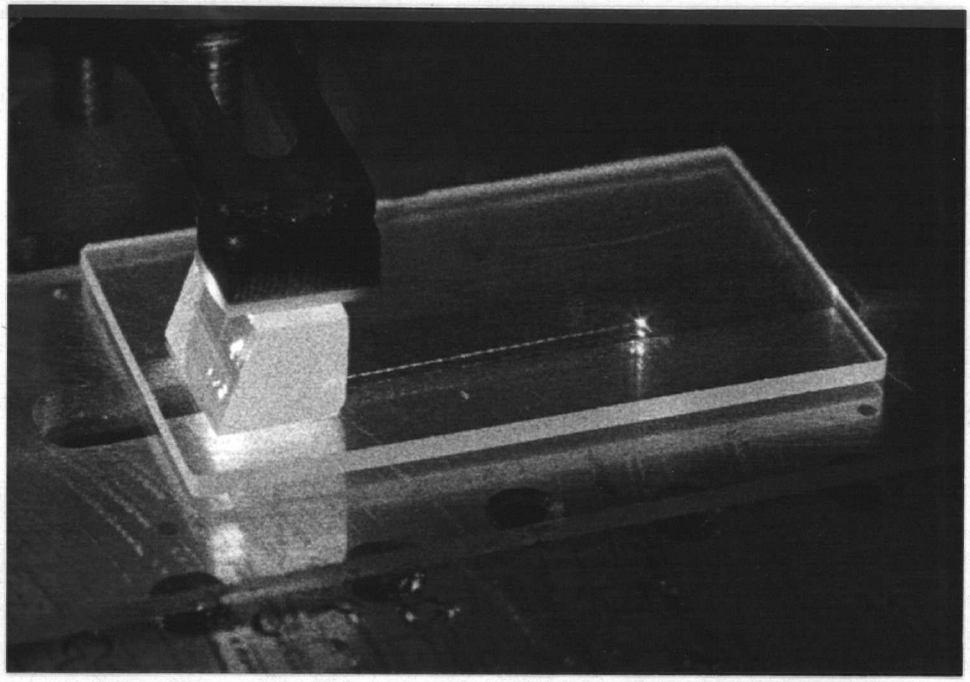

Fig. 2.28 Two Mode Ni-Diffused Guide Showing Mode Beating between the TE_o & TM_o Modes.

corresponded to the direction of transmittance of TE waves.

Propagation losses were measured by placing the output coupling prism at several points along the path of wave propagation. Light output was maximized each time by adjusting the output prism clamp, and the output power was measured with an Alphametrics dc1010 lightmeter. Use of the relation $P_{z2} = P_{z1} \exp[-\alpha(z2 - z1)]$ gave loss coefficients of 1 db/cm or less.

Figure 2.30 shows the modes coupled out of the 6-mode Ni/$LiNbO_3$ waveguides used for acoustooptic experiments. The direction of light propagation in the crystal was 21.4° from the crystal X axis. The three spots on the right are the TE_o, TE_1 and TE_2 modes, and the weaker spots on the left are the corresponding TM modes. The input light beam was unpolarized, so both TE and TM modes were excited. By careful adjustment of the prism and angle of light incidence, it was possible to excite just one mode at a time. The prism pressure was reduced to a minimal value, and the coupling angles μ_m were measured for the TE modes. The prism angle was found to be 68° 12' ± 1' by reflecting the incident light back on itself from both the substrate and prism face.

The mode indices were calculated from the coupling angles using (2.26), with $n_p = 2.582$. Equations (2.19) and (2.20) were solved for the turning points of the TE modes according to the piecewise-linear WKB approximation.* The estimated value of the surface index was varied until the rms second differences (2.21) were minimized, thereby giving the smoothest profile. The results are summarized in Table (2-3). The surface index used was 2.2377, which gave an rms deviation of 6.8×10^{-5}.

*The electric OGW field component along the propagation direction was ignored. A simple calculation shows that $E_z = .024\ E_x$.

Fig. 2.29 Coupling in and out (TE_o mode).

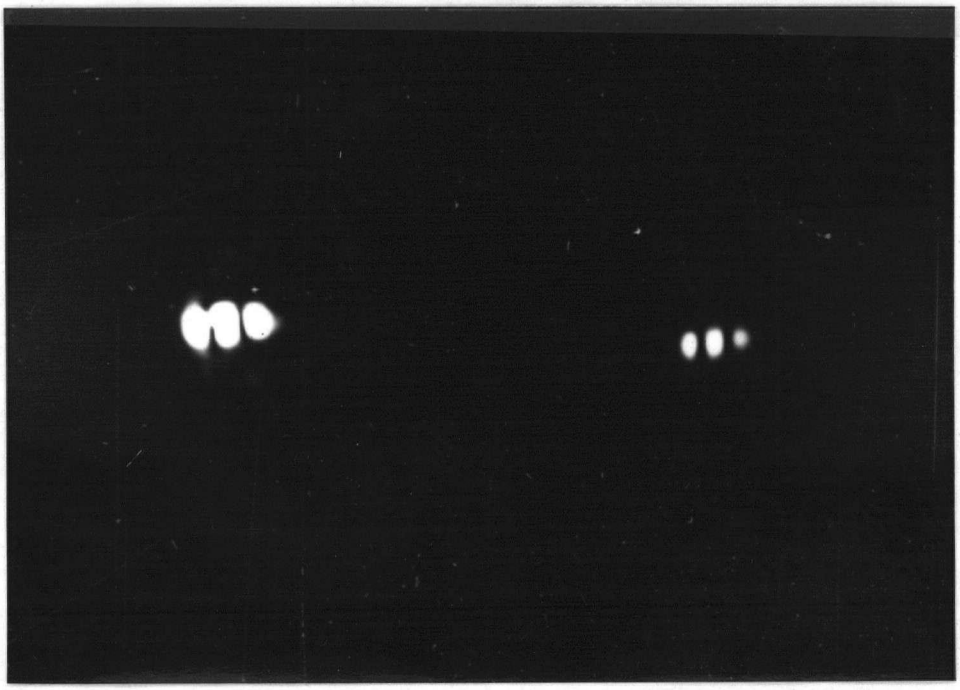

Fig. 2.30 Modes of OWG's Used in Acoustooptic Experiments.

Table 2.3 TE Modes a of $Ni/LiNbO_3$ OWG.

Mode Number	μ_m (±1')	n_m (±.0004)	y_m (μm)
TE_o	21^o 31'	$n_1 = 2.235$	$y_1 = 3.23$
TE_1	21^o 45'	$n_2 = 2.233$	$y_2 = 5.78$
TE_2	21^o 56'	$n_3 = 2.2316$	$y_3 = 8.41$

These measurements were made with an angle of light propagation of 21.4° from the X axis of $LiNbO_3$ in the Y-cut plane. This direction was chosen so the light would intersect at the Bragg angle (.4°) with a 165 MHz acoustic surface wave propagating in the Z - 21.8° direction, as discussed in Chapter 4. The substrate index for TE polarization along this direction can be found as follows.

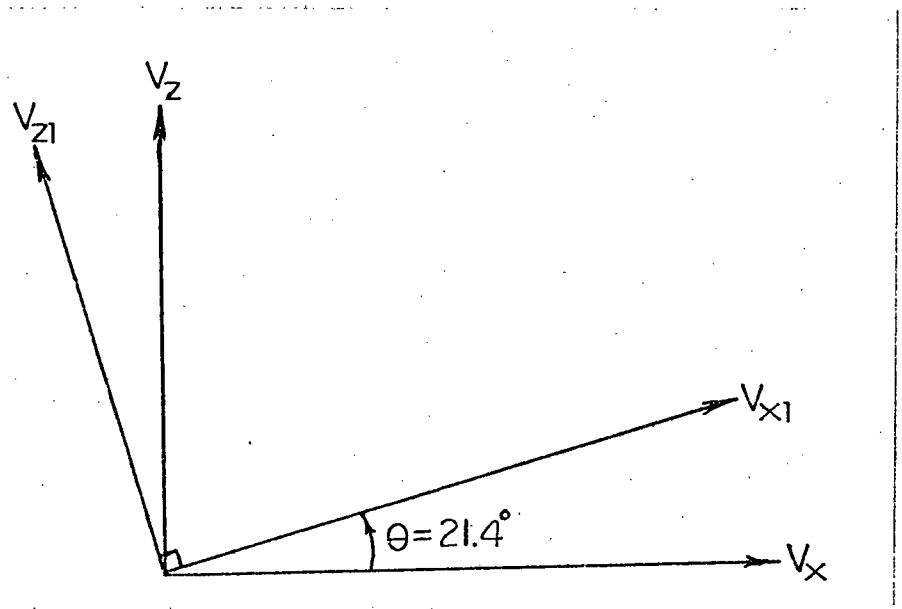

Fig. 2.31 Coordinate Rotation in Phase Velocity Space.

Consider a coordinate rotation in the X-Z plane of the crystal phase velocity space,

$$V_x = V_{x1} \cos\theta - V_{z1} \sin\theta$$

$$V_z = V_{x1} \sin\theta + V_{z1} \cos\theta$$

For plane wave propagation along x1, we have $V = V_{x1}$ and $V_{z1} = V_y = 0$. Then $V_x = V_{x1} \cos\theta$ and $V_z = V_{x1} \sin\theta$. Substitution into the phase velocity surface determinant (Appendix II) and multiplication by $n_{x1}^4 = c^4/V_{x1}^4$ gives

$$(n_y^2 - n_{x1}^2)\ [n_x^2 n_z^2 - n_{x1}^2(n_x^2 \cos^2\theta - n_z^2 \sin^2\theta)] = 0,$$

so that either

$$n_{x1} = n_y \quad \text{(TM)}, \quad \text{or}$$

$$n_{x1} = n_x n_z/(n_z^2 \sin^2\theta + n_x^2 \cos^2\theta)^{1/2} \tag{2.39}$$

for TE waves. Using $n_z = n_e = 2.214$, $n_x = n_o = 2.294$ [4] and $\theta = 21.4^\circ$, the substrate index of propagation for TE waves is $n_s = 2.224$. The waveguide index profile (Fig. 2.32) was fitted quite well by

$$n(y) = 2.2286 + 0.0091 \text{ erfc } (y/11.5), \tag{2.40}$$

with y in μm. The agreement between the index and diffusion profiles, and between the calculated and fitted substrate index, is reasonable.

The electric field distribution of the TE modes was calculated by the WKB method, using equations (2.10)-(2.16). To check whether this method was in fact applicable to the problem, the index profile

$$n(y) = n_s + \Delta n \text{ erfc } (y/b)$$

was differentiated to obtain

$$\frac{d\kappa}{dy} = -\frac{2k \cdot n(y) \cdot \Delta n}{\sqrt{\pi} \cdot b \cdot \sqrt{n(y)^2 - n_m^2}} \exp(-y^2/b^2) \tag{2.41}$$

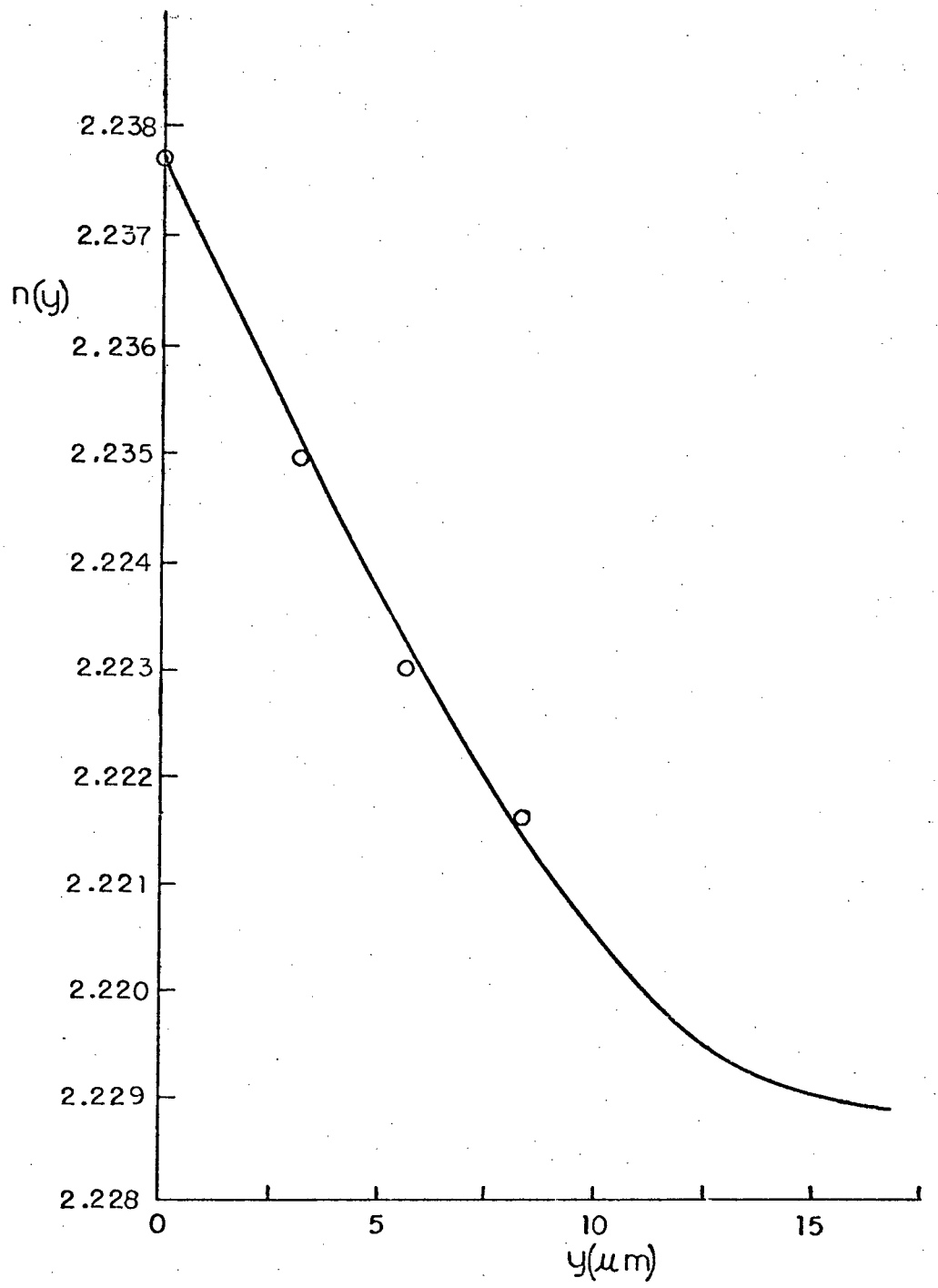

Fig. 2.32 $Ni/LiNbO_3$ OWG Index Profile.

Substitution of the values $\Delta n = .0091$, $b = 11.5$ μm, $\lambda = .6328$ μm, $y = 0$, $n_s = 2.2286$, and $n_m = 2.233$ (TE_1 mode) gave

$$|d\kappa/dy| = .014k \quad \text{and} \quad \kappa/\lambda = .23k,$$

so that inequality (2.17) is satisfied.

In the region $y < 0$, the exact solution of the wave equation was used, and the constant A was chosen to match the solution for $y = 0$ at the waveguide surface. For $y \geq 0$ and up to y_o, the last zero of E_x, (2.11) was used. The integrals were evaluated numerically by the trapezoidal rule.

For $y \geq y_o$, the usual approach in the WKB method is to make a linear approximation [34] of the index profile, setting

$$n(y) \sim n_m + n_m'(y - y_m)$$

where n_m is the index at the turning point and

$$\begin{aligned} n_m' &= |dn(y)/dy|_{y=y_m} \\ &= \frac{2\Delta n}{\sqrt{\pi}\, b} \exp(-y_m^2/b^2) \end{aligned} \tag{2.43}$$

for the case of an erfc profile. Neglecting terms of second order in Δn, $\kappa(y)$ becomes

$$\kappa^2(y) = 2k^2 n_m n_m' (y - y_m) \tag{2.44}$$

In the region of the turning point, the wave equation is then approximated by

$$\frac{d^2E_x}{dy^2} + (y - y_m)g\, E_x = 0. \tag{2.45}$$

where $g = 2k^2 n_m n_m'$.

The change of variable

$$\tilde{z} = g^{1/3}(y_m - y) \tag{2.46}$$

gives

$$\frac{d^2E_x}{d\tilde{z}^2} - \tilde{z}\, E_x = 0 \tag{2.47}$$

The solution of this equation can be expressed in terms of fractional order Bessel or Hankel functions, or, more conveniently, in terms of the Airy function Ai ($\tilde{z}$). The problem is to match the solution of (2.47) to the WKB solutions on either side. Marcuse gives

$$E_x(y) = (AB/2j)(\kappa_o \pi (y_m - y)/3)^{1/2} [\exp(2\pi j/3) H^{(1)}_{1/3}(\zeta) + \exp(\pi j/3) H^{(2)}_{1/3}(\zeta)], \tag{2.48}$$

where $\zeta = (2/3)\tilde{z}^{3/2}$, in the vicinity of the turning point. Use of the identity [36]

$$Ai(-\tilde{z}) = (1/2)\sqrt{\tilde{z}/3}\ [\exp(\pi j/6) H^{(1)}_{1/3}(\zeta) + \exp(-\pi j/6) H^{(2)}_{1/3}(\zeta)] \tag{2.49}$$

gives

$$E_x(y) = (AB/g^{1/6})\sqrt{\kappa_o \pi}\ Ai(-\tilde{z})$$

$$= (AB/g^{1/6})\sqrt{\kappa_o \pi}\ Ai\ [g^{1/3}(y - y_m)] \tag{2.50}$$

The Airy function has the convenient property that $\tilde{z} = 0$ at the turning point, where

$$Ai(0) = 3^{-2/3}/\Gamma(2/3)$$

$$= 0.35502$$

Thus, the electric field at the turning point is

$$E_x(y_m) = AB\sqrt{\kappa_o \pi}/(g^{1/6}\Gamma(2/3)3^{2/3}) \tag{2.51}$$

This differs from Marcuse's expression [9], which appears to underestimate the magnitude of the electric field.

To calculate the electric field in the vicinity of the turning point, the Airy function was generated with the series representation [36]

$$Ai(\tilde{z}) = c_1\ f(\tilde{z}) + c_2\ g(\tilde{z}), \tag{2.52}$$

where

$$f(\tilde{z}) = 1 + \frac{\tilde{z}^3}{3!} + \frac{1.4}{6!}\tilde{z}^6 + \frac{1.4.7}{9!}\tilde{z}^9 + \ldots$$

$$g(\tilde{z}) = \tilde{z} + \frac{2}{4!}\tilde{z}^4 + \frac{2.5}{7!}\tilde{z}^7 + \frac{2.5.8}{10!}\tilde{z}^{10} + \ldots$$

with $$c_1 = \mathrm{Ai}(0)$$

and $$c_2 = -d\mathrm{Ai}(0)/d\tilde{z} = 0.25881$$

Figure 2.33 shows this function for $-8 < \tilde{z} < 4$. Since our interest was only in the vicinity of the final maximum of the function, where $|\tilde{z}| < 3$, 8 terms of the series were adequate for five decimal place accuracy.

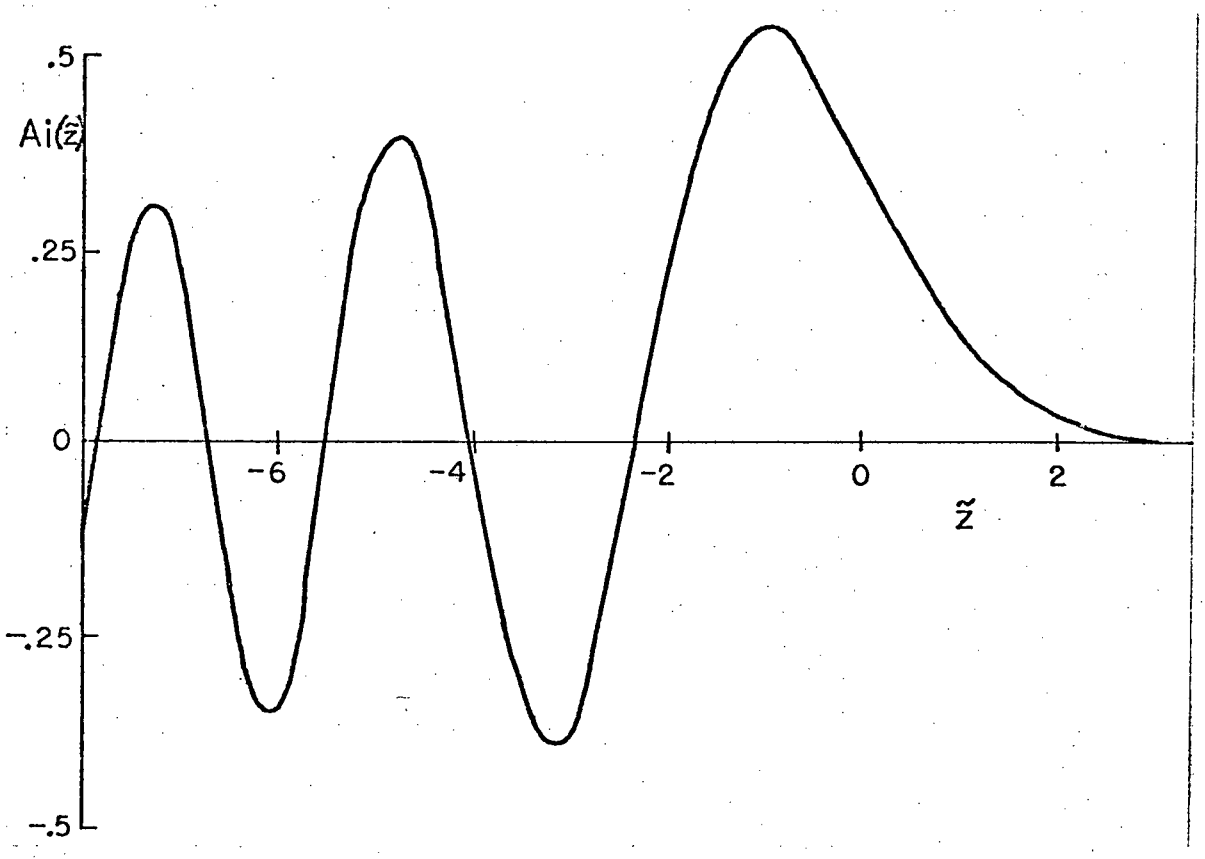

Fig. 2.33 The Airy Function.

In the region $y > y_m$, the WKB solution was found to agree very closely with the Airy function solution, so the latter was used exclusively for $y \geq y_o$. For the TE_o mode, most of the solution is in the vicinity of the turning point, so the Airy function was used entirely for $y \geq 0$. For higher order modes, the Airy function deviates

from the correct solution when $y < y_o$, so the WKB method (2.11) was used for $0 \leq y \leq y_o$. In Fig. 2.34, a comparison is made between the Airy function and WKB solutions for the TE_1 mode.

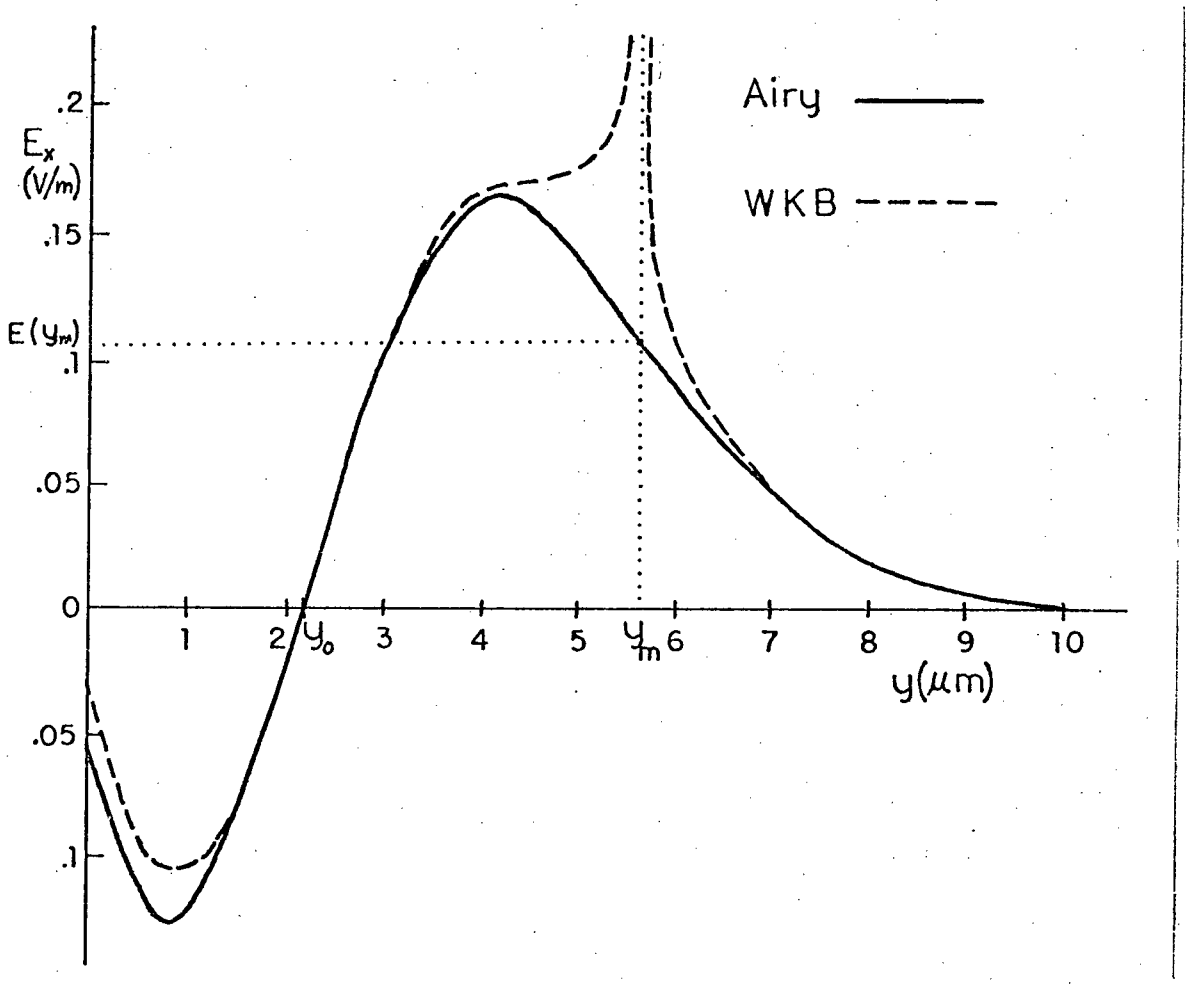

Fig. 2.34 Comparison of Airy Function and WKB Solutions for TE_1 Mode of 6-Mode $Ni/LiNbO_3$ OWG.

To summarize, the best approach seems to be as follows:

$$E_x = A \exp(-\gamma y), \qquad y \leq 0, \tag{2.53}$$

$$E_x = AB\sqrt{\kappa_o/\kappa(y)}\, \cos(\pi/4 - \int_y^{y_m} \kappa(y)dy), \qquad 0 \leq y \leq y_o, \tag{2.54}$$

and

$$E_x = (AB/g^{1/6})\sqrt{\kappa_o \pi}\ \ Ai[g^{1/3}(y - y_m)], \qquad y_o \leq y < \infty. \qquad (2.55)$$

Solutions of these equations for the three TE modes of the 6-mode $Ni/LiNbO_3$ waveguides studied are shown in Fig. 2.35 for propagation in the X + 21.4° direction of Y cut $LiNbO_3$. The modes have been normalized so that each carries a power of 1 watt/meter. These electric field distributions are used later (section 4.6) to calculate the acoustooptic overlap integrals, as discussed in Chapter 4.

The value of the normalization integral was used in (2.30) to estimate the coupling efficiency of the rutile prism used. All three TE modes had a maximum coupling efficiency of about 55% for a 1 mm coupling length. In Fig. 2.36, the coupling efficiency η_t is plotted as a function of gap thickness for the TE_2 mode, using the values $W = \ell = 1$ mm, $n_p = 2.582$, $\alpha = 68° 12'$, $\mu = 22° 45'$, which corresponded approximately to the experimental situation. The maximum coupling efficiency actually observed was 10-15%. Since η_t does not include the light loss on reflection from the prism face ($\sim$ 25%), the agreement between theory and experiment is quite reasonable. The pressure required to attain this degree of coupling efficiency cracked the substrate, so further experiments were conducted with 5% efficiency or less.

A quick estimate of the maximum value of α_c can be obtained by approximating the index profile with a constant, so that

$$\kappa(y) \sim (1/2)\ \kappa_o$$

The value of the normalization integral is small outside the range $0 \leq y < y_m$, so we can write

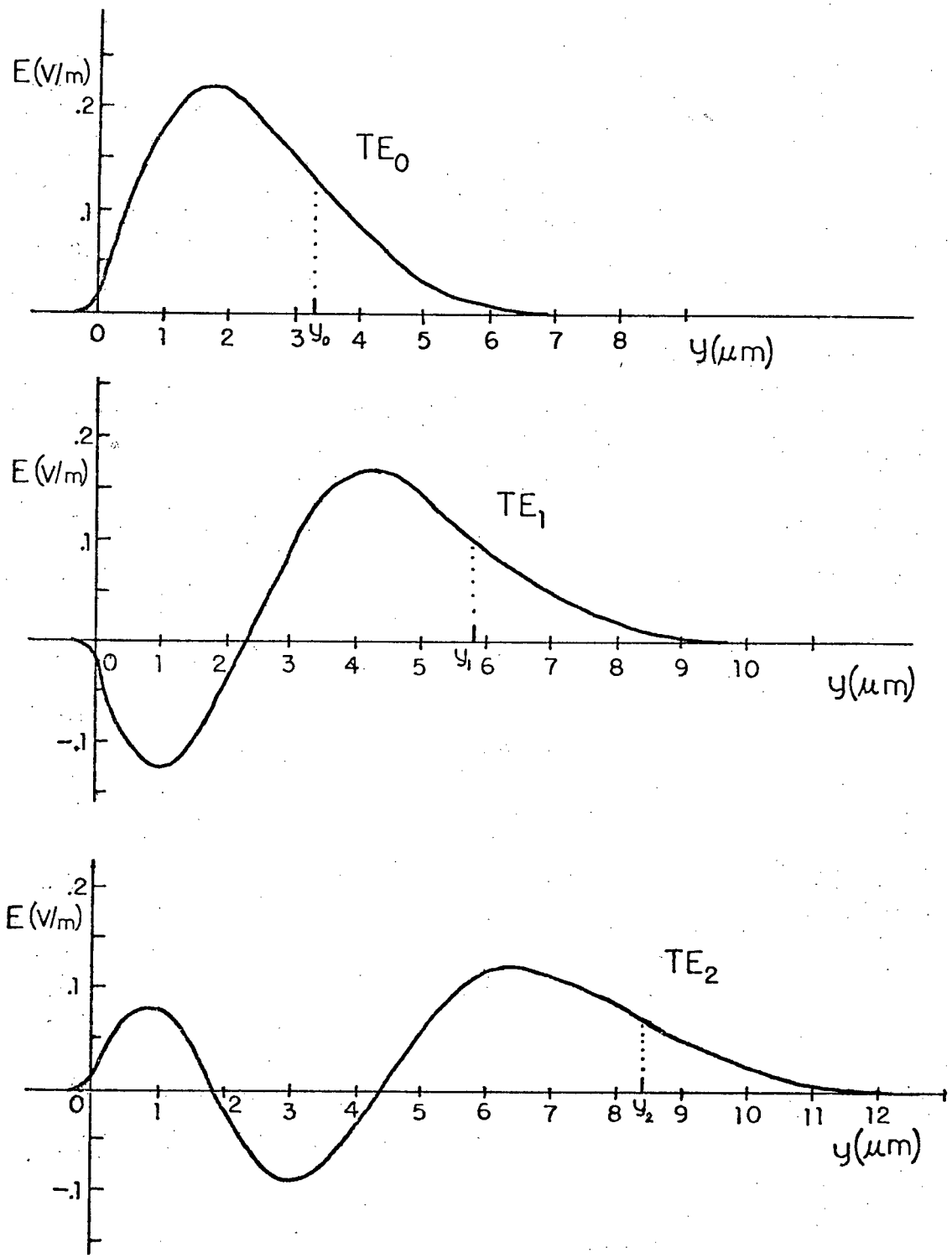

Fig. 2.35 TE Modes of a Ni/$LiNbO_3$ OWG.

$$\int_{-\infty}^{\infty} E_x^* E_x dy \approx 2A^2B^2 \int_o^{y_m} \cos^2\left(\int_o^{y_m} (\kappa_o/2)dy - \pi/4\right)dy$$

$$= A^2B^2[y_m + (1/\kappa_o)\cos(\kappa_o y_m)]$$

The second term is smaller than the first, particularly for higher modes, for which it can be neglected. Setting D = 0 in (2.30) gives

$$(\alpha_c)_{max} \approx y_m^{-1}(n_p^2/n_m^2-1)^{1/2}[1 + (n_p^2/n_m^2-1)^{1/2}(n_o^2/n_m^2-1)^{-1/2}]^{-2} \quad (2.56)$$

This expression appears to be accurate within about 10%. For example, for the case discussed earlier, (2.56) gives $(\alpha_c)_{max} \approx 0.88$ mm^{-1} rather than the correct value of 0.79. Use of the approximate value gives the maximum coupling efficiency as 27% rather than 25.5%.

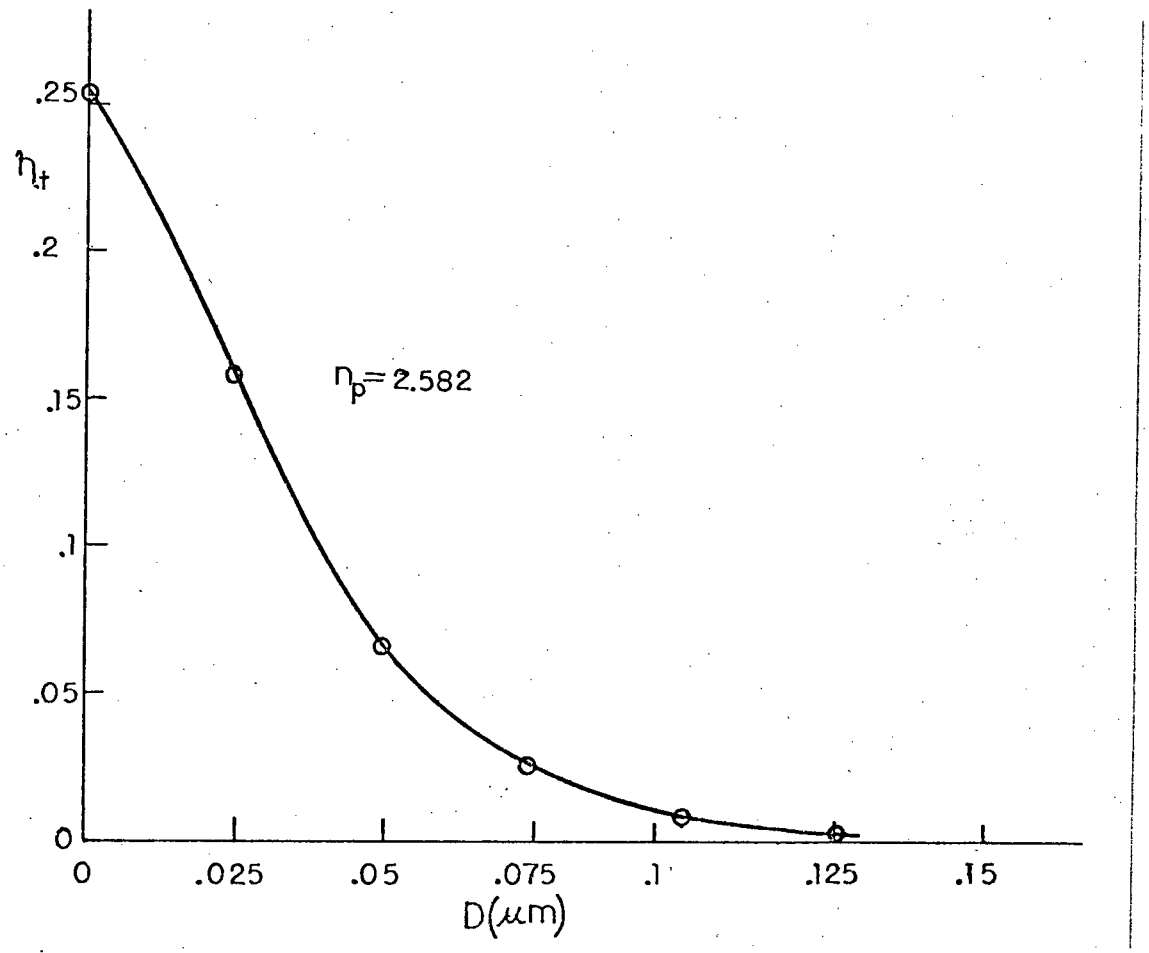

Fig. 2.36 Prism Coupler Efficiency.

3. PROPAGATION AND GENERATION OF ACOUSTIC SURFACE WAVES

3.1 Introduction

Elastic surface waves have been studied since their prediction by Lord Rayleigh in 1887. At the free surface of a solid medium, sound waves propagate with a reduced phase velocity and are guided in a layer about one wavelength deep. Particle motion is elliptical, with components normal and parallel to the surface, and an exponential decay in amplitude away from the surface.

These waves found their first application in the study of seismic phenomena, and were later used for flaw testing in materials. They were not seriously considered for electronic signal processing applications until 1965, when White and Voltmer [37] demonstrated a simple and efficient method of direct coupling to surface acoustic waves (SAW's) by means of an interdigital electrode array on the surface of a piezoelectric solid. Since that time, SAW devices have found application in high performance delay lines and filters, and promise the realization of more complex circuit functions, such as real-time convolution of two signals. In this chapter, the propagation and generation characteristics of SAW's on anisotropic piezoelectric materials is reviewed, with particular emphasis on $LiNbO_3$ as the acoustic medium. Experiments with an 85 MHz SAW delay line are described, and measurements are compared with predictions of an equivalent circuit model.

3.2 Surface Waves in Piezoelectrics

Consider an infinite slab of piezoelectric material as illustrated in Fig. 3.1.

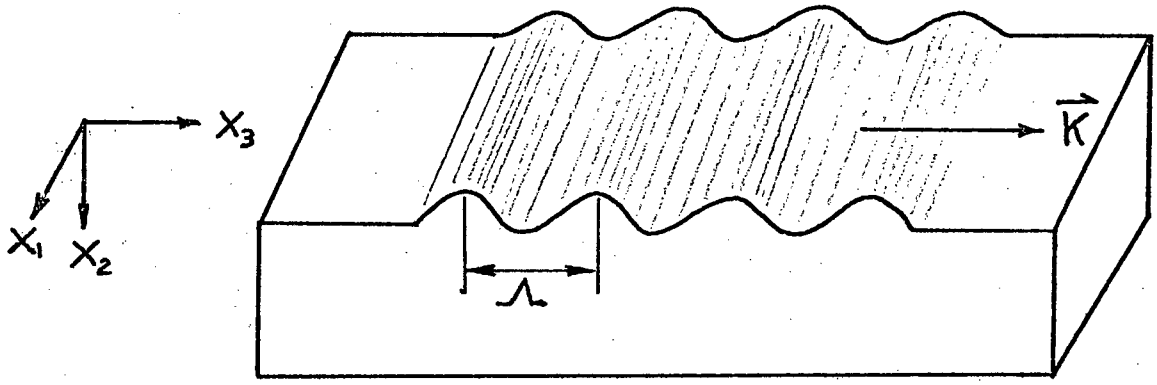

Fig. 3.1 SAW Propagation.

An acoustic surface wave of wavevector $\vec{K}$ and wavelength Λ propagates along the x_3 coordinate axis. The slab is assumed to be many wavelengths thick, so that the lower boundary has no effect on wave propagation. Let u_k represent the excursion from the equilibrium point x_k of a particle in the solid. The elastic strain tensor is defined as [38]

$$S_{k\ell} = \frac{1}{2} (u_{k,\ell} + u_{\ell,k}) , \tag{3.1}$$

where the symbols ",ℓ" denote partial differentiation with respect to x_ℓ. In a piezoelectric material the relation between stress and strain involves the piezoelectric constitutive relations, which can be written as [39]

$$T_{ij} = c^E_{ijk\ell} S_{k\ell} - e_{kij} E_k \tag{3.2}$$

$$D_i = e_{ik\ell} S_{k\ell} + \varepsilon^S_{ik} E_k \tag{3.3}$$

where T_{ij} is the stress tensor, $c^E_{ijk\ell}$, $e_{ik\ell}$ and ε^S_{ik} are the elastic stiffness tensor (at constant electric field), the piezoelectric tensor, and the dielectric tensor (at constant strain), respectively.

In a stationary solid not subject to external body forces, consideration of an infinitesimal volume element centered at x_k gives the particle equation of motion,

$$\rho \ddot{u}_j = T_{ij,i} \ , \tag{3.4}$$

where ρ is the density and "$\cdot$" denotes differentiation with respect to time.

Use of the relations

$$E_k = - \Phi_{,k} \ , \tag{3.5}$$

$$D_{i,i} = 0 \ , \tag{3.6}$$

and substitution of (3.2) into (3.4) gives the SAW equations of motion,

$$\rho \ddot{u}_j = c^E_{ijk\ell} \, u_{k,\ell i} + e_{kij} \, \Phi_{,ki} \tag{3.7}$$

and

$$0 = e_{ik\ell} \, u_{k,\ell i} - \varepsilon^s_{ik} \, \Phi_{,ki} \ . \tag{3.8}$$

Strictly speaking, (3.5) is approximate. However, since the propagation velocity of surface waves is some five orders of magnitude less than the velocity of light, the electrostatic form of Maxwell's equations can be used with very little loss in accuracy.

Solutions to (3.7) and (3.8) have the form [40]

$$u_k = \beta_k \exp(-\alpha K x_2) \exp j(\Omega t - K x_3) \ , \qquad k = 1, 2, 3 \tag{3.9}$$

and

$$\phi = \beta_4 \exp(-\alpha K x_2) \exp j(\Omega t - K x_3) \tag{3.10}$$

for wave propagation in the x_3 direction. Substitution into (3.7) and (3.8) gives a linear homogeneous system in the unknowns β_k, $k = 1, 4$.

For a non-trivial solution, the determinant of coefficients must be zero, giving an eighth-degree polynomial equation in α. Since the fields are bounded, only solutions with non-negative real parts can

be used. In general, four complex roots can be found which are satisfactory. Each value of α can then be substituted back into the homogeneous equations in β_k, giving four (generally complex) values of β_k. Using the other boundary conditions the partial field amplitudes (those corresponding to each value of α) can be found by numerical methods to complete the solution.

The problem can only be solved by iterative computer techniques. The first such solutions for SAW's on $LiNbO_3$ were obtained by Campbell and Jones [41] in 1968. They calculated SAW velocities in different propagation directions for both free and metallized surfaces. The difference between the two velocities is an important parameter indicating the strength of interaction between SAW's and electric fields generated by means of surface electrodes. This will be discussed further in the section on interdigital transducers.

The complete description of YZ (Y cut, Z propagating) SAW's on $LiNbO_3$ is given by Spaight and Koerber [42]. Fourteen complex coefficients are required to describe the essentially exponential SAW decay with depth. Solutions for this and other major crystal cuts are given in the Microwave Acoustics Handbook [40].

To summarize, the description of acoustic surface waves on $LiNbO_3$ and similar materials is quite complex. In general, the waves have both displacement and electric field components normal and perpendicular to the surface. Outside the material, the electric fields decay exponentially; inside, all fields exhibit a slower oscillatory decay. The solutions may be written in the form

$$u_k(\vec{x},t) = \beta_k^m \exp j(\Omega t - Kx_3) \qquad (3.11)$$

where

$$\beta_k^m = \sum_{q=1}^{3} A_{kq} \exp(\alpha_q Kx_2)$$

and

$$E_k = -\frac{\partial \phi}{\partial x_k} = \beta_k^E \exp j(\Omega t - Kx_3) \tag{3.12}$$

where

$$\beta_k^E = \sum_{q=1}^{3} B_{kq} \exp(\alpha_q Kx_2) \ .$$

The time average power flow in the SAW is the sum of two parts [75], one due to the mechanical displacement field,

$$P_{ma} = \frac{1}{2} \sum_i \mathrm{Re} \int_0^\infty j\Omega \ T_{ij} \ u_j^* \ dx_2 \tag{3.13}$$

and the other due to the SAW electric field,

$$P_{ea} = \frac{1}{2} \sum_i \mathrm{Re} \int_0^\infty j\Omega \ \phi \ D_i^* \ dx_2 \ , \tag{3.14}$$

where D_i^* is the complex conjugate of the ith component of the electric displacement vector. The A_{kq} and B_{kq} coefficients are usually normalized so that the total power is one watt/m.

3.3 Diffraction of Surface Waves

The diffraction of elastic surface waves may be treated by methods similar to those used for electromagnetic waves. In anisotropic crystals, the situation is complicated by the fact that the phase and group velocities of propagation are non-collinear with the exception of a few symmetry (pure-mode) axes. Cohen [43] studied the diffraction of bulk ultrasonic waves in a number of anisotropic materials. He used a parabolic fit to the crystal phase velocity surface,

$$v(\theta) = v_o(1 - b\theta^2) \tag{3.15}$$

in the vicinity of pure-mode axes. He found excellent agreement between calculations based on the above approximation and experiments in a number of materials.

Weglein et al [44] applied this approximation to the spreading of 100 MHz surface waves propagating in the Z and Z ± 21.8° directions in Y-cut $LiNbO_3$. Exact agreement between theory and experiment was not obtained. Analytic expressions for the far-field beam divergence half-angle $\psi_{1/2}$ and the Fresnel distance r_f have been obtained by Crabb et al [45],

$$\psi_{1/2} = \frac{\Lambda\ (1 + d\phi/d\theta)}{W\ \sec\phi} \tag{3.16}$$

$$r_f = \frac{W^2\ \sec\phi}{4\Lambda(1 + d\phi/d\theta)} \tag{3.17}$$

where W is the source width and $\tan\phi = \frac{1}{v}\frac{dv}{d\theta}$. Use of the parabolic approximation gives

$$\psi_{1/2} = \frac{\Lambda}{W}\ (1 - 2b) \tag{3.18}$$

and

$$r_f = \frac{W^2}{4\Lambda(1 - 2b)}\ , \tag{3.19}$$

for small angles θ about the pure mode axis. Except for the factor (1 - 2b), these equations are identical with those applicable to isotropic diffraction. The walk-off angle ϕ between the phase and group velocities is given by

$$\phi = -2b\theta. \tag{3.20}$$

Szabo and Slobodnik [46] give an excellent review of surface wave diffraction on anisotropic substrates. They compare isotropic, parabolic and exact theoretical calculations with experimental observation (the exact calculations were done by Kharusi and Farnell [47]).

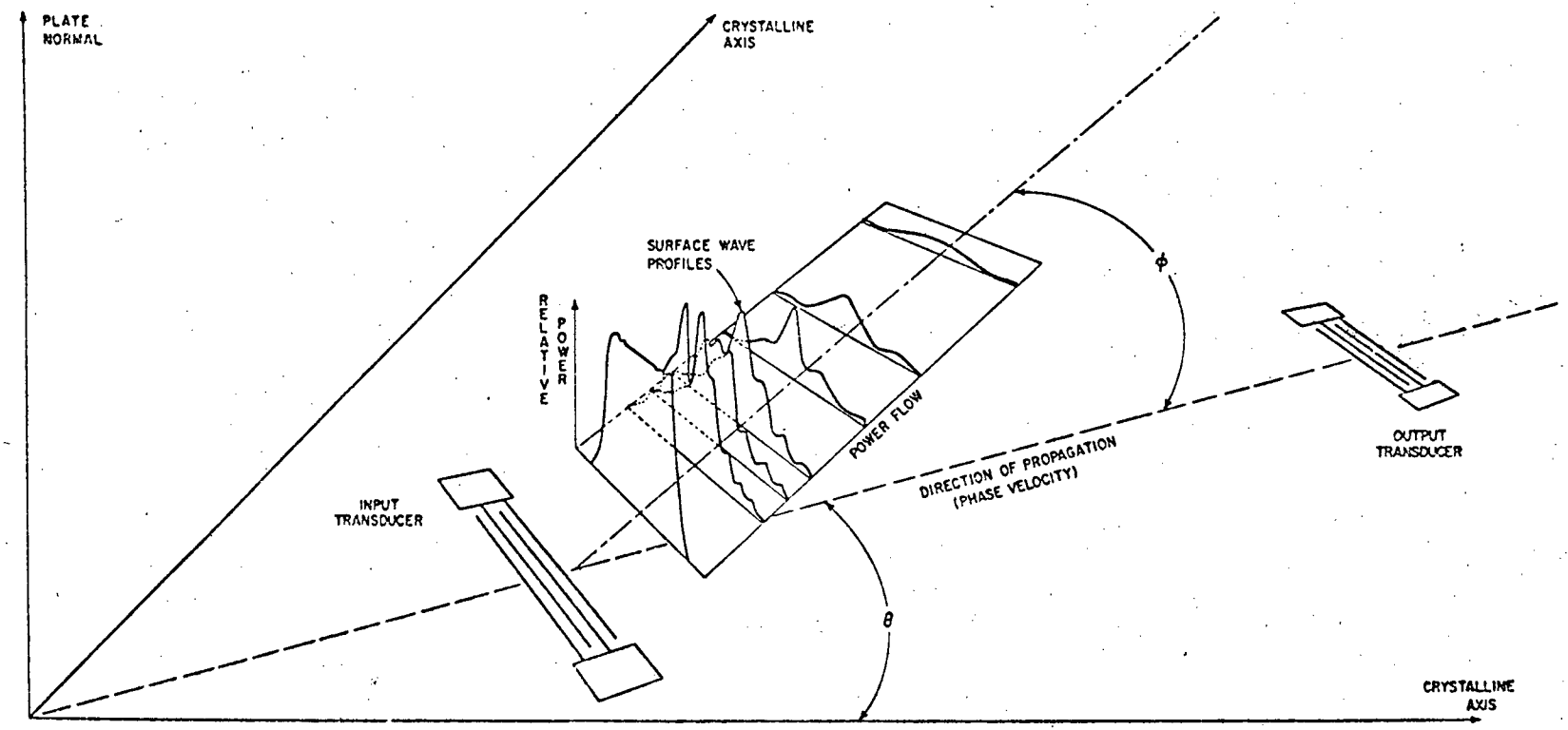

Fig. 3.2 SAW Propagation in Anisotropic Materials [40]

For propagation in the Z direction on YZ $LiNbO_3$, the parabolic theory does not give accurate results. The reason for this is that $1 + d\phi/d\theta \sim 0$ in this case, so that the value of b must be very accurately known. This is not possible at the present time because the material constants have not been determined with sufficient accuracy.

However, for propagation in the Z ± 21.8° direction (where $1 + d\phi/d\theta \sim 1.37$) good accuracy is obtainable, as demonstrated by Wilkinson et al [48].

In Table 3.1, the anisotropy parameter is given for these two propagation directions. For YZ waves, beam spreading is much less than in the case of isotropic diffraction; hence, this cut is useful for SAW delay lines. For Z ± 21.8° propagation, beam spreading is greater than in the isotropic case. This property makes this cut useful for beam-steered light deflectors.

Table 3.1 Anisotropy Parameter b.

Cut	Propagation Direction	b [44]
Y	Z	0.54
Y	Z ± 21.8°	-0.187

3.4 SAW Generation; the Interdigital Transducer

Consider the idealized interdigital transducer (IDT) in Fig. 3.3. A grid of infinitely long electrodes on an infinite piezoelectric slab are alternately connected to an r.f. generator. The material thickness is assumed to be much greater than the electrode spacing.

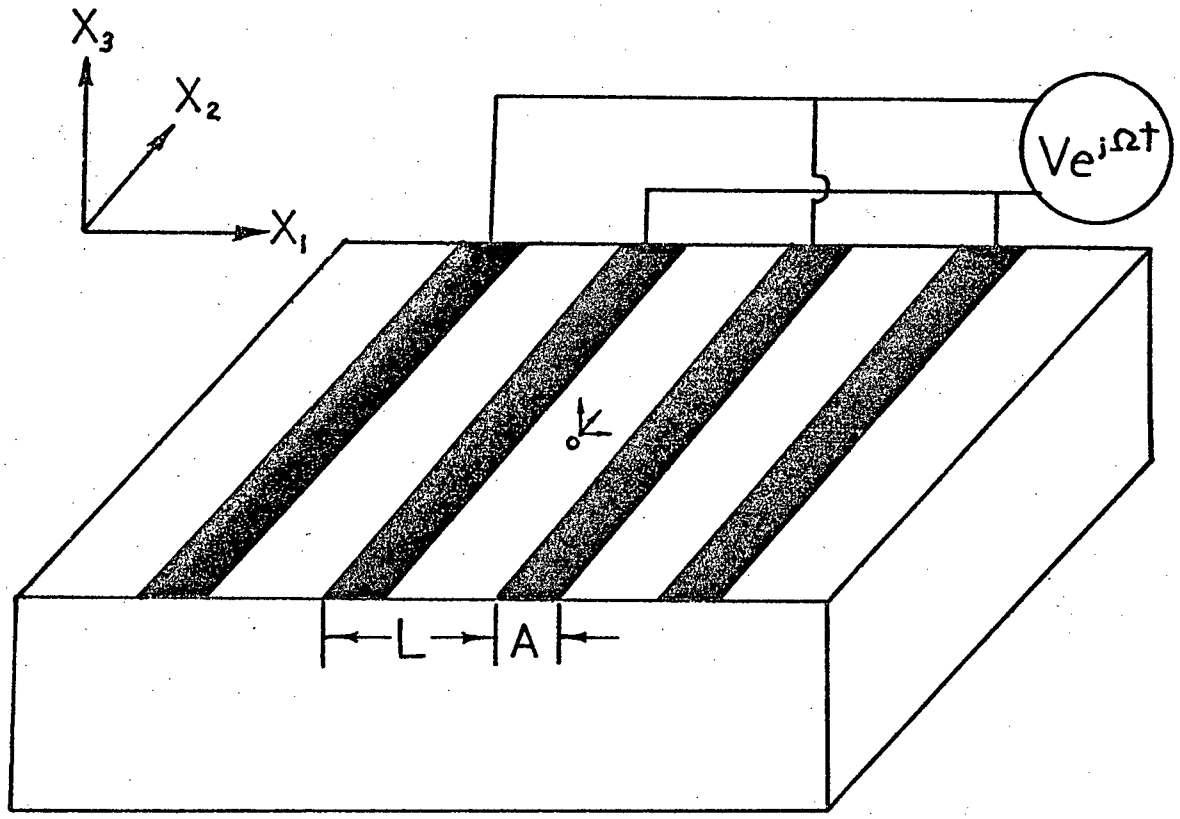

Fig. 3.3 Section of an Idealized IDT.

The problem is to develop an equivalent circuit model. To make the calculation at all reasonable, it is necessary to make a number of assumptions:

(1) the electrodes are massless, perfectly conducting and infinitely long (so that the problem becomes two-dimensional),

(2) the quasi-static approximation is assumed, i.e., $\vec{E} = -\nabla\Phi$,

(3) the piezoelectric is assumed to have no non-linearity, and

(4) the driving voltage and the SAW's have the time dependence $e^{j\Omega t}$.

The equations of state of a linear piezoelectric, (3.1)-(3.6), were discussed in section 3.2. Since the actual problem to be solved

is essentially two-dimensional, these relations can be reduced to the following [49], using reduced matrix notation:

$$\rho\Omega^2 u_1 + T_{1,1} + T_{5,3} = 0 \qquad (3.21)$$

$$\rho\Omega^2 u_3 + T_{5,1} + T_{3,3} = 0$$

where

$$T_1 = c_{11}^E S_1 + c_{13}^E S_3 - e_{31} E_3 ,$$

$$T_3 = c_{13}^E S_1 + c_{33}^E S_3 - e_{33} E_3 ,$$

$$T_5 = c_{44}^E S_5 - e_{15} E_1 ,$$

$$S_1 = u_{1,1}$$

$$S_3 = u_{3,3}$$

$$S_5 = u_{1,3} + u_{3,1}$$

$$E_1 = -\Phi_{,1}$$

and $$E_3 = -\Phi_{,3} .$$

Using Gauss' Law,

$$D_{1,1} + D_{3,3} = 0 ,$$

and making the indicated substitutions gives three partial differential equations in terms of u_1, u_3 and Φ:

$$\rho\Omega^2 u_1 + c_{11}^E u_{1,11} + c_{44}^E u_{1,33} + (c_{13}^E + c_{44}^E) u_{3,13} + (e_{15} + e_{31}) \Phi_{,13} = 0 \qquad (3.23)$$

$$(c_{13}^E + c_{44}^E) u_{1,13} + \rho\Omega^2 u_3 + c_{44}^E u_{3,11} + c_{33}^E u_{3,33} + e_{15} \Phi_{,11} + e_{33} \Phi_{,33} = 0 \qquad (3.24)$$

$$(e_{15} + e_{31})u_{1,13} + e_{15}u_{3,11} + e_{33}\,u_{3,33} - \varepsilon_{11}^{s}\,\Phi_{,11} - \varepsilon_{33}^{s}\,\Phi_{,33} = 0 \tag{3.25}$$

The mechanical boundary conditions are

$$\begin{aligned} T_3 &= 0 \quad \text{at} \quad x_3 = 0 \\ T_5 &= 0 \quad \text{at} \quad x_3 = 0\ . \end{aligned} \tag{3.26}$$

Most frequently, the electrical boundary conditions have been chosen to be

$$\begin{aligned} \Phi &= \frac{V}{2} \quad \text{at} \quad x_3 = 0\ , \qquad \frac{L-A}{2} \le |x_1| \le \frac{L+A}{2} \\ D_3 &= 0 \quad \text{at} \quad x_3 = 0\ , \qquad 0 \le |x_1| \le \frac{L-A}{2} \end{aligned} \tag{3.27}$$

The second condition is an approximation, since it ignores the electric field outside the crystal where the surface is not metallized. This is quite accurate in high permittivity materials, such as $LiNbO_3$.

Equations (3.23)-(3.27) constitute a statement of the problem, which is to find the coupled electrical and mechanical fields when an alternating voltage is applied. A variety of solutions have been attempted. No exact analytic solution is possible. Usually, the weak coupling approximation (which means ignoring the piezoelectric terms $e_{kij}\,E_k$ in the constitutive relations) is made. This is equivalent to ignoring the coupling between electrical and mechanical SAW fields. In the literature, the problem has been treated as either entirely mechanical [39,50], or the solution of the electrical fields (through Laplace's equation) has been considered independent of the acoustic strain fields [51,52,53]. As pointed out by Milsom and Redwood [49], neither approach is entirely satisfactory, since accuracy and information

are lost. They solved (3.23)-(3.27) with variational techniques, which appear to give very accurate solutions over extended frequency ranges. Unfortunately, their solution is not convenient to apply in design problems, since it does not lead to a simple equivalent circuit.

Campbell and Jones suggested that Δv, the change in SAW velocity when a conducting sheet was applied to the piezoelectric surface, could be used as a measure of coupling strength between the SAW electrical and mechanical fields, and hence between the transducer and a surface wave. Figure 3.4 shows the surface wave velocity and $\Delta v/v$ for Y cut $LiNbO_3$. They found a large $\Delta v/v$ value for YZ propagation, implying that high coupling efficiency was possible. This was verified by Collins et al [54].

A number of authors [39,51,53,55,56] have shown that the physical description can lead to an equivalent circuit model when suitable simplifying assumptions are made. A more empirical approach was taken by Smith et al [57], who used a circuit model formulated by Mason for each finger pair. They proceeded to find an admittance matrix for the transducer as a whole by cascading sections. Two cases were treated, which give differing equivalent circuits:

(1) the in-line model assumes surface wave generation is by compressional excitation, resulting in a series equivalent circuit, and

(2) the crossed-field model, having a shunt equivalent circuit, which assumes SAW generation by shear excitation.

Generally, transducers generate surface waves by both methods simultaneously, but frequently one mechanism predominates. The actual model applicable may be determined by calculating the relative power in

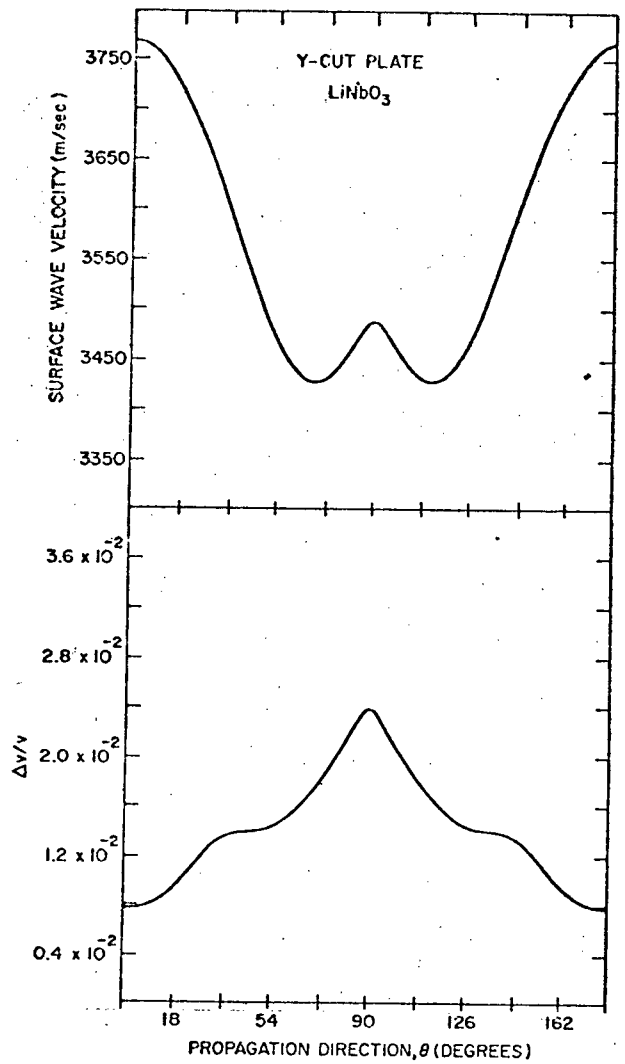

Fig. 3.4 SAW Velocity and Coupling Constant for Y-Cut $LiNbO_3$ [40].

the shear and compressional wave components. For YZ $LiNbO_3$, Smith et al calculated that the shear component is one order of magnitude greater, so that a shunt model is more appropriate. However, if certain conditions are met (for example, if the IDT has few fingers) the two models may be considered equivalent.

Smith et al's model was modified slightly by Auld and Kino [53], who solved the physical problem by means of a perturbed normal mode expansion technique and the weak coupling approximation. They used

Engan's [52] expression for transducer static capacitance,

$$C_T = WC_s$$

$$= WN(\varepsilon_o + \varepsilon_p)K(q)/K'(q) \qquad (3.28)$$

where W is the transducer width,

N is the number of finger pairs,

ε_p is the relevant dielectric constant,

$q = \cos[\frac{\pi}{2}(1 - a)]$, where $a = A/L$,

and K and K' are complementary elliptic integrals of the first kind. This expression takes into account the effect of the ratio a of metallized to free surface under the transducer, which Smith et al's model does not. The shunt model has the equivalent circuit

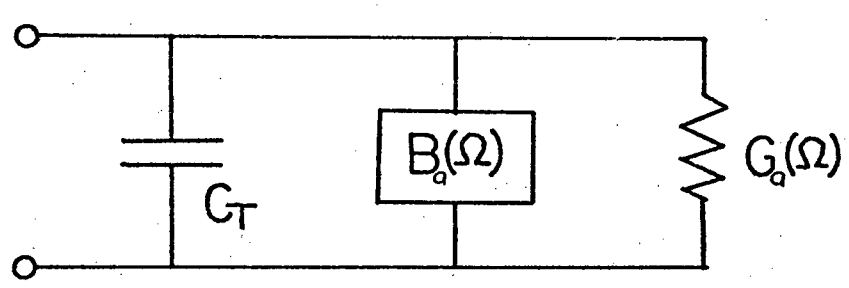

Fig. 3.5 IDT Shunt Model Equivalent Circuit.

The radiation conductance at the center frequency $\Omega_o = \frac{\pi V}{L}$ is

$$G_o = \frac{\Omega_o C_T N\pi^2 \Delta}{K(q)\ K'(q)} \qquad (3.29)$$

where $\Delta = \Delta v/v$ is the change in wave velocity when the surface is metallized. When the frequency deviation is small ($\sim$ 20%),

$$G_a(\Omega) = G_o\ \mathrm{sinc}^2 x \qquad (3.30)$$

and

$$B_a(\Omega) = G_o\left(\frac{\sin(2x) - 2x}{2x^2}\right), \qquad (3.31)$$

where $x = N\pi\Delta\Omega/\Omega_o = N\pi\Delta f/f_o$ and sinc x = sinx/x.

It is usually more convenient to use the series model, which has the following circuit.

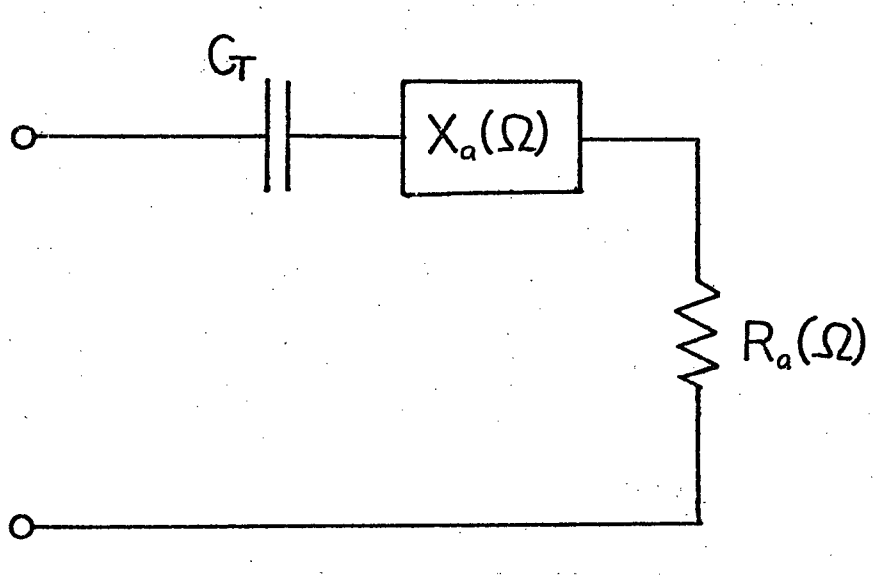

Fig. 3.6 Series Equivalent Circuit.

Here, the radiation resistance at resonance is

$$R_o = \frac{N\pi^2\Delta}{\Omega_o C_T K(q) K'(q)} \qquad (3.32)$$

For the two models to be equivalent at resonance, we require that

$$R_o + \frac{1}{j\Omega_o C_T} \approx \frac{1}{G_o + j\Omega_o C_T}$$

This implies that

$$R_o \approx \frac{G_o}{G_o^2 + \Omega^2 C_T^2}$$

From (3.28) and (3.29), with a = 0.5 so K = K' = 1.854,

$$\frac{G_o^2}{\Omega_o^2 C_T^2} = 8.24\, N^2\Delta^2 .$$

(Smith et al's equivalent expression is $5.1\, N^2\Delta^2$).

Thus, when

$$8.24\ N^2\Delta^2 << 1, \tag{3.33}$$

$$R_o \approx \frac{G_o}{\Omega_o^2 C_T^2}, \tag{3.34}$$

and the two models are equivalent. For example, for 3 finger pairs and propagation in the Z ± 21.8° direction, $8.24\ N^2\Delta^2 = .024 << 1$, so the equivalence is valid. It is interesting to note that $G_o \propto N^2$, but R_o is independent of N.

The frequency dependence of R and X is then given by

$$R_a(\Omega) = R_o\ \mathrm{sinc}^2 x \tag{3.35}$$

$$X_a(\Omega) = R_o\ \left(\frac{\sin(2x) - 2x}{2x^2}\right) . \tag{3.36}$$

Usually, the transducer bandwidth is taken to be 2/N, half the relative frequency difference between the zeros of the central radiation lobe. More useful is the -3 dB bandwidth, where $\mathrm{sinc}^2 x = \frac{1}{2}$, or x = 1.392. Then the acoustic bandwidth is given by

$$\frac{\Delta\Omega}{\Omega_o} = \frac{\Delta f}{f_o} = \frac{2.78}{N\pi} \approx \frac{.9}{N} . \tag{3.37}$$

In order to reduce the insertion loss, a series inductor is usually added to the circuit of Fig. 3. The inductance is selected so that it is resonant with C_T at the center frequency (since $x(\Omega_o) = 0$), that is,

$$L_s = \frac{1}{\Omega_o^2 C_T} \tag{3.38}$$

It is possible to make a number of extensions to this circuit model to increase its accuracy and frequency range. Emtage [56] has shown that an interdigital transducer produces surface waves at the frequencies

$$f_n = (2n + 1)f_o , \qquad n = 1, 2 \ldots . \tag{3.39}$$

Bahr and Lee [58] obtained expressions for the radiation conductance of the pth harmonic of the fundamental resonance, where $p = 2n + 1$, $n = 1, 2 \ldots$. They found

$$G(\Omega_p) = \Omega_p C_T N \pi^2 \Delta \frac{P^2_{1/2(p-1)}[\cos(\pi a)]}{K(q)\, K'(q)} \tag{3.40}$$

where P is a Legendre polynomial.

This expression shows reasonable agreement with experimental results by Weglein [59] and Marshall [60] for YZ $LiNbO_3$.

Bulk acoustic wave generation is not predicted by the circuit model, although it does occur. Schmidt [61] estimated that as much as 10% of the input power goes into bulk wave generation in YZ $LiNbO_3$ at 112 MHz. However, Milsom and Redwood's calculations, which are probably more accurate, predict only 1.6% for this configuration. They show a bulk resonance at $2f_o$, which was observed by Daniel and Emtage [62]. In later use of the circuit model here, bulk effects are ignored.

A useful addition to the model has been made by Lakin [63], who determined the effect of finger resistance on transducer impedance.

The additional series resistance is

$$R_e = \frac{8}{3\Lambda} \rho_s \eta_e W \tag{3.41}$$

where ρ_s is the electrode sheet resistivity,

W is the electrode width in meters,

and

$$\eta_e = \frac{3}{4}\left\{1 + \frac{\sinh(W\alpha_r)/W\alpha_r - \sin(W\alpha_i)/W\alpha_i}{\cosh(\alpha_r W) - \cos(\alpha_i W)}\right\}. \tag{3.42}$$

Lakin inconveniently gives many of his variables in units of wavelengths or ohm-wavelengths (for example, his radiation resistance

is given in $\Omega\cdot\Lambda$). In terms of MKS units, the phase factor α for $LiNbO_3$ may be approximated by

$$\alpha = \alpha_r + j\alpha_i = \left(\frac{8\Delta\rho_s C_s f^2}{v}\right)^{1/2}(1 + j) \qquad (3.43)$$

For example, consider an aluminum transducer of thickness $t = 0.1\ \mu m$ exciting surface waves in the $Z \pm 21.8°$ direction on Y cut $LiNbO_3$. Assuming the bulk resistivity of aluminum, $\rho_{A\ell} = 2.83 \times 10^{-8}\ \Omega$-m, and using $N = 3$, $\Delta = 0.018$, $f = 200$ MHz, $W = 1$ cm, $v = 3427$ m/sec, $a = 0.5$ and $\varepsilon_p = 56\ \varepsilon_o$, we obtain from (3.28) and (3.43) $W\alpha_r = W\alpha_i = 0.269$. Then (3.42) gives $\eta_e = 1.0$ to five figure accuracy, so we may use

$$R_e = \frac{8}{3\Lambda}\rho_s W .$$

This expression only applies to a metallization factor of $a = 0.5$ and one finger pair. The effect of N finger pairs will be to connect N resistors R_e in parallel, so for N finger pairs,

$$R_e = \frac{8\ \rho_s W}{3\ N\Lambda} .$$

If the metallization factor is increased to some value greater than 0.5, we expect the resistance to decrease by the factor $a/.5 = 2a$. Using the definition of sheet resistivity $\rho_s = \rho/t$, the expression for finger resistance then becomes

$$R_e = \frac{4\rho W}{3Nat\Lambda} \qquad (3.44)$$

The dielectric permittivity ε_p which appears in the equation for static capacitance, (3.28) is given by Auld and Kino [53] to be

$$\varepsilon_p = (\varepsilon_{yy}\ \varepsilon_{zz} - \varepsilon_{yz}^2)^{1/2} \qquad (3.45)$$

for Z propagation in the Y plane of $LiNbO_3$. They state that ε_p varies only slightly for the major crystal cuts, and that the stress-free

permittivity ε^T is the most appropriate. Switching to tensor notation, with (1,2,3) ≡ (x,y,z), Warner et al [64] give

$$\varepsilon^T_{yy} = \varepsilon^T_{xx} = \varepsilon^T_{11} = 84\ \varepsilon_o$$

$$\varepsilon^T_{zz} = \varepsilon^T_{33} = 30\ \varepsilon_o$$

$$\varepsilon^T_{yz} = 0\ .$$

Thus, for YZ propagation,

$$\varepsilon_p = 50.2\ \varepsilon_o\ .$$

For Z ± 21.8° propagation, we must use the second rank tensor transformation rule,

$$\varepsilon'_{ij} = a_{ik}\ a_{j\ell}\ \varepsilon_{k\ell} \qquad (3.46)$$

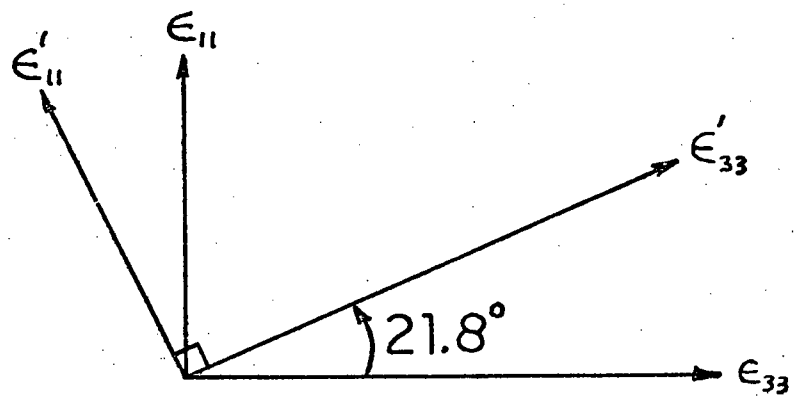

Fig. 3.7. Permittivity Transformation.

Thus,

$$\varepsilon'_{33} = a^2_{31}\ \varepsilon_{11} + a^2_{33}\ \varepsilon_{33}$$

$$= \varepsilon_{11}\ \sin^2 21.8° + \varepsilon_{33}\ \cos^2 21.8°$$

$$= 37.45\ \varepsilon_o.$$

Hence, $\varepsilon_p' = (\varepsilon_{11}\ \varepsilon_{33}')^{1/2} = 56.1\ \varepsilon_o$.

In Table 3.2 below, the properties of $LiNbO_3$ required for IDT calculations are summarized for several crystal cuts.

Table 3.2 Constants for $LiNbO_3$ [40]

Cut	Propagation Direction	V(m/s)	$\Delta = \Delta v/v_\infty$	ε_p
X	Z	3483.092	0.02598	$50.2\ \varepsilon_o$
Y	Z	3487.762	0.02409	$50.2\ \varepsilon_o$
Y	Z ± 21.8°	3427.641	0.01727	$56.1\ \varepsilon_o$

The complete circuit model, with matching series inductor, is

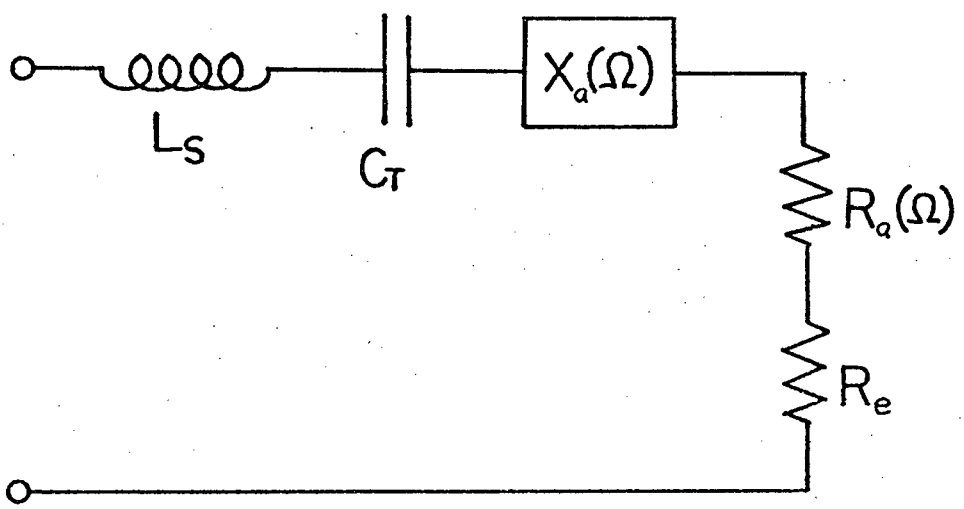

Fig. 3.8. Series Circuit Model.

To summarize, the equations for the circuit elements are as follows:

$$C_T = WN(\varepsilon_o + \varepsilon_p)\ K(q)/K'(q)$$

$$R_e = \frac{4\rho W}{3NatA}$$

$$R_o = \frac{N\pi^2\Delta}{\Omega_o C_T K(q) K'(q)}$$

$$R_a = R_o \operatorname{sinc}^2 x$$

$$X_a = R_o\left(\frac{\sin(2x) - 2x}{2x^2}\right) \qquad (3.47)$$

$$L_s = (\Omega_o^2 C_T)^{-1}$$

$$x = N\pi\Delta f/f_o$$

When a voltage $\sqrt{2}\, V_o e^{j\Omega t}$ is applied to this circuit, the acoustic power launched in the forward direction is

$$P_a = V_a^2/2R_a \,, \qquad (3.48)$$

where $V_a = V_o R_a/|Z|$, and the factor of 2 arises from the bidirectional radiation characteristic of the IDT.

The efficiency with which surface waves are generated in the forward direction, relative to the electrical power P_{eo} dissipated when $f=f_o$, is

$$\frac{P_a}{P_{eo}} = \frac{P_a}{V_o^2/(R_o + R_e)} = \frac{R_a(R_o + R_e)}{2|Z|^2}$$

so that the power insertion loss is

$$\text{R.I.L.} = -10 \log\left(R_a(R_o + R_e)/2|Z|^2\right) \qquad (3.49)$$

where

$$|Z|^2 = (R_a(\Omega) + R_e)^2 + \left(\Omega L_s = \frac{1}{\Omega C_T} + X_a(\Omega)\right)^2 .$$

At resonance, with $R_e = 0$, we see that the minimum insertion loss is 3 dB.

The Q of the electrical equivalent circuit is

$$Q_e = 1/\Omega_o C(R_o + R_e) \ . \tag{3.50}$$

From equation (3.37), the acoustic Q is

$$Q_a \approx \frac{N\pi}{2.78} \approx \frac{N}{.9} \tag{3.51}$$

In order to achieve the greatest device bandwidth, it is necessary that

$$Q_a \leq Q_e \ ; \tag{3.52}$$

otherwise, the bandwidth will be limited by Q_e. It is possible to achieve greater bandwidth at the expense of insertion loss if $Q_e > Q_a$ and L_s is detuned, so that the acoustic and electrical resonant frequencies differ.

3.5 Experimental Work

In order to check the validity of the circuit models and gain some experience in working with surface waves, an 85 MHz SAW delay line was made on an XZ $LiNbO_3$ substrate. Artwork for a 10-finger pair transducer was cut on rubylith and sent to Shaw Photogrammetrics in Ottawa, Ont., for photographic reduction by 100 X. The resulting photomask had fingers 2.05 mm wide and a periodicity of 41 μm. The fingers were considerably thicker than the spaces between them, presumably because of a loss in resolution in the photographic process. In order to obtain satisfactory transducers, it was necessary to reduce the finger width by means of overexposure of the photoresist.

Transducers were made 2 cm apart of 0.25 μm thick aluminum using Gaf PR-102 positive photoresist and an alkaline ferricyanide etchant. (More details on photolithographic processing are given in Chapter 5.) Electrical connection was made with fine gold wire and

silver paint. Tests on an aluminum film revealed that the silver paint gave a contact resistance of no more than a few ohms.

Transducer impedance measurements were made over a 10-250 MHz frequency range with a Boonton 250 A RX meter. Correction was made for the 1cm-long leads to the bridge terminals by balancing the meter with only the wires connected. The effect of acoustic reflections was minimized by covering the ends of the substrate with vinyl electrical tape.

Fig. 3.9 shows the conductance and susceptance of a typical transducer. The first maximum corresponds to SAW generation at the

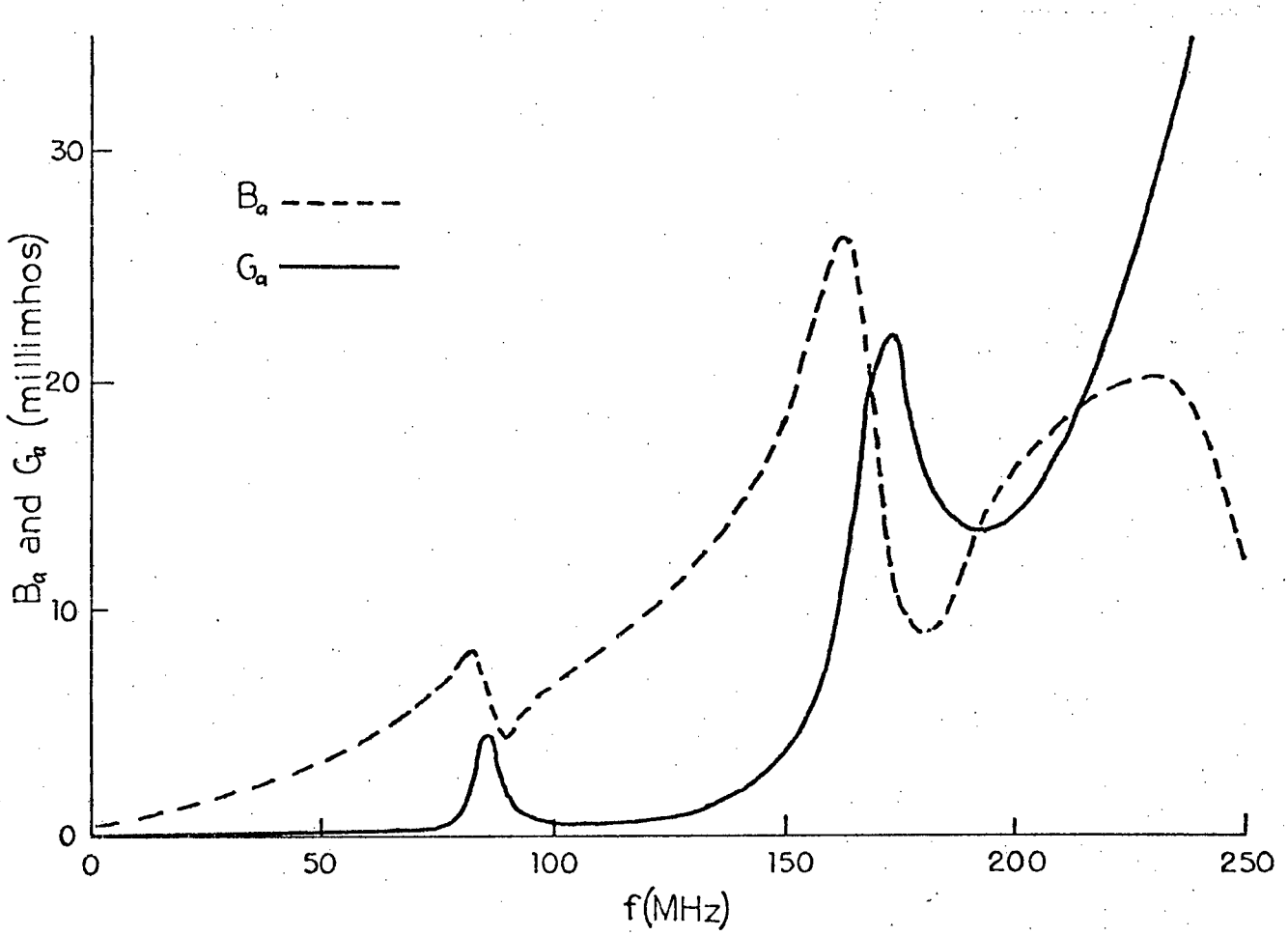

Fig. 3.9 Transducer Conductance and Susceptance.

fundamental resonant frequency f_o = 84.5 MHz. According to Reilly et al [65], the second resonance at about 165 MHz is due to the generation of bulk shear waves.

The shunt circuit model was used in calculations, because Smith et al [57] indicate it is more appropriate for XZ substrates. The simple equivalence (3.34) between shunt and series models does not apply to this transducer, since

$$8.24\ N^2\Delta^2 \sim .5\ ,$$

so that (3.33) is not satisfied. Figure 3.10 shows the transducer admittance in the vicinity of f_o. The circled points are experimental and the curves are calculated from the shunt model using (3.28)-(3.31) and the relevant parameters for XZ $LiNbO_3$ from Table 3.2. Microscopic examination of the IDT revealed that the metallization factor a was 0.6. The experimental values C_T = 10.9 pf and G_o = 4.20 millimhos compare favourably with the calculated values, 10.74 and 4.173. By comparing the magnitude of R_o and R_e in the series model, it can be shown that finger resistance effects were negligible in this transducer (the series model, although inaccurate, is adequate for a rough comparison).

A substrate with transducers 1.8 cm apart was connected as a delay line. Both IDT's were connected with 3.3 μH slug-tuned inductors in parallel.

These cancelled the capacitive transducer susceptance at the resonant frequency f_o, thereby reducing the insertion loss for SAW generation. A grounded aluminum shield was connected across the center of the delay line to minimize stray rf coupling between input and output. The input transducer was driven with a 50 Ω rf power amplifier, and the output was detected with a low capacitance oscilloscope probe. Use of

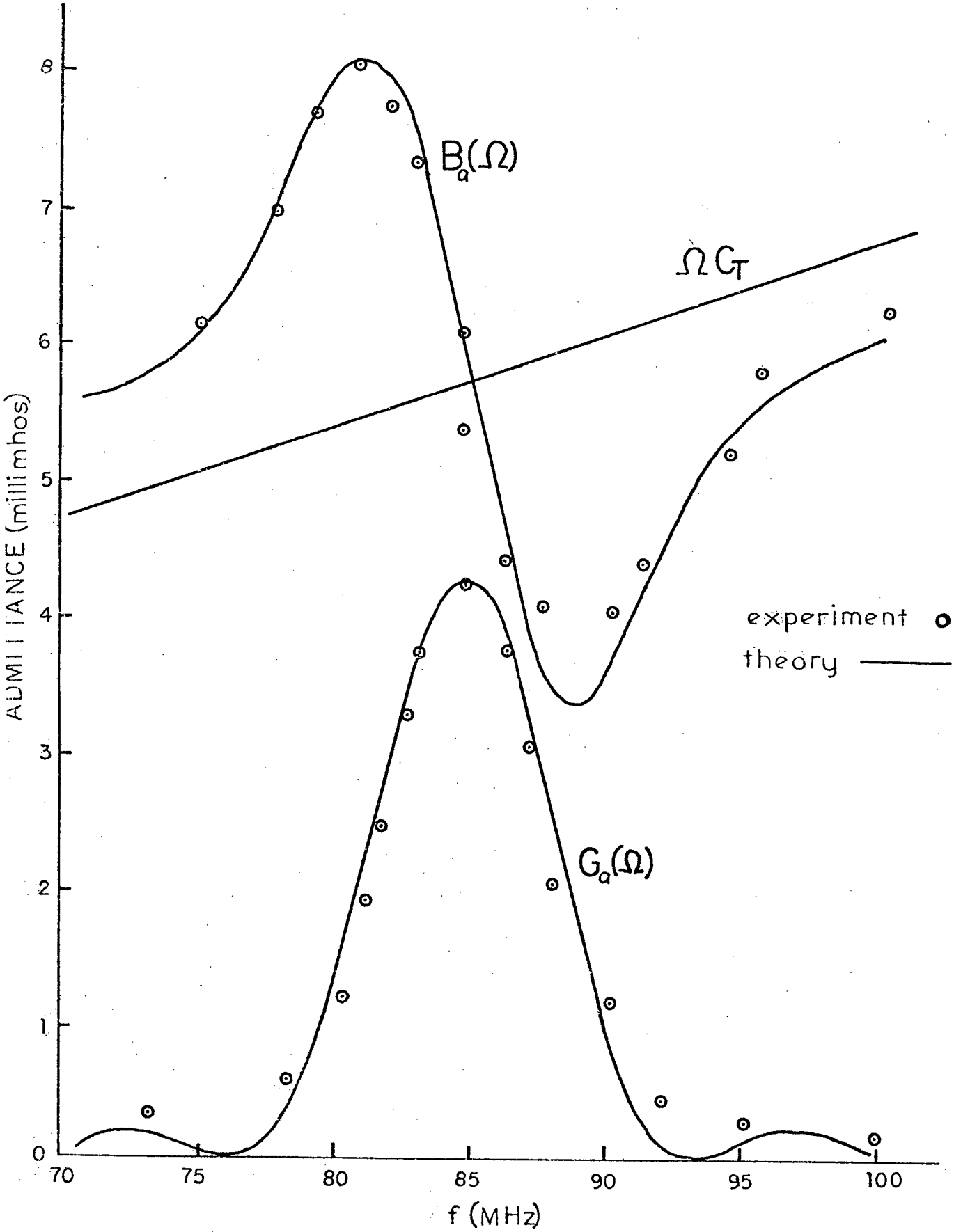

Fig. 3.10 Transducer Admittance near Resonance.

pulse excitation and a storage oscilloscope gave a propagation delay of 5 μs, in close agreement with the predicted value of 5.17 μs. With sine-wave excitation at the center frequency, the measured power insertion loss at the center frequency was 26 dB. Both transducers were matched with parallel inductors. The equivalent drive and IDT circuit is shown in fig 3.11. The electrical power into the device is given by $P_e = P_o(1 - |\rho_r|^2)$, where P_o is the forward power on a matched transmission line, and the reflection coefficient is given by $\rho_r=(Y_c-Y)/(Y_c+Y)$. Y_c is the characteristic line impedance, and Y is the IDT equivalent circuit admittance.

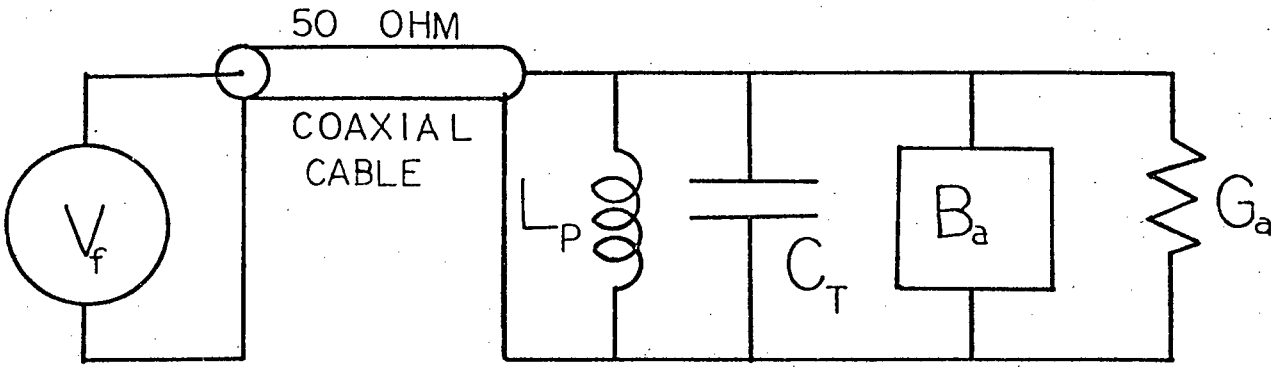

Fig. 3.11 Radiating IDT Equivalent Circuit

The acoustic power in the forward direction is half of P_e. The ratio of acoustic forward power to matched electrical power is thus given by

$$\frac{P_a}{P_o} = \frac{2Y_c G_a}{(Y_c + G_a)^2 + (B_a + \Omega C_T + 1/(\Omega L_p))^2} \qquad (3.53)$$

The power insertion loss is then given by

$$I.L. = -10 \log(P_a/P_o). \qquad (3.54)$$

At the center frequency , with $Y_c = G_a$, the minimum insertion

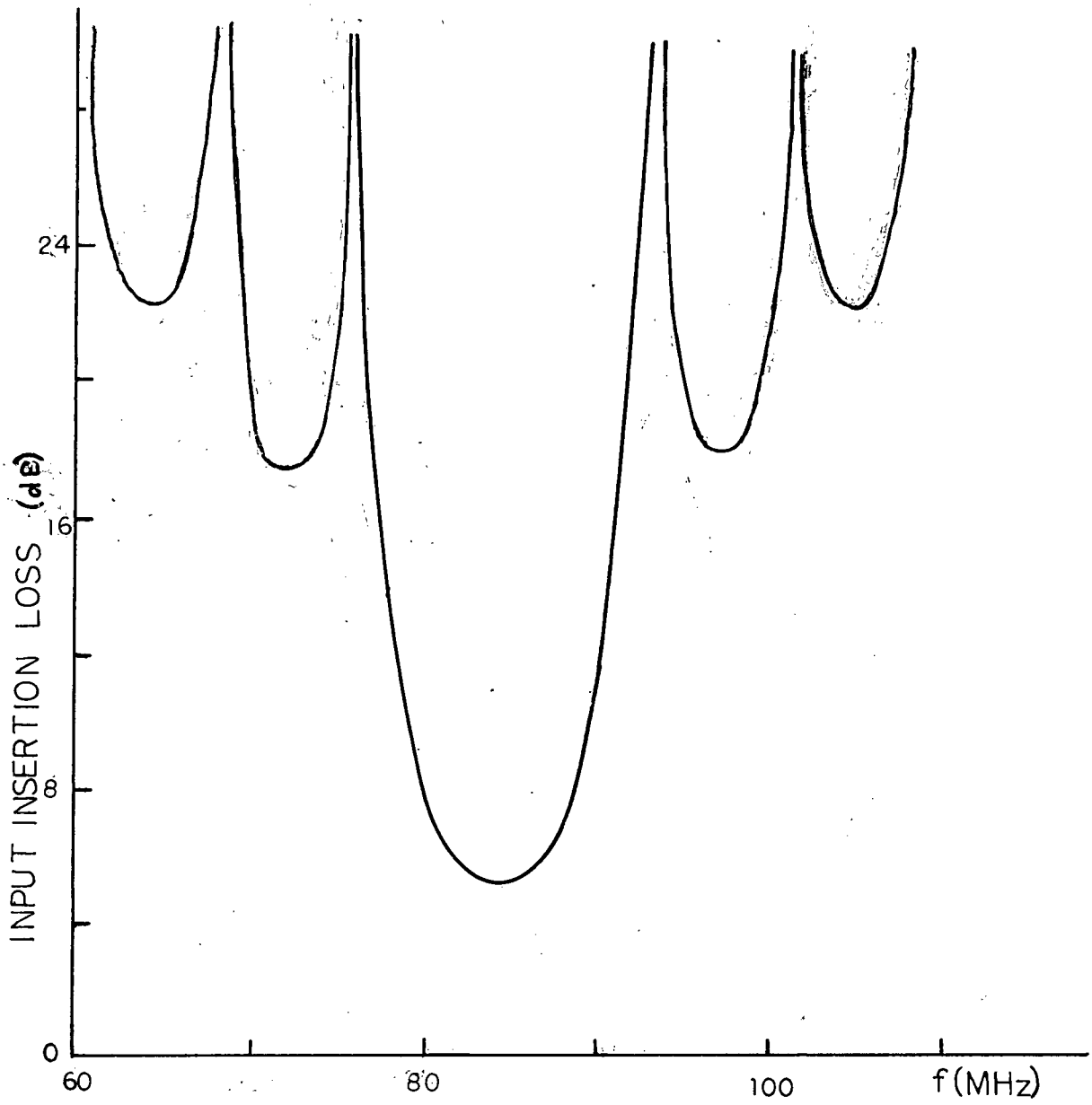

Fig. 3.12 Power Insertion Loss.

loss would be 3 dB. The calculated insertion loss of the input transducer of the experimental delay line is shown in fig. 3.12 as a function of frequency. At the center frequency, the insertion loss is 5.4 dB. The large overall loss observed experimentally was due to impedance mismatch of the output transducer and probably also due to a lack of accurate alignment between the input and output transducers.

SAW wavelength and amplitude measurements were made by diffracting light from propagating waves. In the limit of small deflection angles, the Raman-Nath theory [66] of light diffraction gives [67]

$$I_d = I_o J_1^2(2AK)$$
$$\approx I_o (AK)^2 \qquad (3.55)$$

for the deflected light intensity. The approximation is valid for small amplitudes A of the sound wave.

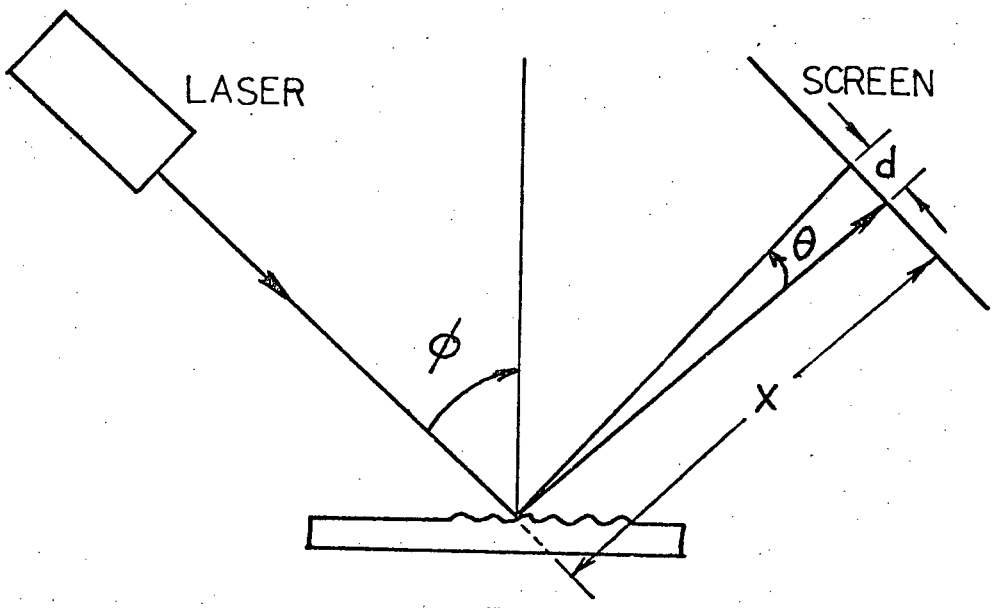

Fig. 3.13 Raman-Nath Diffraction of Light by Surface Waves.

With reference to Fig. 3.13, Raman-Nath theory gives [67]

$$\theta = \frac{\lambda}{\Lambda \cos\phi} = \frac{d}{x} \qquad (3.56)$$

for small angles. The experimental values d = 3.3 ± .1 cm, x = 154.8 ± .5 cm, $\phi = 45°$ and λ = .6328 μm, give

$$\Lambda = 42 \pm 1.5 \text{ μm} .$$

for the sound wavelength. This agrees well with the measured IDT finger spacing of 20.5 μm.

When the input rf power was increased to a certain point, the transducer was destroyed, apparently by arcing between the fingers. The maximum wave amplitude was found to be

$$A_{max} = 1.89 \text{ nm}$$

by measuring the ratio of deflected to incident light intensity. Figure 3.14 shows the I/I_o ratio plotted against the square of the driving voltage. As expected from (3.55), a straight line is obtained.

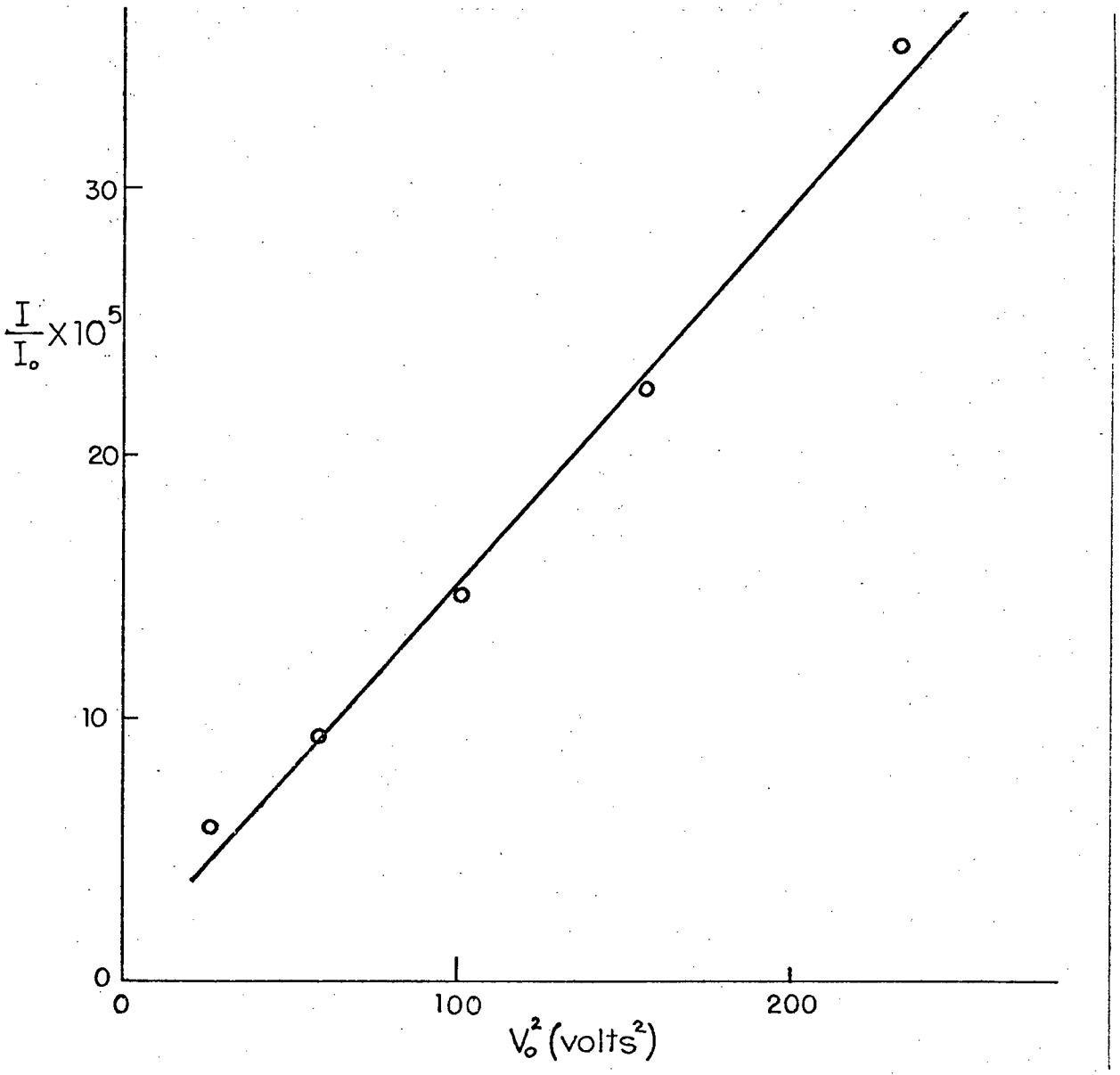

Fig. 3.14 Relative Deflected Light Intensity vs. V_o^2.

In spite of the approximations used to obtain an equivalent circuit model for interdigital transducers, the disagreement between theory and experiment is less than 5%. This is better than the 10% claimed by Smith et al, possibly because Auld and Kino's expressions for G_a and R_a, and Engan's C_T take into account variation of the transducer metallization factor.

In the next chapter, the series equivalent circuit modelddeveloped in section 3.4 will be used for the analysis of interdigital arrays in acoustooptic light deflectors.

4. BRAGG BEAM-STEERED SURFACE WAVE ACOUSTO-OPTIC LIGHT DEFLECTORS

4.1 Introduction

The phenomenon of light diffraction by ultrasonic bulk waves was first predicted by Brillouin [68] in 1922, and experimentally confirmed ten years later by Debye and Sears [69]. Since that time, a great deal of theoretical and experimental work has been done. More recently, advances in acoustic wave generation techniques, development of the optical laser, and the discovery of new materials have spurred the development of optical modulators, frequency shifters and deflectors. In particular, since the demonstration of efficient interaction between acoustic surface waves and guided optical surface waves by Kuhn et al in 1970 [70], the possibility of fabricating high-performance acousto-optic surface wave devices has become a topic of interest.

The surface-wave acousto-optic interaction has a number of advantages over the corresponding bulk interaction. In the latter case, ultrasonic waves are generated by applying rf voltages across thinly ground piezoelectric crystals bonded to the acousto-optic medium. Stepped bulk transducer arrays are difficult to make, and beam diffraction limits the usable acousto-optic interaction length. In the case of surface-wave devices, interdigital transducers are more easily made, using a photolithography process. The tight confinement of acoustic and optical fields allows long interaction lengths to be used. Efficient deflectors can be made even in materials with unexceptional acousto-optic figures of merit. For example, Schmidt and Kaminow [71] in 1975 reported 70% light deflection with only 50 mW of electrical drive power in a Ti/$LiNbO_3$ diffused OWG.

In this chapter, the improvement in deflector performance obtained when acoustic surface waves are generated by a beam-steering IDT array is investigated. A model of the device is developed which takes into account the IDT equivalent circuit parameters and the nature of the acoustic and optical fields, and predictions of this model are compared with experimental observation.

4.2 Theory of the Surface-Wave Acousto-Optic Interaction

The problem of diffraction of a guided optical wave by a surface acoustic wave has received the attention of several workers in recent years [72-76]. A treatment applicable to non-uniform waveguides in anisotropic piezoelectrics will be given here which combines features of the above references.

Consider a light wave propagating in the mth guided mode incident on an acoustic surface wave of width L and wavelength Λ. Let θ_{mo} be the angle of incidence between the light wavevector $\vec{k}_{mo}$ and the planes of constant phase of the sound wave, which produces a phase diffraction grating in the solid by means of a periodic perturbation of the refractive index. When a suitable phase matching condition is met, the light will in general be deflected into a diffracted beam of order ℓ propagating in the nth guided mode at an angle $\theta_{n\ell}$. The interaction may be regarded as a collision where conservation of energy and momentum obey the relations

$$\omega_\ell = \omega_o \pm \ell\Omega$$

and

$$\vec{k}_{n\ell} = \vec{k}_{mo} \pm \ell\vec{K} \ . \qquad (4.1)$$

Here ω_o and $\vec{k}_{mo}$ refer to the incident light wave, and Ω and $\vec{K}$ are the sound wave angular frequency and wavevector, respectively.

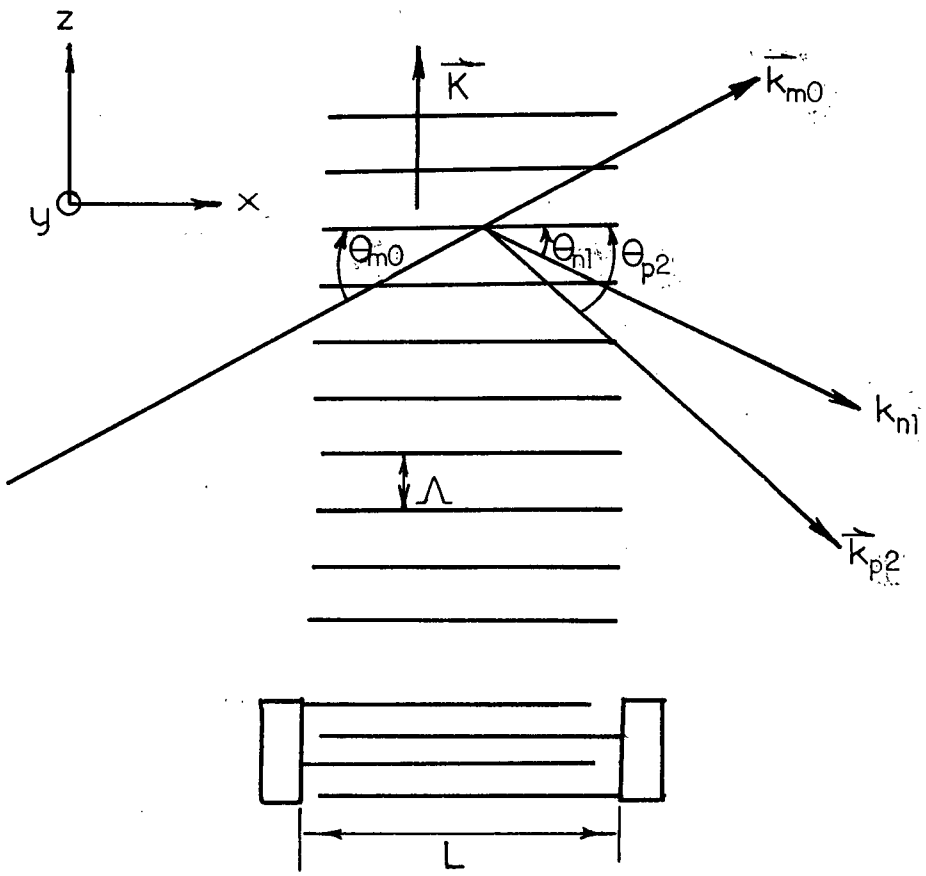

Fig. 4.1 Deflection of an OWG by a SAW.

In the discussion to follow, a Cartesian coordinate system (x,y,z) will be used; however, when tensor properties of the acousto-optic medium are needed, this is to be considered equivalent to (x_1,x_2,x_3).

The diffraction problem can be solved either by integral or differential equations [77]. Solution of the wave equation in the periodically modulated medium gives the greatest insight into the problem, so this approach will be taken here.

In a non-magnetic, non-conducting medium with dielectric permittivity tensor $\hat{\varepsilon}(\vec{x},t)\,\varepsilon_o$, Maxwell's Equations are

$$\nabla \times \vec{E} = -\mu_o \frac{\partial \vec{H}}{\partial t}$$

$$\nabla \times \vec{H} = \frac{\partial \vec{D}}{\partial t} \qquad (4.2)$$

$$\nabla \cdot \vec{H} = 0$$

and

$$\nabla \cdot \vec{D} = 0$$

Use of the relation $\vec{D} = \epsilon_o \hat{\epsilon}(\vec{x},t).\vec{E}$ and elimination of H from the first two equations gives

$$\nabla \times \nabla \times \vec{E} = -\frac{1}{c^2} \frac{\partial^2}{\partial t^2} (\hat{\epsilon}(\vec{x},t).\vec{E}) \tag{4.3}$$

In the isotropic case, use of $\nabla \times \nabla \times \vec{E} = \nabla(\nabla.\vec{E}) - \nabla^2\vec{E}$ and $\nabla.\vec{D} = 0 = \epsilon_o \nabla\epsilon.\vec{E} + \epsilon_o \epsilon \nabla.\vec{E}$ gives

$$\left(\frac{1}{\epsilon} \nabla\epsilon \cdot \vec{E}\right) - \nabla^2\vec{E} = -\frac{1}{c^2} \frac{\partial^2}{\partial t^2} (\epsilon\, E) \tag{4.4}$$

It can be shown [78] that the first term on the left is of the order of $\frac{\delta\epsilon.\lambda}{\Lambda}$ times the second term. In $LiNbO_3$, for example, a 200 MHz SAW gives approximately 10^{-5} for this factor, so the first term in (4.4) may be ignored. The wave equation is then

$$\nabla^2\vec{E} = \frac{1}{c^2} \frac{\partial^2}{\partial t^2} (\hat{\epsilon}(\vec{x},t).\vec{E}) \tag{4.5}$$

In the interaction region, the permittivity is

$$\hat{\epsilon} = \hat{\epsilon}_s + \Delta\hat{\epsilon}\ (\vec{x},t)\ ,$$

where $\hat{\epsilon}_s$ is the unperturbed value. In an anisotropic, piezoelectric solid, the SAW consists of a mechanical strain wave with up to six components and an associated electric field with up to three components. In general, perturbation of the permittivity may be treated as the sum of three parts: one due to the SAW electric field (linear electro-optic effect), another by the SAW strain field (photoelastic effect) and the third due to surface corrugation of the waveguide. Lean [73] has shown the latter contribution to be small with respect to the other

terms for $LiNbO_3$, so it will be neglected here, so that

$$\hat{\varepsilon} = \hat{\varepsilon}_s + \Delta\hat{\varepsilon}^e + \Delta\hat{\varepsilon}^p \tag{4.6}$$

where the superscripts refer to the electrooptic and photoelastic effects, respectively. The change in permittivity may be evaluated by use of the inverse dielectric permittivity tensor $\hat{B}$, which is defined by

$$\hat{B} \cdot \hat{\varepsilon} = 1$$

Taking differentials and multiplying by $\hat{\varepsilon}$ gives

$$\Delta\hat{\varepsilon} = - \hat{\varepsilon}\ \Delta\hat{B}\ \hat{\varepsilon}$$

In subscript notation, this relation is

$$\Delta\varepsilon_{i\ell} = - \varepsilon_{ij}\ \Delta B_{jk}\ \varepsilon_{k\ell} \ . \tag{4.7}$$

Consideration of equations (3.1), (3.9) and (3.10) enables us to write the real part of the elastic strain and electric SAW fields in the form

$$\tilde{S}^r_{ij}(\vec{x},t) = S^r_{ij}(y)\ \cos(\Omega t - Kz) \tag{4.8}$$

and

$$\tilde{E}^r_i\ (\vec{x},t) = E^r_i\ (y)\ \cos(\Omega t - Kz)\ , \tag{4.9}$$

where

$$E^r_i(y) \equiv \mathrm{Re}\{E_i(y)\}$$

The change in the inverse permittivity tensor due to the SAW strain field is [75,79]

$$\Delta B^p_{ij} = p_{ijk\ell}\ \tilde{S}^r_{k\ell}\ ,$$

where $p_{ijk\ell}$ are the photoelastic constants at constant E. Similarly, the change due to the linear electrooptic effect is

$$\Delta B^e_{ij} = r_{ijk}\ \tilde{E}^r_k\ ,$$

where r_{ijk} are the linear electrooptic coefficients at constant strain. The change in permittivity due to the SAW is therefore

$$\Delta\varepsilon_{in}(\vec{x},t) = \delta\varepsilon_{in} \cos(\Omega t - Kz) \tag{4.10}$$

where $$\delta\varepsilon_{in} = \varepsilon_{ij}(p_{jk\ell m}S^{r}_{\ell m} + r_{jk\ell}\, E^{r}_{\ell})\varepsilon_{kn} \tag{4.11}$$

Since the acoustic angular frequency Ω is much less than the optical frequency ω, the time derivatives of $\Delta\hat{\varepsilon}(\vec{x},t)$ may be neglected, and the wave equation becomes

$$(\nabla^2_{xz} - \frac{\hat{\varepsilon}\cdot}{c^2}\frac{\partial^2}{\partial t^2})\vec{E} = \frac{\Delta\hat{\varepsilon}(\vec{x},t)}{c^2}\cdot\frac{\partial^2\vec{E}}{\partial t^2} \tag{4.12}$$

For the permittivity function given in (4.10), this is a form of Mathieu's equation. The right-hand term may be regarded as a source of the guided modes described by the expression on the left. Solutions are given by Chu and Tamir [80] for the similar problem of diffraction of a plane electromagnetic wave by acoustic microwaves. The TE_m mode of a graded-index OWG propagating in the xz plane may be written as

$$E_m(\vec{x},t) = U_m(y)\exp j(\omega t - k_{mx}x - k_{mz}z) \tag{4.13}$$

where only the real part is assumed to have physical significance. Following Chu and Tamir, we may write solutions of the wave equation (4.12) in terms of an infinite set of coupled diffraction modes,

$$E(x,z,t) = \sum_{m=0}^{M}\sum_{\ell=-\infty}^{\infty} \phi_{\ell}(x)U_{m\ell}(y)\exp j(\omega_{\ell}t - k_{m\ell x}x - k_{m\ell z}z) \tag{4.14}$$

where $$\omega_{\ell} = \omega_0 + \ell\Omega\ ,$$

ℓ is the diffraction order, and $\phi_\ell(x)$ is a coupling constant dependent on $\delta\hat{\varepsilon}$ and the width of the interaction region.

Since the waveguide permittivity has a modulation of periodicity Λ, the transverse wavenumber in isotropic materials satisfies

$$k_{\ell z} = k_{0z} + \ell K , \qquad \ell = 0, \pm 1, \pm 2 \ldots \tag{4.16}$$

by the Floquet Theorem [80], where the guided-mode subscript m has been dropped. The longitudinal wavenumber is

$$\begin{aligned} k_{\ell x}^2 &= k_0^2 - k_{\ell z}^2 \\ &= k_0^2 - (k_{0z} + \ell K)^2 . \end{aligned} \tag{4.17}$$

Figure (4.2) shows the acousto-optic dispersion curves implied by this relation, for the case $\delta\hat{\varepsilon} = 0$. Only the incident ($\ell = 0$) mode propagates;

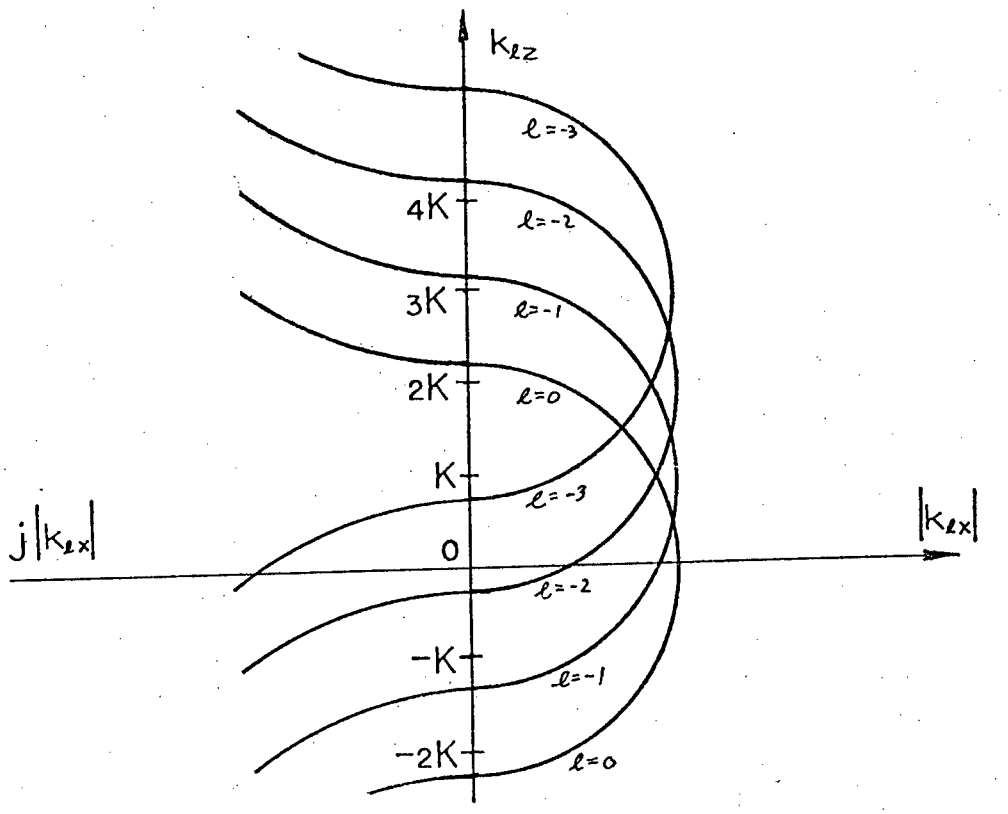

Fig. 4.2. Isotropic Acousto-Optic Dispersion Curves for $\Delta\hat{\varepsilon} = 0$.

however, the other modes may still be regarded as part of the solution even though their amplitude is zero. The rigorous solution of Mathieu's equation shows that a non-zero driving term in the wave equation introduces stop bands into the dispersion curves at their intersection points, which now become the Bragg regimes where coupling between diffraction modes is possible. For example, when $k_{0z} = K/2$, coupling is strong between the incident and first diffracted modes. In general, where $k_{0z} = \mp \ell K/2$, energy is coupled from the incident to the ℓth order diffraction mode. These modes propagate at the angles

$$\sin\theta_\ell = k_{\ell z}/k_0 = \sin\theta_0 + \ell K/k_0 \qquad (4.18)$$

When the acoustic frequency is well below the microwave region, the circles in the dispersion diagram are close together. If the angle

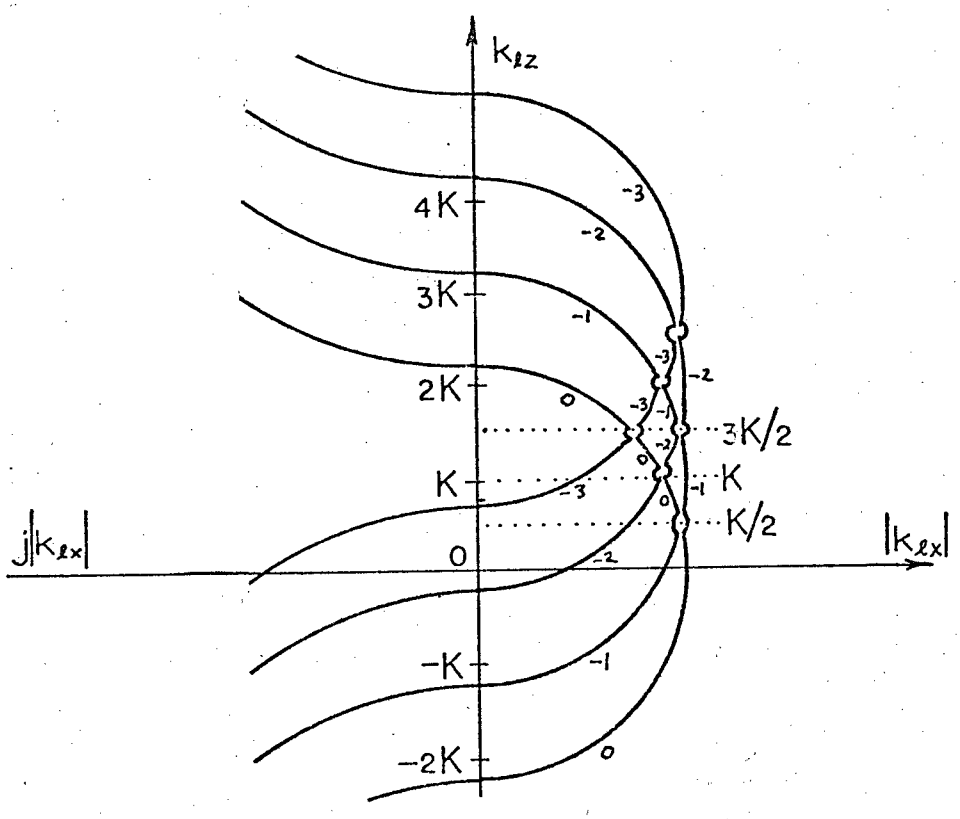

Fig. 4.3 Isotropic Acousto-Optic Dispersion Curves in a Modulated Medium.

of incidence is near zero, weak coupling occurs between many adjacent modes [77]. This is the Raman-Nath (or thin grating) limit. Strong coupling is possible only at the Bragg regimes, where $\theta_0 = \theta_\ell = \theta_b$, the Bragg angle. Then

$$\sin\theta_b = \ell K/(2k_0) = \ell\lambda/(2n\Lambda), \tag{4.19}$$

where λ is the vacuum wavelength of light and n is the refractive index.

In anisotropic materials, the situation is further complicated by the fact that the incident and diffracted rays propagate with different indices of refraction. For Bragg diffraction into the first order, Dixon [82] gives

$$\sin\theta_0 = \frac{\lambda}{2n_0\Lambda}\left(1 + \frac{\Lambda^2}{\lambda^2}(n_0^2 - n_1^2)\right) \tag{4.20}$$

and

$$\sin\theta_1 = \frac{\lambda}{2n_1\Lambda}\left(1 - \frac{\Lambda^2}{\lambda^2}(n_0^2 - n_1^2)\right) \tag{4.21}$$

for the angles of incidence and diffraction. In $LiNbO_3$ metal-diffused waveguides, n_0 and n_1 typically differ by 1% or less, so the diffraction may be treated as isotropic with little loss of accuracy.

For the strongest possible coupling into the first diffraction order, it is essential that the acoustic phase grating be thick enough to suppress diffraction into higher orders. The condition for this given by Alphonse [27] is

$$L > n\Lambda^2/\lambda \tag{4.22}$$

(frequently $L > 5n\Lambda^2/(\pi\lambda)$ is used instead). In the following discussion, it is assumed that (4.22) is satisfied, so that deflector operation is in the first-order Bragg regime. Only two terms remain in the solution (4.14) of the wave equation: the incident wave,

$$E_0(\vec{x},t) = \phi_0(x)U_0(y)\exp j(\omega_0 t - k_{0x}x - k_{0z}z) \qquad (4.23)$$

and the diffracted wave,

$$E_1(\vec{x},t) = \phi_1(x)U_1(y)\exp j(\omega_1 t - k_{1x}x - k_{1z}z) \qquad (4.24)$$

We require the coefficients $\phi_0(x)$ and $\phi_1(x)$, which describe continuous coupling between the waves in the interaction region. The acoustic surface wave is assumed to be propagating along the z coordinate axis. In the following derivation, guided-mode subscripts are omitted for brevity, and alphabetic rather than numerical coordinate axis subscripts are used for clarity. The functions $U_i(y)$ describe the electric field variation of TE optical guided modes with depth. They are normalized by the integral

$$\frac{k_i}{2}\int_{-\infty}^{\infty} U_i^2(y)dy = 1 \ . \qquad (4.25)$$

Since E_0 and E_1 are also solutions of the unperturbed ($\delta\varepsilon = 0$) wave equation, it follows that

$$k_{0x}^2 + k_{0z}^2 + \frac{n_0^2\omega_0^2}{c^2} = 0 \qquad (4.26)$$

and

$$k_{1x}^2 + k_{1z}^2 + \frac{n_1^2\omega_1^2}{c^2} = 0 \qquad (4.27)$$

In general, the two waves will propagate in different directions, and may be in different guided modes, so the unperturbed permittivities n_0^2 and n_1^2 will differ. Substitution of (4.23) and (4.24) into the wave equation (4.12) such that each wave is regarded as the source of the other gives [illegible] the [illegible] c he

$$(\phi_0'' U_0 - 2jk_{0x} U_0 \phi_0') \exp j(\omega_0 t - k_{0x} x - k_{0z} z) =$$
$$- \frac{\omega_1^2}{c^2} \Delta\varepsilon U_1 \phi_1 \exp j(\omega_1 t - k_{1x} x - k_{1z} z) \qquad (4.28)$$

and

$$(\phi_1'' U_1 - 2jk_{1x} U_1 \phi_1') \exp j(\omega_1 t - k_{1x} x - k_{1z} z) =$$
$$- \frac{\omega_0^2}{c^2} \Delta\varepsilon U_0 \phi_0 \exp j(\omega_0 t - k_{0x} x - k_{0z} z) \; . \qquad (4.29)$$

The primes denote differentiation with respect to x. The second derivatives may be neglected, if we assume that $\phi(x)$ varies slowly. When the $\cos(\Omega t - Kz)$ factor in $\Delta\varepsilon$ is written as the sum of exponentials, it becomes clear that these equations describe diffraction into both the $\ell = 1$ and $\ell = -1$ orders. If deflector operation is well in the Bragg regime, it is possible to deflect light into only one of these at a time, so the $\ell = -1$ order may be dropped. Multiplying (4.28) by U_0 and (4.29) by U_1, integrating over all y, and using (4.11) and (4.25) gives two coupled-mode equations in ϕ_0 and ϕ_1,

$$\phi_0' = - j\alpha_0 \phi_1 \exp(jB) \qquad (4.30)$$

and

$$\phi_1' = - j\alpha_1 \phi_0 \exp(-jB) \; , \qquad (4.31)$$

where

$$B = \Delta k_x x + (\Delta k_z - K) z - (\Delta\omega - \Omega) t,$$

with

$$\alpha_0 = \frac{\omega^2 \Gamma_{01}}{8c^2 \cos\theta_0}$$

and

$$\alpha_1 = \frac{\omega^2 \Gamma_{01}^*}{8c^2 \cos\theta_1} = \frac{\omega^2 \Gamma_{10}}{8c^2 \cos\theta_1} \qquad (4.32)$$

In full subscript notation the overlap integral Γ_{01} is

$$\Gamma_{m0n1} = \int_{-\infty}^{\infty} U^*_{m0p} \delta\varepsilon_{pq} U_{n1q} \, dy \, , \tag{4.33}$$

where the subscripts of U, from left to right, refer to the TE guided mode number, the diffraction order, and the Cartesian coordinate axis. Equations (4.32) were obtained by use of the fact that $\omega_0 \approx \omega_1 = \omega$ (since usually $\Omega << \omega$), and the relation $k_{\ell x} = k_\ell \cos\theta_\ell$. For reasons discussed earlier, coupling occurs only in the vicinity of $\Delta k_z = K$ and $\Delta\omega = \Omega$.

Differentiation of (4.30) with respect to x and substitution for ϕ_1' and ϕ_1 from (4.31) and (4.30) gives the uncoupled equation

$$\phi_0'' - 2jp\phi_0' + \alpha_0\alpha_1\phi_0 = 0, \tag{4.34}$$

where $p = \Delta k_x/2$.

Similarly, it can be shown that

$$\phi_1'' + 2jp\phi_1 + \alpha_0\alpha_1\phi_1 = 0. \tag{4.35}$$

If we assume solutions of the form $\exp(j\beta_i x)$, substitution gives quadratic equations in β_0 and β_1,

$$\beta_0^2 - 2p\beta_0 - \alpha_0\alpha_1 = 0 \tag{4.36}$$

and

$$\beta_1^2 + 2p\beta_1 - \alpha_0\alpha_1 = 0 \, , \tag{4.37}$$

from (4.34) and (4.35), respectively.

Setting $q = \sqrt{p^2 + \alpha_0\alpha_1}$, we obtain the solutions

$$\beta_0 = p \pm q \tag{4.38}$$

and

$$\beta_1 = -(p \pm q) \, . \tag{4.39}$$

Solutions for ϕ_0 and ϕ_1 are

$$\phi_0(x) = A_1 \exp(jx(p+q)) + A_2 \exp(jx(p-q)) \tag{4.40}$$

$$\phi_1(x) = A_3 \exp(-jx(p+q)) + A_4 \exp(-jx(p-q)) \tag{4.41}$$

The boundary conditions to be satisfied are

$$\phi_0(0) = 1 ,$$

$$\phi_1(0) = 0 ,$$

$$\phi_0'(0) = 0 ,$$

and

$$\phi_1'(0) = -j\alpha_1 , \tag{4.42}$$

where the last two are obtained by applying the first two to (4.30) and (4.31). Use of these boundary conditions with (4.40) and (4.41) gives the constants A_1 through A_4. Then

$$\phi_0(x) = \exp(jpx)(\cos(qx) - j \frac{p}{q} \sin(qx)) \tag{4.43}$$

and

$$\phi_1(x) = -j \frac{\alpha_1}{q} \exp(-jpx) \sin(qx) . \tag{4.44}$$

In a lossless medium (a reasonable approximation for $LiNbO_3$), the deflector diffraction efficiency is given by

$$\eta = \phi_1\phi_1^* = 1 - \phi_0\phi_0^*$$

$$= \alpha_0\alpha_1 L^2 \operatorname{sinc}^2 qL , \tag{4.45}$$

where sinc $x \equiv \sin x/x$ and L is the acousto-optic interaction length. When the angle of light incidence deviates slightly from the Bragg angles by an amount $\Delta\theta$,

$$\Delta k_x \approx K\Delta\theta , \tag{4.46}$$

as can be inferred from the momentum conservation diagram (Fig. 4.4). (Usually, $n_0 \sim n_1$, so that $k_0 \sim k_1$, and the triangle in Fig. 4.4 is nearly isosceles.)

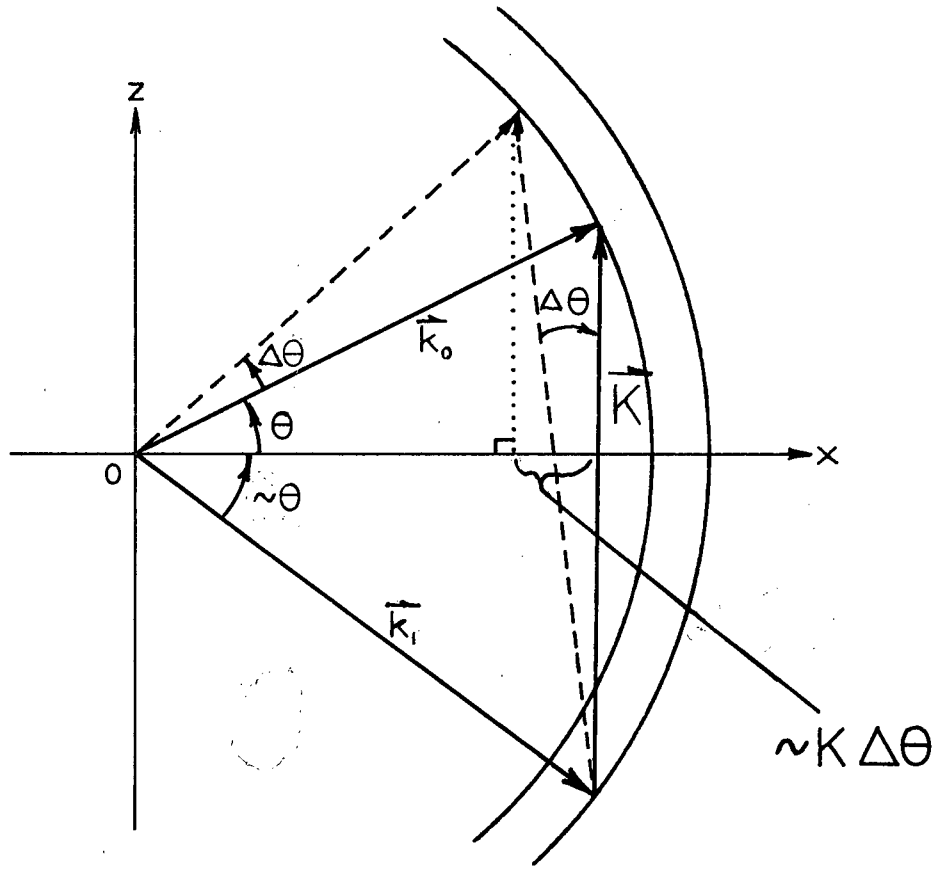

Fig. 4.4 Momentum Conservation in Anisotropic Bragg Diffraction.

If we regard the SAW normalized in the sense discussed at the end of section 3.2, then the expressions obtained so far are for an acoustic power of 1 watt/meter. For an acoustic beam L meters wide with an acoustic power P_a, the permittivity change $\delta\hat{\epsilon}$ must be multiplied by $\sqrt{P_a/L}$, the change in SAW amplitude. Using this, along with (4.46) and the definition of q, the diffraction efficiency becomes

$$\eta = g^2 \mathrm{sinc}^2[g^2 + (K\Delta\theta L/2)^2]^{1/2} , \qquad (4.47)$$

with

$$g^2 = \alpha_0\alpha_1 P_a L = \frac{\pi^4 \Gamma^2 P_a L}{4\lambda^4 \cos\theta_0 \cos\theta_1} . \qquad (4.48)$$

For light incident at the Bragg angle, $\Delta\theta = 0$, so (4.47) becomes

$$\eta_0 = \sin^2 g . \qquad (4.49)$$

Whe $g = \pi/2$, 100% diffraction efficiency is obtained. The acoustic power required for this is approximately

$$P_{100} = \frac{\lambda^4}{\pi^2 \Gamma^2 L} , \qquad (4.50)$$

since usually $\cos\theta_0 \sim \cos\theta_1 \sim 1$.

The deflection angle is altered by varying the acoustic frequency f. The diffraction efficiency falls off, since light is no longer incident at the Bragg angle. The usable limits will be set by either the angular spread of the sound beam, or by the limited bandwidth of the interdigital transducer. In either case, the half-power points of (4.47) are obtained when the argument of the sinc^2 changes by 1.3916 away from the central maximum. Usually the Bragg angle is of the order of one degree, so the change in deflection angle as a function of frequency change Δf is obtained from (4.19)

$$\Delta\theta_b = \frac{\lambda\Delta f}{2nv} \qquad (4.51)$$

Thus,

$$\frac{K\Delta\theta L}{2} = \frac{\pi\lambda L f \Delta f}{2nv^2} = 1.3916$$

at the half-power points. Deflectors are usually transducer bandwidth limited, so this equation gives half the maximum usable interaction length as a function of deflector bandwidth,

Thus,
$$L_{max} = \frac{1.8\ nv^2}{\lambda f_o \Delta f} . \tag{4.52}$$

As pointed out by Gordon [83], both spatial and temporal coherence are preserved when light undergoes acousto-optic deflection, provided that the angular spread $\Delta\theta_s$ of the sound beam is much greater than the corresponding spread $\Delta\phi$ of the light beam. Since the angle of deflection is twice the Bragg angle, the number of resolvable spots to which light can be focussed is

$$N_s = 2\Delta\theta_b/\Delta\phi \tag{4.53}$$

For light emerging from an aperture of width A, the optical beam spread is

$$\Delta\phi = \frac{\lambda}{nA}$$

for a rectangular beam intensity profile and the Rayleigh criterion of spot resolution [77]. Use of (4.51) gives

$$N_s = \Delta f_m A/v = \Delta f_m\ \tau\ , \tag{4.54}$$

where τ is the transit time of the acoustic wave across the light beam and Δf_m is the half-power bandwidth.

In the expressions derived so far, it was assumed that the acoustic beam has a rectangular intensity profile in the interaction region. In the next section, the effects of acoustic beam diffraction and techniques for increasing deflector bandwidth will be discussed.

4.3 Acoustic Beam Steering

Acoustic beam steering has been in use for some time as a means of improving the performance of bulk acousto-optic deflectors. One of the earliest applications was by Korpel et al [84], who worked

with 20 MHz ultrasonic waves in water. The underlying principle consists of varying the direction of sound wave propagation as the acoustic frequency is altered, so as to track the Bragg angle and thereby increase the usable deflector bandwidth.

Consider the propagation of acoustic surface waves generated by a stepped interdigital transducer array (Fig. 4.5). Each transducer section has a radiating aperture of width D and an overall width G. Generation of surface waves is equivalent to normal incidence of a plane wave on the array, except for a factor of 1/2 due to the bidirectional radiation from interdigital transducers. The step heights are an integer (P) multiple of $\Lambda_0/2$, where waves with $\Lambda = \Lambda_0$ will propagate straight ahead after excitation by the array. If the transducers are driven out of phase, P must be odd; if they are in phase, P is even.

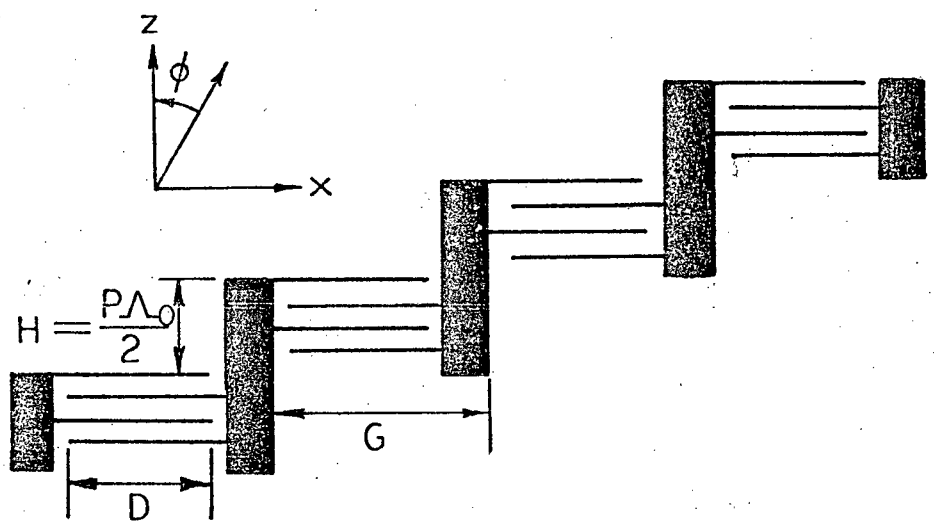

Fig. 4.5 Beam Steering Transducer.

In the far radiation field, the sound wave amplitude is given by the Fresnel-Kirchoff integral [85],

$$S(\phi) = \int_0^{MG} \exp j(Kx \sin\phi - \gamma(x))\, dx \qquad (4.55)$$

with $\gamma(x)$ being a phase factor to account for the transducer steps and MG being the overall width of an M-section transducer. Usually, the Bragg deflection of light occurs in the near radiation field, because the Fresnel distance is excessively long. However, the analysis is done in the far radiation field for convenience.

Consider the effect of one of the steps (Fig. 4.6). The phase change across each aperture is $Kx \sin\phi \sim K\phi x$ for small angles.

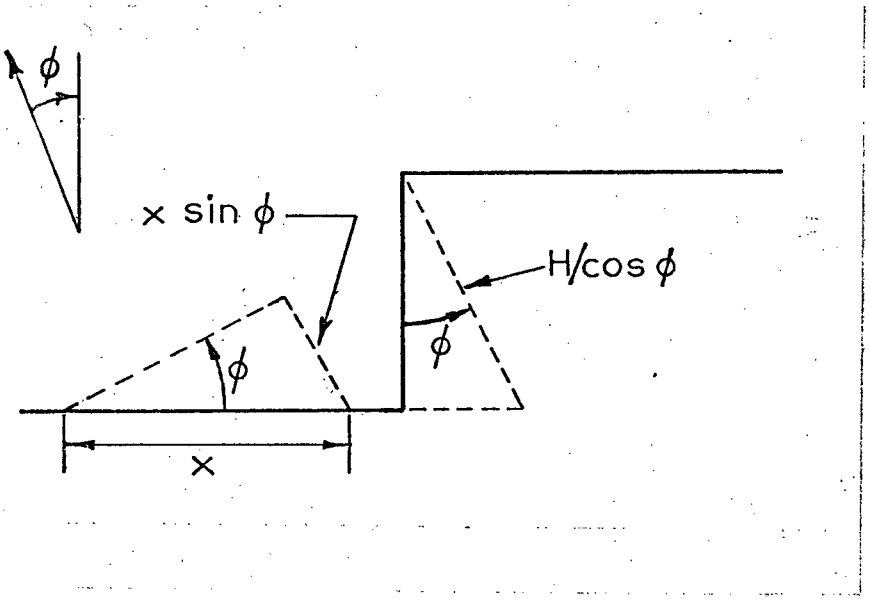

Fig. 4.6 Phase Change across One Step.

The phase change between corresponding points on wavefronts from adjacent apertures is

$$K(P\frac{\Lambda}{2} - H)/\cos\phi \sim \frac{KP}{2}(\Lambda - \Lambda_0) = P\pi(1 - K/K_0)$$

for small angles ϕ. Thus, the diffraction integral becomes

$$S(\phi) = \sum_{n=0}^{M-1} \int_{nD}^{nD+G} \exp j(K\phi x - nP\pi(1 - K/K_0))\, dx$$

$$= \frac{\exp(jK\phi G) - 1}{jK\phi} \sum_{n=0}^{M-1} \exp jn[K\phi D - P\pi(1 - K/K_0)]$$

$$= S_0 \operatorname{sinc}(\tfrac{1}{2} KG\phi) \frac{\sin\{\frac{1}{2} M\,[KD\phi - P\pi(1 - K/K_0)]\}}{M \sin\{\frac{1}{2}\,[KD\phi - P\pi(1 - K/K_0)]\}} ,$$

where S_0 is a constant. (4.56)

The sound wave intensity is

$$I(\phi) = S^2(\phi) = I_0 A^2(\phi) B^2(\phi) , \qquad (4.56)$$

where I_0 is a constant, $A(\phi) = \operatorname{sinc}(\frac{1}{2} KG\phi)$ is the aperture function, and $B(\phi)$ is the array function.

The principal maximum of the array function is at the angle ϕ_0, determined by

$$\tfrac{1}{2} M\,[KD\phi_0 - P\pi(1 - K/K_0)] = 0 ,$$

or

$$\phi_0 = \frac{Pv}{2D} \left(\frac{1}{f} - \frac{1}{f_0}\right) \qquad (4.58)$$

The array function is more simply expressed in terms of ϕ_0,

$$B(\phi) = \frac{\sin[\frac{MKD}{2} (\phi - \phi_0)]}{M \sin[\frac{KD}{2} (\phi - \phi_0)]} \qquad (4.59)$$

The maxima are at the angles

$$\phi_{Bmax} = \phi_0 + q \frac{\Lambda}{D} , \qquad (4.60)$$

where q is an integer. The minima of $A(\phi)$ are at

$$\phi_{Amin} = q \frac{\Lambda}{G} . \tag{4.61}$$

Figure 4.7 shows the array and aperture functions where $\Lambda = \Lambda_0$ and $G \sim D$. The latter condition is desirable, since most of the transducer width is then utilized for SAW generation. This gives a longer acousto-optic interaction length and higher deflector efficiency (4.50). Furthermore, the secondary maxima of $B(\phi)$ then occur near the zeros of $A(\phi)$, so little acoustic power is carried outside the central peak. When $\Lambda \neq \Lambda_0$, the maximum of $B(\phi)$ shifts away from the maximum of $A(\phi)$, and it decreases in amplitude (Fig. 4.8).

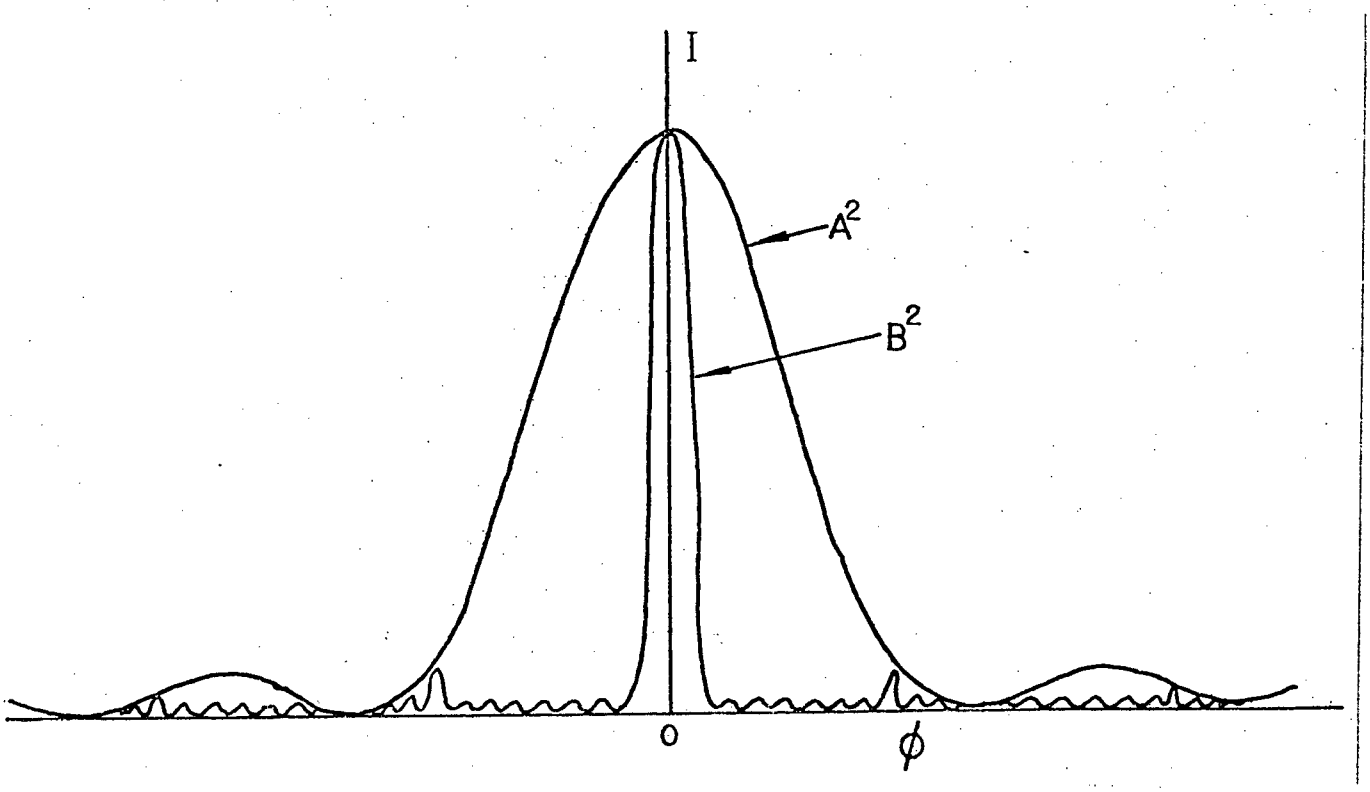

Fig. 4.7 The Aperture and Array Functions for $\Lambda = \Lambda_0$ and $D \sim G$.

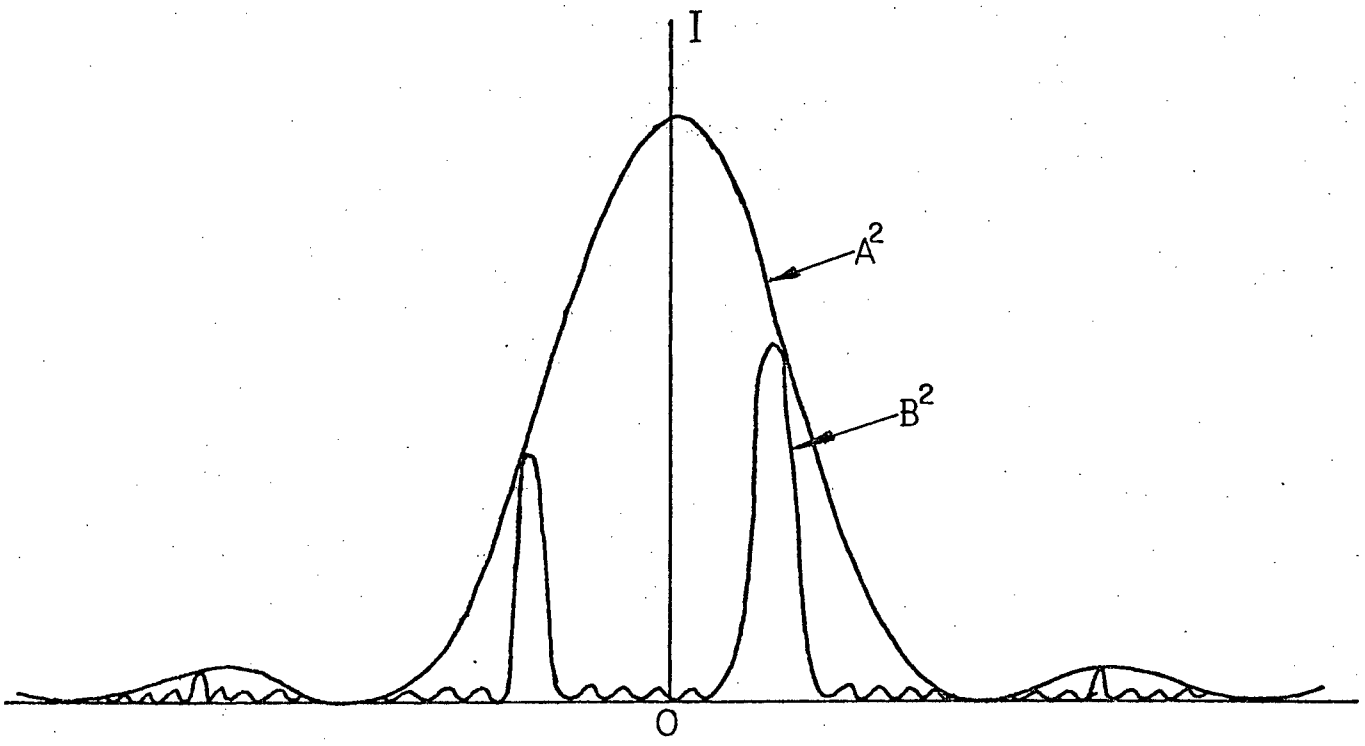

Fig. 4.8 The Aperture and Array Functions for $\Lambda \neq \Lambda_0$.

In anisotropic materials, the direction of power flow is not in general collinear with the propagation vector. If the angles in (4.56) are all changed by a factor of $\alpha = (1 - 2b)$, where b is the parabolic constant defined in 3.15, we obtain the disribution of acoustic power for anisotropic propagation,

$$I_{an}(\phi) = I_0 \text{sinc}^2\left(\frac{KG\alpha\phi}{2}\right) \frac{\sin^2\left[\frac{MKD\alpha}{2}(\phi - \phi_0)\right]}{M^2 \sin^2\left[\frac{KD\alpha}{2}(\phi - \phi_0)\right]} \quad . \tag{4.62}$$

The maximum power in the SAW is in the vicinity of the central maximum of the array function B, where $\phi = \phi_0$. Thus, the peak intensity of the SAW varies with ϕ according to the equation

$$I_{an} = I_0 \text{sinc}^2(\tfrac{1}{2} KG\alpha\phi). \tag{4.63}$$

To apply these results to Bragg deflectors, we require that the Bragg angle be matched at two frequencies, f_ℓ and f_h (Fig. 4.9). The steering angle (4.58) is a hyperbolic function of frequency, and the Bragg angle with respect to an arbitrary direction is [85]

$$\phi_b = c - \frac{\lambda f}{2nv}, \tag{4.64}$$

where c is a constant. (The angle of SAW propagation relevant to the Bragg interaction is ϕ_0 (4.58), even for anisotropic materials, since it is the sound wavevector rather than the power flow direction that matters.)

Since the Bragg angle is satisfied at f_ℓ and f_h, and ϕ_b is a linear function of f,

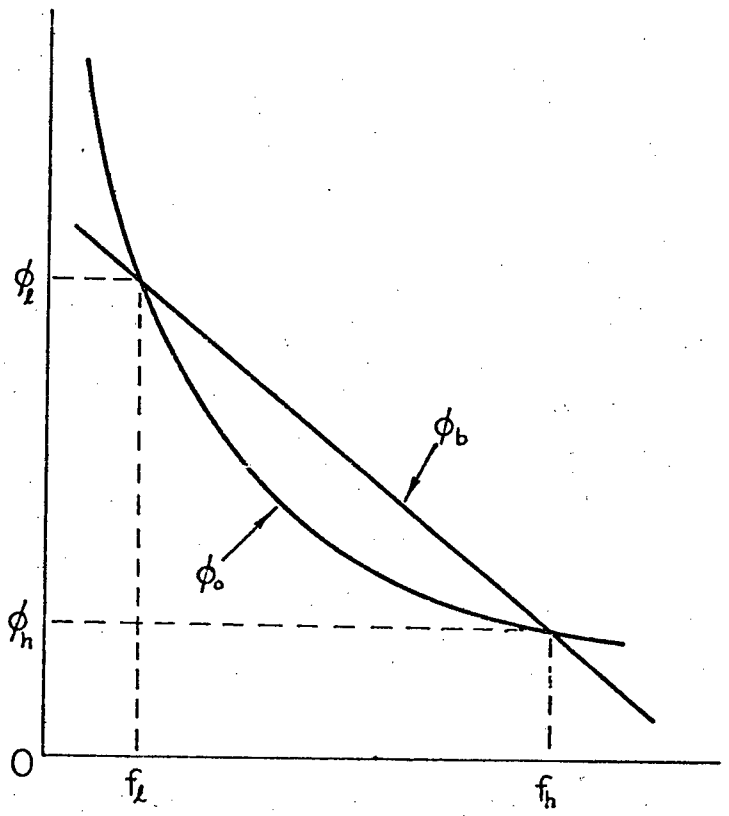

Fig. 4.9. Bragg-Angle Tracking.

$$\frac{\phi_h - \phi_\ell}{f_h - f_\ell} = \frac{\phi_h - \phi_b(f)}{f_h - f} \tag{4.65}$$

Using (4.58), we obtain

$$\phi_b(f) = \frac{Pv}{2D}\left(\frac{1}{f_h} - \frac{1}{f_0} + \frac{1}{f_\ell} - \frac{f}{f_\ell f_h}\right) . \tag{4.66}$$

The angle of intersection of light and sound waves deviates from the Bragg angle by the steering error,

$$\Delta\theta = \phi_b(f) - \phi_0(f) \tag{4.67}$$

Let us define an array frequency f_1 such that $\Delta\theta(f_1)$ is a maximum. The condition

$$\frac{d}{dt}(\Delta\theta) = 0 \tag{4.68}$$

gives

$$f_1^2 = f_\ell\, f_h . \tag{4.69}$$

This differs from Pinnow's [86] result $f_1 = \frac{1}{2}(f_\ell + f_h)$, which was obtained by use of an arbitrary adjustable parameter to optimize transducer performance, rather than the more natural condition (4.68). Using (4.69), the steering error becomes

$$\Delta\theta(f) = \frac{Pv}{2D}\left(\frac{1}{f_h} + \frac{1}{f_\ell} - \frac{1}{f} - \frac{f}{f_1^2}\right) . \tag{4.70}$$

Equating the slopes in equations (4.64) and (4.66) fixes the P/D ratio,

$$\frac{P}{D} = \frac{\lambda f_1^2}{nv^2} . \tag{4.71}$$

4.4 Diffraction Efficiency of Beam-Steered Transducers

It is now possible to write expressions for the diffraction efficiency of a beam-steered deflector as a function of SAW frequency. With reference to equation (4.47), define

$$h = \frac{K\Delta\theta L}{2} = \frac{\pi PLf}{2D}\left(\frac{1}{f_h} + \frac{1}{f_\ell} - \frac{1}{f} - \frac{f}{f_1^2}\right) . \tag{4.72}$$

The amplitude of the central maximum of the array function is $\mathrm{sinc}(\frac{1}{2} KG\alpha\phi_0)$ from (4.63), so the SAW acoustic power must include the spatial variation $\mathrm{sinc}^2(\frac{1}{2} KG\alpha\phi_0)$. If an interdigital transducer to which the series model applies is used for SAW generation, the acoustic power is given by (3.48),

$$P_a = R_a V^2/(2|Z_i|^2)$$

for a driving voltage V. Thus, g^2 (4.48) becomes

$$g_b^2 = \frac{\pi^4 \Gamma^2 P_a L}{4\lambda^4 \cos\theta_0 \cos\theta_1} \mathrm{sinc}^2(\pi f G\alpha\phi_0/v) ,$$

where ϕ_0 is given by (4.58). The anisotropy parameter α enters into this expression, although it is not in (4.72), since diffraction is from the planes of constant phase of the SAW.

The diffraction efficiency of a beam-steered deflector is therefore

$$\eta_b = g_b^2 \, \mathrm{sinc}^2(g_b^2 + h^2)^{1/2} , \tag{4.73}$$

where

$$h = \frac{\pi PLf}{2D}\left[\frac{1}{f_\ell} - \frac{1}{f} + \frac{f_\ell - f}{f_1^2}\right], \tag{4.74}$$

and

$$g_b^2 = \frac{\omega^4 \Gamma^2 P_a L}{32c^4 \cos\theta_0 \cos\theta_1} \operatorname{sinc}^2\left[\frac{\pi P G \alpha}{2D}(1 - f/f_0)\right] , \qquad (4.75)$$

with

$$P_a = \frac{V^2 R_a}{2[(R_a + R_e)^2 + (\Omega L_s - 1/(\Omega C_T) + X_a)^2]} \qquad (4.76)$$

and

$$R_a = R_0 \operatorname{sinc}^2 x ,$$

$$X_a = R_0 [\sin(2x) - 2x]/(2x^2) ,$$

where $x = N\pi(f - f_0)/f_0$. The IDT array circuit elements R_a, R_e, L_s and C_T are obtained from the appropriate series/parallel combination of the individual transducer sections.

These equations for the acoustic power P_a apply when a voltage $Ve^{j\Omega t}$ is applied to the series equivalent circuit (Fig. 3.8) representation of the beam-steering transducer. If the device is driven by a coaxial transmission line of characteristic impedance Z_c, the equations take a different form. We will assume that the rf generator is isolated from the load, and that there are no significant multiple reflections on the line. Then the electrical power dissipated in the IDT with impedance $Z = R + jX$ is given by

$$P_e = P_o(1 - |\rho_r|^2),$$

where $P_o = V_f^2/Z_c$ is the power that would be dissipated if the line were matched and V_f is the forward r.m.s. voltage on the line. The reflection coefficient ρ_r is given by

$$\rho_r = \frac{Z - Z_c}{Z + Z_c} .$$

After some algebra, we obtain

$$P_e = \frac{4V_f^2 R}{(R + Z_c)^2 + X^2} .$$

The current flowing in the series equivalent circuit is given by $P_e = i^2 R$. The usable acoustic power is half the power dissipated in the IDT radiation resistance, that is,

$$P_a = \frac{1}{2} i^2 R_a = \frac{2 V_f^2 R_a}{\left[(R_a + R_e + Z_c)^2 + (\Omega L_s + X_a - \frac{1}{\Omega C_T})^2\right]} \qquad (4.77)$$

4.5 Acousto-Optic Overlap Integral Calculation

The overlap integral (4.33) was evaluated for the TE guided modes shown in Fig. 2.35 interacting with a Z ± 21.8° propagating SAW on Y-cut $LiNbO_3$. The permittivity, electro-optic and photoelastic tensors are given in Appendix I in matrix form for the principal axes system (X,Y,Z). To calculate these in the system (x_1,x_2,x_3), which is rotated by 21.8° about the $Y = x_2$ axis, it is preferable to revert to tensor notation in order to use the usual transformation laws [88],

$$\begin{aligned} \varepsilon'_{ij} &= a_{im}\, a_{jn}\, \varepsilon_{mn} \\ r'_{ijk} &= a_{im}\, a_{jn}\, a_{kp}\, r_{mnp} \\ p'_{ijk\ell} &= a_{im}\, a_{jn}\, a_{ko}\, a_{\ell p}\, p_{mnop} \end{aligned} \qquad (4.78)$$

The transformation matrix is

$$a_{ij} = \begin{bmatrix} \cos\theta & 0 & \sin\theta \\ 0 & 1 & 0 \\ -\sin\theta & 0 & \cos\theta \end{bmatrix}, \qquad (4.79)$$

with $\theta = 21.8°$. The direction of OGW propagation was only about 1° off the x_1' axis, so little accuracy is lost by assuming it to be along x_1' exactly. In the experiments, no mode conversion was observed, so the overlap integral reduces to

$$\Gamma = \int_{-\infty}^{\infty} U_{m03}^2(y)\ \delta\varepsilon_{33}'\ dy \tag{4.80}$$

The rotated permittivity, electro-optic and photoelastic tensors are given in Appendix I, along with the permittivity change factors $\delta\varepsilon_{ij}'$ $\varepsilon_{3i}'\ p_{ijk\ell}\ \varepsilon_{j3}'$ and $\varepsilon_{3i}'\ r_{ijk}\ \varepsilon_{j3}'$.

The necessary SAW parameters for the complete evaluation of $\delta\varepsilon_{33}'$ were obtained from reference [40]. Unfortunately, this reference does not give full analytic solutions, in that the β_k^m coefficients of equations (3.11) and (3.12) are missing. However, it is possible to find the acoustic strain and electric fields using*

$$E_i = -\frac{\partial\Phi}{\partial x_i} \tag{4.81}$$

and

$$S_{ij} = \frac{1}{2}\left(\frac{\partial u_i}{\partial x_j} + \frac{\partial u_j}{\partial x_i}\right) \tag{4.82}$$

with plots of the magnitude of the SAW mechanical displacements u_i (Fig. 4.10) and electric potential $|\Phi|$ (Fig. 4.11) [40]. The quantities shown have been normalized to remove the frequency dependence; for a mechanical power flow component P_{3M} along x_3, the actual magnitudes are

$$x_2 = x_2^N/\Omega\ ,$$

$$|u_i| = \sqrt{P_{3M}}\ |u_i^N|/\sqrt{\Omega}\ ,$$

$$|\Phi| = \sqrt{P_{3M}}\ |\Phi^N|/\sqrt{\Omega}\ ,$$

*The primes are omitted in the rest of this section. All quantities are in the rotated coordinate system.

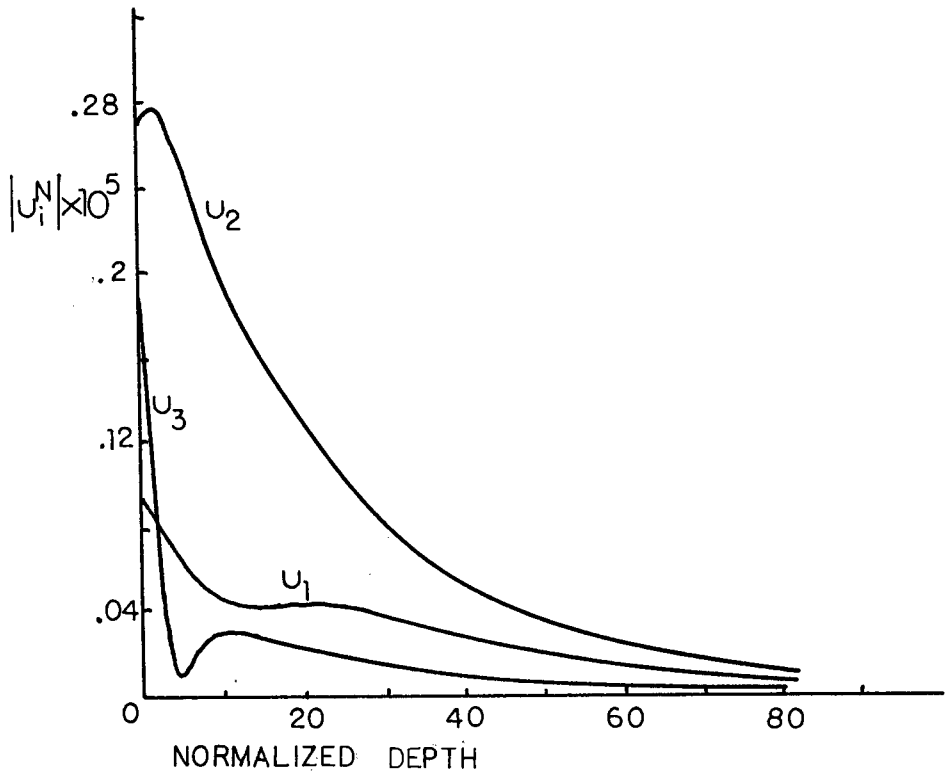

Fig. 4.10

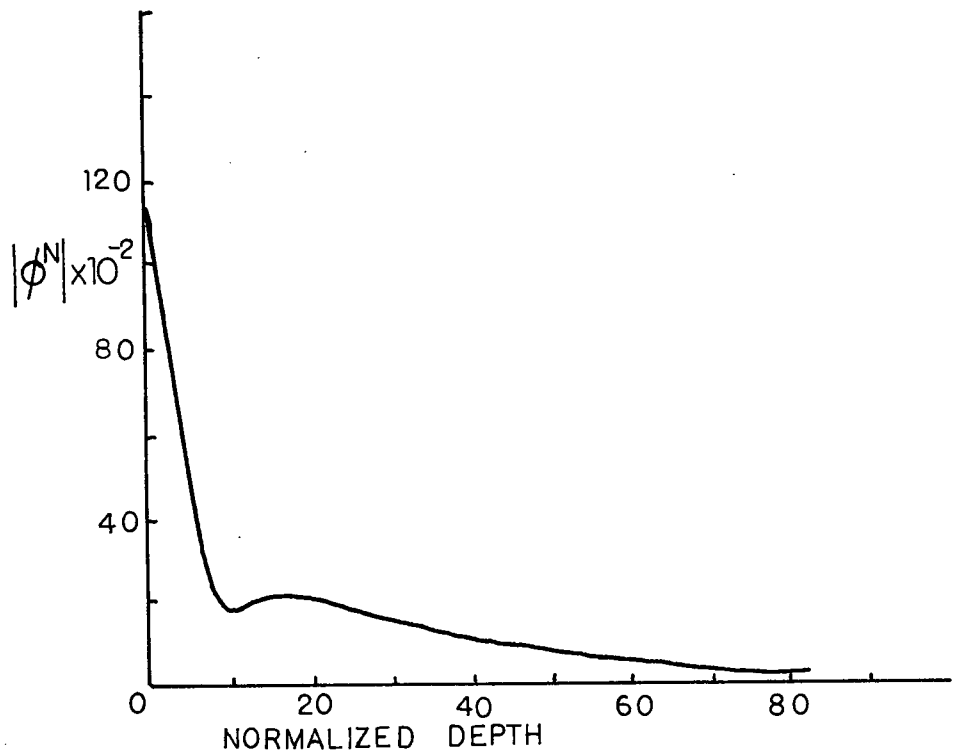

Fig. 4.11

$$|S_{ij}| = \sqrt{P_{3M}\Omega}\ |S^N_{ij}| \ ,$$

and

$$|E_i| = \sqrt{P_{3M}\Omega}\ |E^N_i| \ , \tag{4.81}$$

where N indicates the normalized values. For SAW propagation along x_3, it is clear from (3.11) and (3.12) that there is no x_1 variation, and that the operator identification $\partial/\partial x_3 \rightarrow j\Omega/v$ can be made. Differentiation with respect to x_2 must be done numerically; since only the magnitudes of the fields are plotted, complex phase factors C_2 and C_{2i}, defined by

$$C_{2i}\ \frac{\partial|u_i|}{\partial x_2} = \frac{\partial u_i}{\partial x_2}$$

and

$$C_2\ \frac{\partial|\Phi|}{\partial x_2} = \frac{\partial\Phi}{\partial x_2} \tag{4.82}$$

are missing. The magnitude and phase of the normalized fields are given in reference [40] at y = 0, so these factors can be evaluated there. For example,

$$S_{23} = \frac{1}{2}\left(\frac{\partial u_2}{\partial x_3} + \frac{\partial u_3}{\partial x_2}\right)$$

$$= \frac{1}{2}\left(-j\ \frac{\Omega}{v}\ u_2 + C_{32}\ \frac{\Delta|u_3|}{\Delta x_2}\right) \ . \tag{4.83}$$

At y = 0,

$$\ddot{u}^N_2\ (0) = 2.656 \times 10^{-6}(.0366 + .999j)$$

and

$$S^N_{23}(0) = 3.22 \times 10^{-12}(-.606 + .795j) \ .$$

Only the real parts of the strain and electric fields contribute to $\delta\varepsilon_{33}$, so we have

$$\text{Re } S_{23}^N = \frac{1}{2}\left(.999\,\frac{|u_2^N|}{v} + C_{23}\,\frac{\Delta|u_3^N|}{\Delta x_2^N}\right) \tag{4.84}$$

at $y = 0$. This gives $C_{23} = 1.102$. The equations obtained in this manner for the real parts of the strain and electric fields are

$$S_{11} = 0 ,$$

$$\text{Re } S_{22} = S_{22}^r = .0593\,\sqrt{\Omega}\,\frac{\Delta|u_2^N|}{\Delta x_2^N} ,$$

$$S_{33}^r = 0 ,$$

$$S_{23}^r = -\sqrt{\Omega}\left(1.102\,\frac{\Delta|u_3^N|}{\Delta x_2^N} + \frac{|u_2^N|}{v}\right) ,$$

$$S_{13}^r = -.352\,\sqrt{\Omega}\,\frac{|u_1^N|}{v} ,$$

$$S_{12}^r = .0583\,\sqrt{\Omega}\,\frac{\Delta|u_1^N|}{\Delta x_2^N} ,$$

$$E_2^r = .256\,\sqrt{\Omega}\,\frac{\Delta|\Phi^N|}{\Delta x_2^N} ,$$

and

$$E_3^r = -.293\,\sqrt{\Omega}\,\frac{|\Phi^N|}{v} . \tag{4.85}$$

In Fig. 4.12, the real parts of the acoustic strains are shown as a function of depth for an acoustic frequency of 165 MHz, and in Fig. 4.13 the corresponding electric fields are shown. Better accuracy would have been obtained by solving equation (14) of reference [40] for the β_k^m coefficients, since the displacement and potential fields could not be measured with great precision near $x_2 = 0$. The permittivity change $\delta\varepsilon_{33}$ is given by

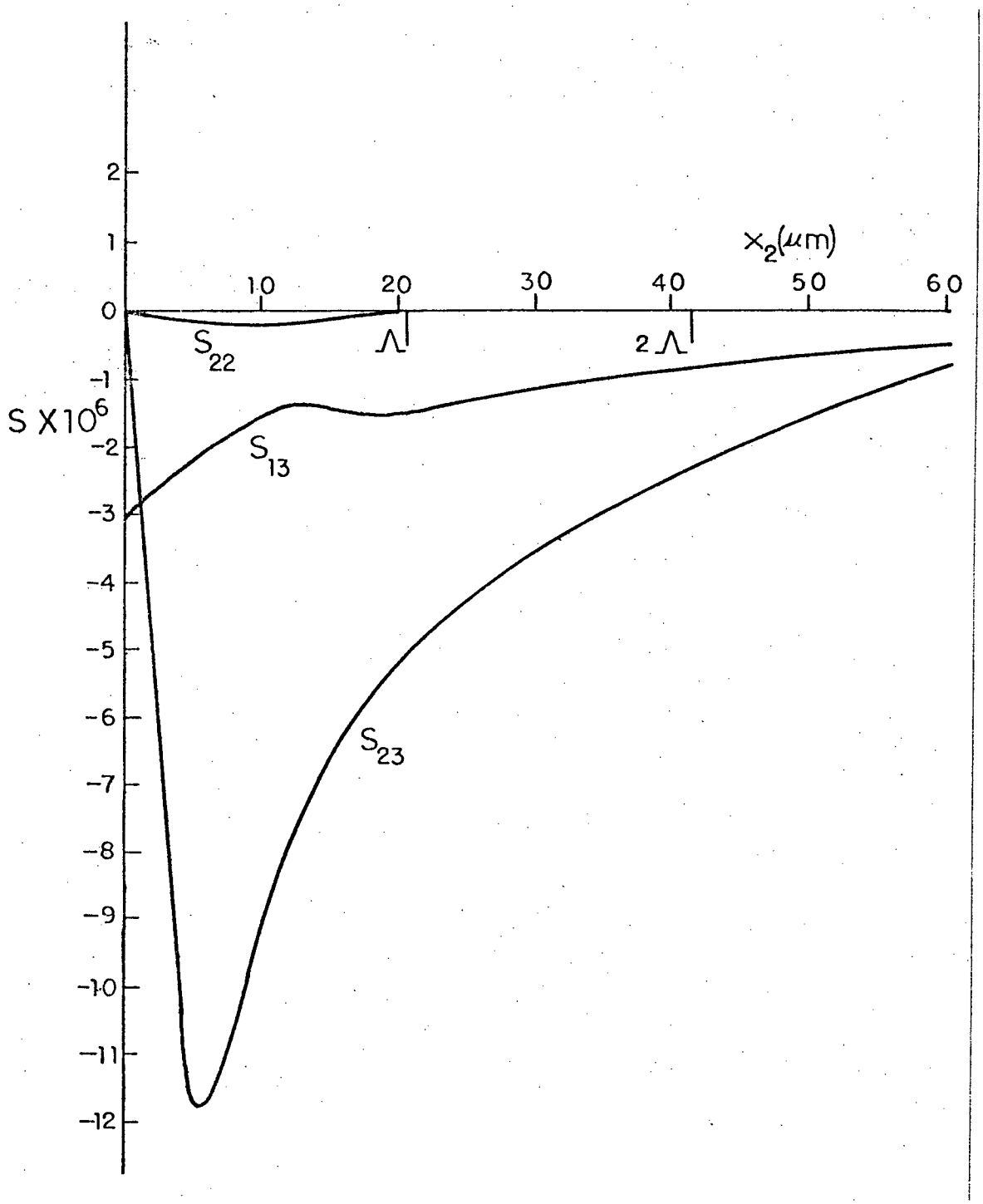

Fig. 4.12 Real Part of the Acoustic Strains vs. Depth for f = 165 MHz.

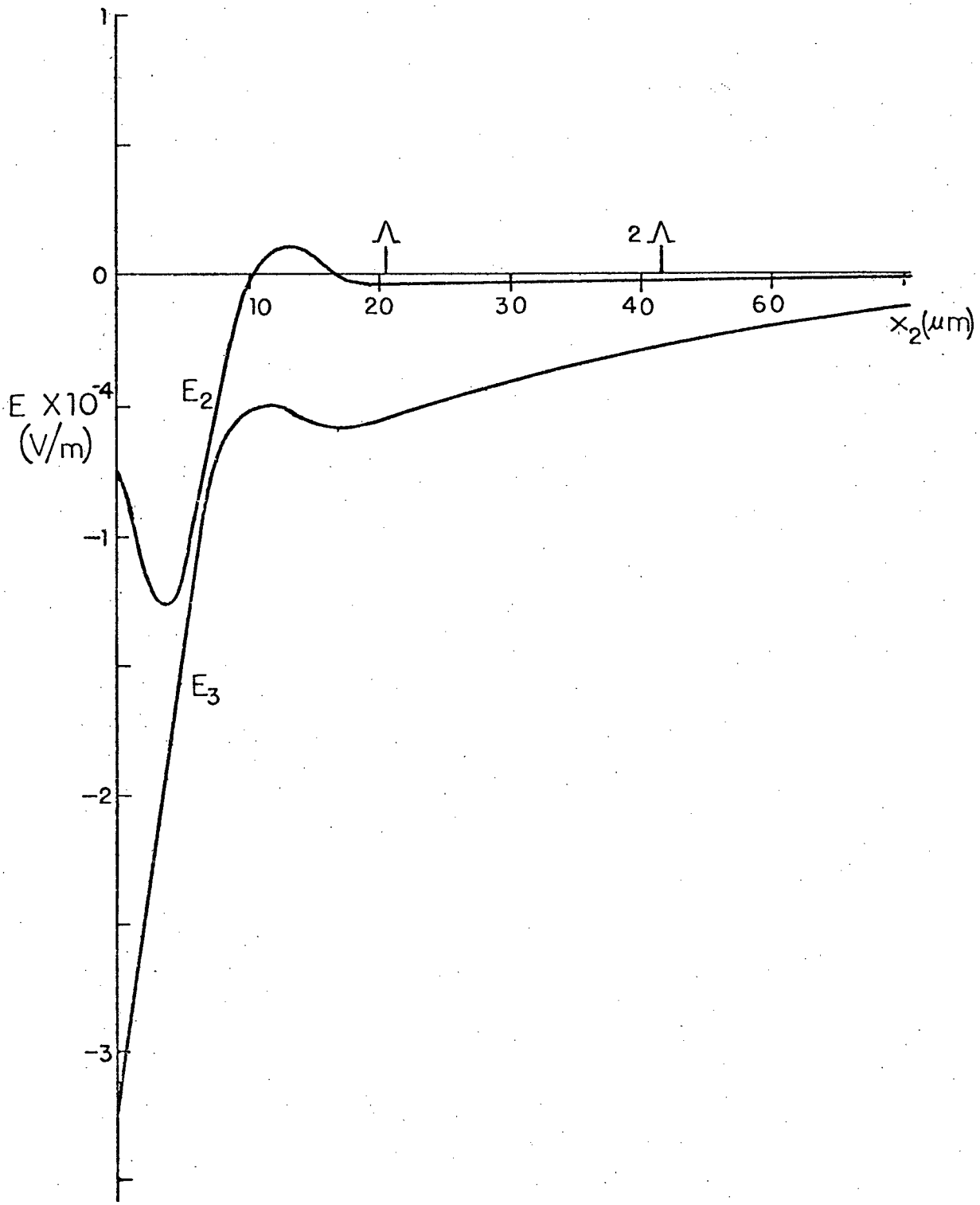

Fig. 4.13 Real Part of Electric Fields vs. Depth for f = 165 MHz.

$$\delta\varepsilon_{33} = -3.96S^r_{22} - .425S^r_{12} - .279S^r_{23} + .63S^r_{13} + 1.29\times10^{-9}E^r_2 - 7.15\times10^{-8}E^r_3 \tag{4.86}$$

The principal strain components are S_{23} and S_{13}, and the principal electric field component is E_3. Figure 4.14 shows the relative contributions with depth to the overlap integral by the photoelastic and electro-optic parts for a TE guided wave with a constant electric field. Comparison with Fig. 4.10 shows that the maximum in the photoelastic contribution corresponds to the minimum in $|u_3|$, where $d|u^N_3|/dx^N_2 = 0$. This is at about one-fifth the acoustic wavelength. Similarly, the minimum in the electro-optic part is at about $\Lambda/2$, since $|\Phi|$ has a minimum there, and $|E_3|$ is proportional to $|\Phi|$.

These results are similar to those obtained by Tsai et al [74], except that these authors appear to have scaled the electric field incorrectly (in fig. 4) by a factor of 2 as a function of depth. This could lead to considerable error in Γ, particularly for guided optical modes propagating very near the surface.

In Fig. 4.15, the factor g is plotted for P_{3M} = 1 watt and L = 1 meter for the three guided TE modes of the OWG. At low acoustic frequencies, only a small fraction of the acoustic power flow overlaps the shallow guided optical waves, and the diffraction efficiency is low. Above about 200 MHz, however, particularly for the higher order modes, the factor g is flat with frequency. This is a desirable characteristic for device applications, since it gives a flatter deflector frequency response. In calculations, it is expedient to write equations in terms of the total acoustic power P_a, rather than P_{3M}. For Y - Z ± 21.8° propagation on $LiNbO_3$, $P_a = 1.05\ P_{3M}$ [40], so the factor g must be divided by $\sqrt{1.05}$ in this case.

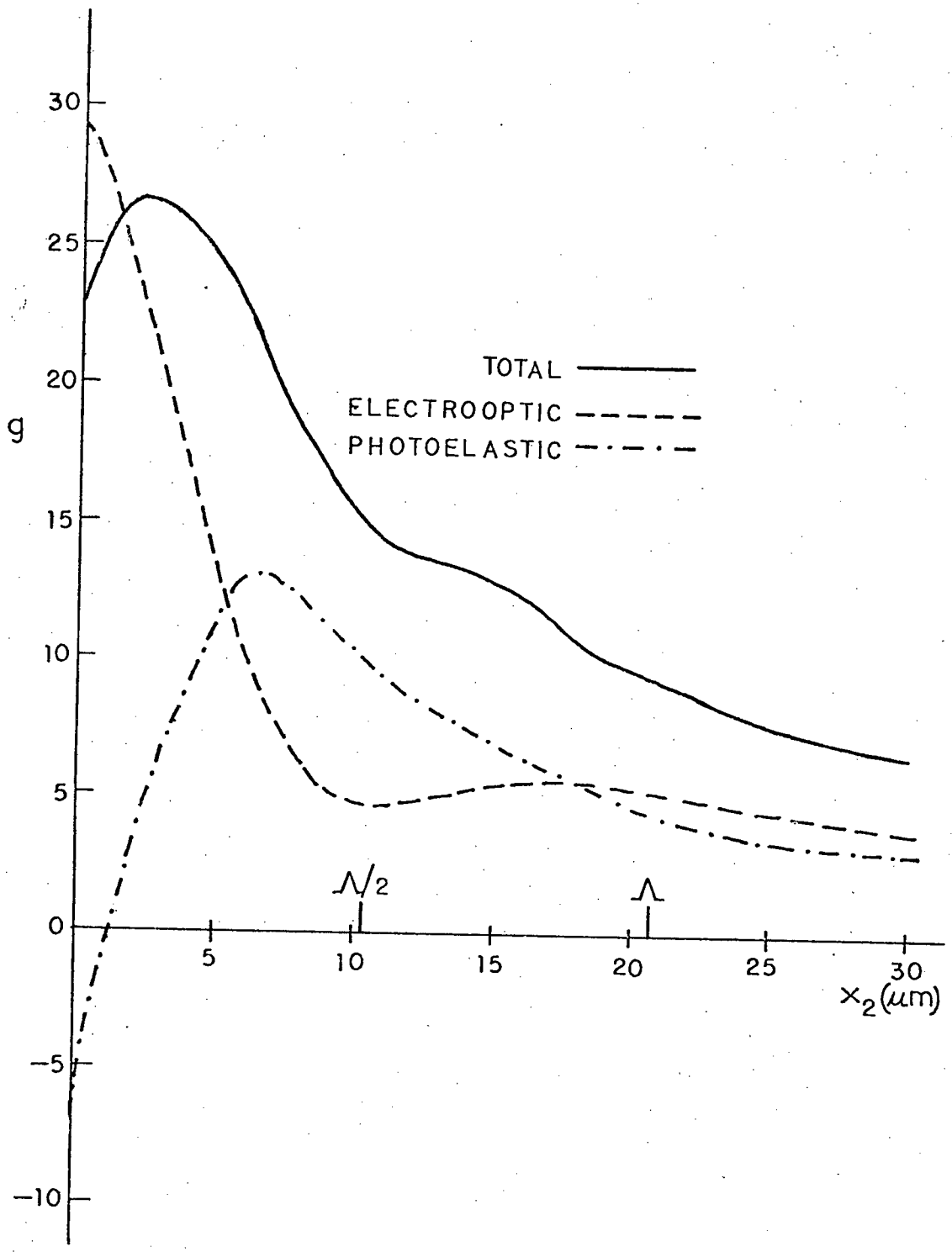

Fig. 4.14 Relative Electro-optic and Photoelastic Contributions to the Overlap Integral for f = 165 MHz.

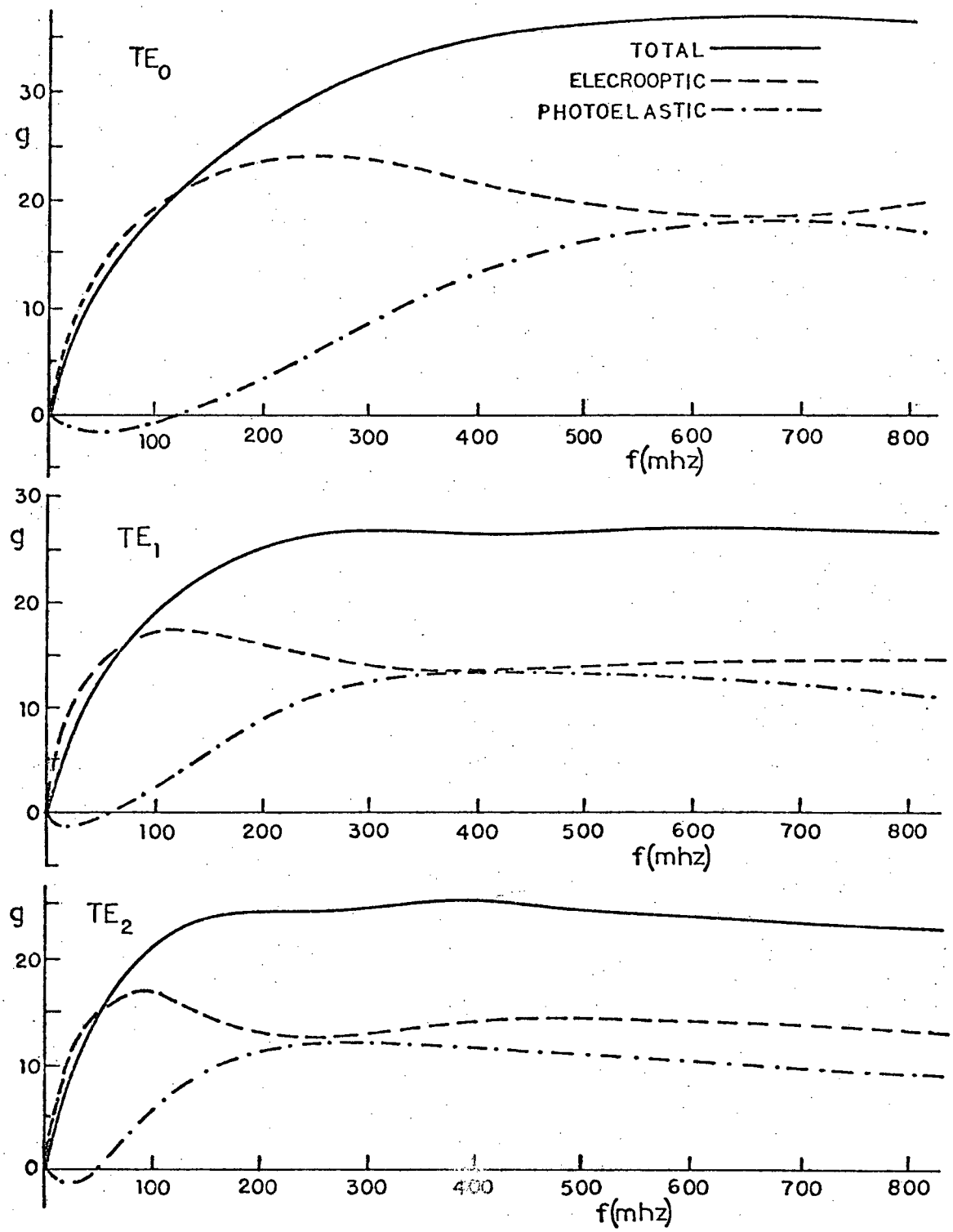
TE0
TOTAL
ELECROOPTIC
PHOTOELASTIC
g
30
20
10
0
100
200
300
400
500
600
700
800
f(mhz)
TE1
TE2

Fig. 4.15.

4.6 Experimental Work

Several beam-steered light deflectors were made. The devices were fabricated on the 6-mode Ni/$LiNbO_3$ diffused OWG characterized in Chapter 2.

The first deflector tested was made before the beam steering theory of Sections 4.3 and 4.4 had been completed, so its design was far from optimal. It consisted of a 2-section phased IDT array with P = 1 (Fig. 4.16). Each section was 1.55 mm wide and had 2 1/2 finger pairs. Transducers with a center frequency of 155 MHz were made by photolithography of vacuum deposited aluminum 0.3 μm thick. (See Chapter 5 for details). The device was oriented so that surface waves propagated at an angle of 21.8° from the Z axis of Y-cut $LiNbO_3$. With the two transducer sections counected in parallel and driven out of phase, impedance measurements at the center frequency gave C_T = 4 pF, and $R_o + R_e$ = 40 Ω.

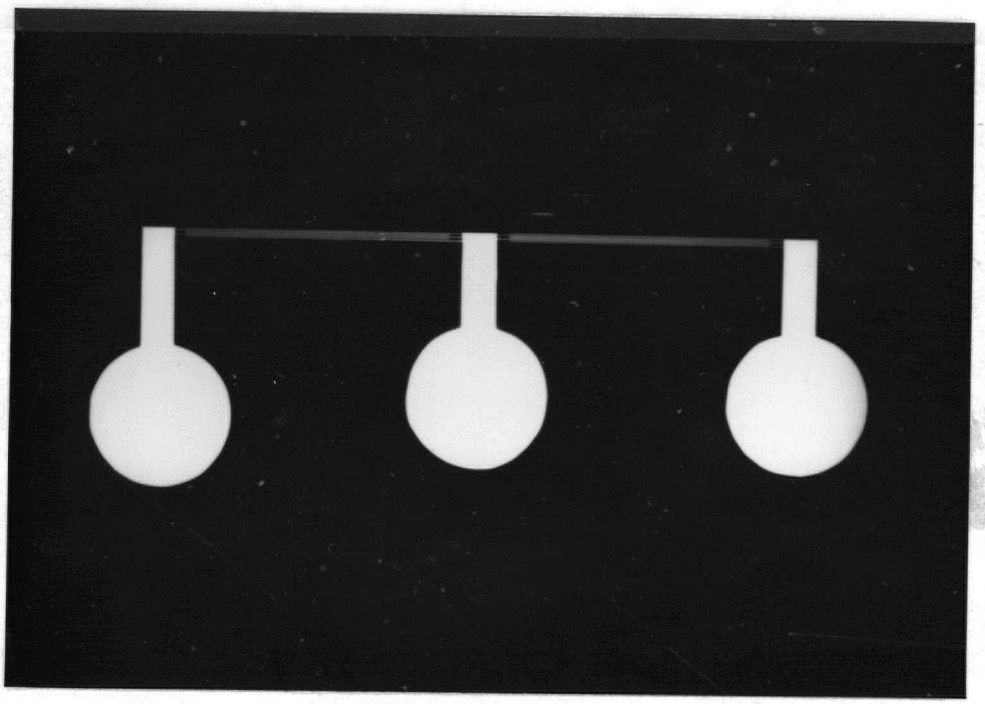

Fig. 4.16 20X Enlargement of Transducer Photolithography Mask.

Vinyl electrical tape was used to minimize acoustic reflections. These values are in reasonable agreement with the parameters of the IDT series equivalent circuit, which are C_T = 3.46 pF, R_o = 38.6 Ω and R_e = 4.9 Ω for a metallization factor of 0.4.

Fig. 4.17 shows the assembled acousto-optic deflector. The IDT is on the right, and SAW propagation is from right to left. Electrical connection was made by thin wires connected with silver conductive paint. Coupling to the optical waveguide was by means of rutile coupling prisms; in the photograph, the deflector output beam can be seen as a bright spot on the base of the lower prism. Electrical tape was used to absorb the surface waves and hold the substrate in place. The prism clamps were adjusted to give reasonable coupling efficiency.

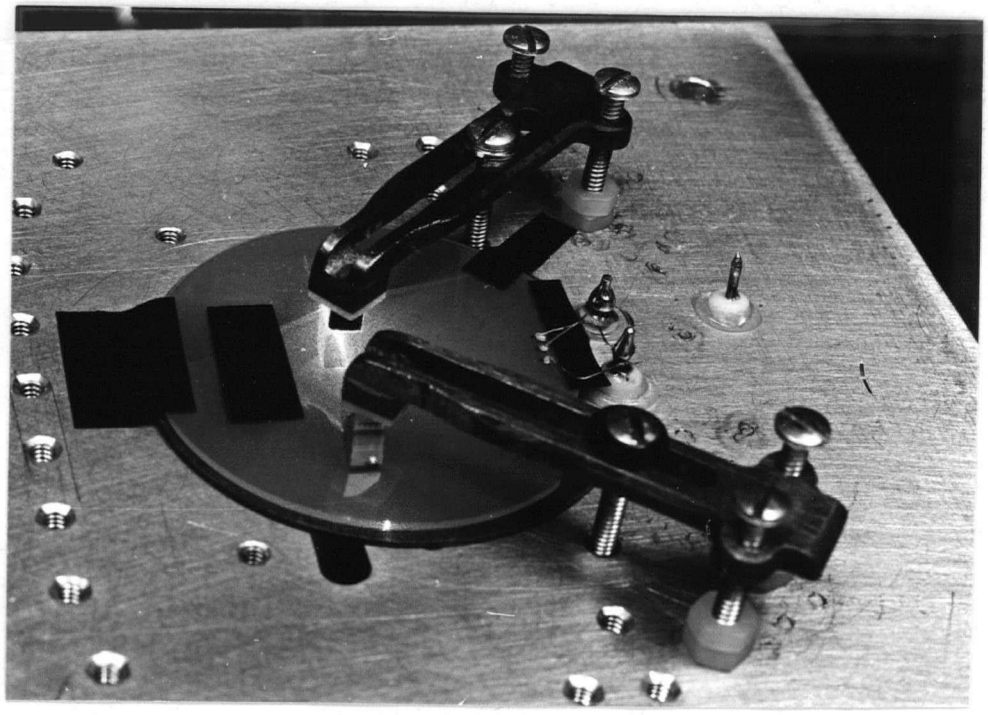

Fig. 4-17 Acousto-Optic Deflector (Actual Size).

Some difficulty was experienced before satisfactory deflector operation was obtained, owing partly to the difficulty of finding a suitable tuning inductor. (Without this inductor, the SAW generation efficiency is very low). The correct value was obtained by trial and error to be 0.19 μH rather than the anticipated 0.31 μH required to resonate with C_T. The difference can be accounted for by the inductance of the lead wires and possibly by additional stray capacitance.

Attempts to observe the surface waves by Raman-Nath diffraction of light from the $LiNbO_3$ surface were successful; however, the high r.f. drive power needed (∿ 1 watt) before the diffracted beams became easily discernible resulted in a number of burnt-out transducers. Figs. 4.18 and 4.19 show two typical failure modes; the first was probably caused by arcing between fingers, and the second by overheating due to finger resistance.

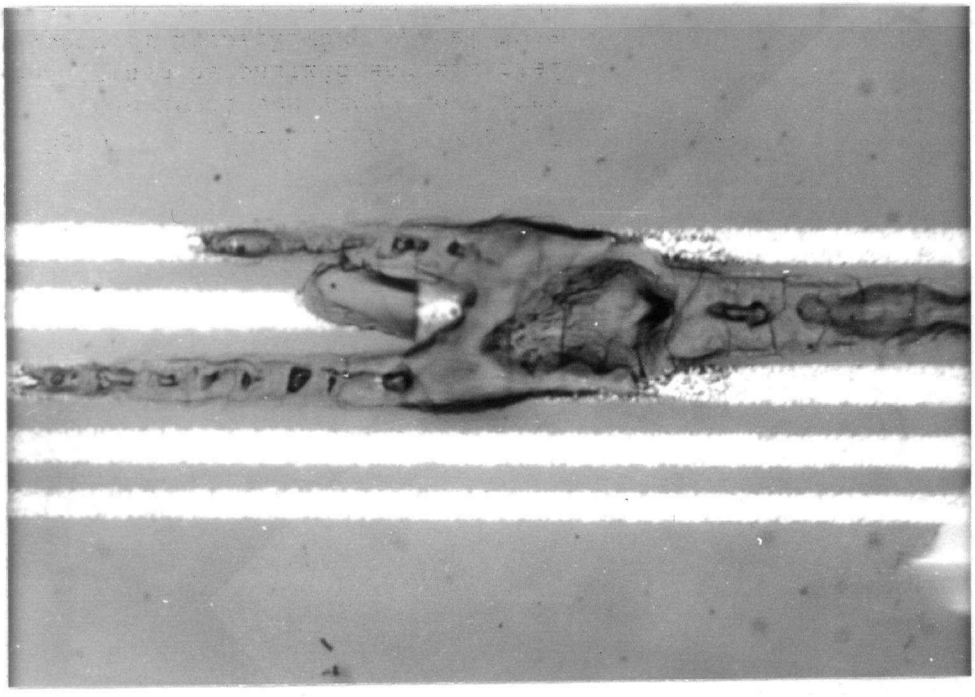

Fig. 4.18 Transducer failure

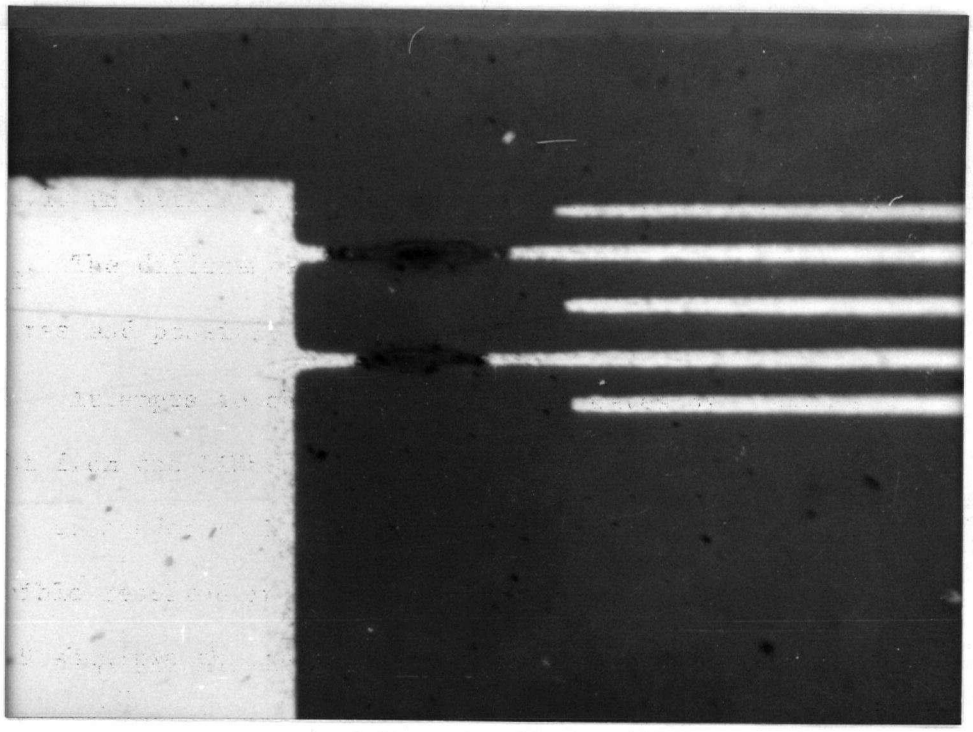

Fig. 4.19

When the device was first connected as shown in Fig. 4.17, the Bragg angle of light propagation in the surface waveguide was hard to find, owing to the delicate adjustments required. The measured -3 dB deflector bandwidth was about 26 MHz; as a result, the angular range over which the interaction was visible was only about 12 minutes of arc, as calculated with eq. 4.51. At angles of incidence nearly normal to the acoustic wavevector, the Raman-Nath diffraction regime was clearly visible (Fig. 4.20). The diffraction efficiency was very low, as anticipated.

Figs. 4.21 and 4.22 show Bragg diffraction of the TE_o and TM_o guided modes with the rf drive off (upper photo) and on (lower photo). The TE_o mode appears on the left, surrounded by scattered light. The diffraction efficiency of the TE mode was about 40%.

The device was driven by a GR 1215-B oscillator followed by a Boonton 230 A rf power amplifier capable of delivering 5 watts into a

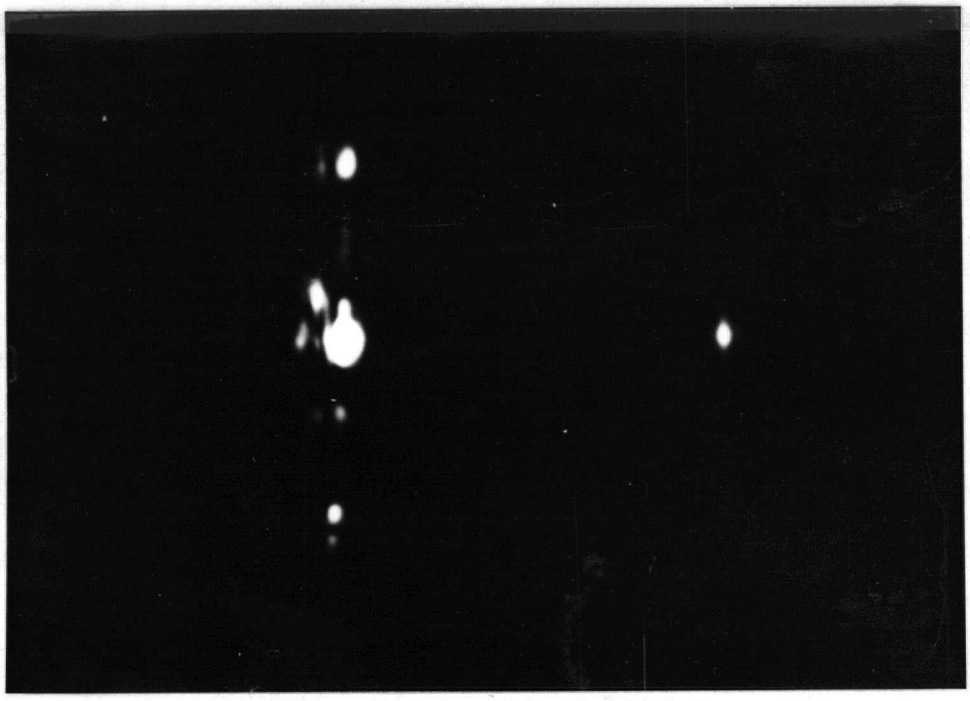

Fig. 4.20 Raman-Nath Diffraction of a Guided TE wave (the upper and lower spots on the left are the diffracted beams; the large spot is the undiffracted TE mode, and the small spot on the right is a TM mode)

50 Ω load. Measurement of the diffraction efficiency frequency response was complicated by multiple reflections on the line and the difficulty of obtaining reliable high-impedance rf voltage measurements. These problems were overcome by connecting a resistive voltage divider across the device and measuring the voltage at the matching inductor with a low capacitance probe on a high-speed oscilloscope.

Fig. 4.23 shows a comparison of the measured and calculated response. The inductor was tuned to give maximum diffraction efficiency at 165 MHz with the Bragg angle matched at that frequency. The response was calculated using equations (4.73) - (4.76) with the values P = 1, L = 3.1 mm, D = 1.55 mm, G = 1.9 mm, α = 1.374, $f_1 = v(nP/\lambda D)^{1/2}$ = 163.4 MHz, R_o = 38.6 Ω, R_e = 4.9 Ω, C_T = 3.16 pF and L_s = 0.31 μH. The experimental

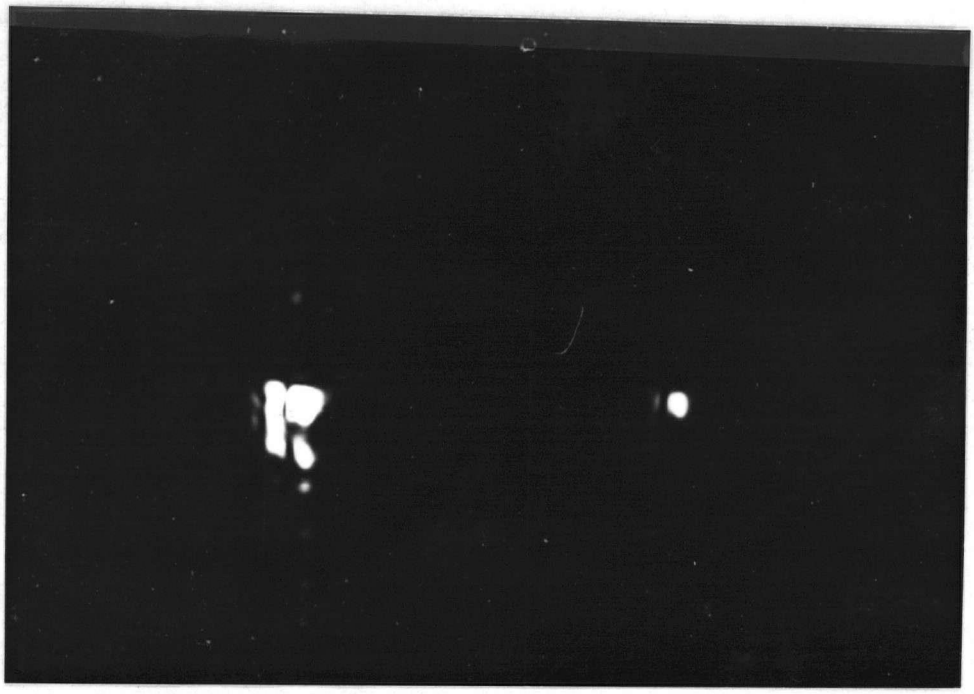

Fig. 4.21 Undiffracted TE_o (left) and TM_o Modes

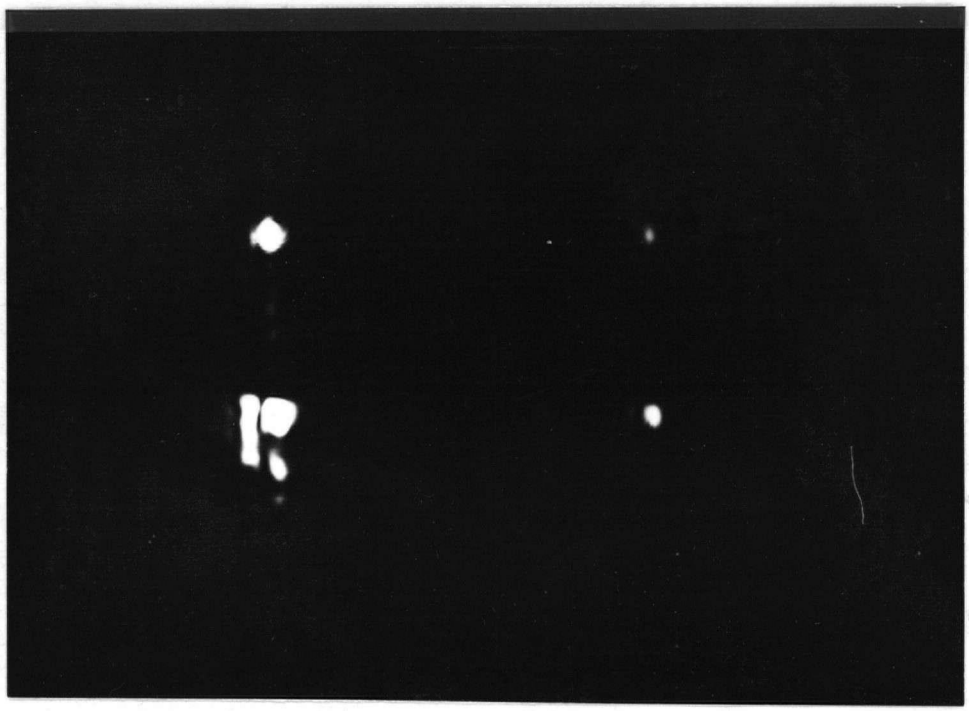

Fig. 4.22 Same with rf Drive Switched On ($\eta \sim 0.4$)

points are the average of several runs, and are for all three TE modes. The prism coupler was adjusted for optimal coupling of the TE_1 mode, so the overlap integral of this mode was used in the calculations. Within about 2%, g_b^2 can be approximated by

$$g_b^2 = 0.040 \sqrt{f} \; P_a L \; \mathrm{sinc}^2 \left[\frac{\pi P G \alpha}{2D} (1 - f/f_0) \right] \qquad (4.87)$$

In the calculation, it was found that the magnitude of the measured rms drive voltage had to be increased by almost 20% in order to match the magnitude of the theoretical curve to the experimental results. Either SAW propagation losses or inaccuracy in the voltage measurements could have been the source of the disagreement. Fig. 4.24 shows the response when the inductor is detuned to a high frequency and the Bragg angle matched at a frequency below 100 MHz. The bandwidth is considerably greater, at the expense of diffraction efficiency. The bandwidth in Fig. 4.23 is limited by the electrical bandwidth of the transducer equivalent circuit, about 24 MHz. In Fig. 4.24 , the IDT acoustic bandwidth of 39 MHz is the limiting factor. The bandwidth of the Bragg interaction itself (4.52) is 146 MHz, so it is clearly the interdigital transducer that limits the overall deflector performance. For a light beam 2 mm wide, the anticipated number of resolvable spots is $N_s = \Delta f \tau = 15$, which is rather a small number. It could be increased by using a wider light beam at the expense of speed and greater difficulty in coupling to the OWG.

According to the condition (4.22), deflector operation was within the Bragg regime by a factor of 1.7. The second order diffracted beam was clearly visible at higher drive power, and accounted for up to 4% of the diffracted light.

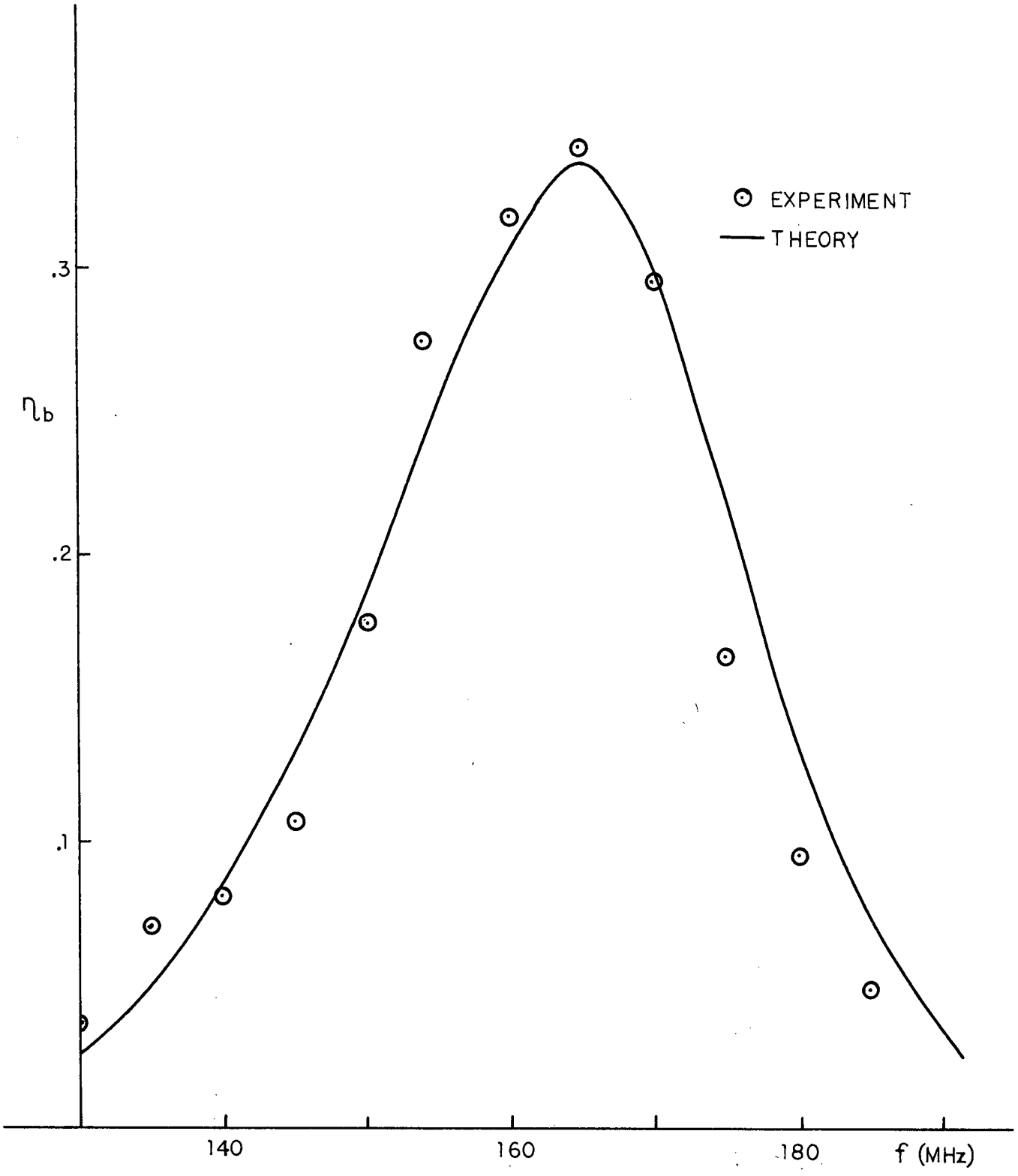

Fig. 4.23 Frequency Response of Deflector Diffraction Efficiency.

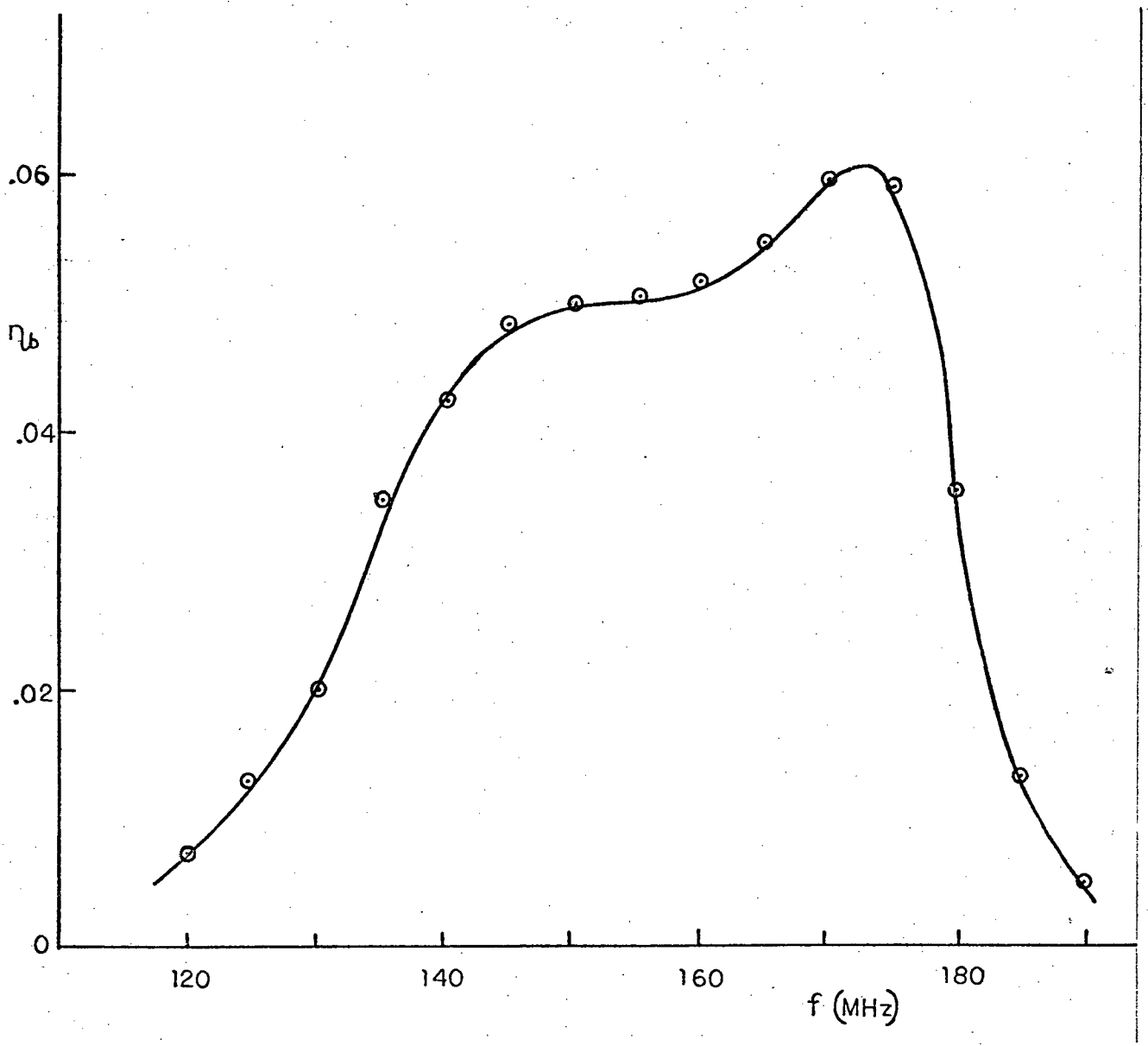

Fig. 4.24

The diffraction efficiency was measured as a function of drive voltage at 165 MHz. When the voltage is corrected by the same amount as before, good agreement is found between experiment and theory. (Fig. 4.25) The small discrepancy that exists may be due to diffraction into the second order beam. The acoustic drive power was calculated on the basis of the IDT equivalent circuit. The maximum diffraction efficiency into the first order beam was 70% at a corrected electrical drive power of 1.35 watts, which corresponds to P_a = 600 mW. At higher voltage, the device burnt out.

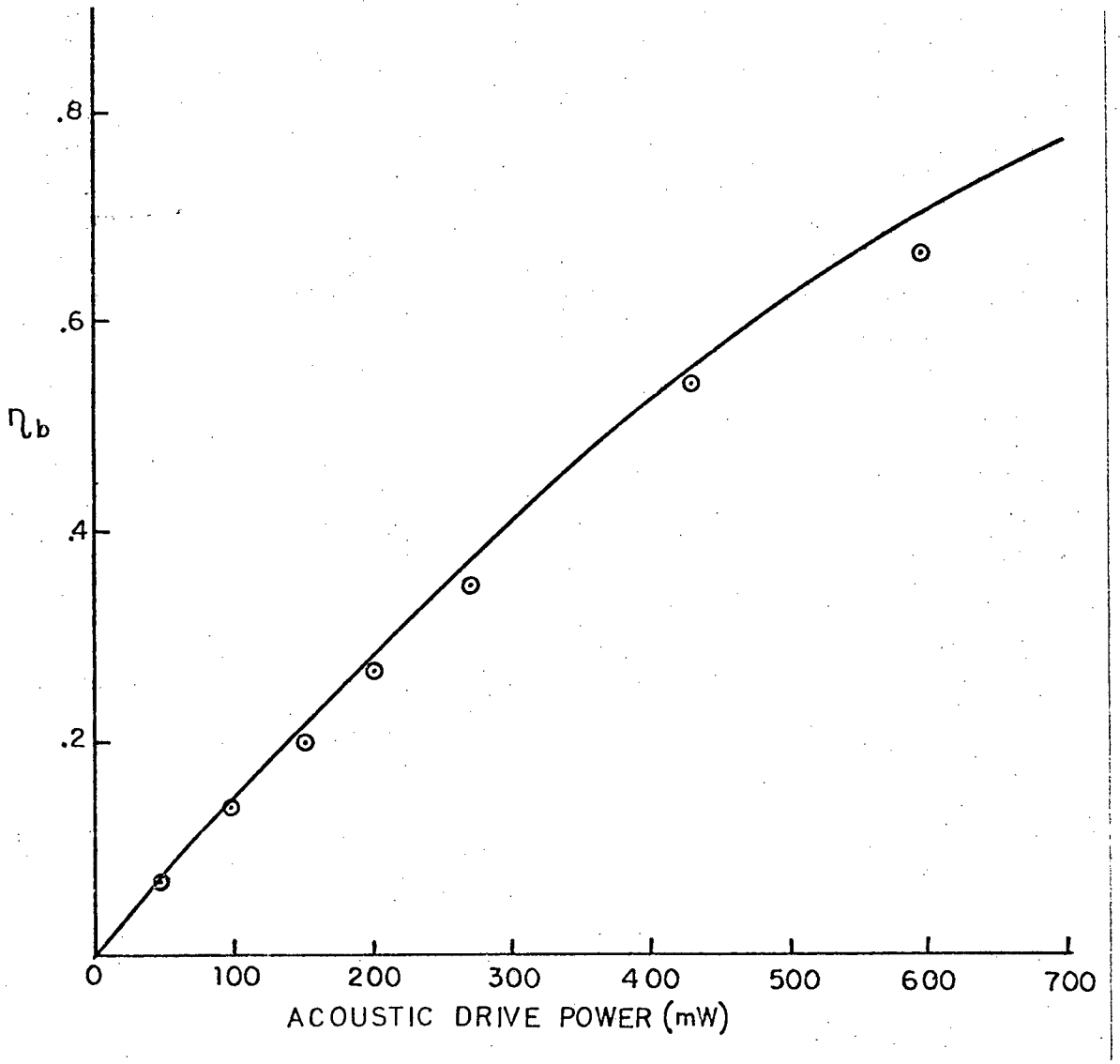

Fig. 4.25

Beam steering was not clearly observable with this device. It is most likely that the response obtained in Fig. 4.24 is the result of acoustic beam steering, but the experimental errors were sufficiently great that no firm conclusion was possible.

On the basis of these experimental findings, the beam-steered deflector theory of Sections 4.3 and 4.4 was put in its final form. An improved transducer with a 200 MHz center frequency was designed using the theory. A higher frequency device would have been desirable (since

greater bandwidth could have been obtained), but 4 μm linewidths were considered to be the resolution limit of the photolithography mask making process used. Since the finest lines that could be ruled on rubylith artwork material were found to be 0.5 mm, the maximum photoreduction ratio was 125:1. The maximum width of artwork that could be handled was about 1.25 meters, owing to the difficulty of cutting and uniformly illuminating greater widths. Consequently, the maximum width of the transducer was about 1cm. On the basis of frequency response calculations, it was concluded that the greatest bandwidth was obtainable when the array frequency f_1 was greater than the IDT center frequency f_o, so the selection f_1 = 205 MHz was made. This fixed the P/D ratio of the transducer array (4.71). For reasons discussed in Section 4.3, the ratio D/G was chosen to be 0.9. A minimum of four transducer sections were required so that the approximate diffraction theory would be reasonably accurate. The final requirement in the design was a transducer impedance near 50 Ω. For a series of integer values of P, the width and impedance of each transducer section were calculated, and various series/parallel combinations were tried until suitable values were found. The final design parameters were P = 2, D = 2.54 mm, L = 10.2 mm (4 sections) and $R_o + R_e$ = 50 Ω. The total resistance was forced to 50 Ω by selecting suitable values of the aluminum electrode thickness and metallization factor a. Control of the former was difficult with the photolithography process used, but the latter could be varied at will.

Three functional devices were fabricated using techniques described in the next chapter. All had similar characteristics. The remainder of this section describes experiments carried out on one device.

Figure 4.26 shows an enlargement of the photolithography mask used. The transducer had three finger pairs and four sections, which were

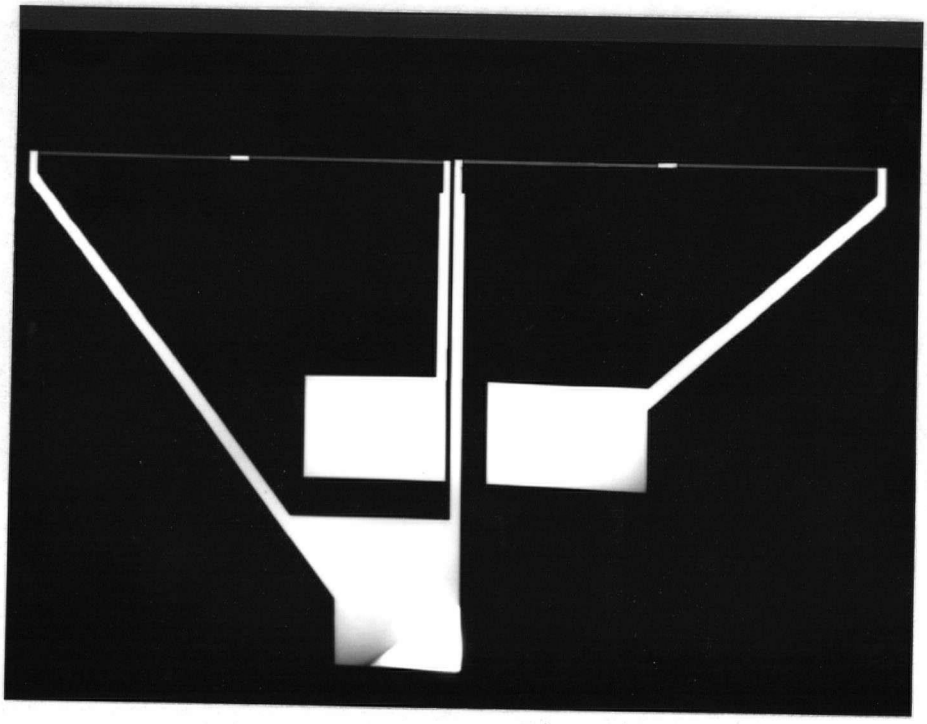

Fig. 4.26 Beam Steering IDT Mask (10X).

connected series-parallel and driven in phase. High-frequency impedance measurements with a Boonton 250A RX meter gave C_T = 5.7 pf and R = 59 Ω. Examination of the transducer in a scanning electron microscope showed an average metallization factor of about 0.45 and an aluminum thickness of 0.4 μm. Four-point probe measurements indicated an aluminum resistivity of 4.5×10^{-8} Ω-m, about 1.6X the bulk value. The transducer had the dimensions D = 2.54 mm and G = 2.83 mm. Comparison with the mask artwork gave a reduction ratio of 1:118.2, which implied that Λ_o = 17.19 μm and f_o = 199.4 MHz for propagation along the Z-21.8° direction on Y-cut $LiNbO_3$. The calculated parameters of the equivalent series circuit model

are C_T = 3.55 pF, R_a = 33.2 Ω and R_e = 16.5 Ω. The discrepancy between these and the measured values can be accounted for approximately when the aluminum conductors and contact pads of the device are taken into account (Fig. 4.26). These had an estimated resistance of 4.5 ohms as well as a capacitance of about 2 pf to the ground plane of the impedance bridge, through the $LiNbO_3$, which has a low-frequency permittivity of about 55. The extra capacitance appears in parallel with the transducer; because the Q is reasonably high, the total equivalent series capacitance would be expected to be comparable in magnitude to the sum of the parallel capacitances. In addition, the silver paint gave a measured contact resistance of 3 Ω at 200 MHz, so the differences are accounted for.

For the acousto-optic experiments, a plexiglass substrate stage was used in order to minimize stray capacitance. Figure 4.27 shows the circuit used to drive the device. A 10 dB power attenuator was used to reduce reflections on the transmission line. SWR measurements were made

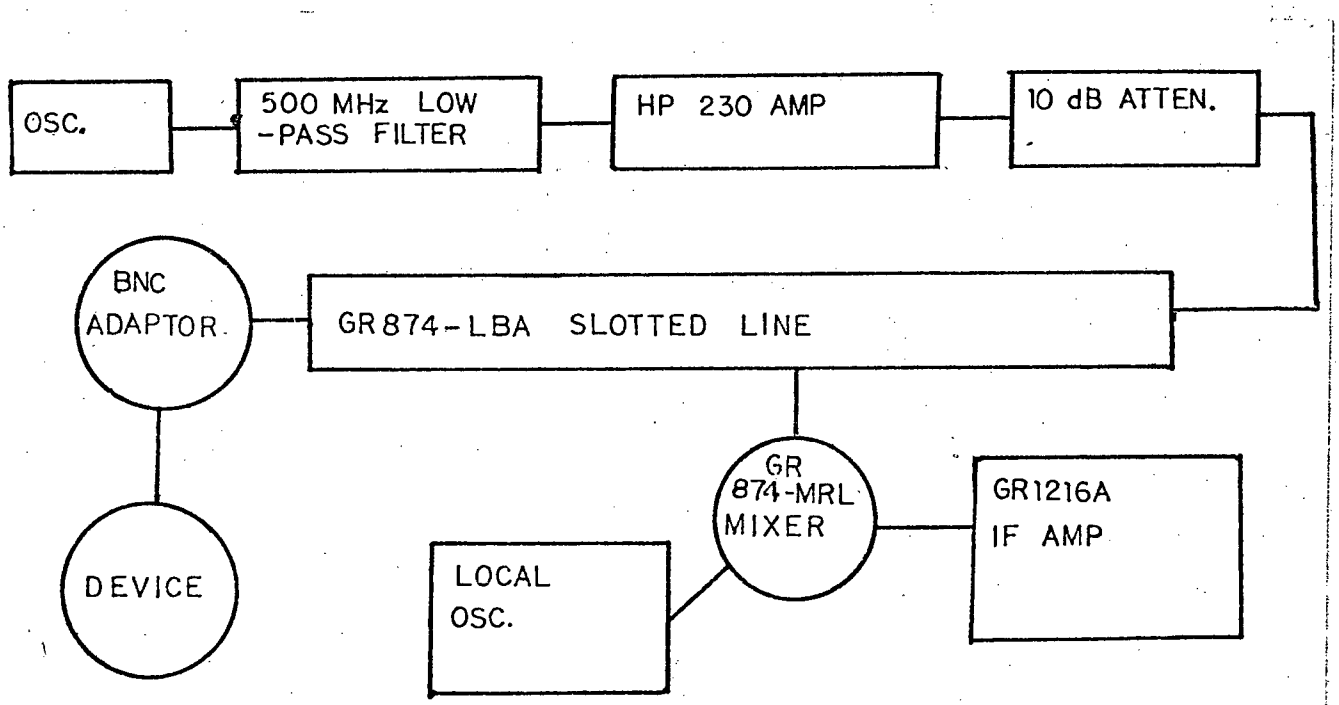

Fig. 4.27 Acousto-Optic Deflector Drive Circuit.

at 200 MHz with a variety of small hand-wound inductors connected in series with the IDT until an optimal match was found. This inductor had $3\frac{1}{2}$ turns and was approximately 4 mm in diameter, with a measured inductance of 0.057 μH. Additional inductance was provided with the connecting leads. This could not be measured directly, but a piece of wire of about the same total length had a measured inductance of .035 μH.

The minimum SWR obtained at 200 MHz was about 2.2; it was subsequently discovered that the GR to BNC adaptor and the BNC connector had an SWR of 2, so the transducer was apparently matched. However, it was necessary to consider the effect of standing waves on the transmission line between the connector and the IDT. An SWR of 2 corresponds to a reflection coefficient of magnitude $|\rho_1| = (2-1)/(2+1) = 0.33$. At the light deflector half-power points, the magnitude of the reflection coefficient ρ_2 at the load calculated from the matched IDT equivalent circuit was less than 0.5. Using $P = P_o(1 - |\rho|^2)$ to find the forward power, it can be shown (Fig. 4.28) that neglect of the multiple reflections leads to a maximum error of only a few percent.

Figure 4.29 shows a scan across the three guided TE modes of the deflected light beam, using a Gamma Scientific Model 2900 Scanning Auto-Photometer. At an acoustic frequency of 200 MHz, comparison with the undiffracted beam intensities indicated that all three modes had comparable diffraction efficiency, with the TE_o mode being somewhat more efficient. This is in agreement with the calculated relative magnitudes of the overlap integrals for the three modes.

When the beam-steering IDT was designed, the anisotropy parameter α was erroneously incorporated into (4.71). As a result, the calculated array frequency was actually 180.4 MHz rather than the 205 MHz

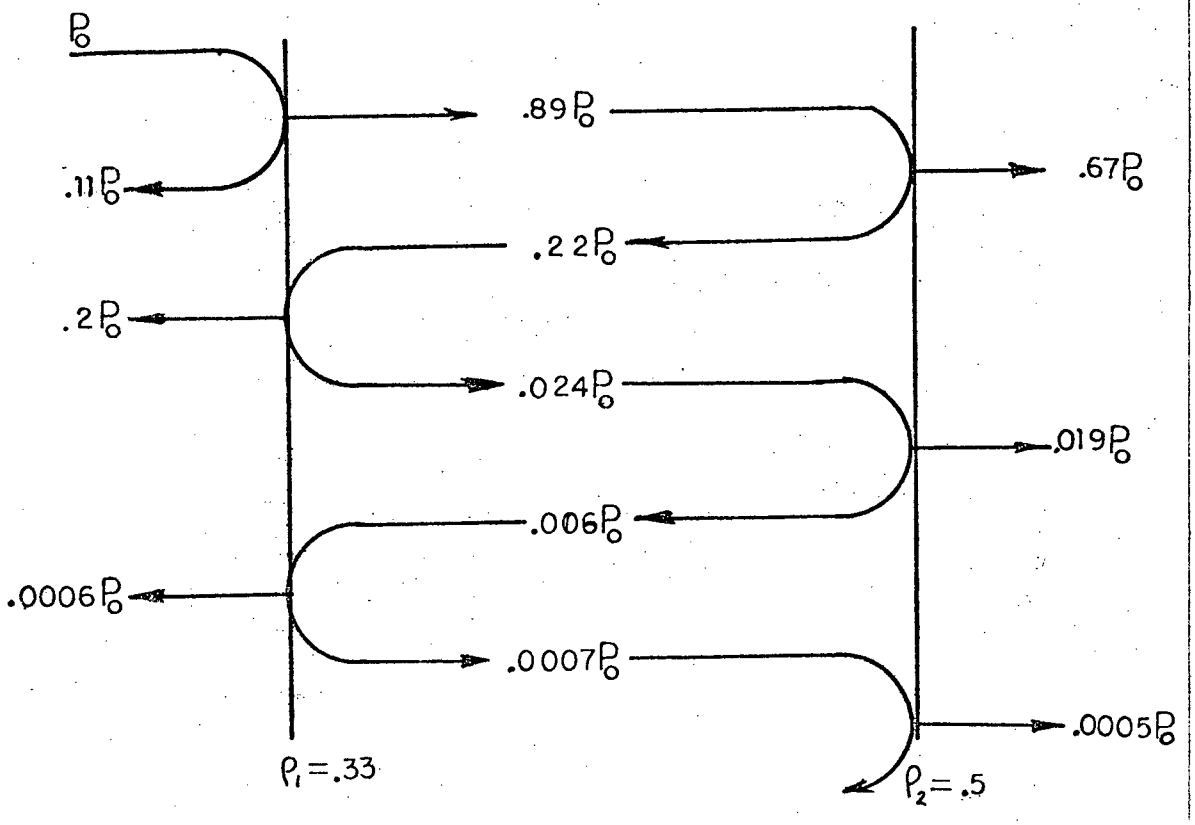

Fig. 4.28 Transmission Line Reflections.

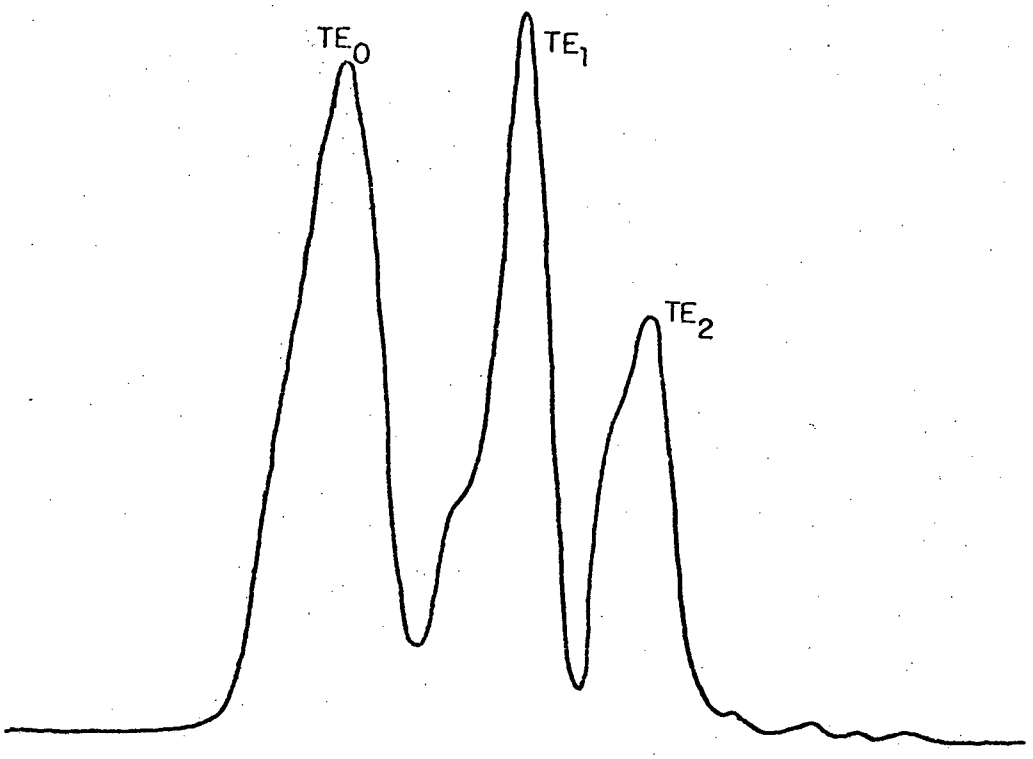

Fig. 4.29 TE Modes of the Deflected Beam.

expected. Figure 4.30 shows the frequency response of the diffraction

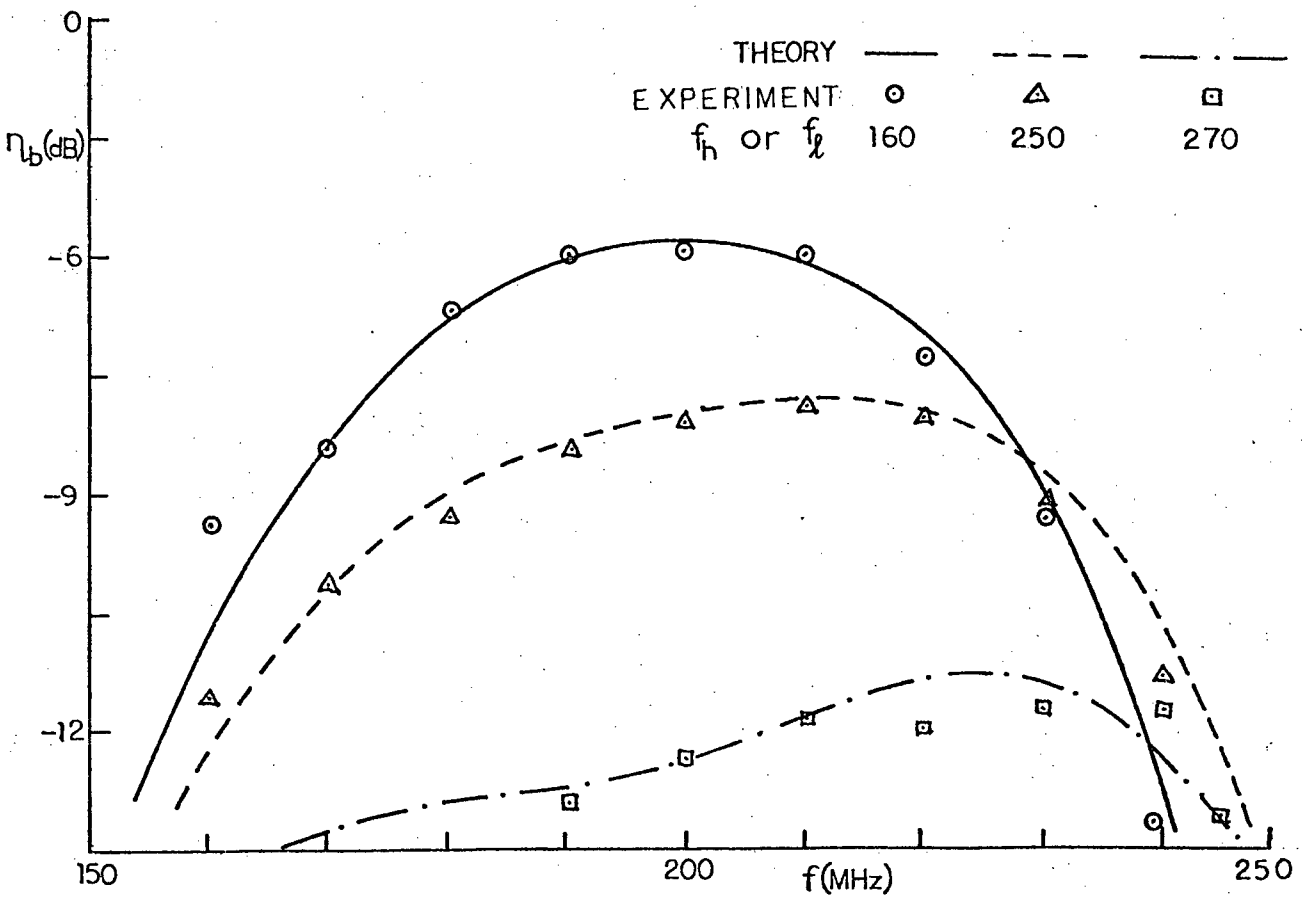

Fig. 4.30 Diffraction Efficiency vs. Frequency.

efficiency for three values of f_ℓ or f_h, the frequency at which the Bragg angle is matched. The theoretical curves were calculated with (4.73)-(4.75) and (4.78), using the values C_T = 3.55pF, L_s = 1.8 μH, R_o = 33.2 Ω, R_e = 32 Ω, V_f = 3.8 V rms, f_1 = 177 MHz, D = 2.54 mm, G = 2.83 mm, L = 10.16 mm, P = 2, Z_c = 53 Ω, n = 2.23 and λ = .6328 μm. The forward voltage on the line was measured with the meter in the rf power amplifier, which was calibrated with an HP 430-C Microwave Power Meter using the 477B thermistor head. The equivalent circuit parameters are within 10% of the best estimates available for the total equivalent impedance of the

transducer, electrodes and matching circuit. Additional series resistance is due to the skin effect in the connecting wires, and additional inductance derives from the wires and feedthroughs (estimated to be .1 μH). The lower value of f_1 used (2% below the calculated value) gave a better fit to the data. The difference could be due to small non-uniformities in the transducer geometry. The exact value of inductance used gave the best fit to the observed frequency response. This approach permits a better comparison between theory and experiment. Variations of ± 10% in the circuit parameters would have given similar results, with minor differences in diffraction efficiency, bandwidth and overall response shape.

The effects of beam steering are clearly evident in Fig. 4.30. When the difference between f_1 and the Bragg frequency is large, beam steering becomes more pronounced; the deflector bandwidth increases from 51 MHz when f_ℓ = 160 MHz to 68 MHz when f_h = 270 MHz. This increase is at the expense of diffraction efficiency, which drops from 0.34 to .04 at the IDT center frequency. Figure 4.31 shows the diffraction efficiency at f = 200 MHz as a function of the Bragg frequency, and Fig. 4.32 shows deflector bandwidth vs. Bragg frequency. These are combined in Fig. 4.33, which illustrates the inherent tradeoff between diffraction efficiency and bandwidth. These characteristics are all predictable from Fig. 4.9. Increasing f_h or decreasing f_ℓ has the effect of raising the ϕ_b curve, which increases the frequency range over which acoustic beam steering is effective.

Figure 4.34 gives a comparison between the calculated response of a conventional and a beam-steered deflector. The latter has the Bragg frequency matched at 160 MHz and the former at 200 MHz. The drive voltage

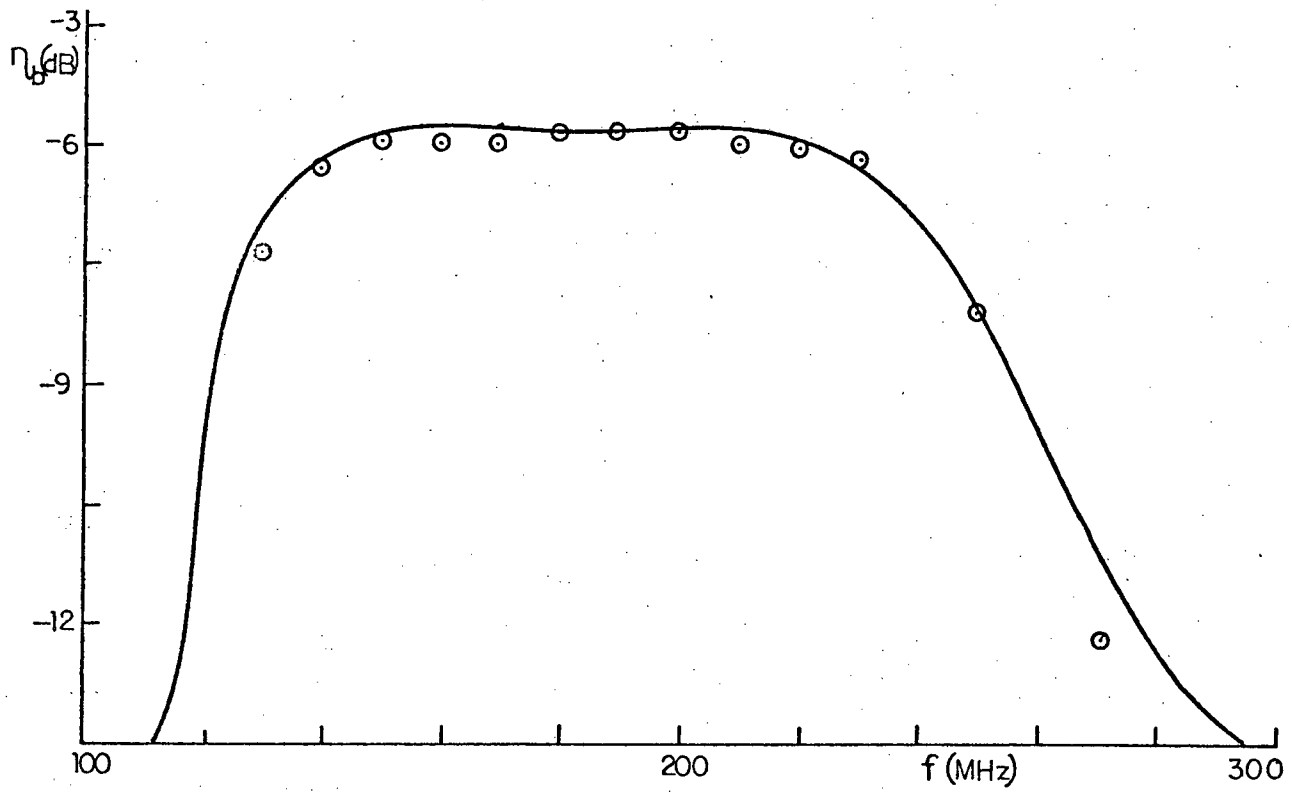

Fig. 4.31 Diffraction Efficiency at f = 200 MHz vs. Bragg Frequency with V_f = 3.8 V rms.

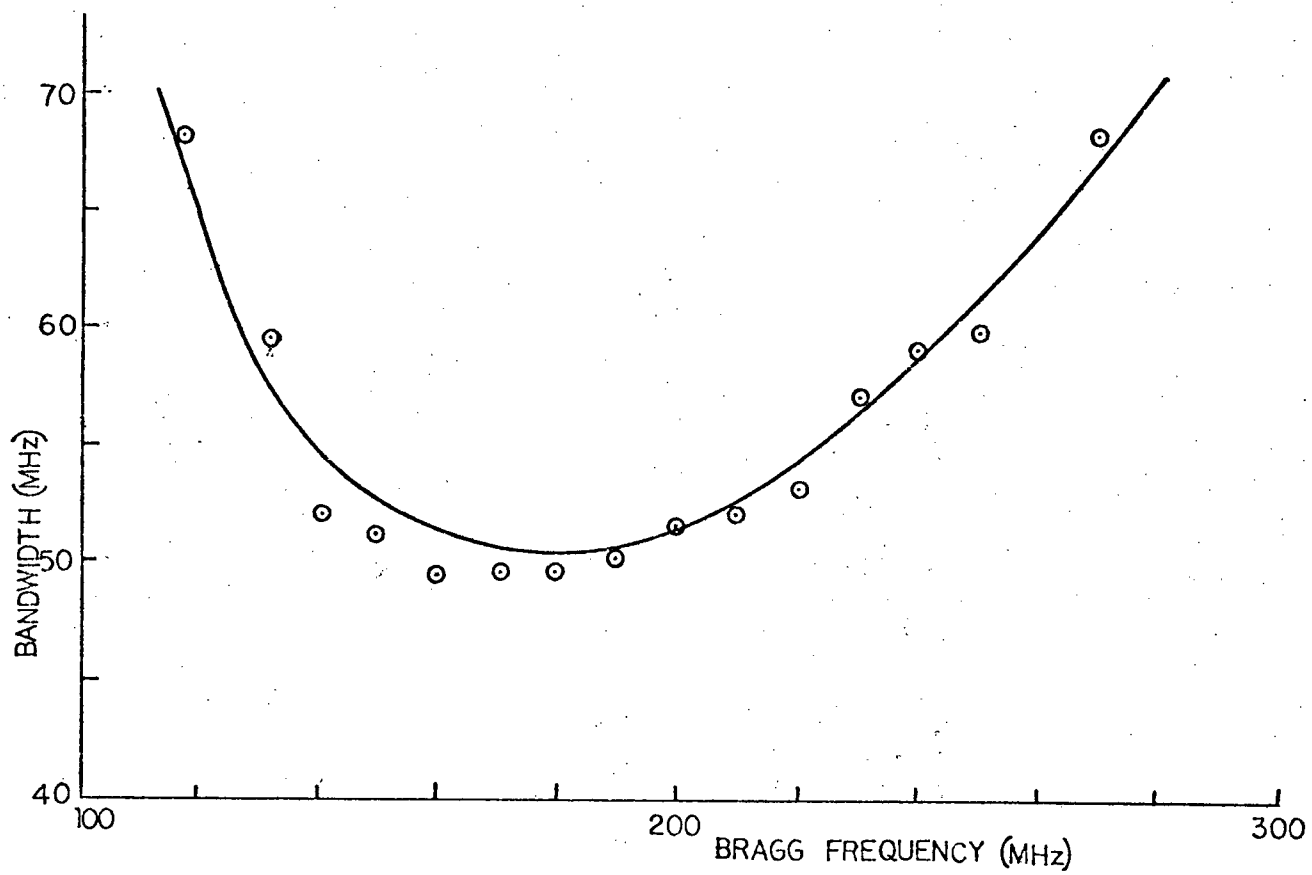

Fig. 4.32 Deflector Bandwidth vs. Bragg Frequency with V_f = 3.8 V rms.

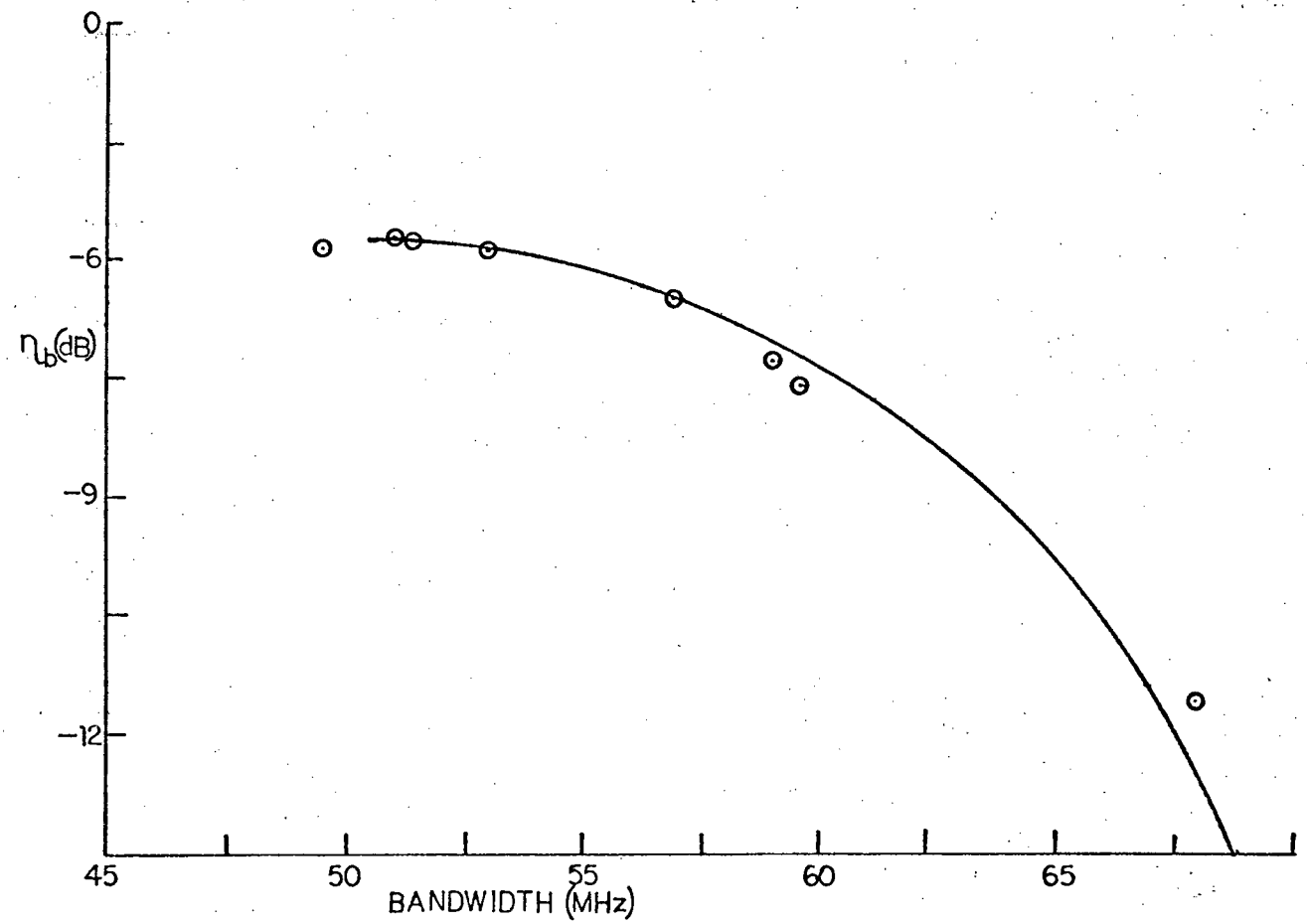

Fig. 4.33 Peak Diffraction Efficiency - Bandwidth Tradeoff with V_f = 3.8 V rms.

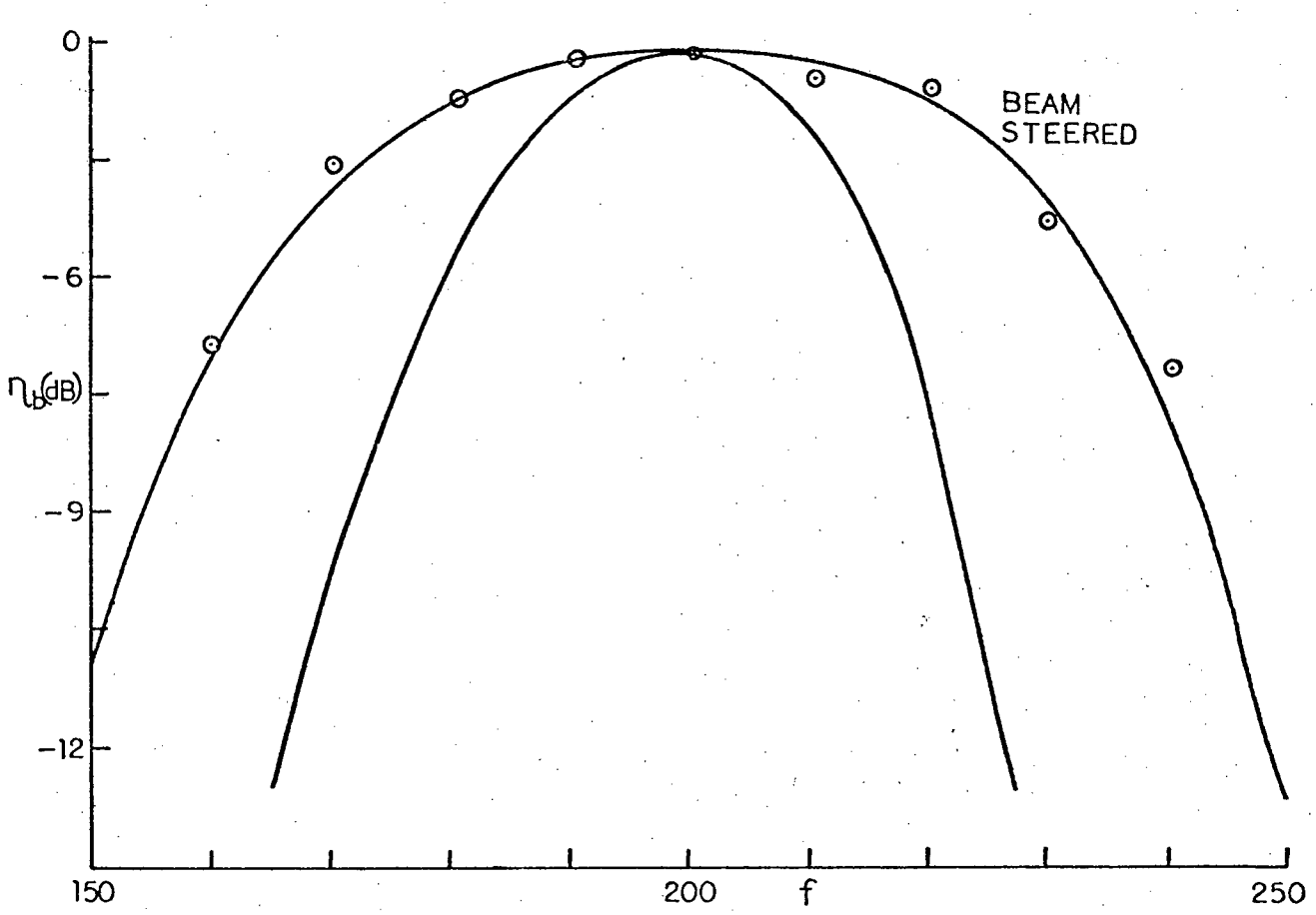

Fig. 4.34 Comparison of Response of Phased-Array and Conventional Bragg Deflector.

is 8 V rms, giving a maximum diffraction efficiency of 0.93. The unsteered deflector diffraction efficiency was found with (4.74) and (4.77), using modified versions of (4.75) and (4.76). The angular deviation from the Bragg angle is

$$\Delta\theta_b = \frac{\lambda}{2nv}\,\Delta f \ ,$$

so that

$$h_c = \frac{K\Delta\theta_b L}{2} = \frac{\pi\lambda}{2nv^2}\ f\Delta f L \ . \qquad (4.88)$$

In (4.76), the factor

$$\mathrm{sinc}^2[\tfrac{\pi PG\alpha}{2D}\,(1 - f/f_o)]$$

must be replaced by the diffraction pattern of the stepless array, which can be shown to be

$$\mathrm{sinc}^2(K\Delta\theta_b L/4) = \mathrm{sinc}^2(h_c/c) \ , \qquad (4.89)$$

when $f_b = f_o$.

The bandwidth of the beam-steered deflector is almost twice as great. The acoustic power (Fig. 4.35) is the same for both devices. The principal reason for the different bandwidths is evident in Fig. 4.36, which shows the Bragg-angle deviation vs. frequency. This limits the bandwidth of the unsteered deflector through h in (4.74). Of lesser importance is the factor $\mathrm{sinc}^2(h_c/2)$, which falls off somewhat more rapidly on either side of the IDT center frequency.

Calculations indicate that greater bandwidths could have been achieved if f_1 had been close to f_o. For example, a six-section transducer with D = 2.18 mm, P = 2 and f_1 = 195 MHz is capable of giving a 78-MHz bandwidth a maximum diffraction efficiency of 0.5 with a drive voltage of 8 V rms when f_ℓ = 150 MHz. The bandwidth is also greater at

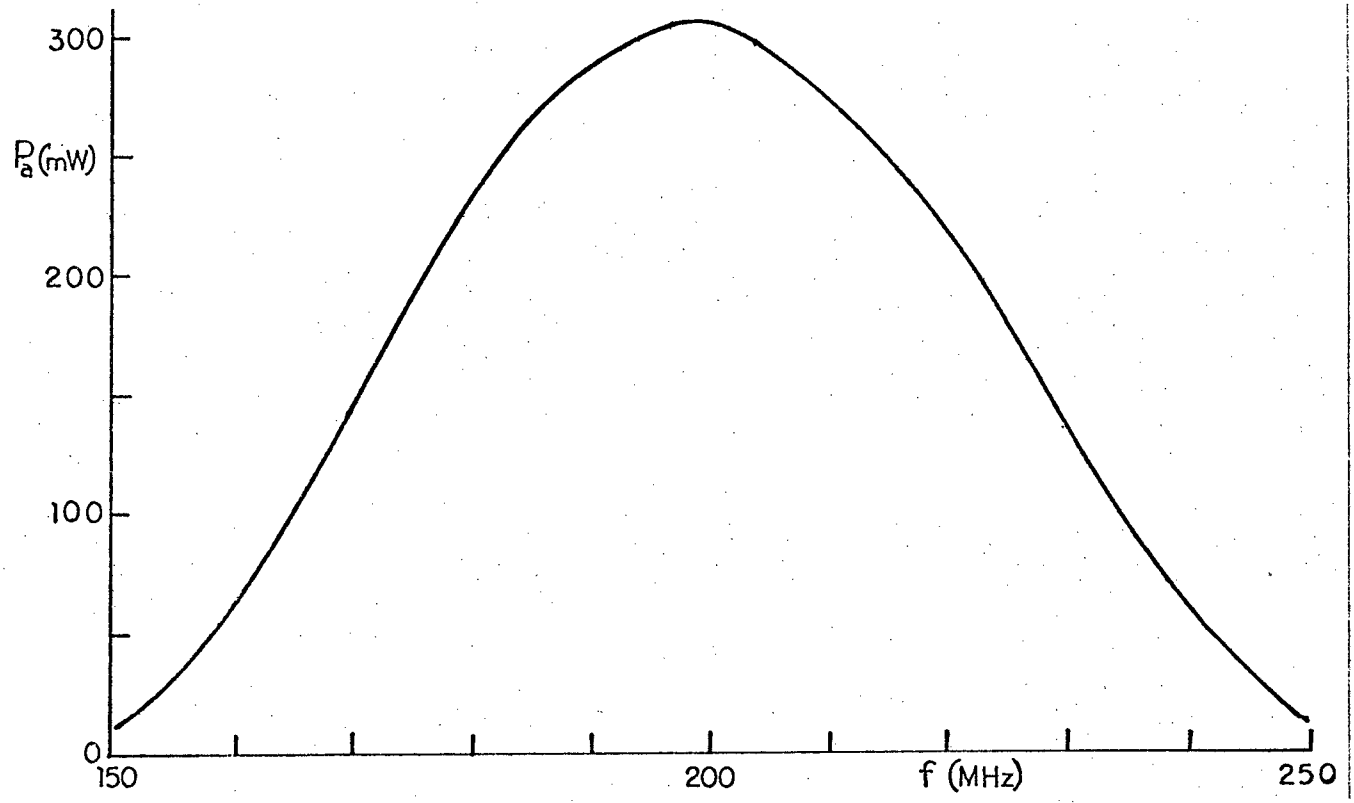

Fig. 4.35 Acoustic Power vs. f.

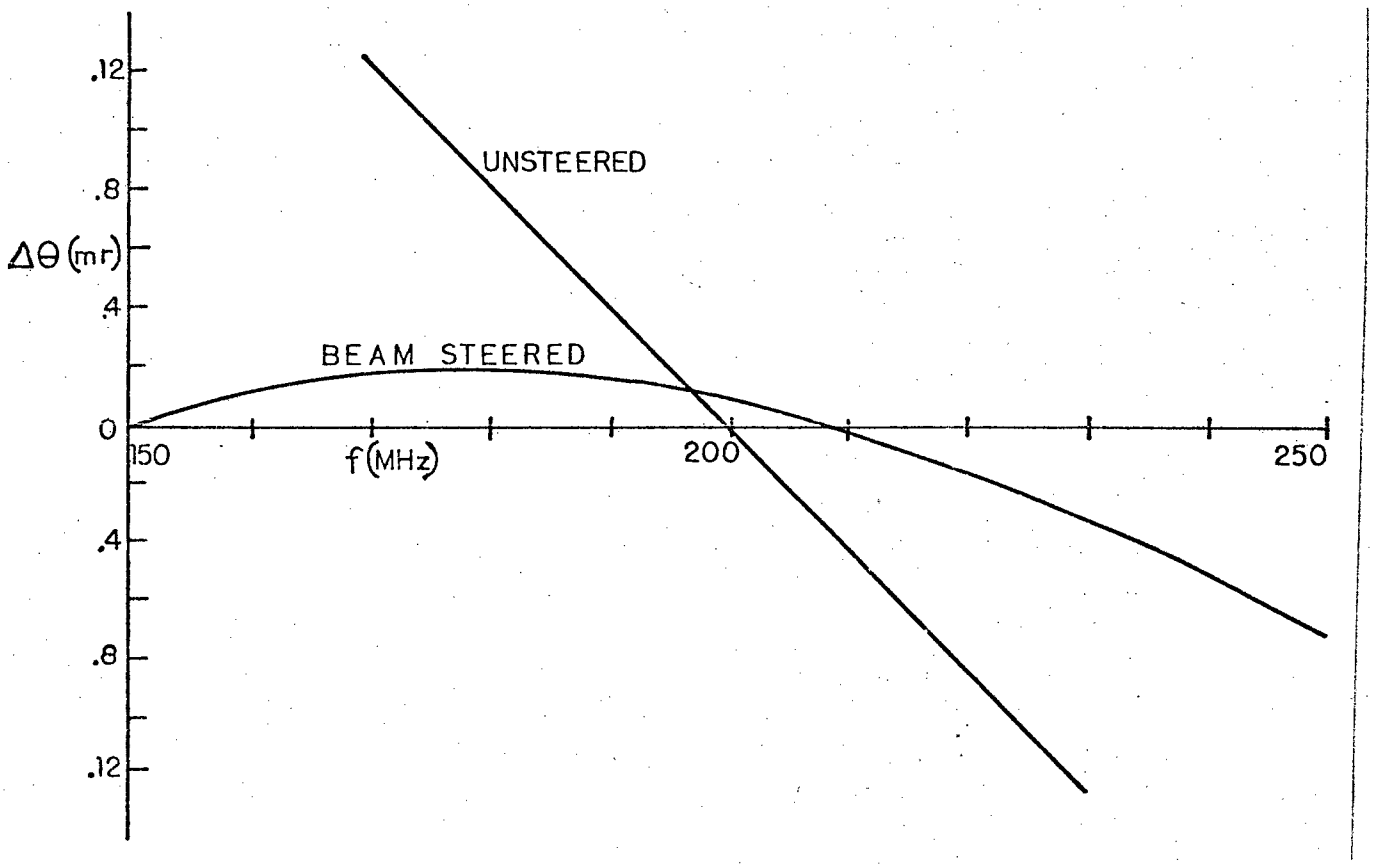

Fig. 4.36 Deviation from Bragg Angle vs. f.

higher drive voltages, as shown in Fig. 4.37 for the device mode. With an rf forward voltage of 10 V rms on the line (P_a = 465 mW) and f_ℓ = 150 MHz,

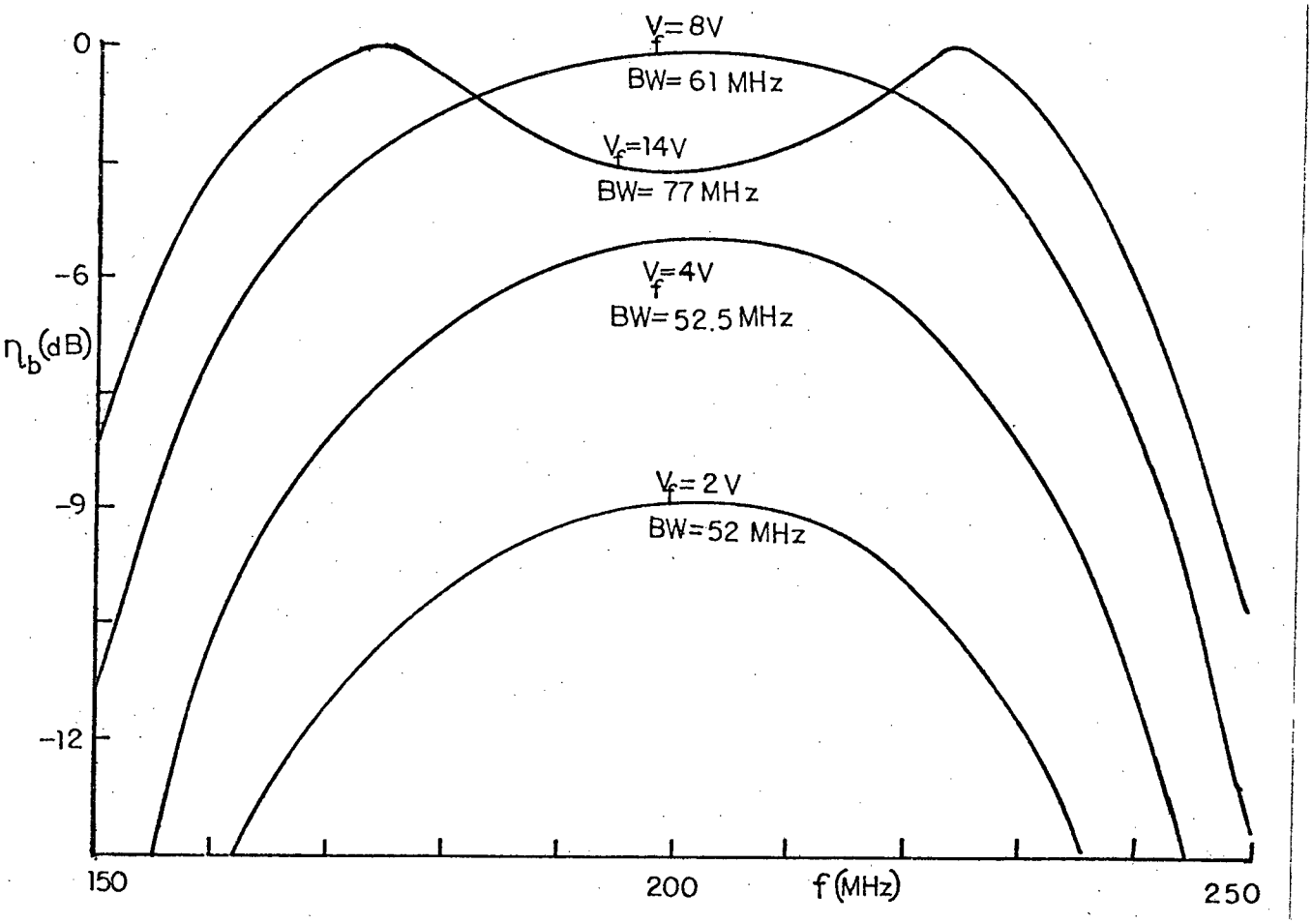

Fig. 4.37 Diffraction Efficiency vs. f for Several Drive Voltages (f_ℓ = 150 MHz).

100% diffraction into the first order beam was observed. The deflector was somewhat unstable at such high input power, due to thermal expansion of the substrate which altered the coupling efficiency into the optical waveguide. The ℓ = -1 and ℓ = +2 diffracted beams were observable, although less than 1% of the total light was diffracted into these orders. Figure 4.38 shows the dependence of diffraction efficiency on drive voltage when f_ℓ = 150 MHz and f = 200 MHz.

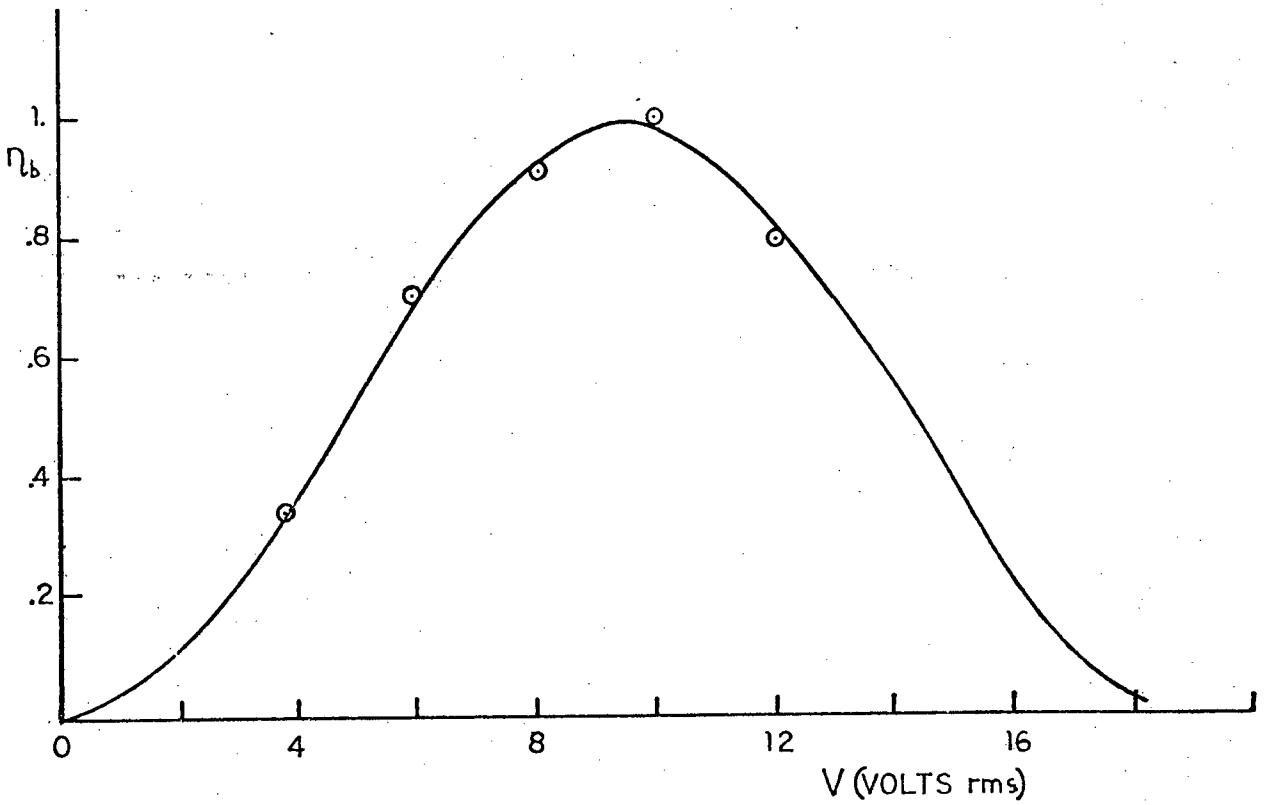

Fig. 4.38.

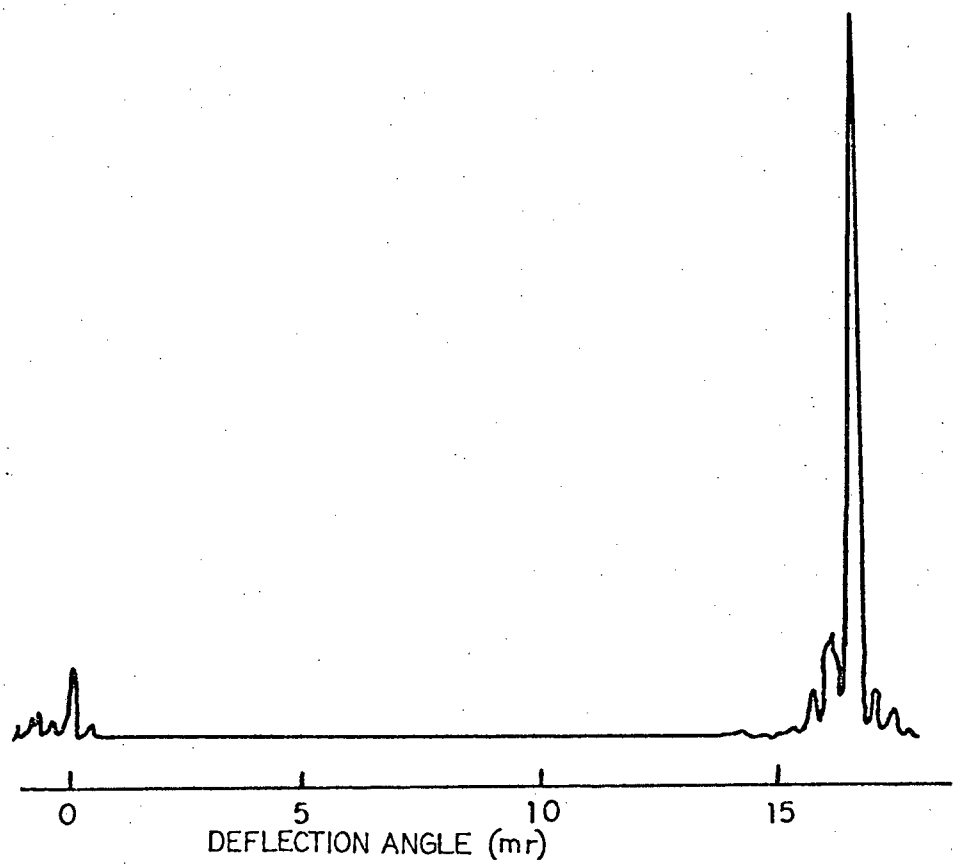

Fig. 4.39 Light Deflector Beam Profiles ($\eta_b \sim .9$).

The deflector light beam profiles are shown in Fig. 4.39 for an rms forward voltage of 8 V at 200 MHz. The range of angular deflection over a 61 MHz deflector bandwidth is $2\Delta\theta_b = 5.05 \times 10^{-3}$ radians. Using the Rayleigh criterion, the number of resolvable spots is $N_s = 2\Delta\theta_b/\Delta\phi = 43$. The maximum number obtainable at either high drive voltage or reduced diffraction efficiency (due to beam steering) is over 50. Optical coupling was effected without a lens over the entire $\sim$ 2.5 mm width of the input coupling prism. The theoretical number of resolvable spots is

$$N_s = \Delta f \tau = 44$$

for a bandwidth of 61 MHz, in good agreement with the observed number. The access time is limited by τ, which is .7 μsec. With a light beam diameter of 1 mm, the device is usable as a modulator with a bandwidth of 3.4 MHz.

The theory of beam-steered deflectors developed in Sections 4.2-4.4 appears to agree within about 10% with the observed characteristics of the device tested. In further experiments, it would be desirable to compare the device impedance obtained from reflection coefficient measurements on the transmission line to the anticipated values based on the IDT equivalent circuit model, matching inductor and connecting wires. Experiments at higher frequency would be a better test of the acoustic diffraction theory, since beam steering would be over a greater angular range.

Better performance could be obtained at higher frequencies, since the IDT bandwidth would be greater. For example, a beam-steered transducer with a center frequency of 500 MHz would give in excess of 500 resolvable spots with a light beam 1 cm wide. Wide bandwidth is likely

to be more easily obtained by using several beam-steered transducers with different center frequencies in parallel, or possibly one transducer with different center frequencies in adjacent sections.

5. SAW TRANSDUCER FABRICATION

In this chapter, a brief summary of the procedures used for interdigital SAW transducer fabrication are given.

Photolithography masks were made on Kodak 649-F 35 mm holography film by the following process. First, the artwork pattern was generated on cut and strip Stabilene film, using the improvised ruling apparatus shown in Fig. 5.1. Linewidths as small as 0.5 mm could be accurately drawn by controlling the straightedge position with verniers, which were adjustable within 0.001 inch. The cutter used is shown in Fig. 5.2. The completed artwork was taped to a sheet of translucent white plexiglass and illuminated from the rear with five 600 W quartz-halogen floodlamps. The level of illumination had to be very uniform across the artwork because both the film and photoresist used were very high contrast materials. The maximum variation tolerable was about 10%. The photoreduction was done with a Canon FTb, using a 28 mm f/2.8 Canon lens. The reduction ratio of a lens of focal length F with a distance x between subject and lens is given by $R = x/F - 1$. The use of a wideangle lens permitted large photoreductions to be made with reasonably small subject to camera separation.

Kodak 649-F film has a panchromatic emulsion, whereas the orange Stabilene film of the artwork was designed for uses with orthochromatic materials. To obtain better contrast, a green filter with strong absorption at wavelengths greater than .55 μm was used during exposure.

A series of time exposures was made and the developed images were examined microscopically for uniformity, contrast and an absence of fog in the clear areas. Best results were obtained with an exposure time of 6 minutes at f/4.5. Vibration due to the building air conditioning

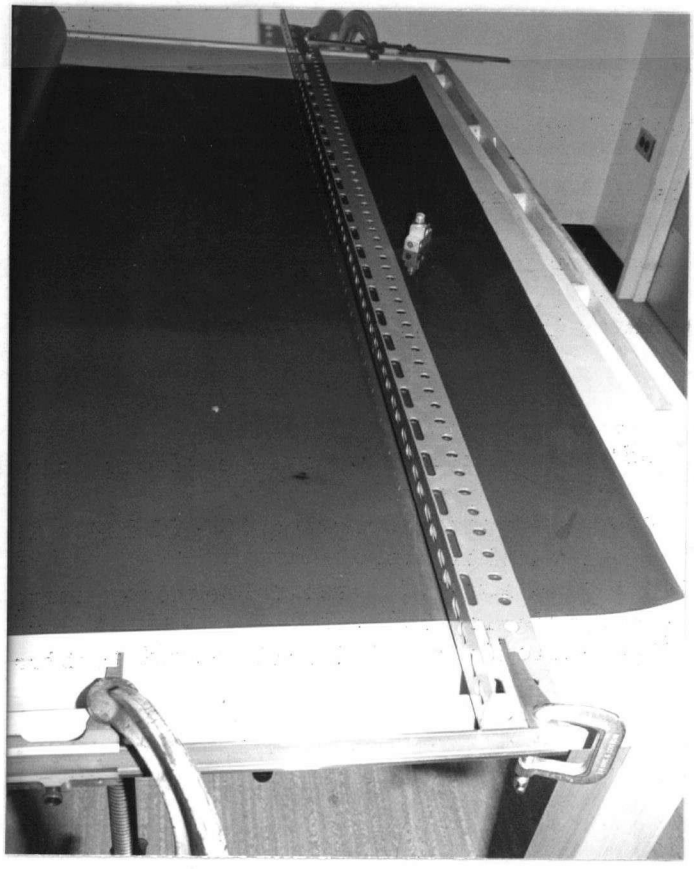

Fig. 5.1.

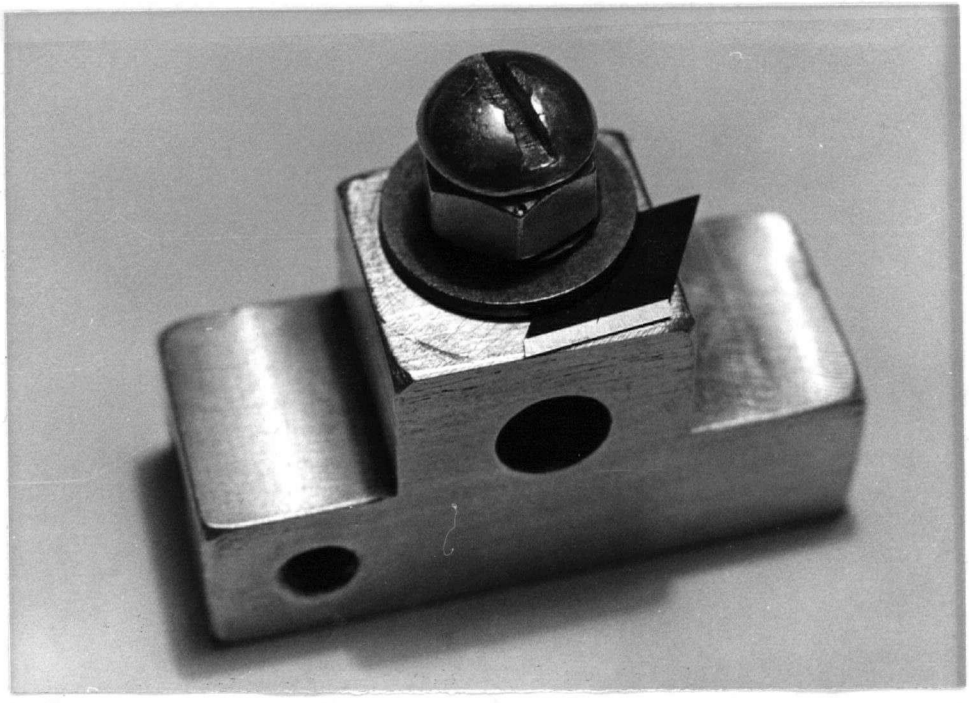

Fig. 5.2.

proved to be a problem, so it was necessary to work at night with all machinery shut off.

The film was developed in Kodak D-19 for 7 minutes at 20°C in a spiral tank with constant agitation. This was followed by a 30 second deionized water rinse and immersion for 45 seconds in a fixing bath. After a five minute wash in flowing water, the film was rinsed with a wetting agent and hung up to dry.

No special problems were encountered with the masks made for the 2-section IDT. Gaf PR-102 positive photoresist was used according to the manufacturers recommendations. Lifting of the photoresist was encountered in acid etchants (Fig. 5.3) or alkaline etchants with strong

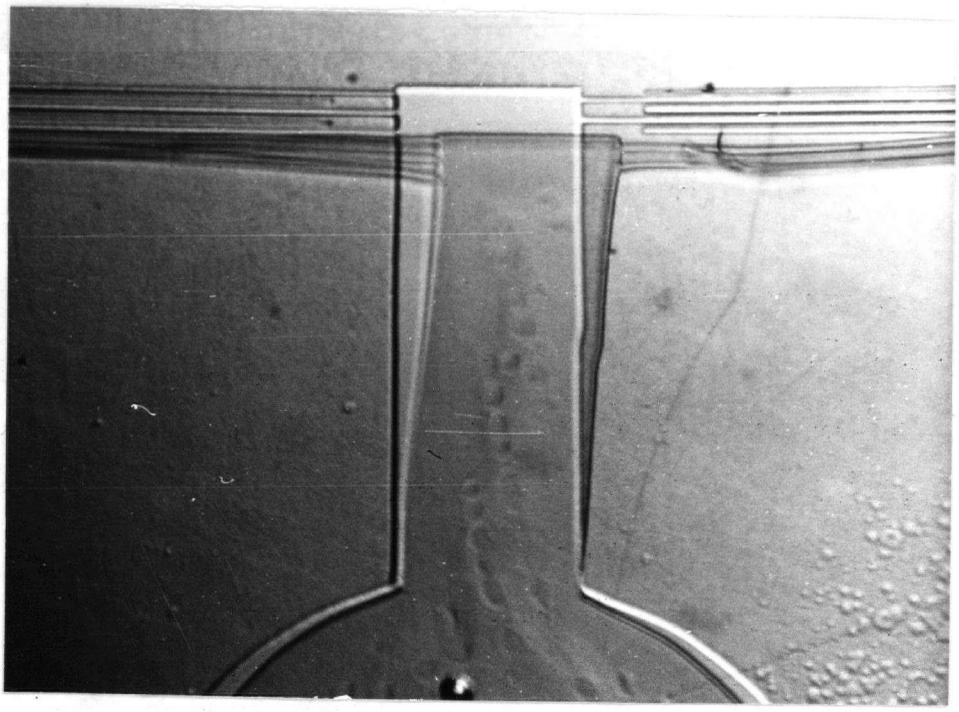

Fig. 5.3 Lifting of Photoresist.

gas evolution. Good results were obtained in an alkaline ferricyanide etchant made with $7\frac{1}{2}$ g K_3 $Fe(CN)_6$, $2\frac{1}{2}$ g NaOH and 200 ml deionized water. The photoresist was exposed under a high-pressure mercury vapour lamp. The optimal exposure and development times were found by trial and error.

For the second beam-steered transducer, the artwork was about 1.3 meters wide and had 0.5 mm linewidths. These dimensions were reduced 118X to about 11 mm and 4.3 μm respectively. Because of the large overall width and the narrow linewidth required, usable masks proved difficult to make. Although the resolving power of the lens was very high, there was a small loss in image contrast 5 mm from the center of the negative. This was sufficient to prevent the photolithography from working. The negative contrast was increased by intensification. Chromium intensifier was tried first, but this actually reduced the image density. The most likely reason was a loss of silver during redevelopment in D-19 by the solvent action of sodium sulfite on the thin (6 μm) film emulsion. Excellent results were obtained with Ansco 331 intensifier [90]. Redevelopment was for 15 seconds; if this step was carried too far, the image density could easily be reduced in a 5% hypo solution. Caution in handling was required with this intensifier, since it contained mercuric chloride and potassium cyanide. Although the intensified masks appeared to have very high contrast, problems were still encountered near the ends of the transducer, probably on account of a faint residual optical density there, between fingers in the photomask. Figure 5.4 shows the typical result in an etched transducer. Increasing the etching time resulted in open fingers before all the aluminum islands dissolved. Figure 5.5 shows the clean photoresist pattern obtained near the center of the mask, where no problems were encountered. The difficulty was finally solved by

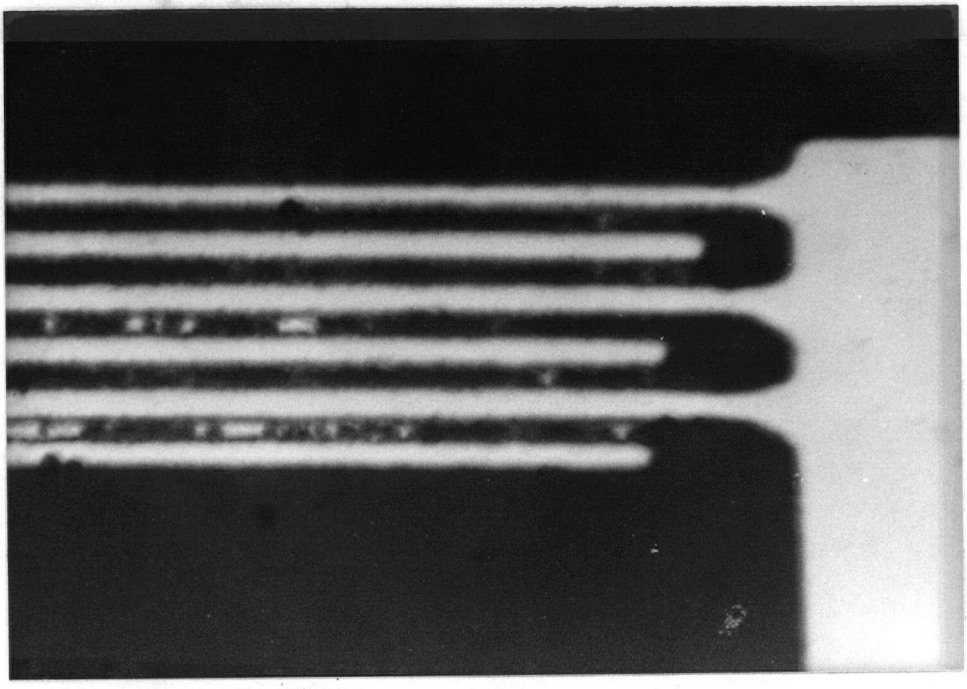

Fig. 5.4 Shorted Transducer.

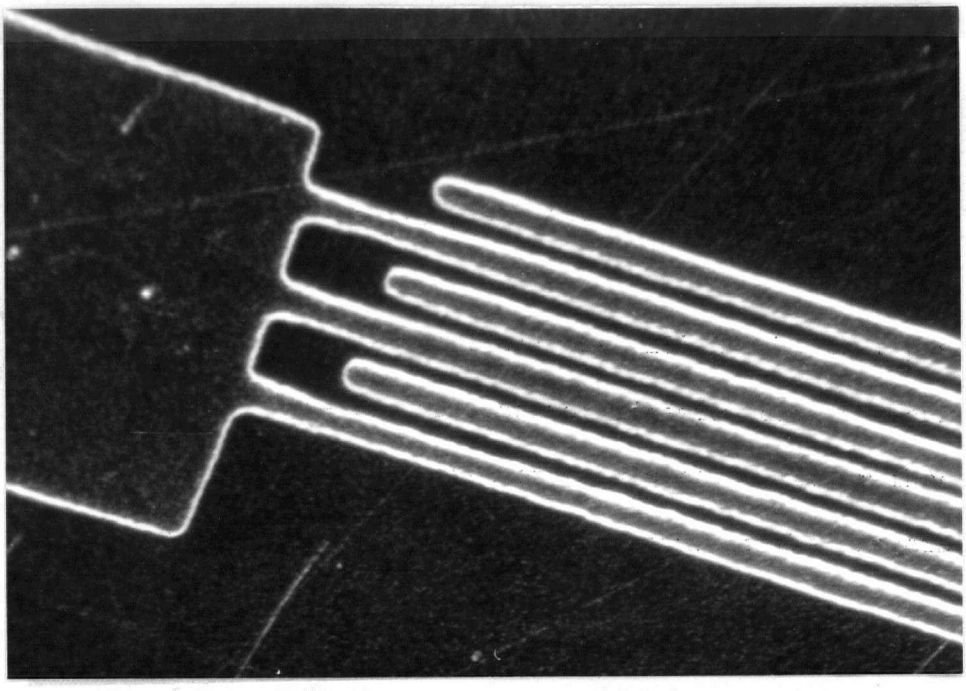

Fig. 5.5 Photoresist Pattern near IDT Center.

adding a 10 minute bake at 100°C between the exposure and development of the photoresist [91]. This had the effect of smoothing out the inhibitor concentration in the exposed areas of the photoresist, thereby increasing the rate and uniformity of development in these areas. This is particularly true near the highly reflective aluminum surface, where standing waves during exposure result in a maximum in inhibitor concentration. Figure 5.6 shows a photograph (taken in a scanning electron microscope) of the excellent results obtained.

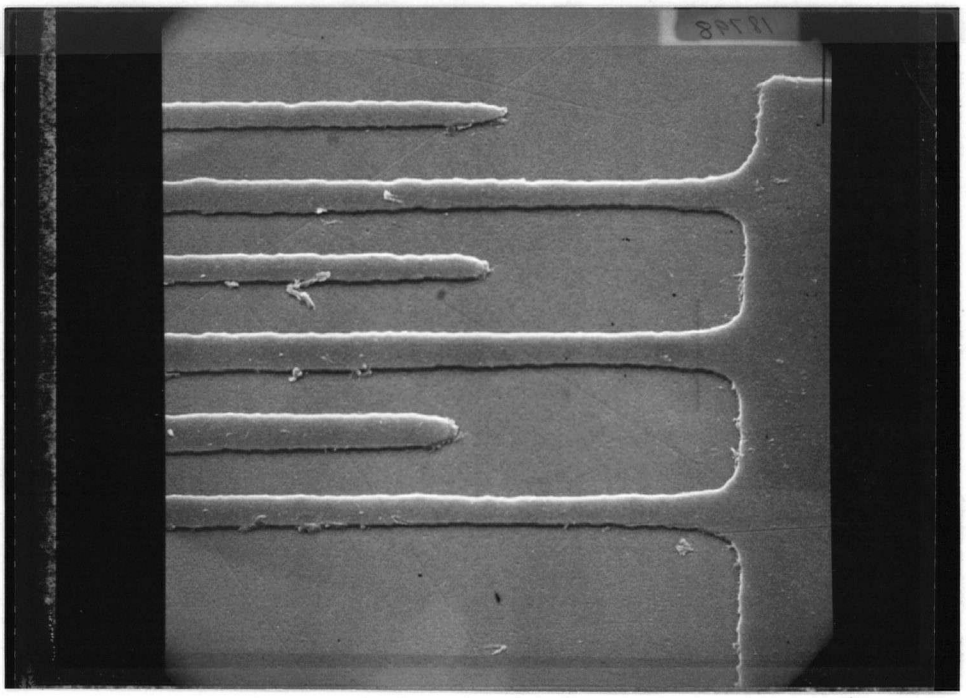

Fig. 5.6 Portion of Beam Steering Transducer used in the Experiments (2000X).

To make this device, Hunt Chemicals LSI 395 Waycoat positive photoresist was used because of its superior adhesion during etching in Transene aluminum etchant type A. Use of this etchant rather than the alkaline ferricyanide resulted in less undercutting of the fingers. The complete procedure was as follows.

(1) The substrate was cleaned ultrasonically in chromic acid, boiled in reagent grade methyl ethyl ketone and blown dry with nitrogen. Figure 5.7 shows the aluminum film lifting during etching on account of inadequate cleaning of the substrate.

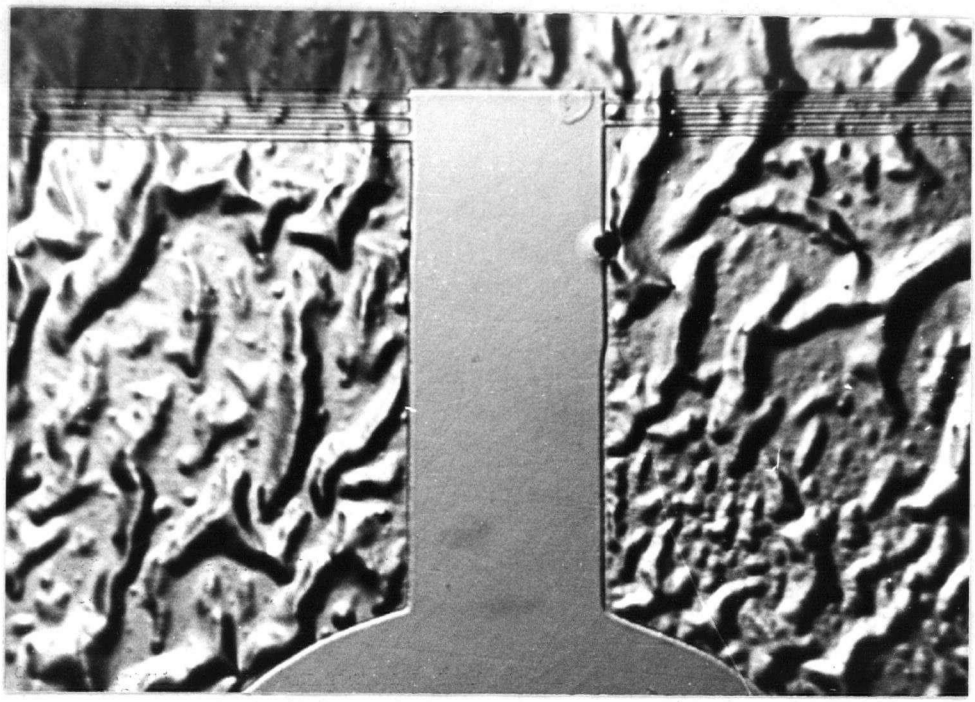

Fig. 5.7 Lifting of Aluminum Film.

(2) A layer of aluminum a few tenths of a micron thick was deposited in a Veeco vacuum system using a tungsten coil as the evaporation source. The thickness was monitored with an Ificon 321 quartz crystal film thickness monitor.

(3) The freshly deposited aluminum film was coated with a 1 μm coating of photresist by spinning at 5000 rpm for 20 seconds.

(4) The photoresist was baked for 90°C for 30 minutes in a convection oven.

(5) The substrate was placed in a vacuum holder designed to assure

close contact between mask and substrate during exposure of the photo-resist. The alignment of the transducer with respect to the substrate crystal axes was done by mounting the holder on a microscope stage (Fig. 5.8) and aligning a square grid in the eyepiece with the straight

Fig. 5.8 Photolithography Station in Laminar Flow Hood.

edge of the substrate, which was normal to the crystal Z axis. The mask was moved by hand until it was aligned in the appropriate direction (Fig. 5.9), at which time the vacuum was turned on.

(6) An exposure of 41 seconds was given at a distance of 10 cm from a high pressure mercury vapor lamp. The lamp required 10 minutes of operating time to reach a stable output level.

(7) The sample was baked for 10 minutes at 100°C.

(8) The sample was developed in Waycoat Positive LSI developer diluted 1:1 with deionized water at 24°C for 60 seconds.

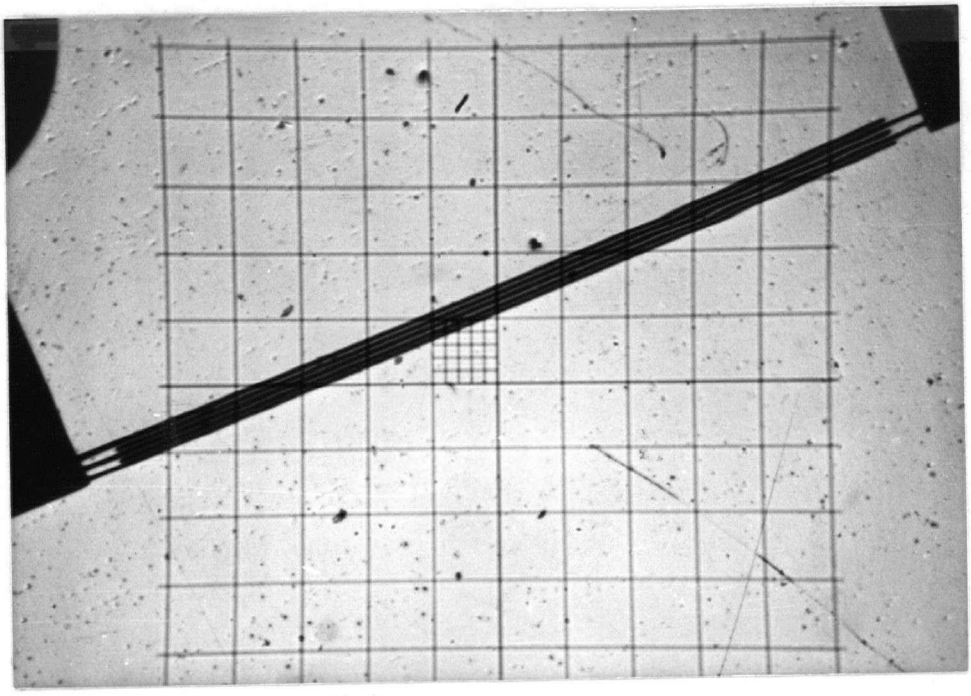

Fig. 5.9 Correct Mask Alignment for Z-21.8° SAW Propagation (tan 21.8° = .4).

(9) A postbake of 30 minutes at 100°C was given.

(10) The aluminum was etched in Transene aluminum etchant (type A) at full strength with constant agitation to remove small bubbles.

(11) The device was rinsed in deionized water, blown dry and examined by microscope.

(12) The photoresist was stripped in methyl ethyl ketone and the finished transducer was blown dry with nitrogen gas.

6. CONCLUSIONS

Acoustic beam steering has been found effective in improving the bandwidth and diffraction efficiency of planar acousto-optic light deflectors. A viable device model has been proposed. The effects of anisotropic acoustic diffraction were taken into account through the parabolic velocity surface approximation. Auld and Kino's equations [53] for the series IDT equivalent circuit model were used so that variations in the electrode metallization factor could be taken into account. The IDT loss resistance was calculated using a modified form of Lakin's theory [63]. Equations for the acoustic power as a function of transmission line and equivalent circuit parameters were developed. A rigorous treatment of the acousto-optic interaction was given, and the diffraction efficiency was calculated using the known and measured properties of $LiNbO_3$ and the SAW and OGW fields. Addition of a modified theory of acoustic beam steering suitable for the analysis of IDT arrays completed the device model. Good agreement was found between theory and experiments. As pointed out in Chapter 4, better performance could have been obtained at higher acoustic frequencies. The fine linewidths required above 500 MHz could be obtained with electron beam lithography.

The indiffusion of nickel was found to be an excellent method for making high quality optical surface waveguides with losses below 1 dB/cm. Longer diffusion times at higher temperatures were found to increase optical absorption, an effect that was not entirely reversible by subsequent baking in oxygen. Small quantities of O_2 or N_2 in the argon gas needed to provide an inert diffusion atmosphere were found to reduce the impurity concentration considerably, probably due to the formation of oxides or nitrides of nickel on the $LiNbO_3$ surface.

The primary limitation in device performance stems from the limited bandwidth of interdigital transducers. It may be possible to improve this by mechanically loading the $LiNbO_3$ surface. Alternatively, if adjacent sections in the beam-steering IDT had different center frequencies, improved performance could probably be obtained. At widely separated frequencies, different parts of the array would radiate surface waves. Before these devices become commercially viable the problem of stable, efficient coupling to the OWG must be solved. Use of grating couplers should improve the performance in this regard. If a laser diode could be used as the light source, it could be permanently fixed to have the correct orientation with respect to the coupler and a small, rugged device would be obtained.

APPENDIX I

In this appendix, a brief summary is given of the properties of $LiNbO_3$ used in the calculations.

There is some variation in the published values of the refractive indices. At $\lambda = 0.6328$ μm, Kaminow and Carruthers [4] give $n_e = 2.214$ and $n_o = 2.294$. These values give the best agreement between experiment and theory. The dielectric permittivity tensor used is therefore

$$\varepsilon_{ij} = \begin{bmatrix} 45.2624 & 0 & 0 \\ 00 & 5.2623 & 0 \\ 0 & 0 & 4.9018 \end{bmatrix} .$$

For the electrooptic tensor, Turner's values [93] were used. In matrix form, these are

$$r^S_{ij} = \begin{bmatrix} 0 & -3.4 & 8.6 \\ 0 & -3.4 & 8.6 \\ 0 & 0 & 30.8 \\ 0 & 28 & 0 \\ 28 & 0 & 0 \\ -3.4 & 0 & 0 \end{bmatrix} \times 10^{-12} \text{ m/V} .$$

in the principal axes system. The matrix form of the elastooptic tensor used is

$$p_{ij} = \begin{bmatrix} .036 & .072 & .092 & .055 & 0 & 0 \\ .072 & .036 & .092 & -.055 & 0 & 0 \\ .178 & .178 & .088 & 0 & 0 & 0 \\ .155 & -.155 & 0 & .019 & 0 & 0 \\ 0 & 0 & 0 & 0 & .019 & .11 \\ 0 & 0 & 0 & 0 & .31 & .048 \end{bmatrix}$$

Most of these are Dixon and Cohen's values [93]. However, these authors do not give p_{14}, p_{44} and p_{66}, so Kludzin's numbers were used for these [93]. On the next three pages, the dielectric permittivity, electrooptic and elastooptic tensors are given in coordinate systems rotated about the crystal z axis. The rotation by 21.8° corresponds to the values used in the overlap integral calculation. The permittivity change factors for acoustic strain, $\epsilon_{3j}p_{jklm}\epsilon_{kn}$, and for the SAW electric field, $\epsilon_{3j}r_{jkl}\epsilon_{k3}$, are also given. They are called DEPSS(L,M) and DEPSE(L), respectively.

ANGLE OF ROTATION IN XZ PLANE = 0.00 DEGREES

DIELECTRIC PERMITTIVITY TENSOR

```
EPSR(11)=  5.26240 00    EPSR(21)=  0.00000-01    EPSR(31)=  0.00000-01
EPSR(12)=  0.00000-01    EPSR(22)=  5.26240 00    EPSR(32)=  0.00000-01
EPSR(13)=  0.00000-01    EPSR(23)=  0.00000-01    EPSR(33)=  4.9018D 00
```

ELECTROOPTIC TENSOR

```
PR(111)= 0.0000-01  PR(211)= 0.0000-01  PR(311)= 1.4000-11  PR(121)= 0.0000-01  PR(221)= 0.0000-01  PR(321)= 0.0000-01
PR(131)= 1.4000-11  PR(231)= 0.0000-01  PR(331)= 0.0000-01  PR(112)=-3.4000-12  PR(212)=-3.4000-12  PR(312)= 0.0000-01
PR(122)=-3.4000-12  PR(222)= 3.4000-12  PR(322)= 1.4000-11  PR(132)= 0.0000-01  PR(232)= 1.4000-11  PR(332)= 0.0000-01
PR(113)= 8.6000-12  PR(213)= 0.0000-01  PR(313)= 0.0000-01  PR(123)= 0.0000-01  PR(223)= 8.6000-12  PR(323)= 0.0000-01
PR(133)= 0.0000-01  PR(233)= 0.0000-01  PR(333)= 3.0800-11  PR(
```

ELASTOOPTIC TENSOR

```
PR(1111)= 3.6000-02  PR(2111)= 0.0000-01  PR(3111)= 0.0000-01  PR(1211)= 0.0000-01  PR(2211)= 7.2000-02  PR(3211)= 7.7500-02
PR(1311)= 0.0000-01  PR(2311)= 7.7500-02  PR(3311)= 1.7800-01  PR(1121)= 0.0000-01  PR(2121)= 1.2000-02  PR(3121)= 2.7500-02
PR(1221)= 1.2000-02  PR(2221)= 0.0000-01  PR(3221)= 0.0000-01  PR(1321)= 2.7500-02  PR(2321)= 0.0000-01  PR(3321)= 0.0000-01
PR(1131)= 0.0000-01  PR(2131)= 7.7500-02  PR(3131)= 4.7500-03  PR(1231)= 7.7500-02  PR(2231)= 0.0000-01  PR(3231)= 0.0000-01
PR(1331)= 4.7500-03  PR(2331)= 0.0000-01  PR(3331)= 0.0000-01  PR(1112)= 0.0000-01  PR(2112)= 1.2000-02  PR(3112)= 2.7500-02
PR(1212)= 1.2000-02  PR(2212)= 0.0000-01  PR(3212)= 0.0000-01  PR(1312)= 2.7500-02  PR(2312)= 0.0000-01  PR(3312)= 0.0000-01
PR(1122)= 7.2000-02  PR(2122)= 0.0000-01  PR(3122)= 0.0000-01  PR(1222)= 0.0000-01  PR(2222)= 3.6000-02  PR(3222)=-7.7500-02
PR(1322)= 0.0000-01  PR(2322)=-7.7500-02  PR(3322)= 1.7800-01  PR(1132)= 2.7500-02  PR(2132)= 0.0000-01  PR(3132)= 0.0000-01
PR(1232)= 0.0000-01  PR(2232)=-2.7500-02  PR(3232)= 4.7500-03  PR(1332)= 0.0000-01  PR(2332)= 4.7500-03  PR(3332)= 0.0000-01
PR(1113)= 0.0000-01  PR(2113)= 7.7500-02  PR(3113)= 4.7500-03  PR(1213)= 7.7500-02  PR(2213)= 0.0000-01  PR(3213)= 0.0000-01
PR(1313)= 4.7500-03  PR(2313)= 0.0000-01  PR(3313)= 0.0000-01  PR(1123)= 2.7500-02  PR(2123)= 0.0000-01  PR(3123)= 0.0000-01
PR(1223)= 0.0000-01  PR(2223)=-2.7500-02  PR(3223)= 4.7500-03  PR(1323)= 0.0000-01  PR(2323)= 4.7500-03  PR(3323)= 0.0000-01
PR(1133)= 9.2000-02  PR(2133)= 0.0000-01  PR(3133)= 0.0000-01  PR(1233)= 0.0000-01  PR(2233)= 9.2000-02  PR(3233)= 0.0000-01
PR(1333)= 0.0000-01  PR(2333)= 0.0000-01  PR(3333)= 8.8000-02  PR(
```

PERMITTIVITY CHANGE FACTORS FOR TE MODE WITH ELECTRIC FIELD ALONG ROTATED Z AXIS

```
DEPSE(1)=      -0.0000000D 00
DEPSE(2)=      -0.0000000D 00
DEPSE(3)=      -0.7400560-09
DEPSS(11)=     -0.4276010 01
DEPSS(12)=     -0.0000000 00
DEPSS(13)=     -0.0000000 00
DEPSS(21)=     -0.0000000 00
DEPSS(22)=     -0.4276010 01
DEPSS(23)=     -0.0000000 00
DEPSS(31)=     -0.0000000 00
DEPSS(32)=     -0.0000000 00
DEPSS(33)=     -0.2114030 01
```

ANGLE OF ROTATION IN XZ PLANE = -21.80 DEGREES

DIELECTRIC PERMITTIVITY TENSOR

EPSR(11)= 5.2127D 00 EPSR(21)= 0.0000D-01 EPSR(31)= 1.2435D-01
EPSR(12)= 0.0000D-01 EPSR(22)= 5.2624D 00 EPSR(32)= 0.0000D-01
EPSR(13)= 1.2435D-01 EPSR(23)= 0.0000D-01 EPSR(33)= 4.9515D 00

ELECTROOPTIC TENSOR

RR(111)=-1.3300D-11 RR(211)= 0.0000D-01 RR(311)= 1.2260D-11 RR(121)= 0.0000D-01 RR(221)=-3.1940D-12 RR(321)= 0.0000D-01
RR(131)= 1.2260D-11 RR(231)= 0.0000D-01 RR(331)=-1.3370D-12 RR(112)=-2.9310D-12 RR(212)=-8.3560D-12 RR(312)=-1.1720D-12
RR(122)=-8.3560D-12 RR(222)= 3.4000D-12 RR(322)= 1.1740D-11 RR(132)=-1.1720D-12 RR(232)= 1.1740D-11 RR(332)=-4.6890D-13
RR(113)= 7.2420D-12 RR(213)= 0.0000D-01 RR(313)=-3.3420D-12 RR(123)= 0.0000D-01 RR(223)= 7.9850D-12 RR(323)= 0.0000D-01
RR(133)=-3.3420D-12 RR(233)= 0.0000D-01 RR(333)= 2.9380D-11 RR(

ELASTOOPTIC TENSOR

PR(1111)= 6.2790D-02 PR(2111)=-7.4040D-02 PR(3111)=-4.4390D-02 PR(1211)=-7.4040D-02 PR(2211)= 7.4760D-02 PR(3211)= 4.2190D-02
PR(1311)=-4.4390D-02 PR(2311)= 4.2190D-02 PR(3311)= 1.4650D-01 PR(1121)=-2.6410D-02 PR(2121)= 1.1000D-02 PR(3121)= 1.4970D-02
PR(1221)= 1.1000D-02 PR(2221)= 1.0210D-02 PR(3221)= 2.5000D-03 PR(1321)= 1.4970D-02 PR(2321)= 2.5000D-03 PR(3321)= 1.6200D-02
PR(1131)=-1.4740D-02 PR(2131)= 4.2190D-02 PR(3131)=-1.4870D-02 PR(1231)= 4.2190D-02 PR(2231)=-6.8960D-03 PR(3231)= 4.5650D-02
PR(1331)=-1.4870D-02 PR(2331)= 4.5650D-02 PR(3331)= 2.6460D-02 PR(1112)=-2.6410D-02 PR(2112)= 1.1000D-02 PR(3112)= 1.4970D-02
PR(1212)= 1.1000D-02 PR(2212)= 1.0210D-02 PR(3212)= 2.5000D-03 PR(1312)= 1.4970D-02 PR(2312)= 2.5000D-03 PR(3312)= 1.6200D-02
PR(1122)= 8.6620D-02 PR(2122)= 2.8780D-02 PR(3122)=-3.6550D-02 PR(1222)= 2.8780D-02 PR(2222)= 3.6000D-02 PR(3222)=-7.1960D-02
PR(1322)=-3.6550D-02 PR(2322)=-7.1960D-02 PR(3322)= 1.6340D-01 PR(1132)= 1.4970D-02 PR(2132)= 2.5000D-03 PR(3132)= 1.6200D-02
PR(1232)= 2.5000D-03 PR(2232)=-2.5530D-02 PR(3232)= 5.7500D-03 PR(1332)= 1.6200D-02 PR(2332)= 5.7500D-03 PR(3332)= 1.0560D-02
PR(1113)=-1.4740D-02 PR(2113)= 4.2190D-02 PR(3113)=-1.4870D-02 PR(1213)= 4.2190D-02 PR(2213)=-6.8960D-03 PR(3213)= 4.5650D-02
PR(1313)=-1.4870D-02 PR(2313)= 4.5650D-02 PR(3313)= 2.6460D-02 PR(1123)= 1.4970D-02 PR(2123)= 2.5000D-03 PR(3123)= 1.6200D-02
PR(1223)= 2.5000D-03 PR(2223)=-2.5530D-02 PR(3223)= 5.7500D-03 PR(1323)= 1.6200D-02 PR(2323)= 5.7500D-03 PR(3323)= 1.0560D-02
PR(1133)= 6.4240D-02 PR(2133)= 4.5650D-02 PR(3133)=-3.1910D-03 PR(1233)= 4.5650D-02 PR(2233)= 8.9240D-02 PR(3233)= 2.9770D-02
PR(1333)=-3.1910D-03 PR(2333)= 2.9770D-02 PR(3333)= 1.0040D-01 PR(

PERMITTIVITY CHANGE FACTORS FOR TE MODE WITH ELECTRIC FIELD ALONG ROTATED Z AXIS

DEPSE(1)= 0.1780000-10
DEPSE(2)= 0.1228560-10
DEPSE(3)= -0.7153440-09
DEPSS(11)= -0.3538680 01
DEPSS(12)= -0.4152080 00
DEPSS(13)= -0.6302560 00
DEPSS(21)= -0.4152080 00
DEPSS(22)= -0.3942060 01
DEPSS(23)= -0.2791010 00
DEPSS(31)= -0.6302560 00
DEPSS(32)= -0.2791010 00
DEPSS(33)= -0.2440070 01

ANGLE OF ROTATION IN XZ PLANE = 90.00 DEGREES

DIELECTRIC PERMITTIVITY TENSOR

```
EPSR(11)=  4.9018D 00    EPSR(21)=  0.0000D-01    EPSR(31)=  0.0000D-01
EPSR(12)=  0.0000D-01    EPSR(22)=  5.2624D 00    EPSR(32)=  0.0000D-01
EPSR(13)=  0.0000D-01    EPSR(23)=  0.0000D-01    EPSR(33)=  5.2624D 00
```

ELECTROOPTIC TENSOR

```
RR(111)= 3.080D-11  RR(211)= 0.000D-01  RR(311)= 0.000D-01  RR(121)= 0.000D-01  RR(221)= 8.600D-12  RR(321)= 0.000D-01
RR(131)= 0.000D-01  RR(231)= 0.000D-01  RR(331)= 8.600D-12  RR(112)= 0.000D-01  RR(212)= 1.400D-11  RR(312)= 0.000D-01
RR(122)= 1.400D-11  RR(222)= 3.400D-12  RR(322)= 3.400D-12  RR(132)= 0.000D-01  RR(232)= 3.400D-12  RR(332)=-3.400D-12
RR(113)= 0.000D-01  RR(213)= 0.000D-01  RR(313)= 1.400D-11  RR(123)= 0.000D-01  RR(223)= 0.000D-01  RR(323)= 0.000D-01
RR(133)= 1.400D-11  RR(233)= 0.000D-01  RR(333)= 0.000D-01  RR(
```

ELASTOOPTIC TENSOR

```
PR(1111)= 8.800D-02  PR(2111)= 0.000D-01  PR(3111)= 0.000D-01  PR(1211)= 0.000D-01  PR(2211)= 9.200D-02  PR(3211)= 0.000D-01
PR(1311)= 0.000D-01  PR(2311)= 0.000D-01  PR(3311)= 9.200D-02  PR(1121)= 0.000D-01  PR(2121)= 4.750D-03  PR(3121)= 0.000D-01
PR(1221)= 4.750D-03  PR(2221)=-2.750D-02  PR(3221)= 0.000D-01  PR(1321)= 0.000D-01  PR(2321)= 0.000D-01  PR(3321)= 2.750D-02
PR(1131)= 0.000D-01  PR(2131)= 0.000D-01  PR(3131)= 4.750D-03  PR(1231)= 0.000D-01  PR(2231)= 0.000D-01  PR(3231)= 1.375D-02
PR(1331)= 4.750D-03  PR(2331)= 1.375D-02  PR(3331)= 0.000D-01  PR(1132)= 0.000D-01  PR(2132)= 4.750D-03  PR(3132)= 0.000D-01
PR(1212)= 4.750D-03  PR(2212)=-2.750D-02  PR(3212)= 0.000D-01  PR(1312)= 0.000D-01  PR(2312)= 0.000D-01  PR(3312)= 2.750D-02
PR(1122)= 1.780D-01  PR(2122)=-7.750D-02  PR(3122)= 0.000D-01  PR(1222)=-7.750D-02  PR(2222)= 3.600D-02  PR(3222)= 0.000D-01
PR(1322)= 0.000D-01  PR(2322)= 0.000D-01  PR(3322)= 7.200D-02  PR(1132)= 0.000D-01  PR(2132)= 0.000D-01  PR(3132)= 7.500D-02
PR(1232)= 0.000D-01  PR(2232)= 0.000D-01  PR(3232)= 0.000D-01  PR(1332)= 7.500D-02  PR(2332)= 0.000D-01  PR(3332)= 0.000D-01
PR(1113)= 0.000D-01  PR(2113)= 0.000D-01  PR(3113)= 4.750D-03  PR(1213)= 0.000D-01  PR(2213)= 0.000D-01  PR(3213)= 1.375D-02
PR(1313)= 4.750D-03  PR(2313)= 1.375D-02  PR(3313)= 0.000D-01  PR(1123)= 0.000D-01  PR(2123)= 0.000D-01  PR(3123)= 7.500D-02
PR(1223)= 0.000D-01  PR(2223)= 0.000D-01  PR(3223)= 0.000D-01  PR(1323)= 7.500D-02  PR(2323)= 0.000D-01  PR(3323)= 0.000D-01
PR(1133)= 1.780D-01  PR(2133)= 7.750D-02  PR(3133)= 0.000D-01  PR(1233)= 7.750D-02  PR(2233)= 7.200D-02  PR(3233)= 0.000D-01
PR(1333)= 0.000D-01  PR(2333)= 0.000D-01  PR(3333)= 3.600D-02  PR(
```

PERMITTIVITY CHANGE FACTORS FOR TE MODE WITH ELECTRIC FIELD ALONG ROTATED Z AXIS

```
DEPSE(1)=          -0.2381620D-09
DEPSE(2)=           0.9815700-10
DEPSE(3)=          -0.0000000D 00
DEPSS(11)=         -0.2547760D 01
DEPSS(12)=         -0.7615640 00
DEPSS(13)=         -0.0000000D 00
DEPSS(21)=         -0.7615640 00
DEPSS(22)=         -0.1903910 01
DEPSS(23)=         -0.0000000D 00
DEPSS(31)=         -0.0000000D 00
DEPSS(32)=         -0.0000000D 00
DEPSS(33)=         -0.9969560 00
```

APPENDIX II

WAVE PROPAGATION IN ANISOTROPIC MEDIA

An anisotropic, non-absorbing medium is characterized by the dielectric tensor

$$\hat{\varepsilon} = \begin{bmatrix} \varepsilon_{11} & 0 & 0 \\ 0 & \varepsilon_{22} & 0 \\ 0 & 0 & \varepsilon_{33} \end{bmatrix} \varepsilon_o$$

in the principal axes system.

The wave equation has the form

$$\nabla \times (\nabla \times \vec{E}) = -\frac{1}{c^2} \frac{\partial^2 \vec{D}}{\partial t^2} . \qquad \text{(II.1)}$$

For plane harmonic waves of the type, $e^{j(\vec{k}\cdot\vec{r} - \omega t)}$ the following operator identification can be made:

$$\nabla \rightarrow j\vec{k}$$

$$\frac{\partial}{\partial t} \rightarrow -j\omega$$

The wave equation then becomes

$$\vec{k} \times (\vec{k} \times \vec{E}) + \frac{\omega^2}{c^2} \vec{D} = 0 , \qquad \text{(II.2)}$$

which can only be satisfied if the wavevector $\vec{k}$ is perpendicular to the electric displacement vector $\vec{D}$, and if $\vec{D}$, $\vec{E}$ and $\vec{k}$ are in the same plane. Expansion of the triple cross product and use of $\vec{k}\cdot\vec{D} = 0$ gives

$$\vec{E}\cdot\vec{D} = ED\cos\theta = \frac{\omega^2}{k^2 c^2} D^2 = \frac{v^2}{c^2} D^2 , \qquad \text{(II.3)}$$

where $v = \frac{\omega}{k}$ is the phase velocity of the wave. Since the power flow direction is given by the Poynting vector

$$\vec{S} = \frac{1}{2} \vec{E} \times \vec{H}^*,$$

we see that planes of constant phase propagate at an angle θ to the direction of power flow, and that $(\vec{D}, \vec{H}, \vec{k})$ as well as $(\vec{E}, \vec{H}, \vec{S})$ constitute a mutually orthogonal triad of vectors. This is illustrated in Fig. II.1. The ray velocity (defined as the velocity of power flow) is then given by

$$u = v/\cos\theta \ . \qquad \text{(II.4)}$$

The principal indices of refraction are defined by

$$n_i = \sqrt{\varepsilon_{ii}} \ . \qquad \text{(II.5)}$$

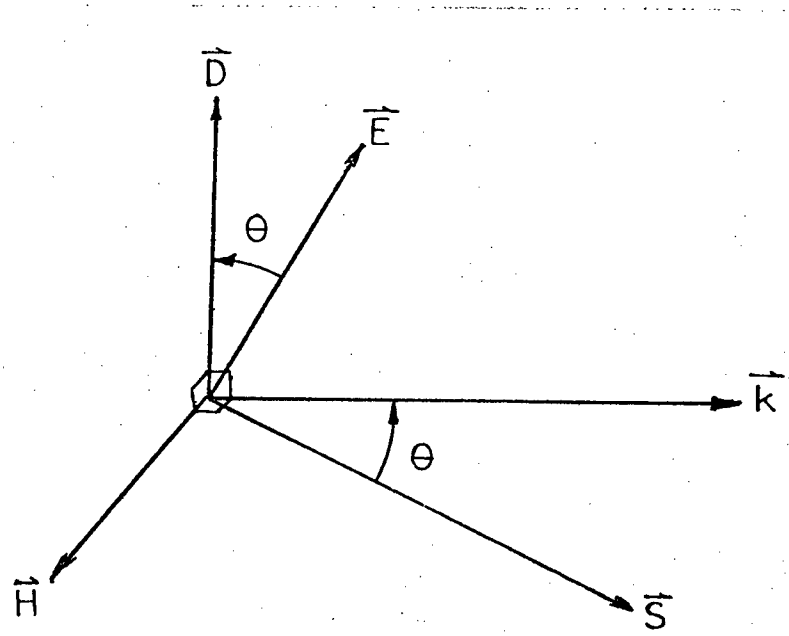

Fig. II.1

When equation (II.2) is written in Cartesian components, three homogeneous linear equations in E_x, E_y and E_z result. A nontrivial solution exists only if the determinant of coefficients [85]

$$\begin{bmatrix} [(n_1\omega/c)^2-k_y^2-k_z^2] & k_xk_y & k_xk_z \\ k_yk_x & [(n_2\omega/c)^2-k_x^2-k_z^2] & k_yk_z \\ k_zk_x & k_zk_y & [(n_3\omega/c)^2-k_x^2-k_y^2] \end{bmatrix} = 0, \quad \text{(II.6)}$$

where the substitution (II.5) has been made. This determinant represents a three-dimensional figure in $\vec{k}$ space. In all directions but those along the optic axes of the medium, the surface is double-valued. It can then be shown that two $\vec{k}$ vectors can exist, corresponding to two mutually orthogonal directions of wave polarization.

If the substitution

$$k_i = v_i \frac{\omega}{v^2}$$

is made in (II.6), the determinant assumes the form

$$\begin{bmatrix} [n_1^2v^4/c^2-v_y^2-v_z^2] & v_xv_y & v_xv_z \\ v_yv_x & [n_2^2v^4/c^2-v_x^2-v_z^2] & v_yv_z \\ v_zv_x & v_zv_y & [n_3^2v^4/c^2-V_x^2-v_y^2] \end{bmatrix} = 0, \quad \text{(II.7)}$$

which represents the double-sheeted phase velocity surface. Two values of phase velocity are possible for orthogonally polarized waves travelling in the same direction.

When $\vec{D}$ is expressed in terms of its projections along $\vec{E}$ and $\vec{u}$,

$$\vec{D} = \vec{E}\frac{D}{E}\cos\theta + \vec{u}\frac{\vec{u}\cdot\vec{D}}{u^2} \quad \text{(II.8)}$$

Writing this in terms of Cartesian components and setting the determinant of coefficients equal to zero gives

$$\begin{bmatrix} \{c^2/n_1^2-u_y^2-u_z^2\} & u_x u_y & u_x u_z \\ u_y u_z & \{c^2/n_2^2-u_x^2-u_z^2\} & u_y u_z \\ u_z u_x & u_z u_y & \{c^2/n_3^2-u_x^2-u_y^2\} \end{bmatrix} = 0, \qquad \text{(II-8)}$$

the equation for the ray velocity surface.

These equations may be utilized as follows. If propagation is, for example, in the xy plane, setting k_z, v_z and u_z equal to zero gives three sets of equations:

$$k_z = 0: \quad k_x^2 + k_y^2 = (n_3\omega/c)^2$$

$$k_x^2/(n_1\omega/c)^2 + k_y^2/(n_2\omega/c)^2 = 1$$

$$v_z = 0: \quad v_x^2 + v_y^2 = c^2/n_3$$

$$v_x^2/n_2^2 + v_y^2/n_1^2 = v^4/c^2$$

$$u_z = 0: \quad u_x^2 + u_y^2 = c^2/n_3^2$$

$$n_2^2 u_x^2 + n_1^2 u_y^2 = c^2 \ ,$$

which describe the propagation characteristics of waves in the xy plane. Waves with $\vec{E} = E_z\vec{z}$ propagate with refractive index n_3, whilst waves with $\vec{E} = E_x\vec{x} + E_y\vec{y}$ propagate with a refractive index with magnitude between n_1 and n_2.

REFERENCES

[1] D. Marcuse, Theory of Dielectric Optical Waveguides, Academic Press, N.Y., Chapter one (1974).

[2] P.K. Tien, Appl. Opt. 10,2395(1971).

[3] I.P. Kaminow and R.V. Schmidt, Appl. Phys. Lett. 25,458(1974).

[4] I.P. Kaminow and J.R. Carruthers, Appl. Phys. Lett. 22,326 (1973).

[5] P.K. Tien, S. Riva-Sanseverino, R.J. Martin, A.A. Ballman and H. Brown, Appl. Phys. Lett. 24, 503(1974).

[6] E. Conwell, Appl. Phys. Lett. 23,328(1973).

[7] E. Conwell, Appl. Phys. Lett. 25,40(1974).

[8] L. Schiff, Quantum Mechanics, McGraw-Hill, 178(1949).

[9] D. Marcuse, IEEE J. Quantum Electron. QE-9,1000(1973).

[10] G.B. Hocker and W.K. Burns, IEEE J. Quantum Electron. QE-11,270 (1975)

[11] J.M. White and P.F. Heidrich, Appl. Opt. 15, 151(1976).

[12] J.M. Hammer and W. Phillips, Appl. Phys. Lett. 24, 545(1974).

[13] W. Phillips, Ferroelectrics 10, 221 (1976).

[14] V. Ramaswamy and R. Standley, Appl. Phys. Lett. 26, 10(1975).

[15] J. Noda, Appl. Phys. Lett. 27,131(1975).

[16] J. Midwinter, IEEE J. Quantum Electron. QE-6,583(1970).

[17] J. Harris and R. Schubert, IEEE Trans., MTT-19, 269(1971).

[18] M. Dakss, L. Kuhn, P.F. Heidrich and B. Scott, Appl. Phys. Lett. 17, 265(1970).

[19] R. Ulrich and R. Torge, Appl. Opt. 12, 2901(1973).

[20] W. Tsang and S. Wang, Appl. Phys. Lett. 24, 196(1974).

[21] J.R. Carruthers, I.P. Kaminow and L.W. Stulz, Appl. Opt. 13(1974). 2333

[22] L. Brown, Metallurgy Department, UBC, private communication.

[23] A. Warner, M. Onoe and G. Coquin, J. Acoust. Soc. Am. 42,1223(1966).

[24] G.B. Brandt, E.P. Supertze and T. Henningsen, Appl. Opt. 12,2898 (1973).

[25] P.A. White and S.E. Smith, Inert Atmospheres, Butterworth and Co., 125 (1962).

[26] Per Kofstadt, Oxidation of Metals, J. Wiley and Sons, N. Y., 170(1966).

[27] W. Ballman and M. Gernand, Phys. Stat. Sol. (a) 9, 301 (1972).

[28] R. Swalin, Thermodynamics of Solids, J. Wiley and Sons, 303 (1962).

[29] Gmelin's Handbuch G57bL2, 414.

[30] ibid., 496.

[31] ibid., 1004.

[32] A.S. Grove, Physics and Technology of Semiconductor Devices, John Wiley and Sons, 45 (1967).

[33] D.L. Staebler and W. Phillips, Appl. Phys. Lett. 24, 268(1974).

[34] J. Powell and B. Craseman, Quantum Mechanics, Addison-Wesley Co., Reading, Mass., 140-147 (1965).

[35] M. Abramowitz and I.A. Stegun, Handbook of Mathematical Functions, 298 (1972)

[36] ibid., 446.

[37] R. White and Voltmer, Appl. Phys. Lett. 7,314(1965).

[38] J. Nye, Physical Properties of Crystals, Oxford, 99 (1969).

[39] G.A. Coquin and H.F. Tiersten, J. Acoust. Soc. Am. 41,921(1966).

[40] A.J. Slobodnik, E.D. Conway and R.T. Delmonico, Editors, Microwave Acoustics Handbook, AFCRL-73-0597 (1973).

[41] J. Campbell and W. Jones, IEEE Trans., SU-15,209(1968).

[42] R. Spaight and G. Koerber, IEEE Trans., SU-18,237(1971)

[43] M.G. Cohen, J. Appl. Phys. 38,3821(1967).

[44] R. Weglein, M. Pedinoff and H. Winston, Electron. Lett. 6,654(1970).

[45] J.C. Crabb, J.D. Maines and N.R. Ogg, Electron. Lett. 7,253(1971).

[46] T.L. Szabo and A.J. Slobodnik, IEEE Trans., SU-20, 240(1973).

[47] M. Kharusi and G. Farnell, J. Acoust. Soc. Am. 48, 665(1970).

[48] R.M. De LaRue, C. Stewart, C.D.W. Wilkinson and I.R. Williamson, Electron. Lett. 9, 326(1973).

[49] R.F. Milsom and M. Redwood, Proc. IEE 118, 831 (1971).

[50] C. Tseng, IEEE Trans., ED-15, 586(1968).

[51] S. Joshi and R. White, J. Acoust. Soc. Am. 46, 17(1968).

[52] H. Engan, IEEE Trans., ED-16, 1014(1969).

[53] B. Auld and G. Kino, IEEE Trans., ED-18, 898(1971).

[54] J. Collins, H. Gerard and H. Shaw, Appl. Phys. Lett. 13, 312(1968).

[55] K. Ingebrigsten, J. Appl. Phys. 40, 2681(1969).

[56] P. Emtage, J. Acoust. Soc. Am. 51, 1142(1972).

[57] W.R. Smith, H. Gerard, J. Collins, T. Reeder and H. Shaw, IEEE Trans., MTT-17, 856 and 865 (1969).

[58] A. Bahr and R. Lee, Electron. Lett. 9, 281(1973).

[59] R. Weglein and G. Nudd, IEEE Trans., ED-16, 1014(1969).

[60] F. Marshall, C. Newton, and E. Paige, IEEE Trans., MTT-21,206(1973).

[61] R.V. Schmidt, J. Appl. Phys., 43, 2498(1972).

[62] M. Daniel and P. Emtage, J. Appl. Phys., 43, 4872(1972).

[63] K. Lakin, IEEE Trans., MTT-22, 418(1974).

[64] A. Warner, M. Onoe and G. Coquin, J. Acoust. Soc. Am. 42,1223(1966).

[65] N. Reilly, R. Milsom and M. Redwood, Electron. Lett., 9, 419(1973).

[66] C. Raman and B. Nath, Proc. Ind. Acad. Sci., 2A, 406, 1933.

[67] W.G. Mayer, G. Lamers and D. Auth, J. Acoust. Soc. Am. 42, 1255(1967).

[68] L. Brillouin, Ann. Phys. (Paris), 9th ser., V17, 88 (1922).

[69] P. Debye and F. Sears, Proc. Nat. Acad. Sci (USA) 18, 409 (1932).

[70] L. Kuhn, M. Kakss, P. Heidrich and B. Scott, Appl. Phys. Lett. 17, 265(1970).

[71] R.V. Schmidt and I.P. Kaminow, IEEE J. Quantum Electron. QE-10, 57(1975).

[72] Y. Ohmachi, J. Appl. Phys. 44, 3928(1973).

[73] J. White, P. Heidrich and E.G. Lean, Electron. Lett. 10,510(1974).

[74] C.S. Tsai, M.A. Alhaider, L.T. Nguyen and B. Kim, Proc. IEEE 64, 318(1976).

[75] K.W. Loh, W.S.C. Chang, W.R. Smith and T. Grudkowski, Appl. Opt. 15, 156(1976).

[76] R.V. Schmidt, IEEE Trans., SU-23, 22(1976).

[77] G.A. Alphonse, RCA Review 33,543(1972).

[78] M. Born and E. Wolf, Principles of Optics, Pergammon Press 569(1965).

[79] J. Nye, Physical Properties of Crystals, Oxford (1969).

[80] R.C. Chu and T. Tamir, IEEE Trans., MTT-17, 1002(1969).

[81] Collin, Field Theory of Guided Waves, McGraw-Hill,368(1960).

[82] R. Dixon, IEEE J. Quantum Electron. 3, 85(1967).

[83] E. Gordon, Proc. IEEE 54, 1391(1966).

[84] A. Korpel, R. Adler, P. Desmarais and W. Watson, Appl. Opt. 5, 1667 (1966).

[85] G.R. Fowles, Introduction to Modern Optics, Holt, Rinehart and Winston, Chapter 4 (1968).

[86] D.A. Pinnow, IEEE Trans., SU-18(1971).

[87] C.S. Tsai, L. Nguyen, S. Yao and M. Alhaider, Appl. Phys. Lett. 26, 140(1975).

[88] B. Kim and C. Tsai, Proc. IEEE 64, 329 (1976).

[89] G.I. Stegeman, IEEE Trans., SU-23, 43(1976).

[90] Black and White Processing Data Book, American Photographic Book Publishing Co. Inc., N.Y. (1975).

[91] E.J. Walker, IEEE Trans., ED-22, 464(1975).

[92] H. Kogelnik, IEEE Trans., MTT-23, 2(1975).